

AN ABSTRACT OF A THESIS

ANALYSIS AND CONTROL OF AN AC/DC PWM RECTIFIER- ASSISTED INDUCTION GENERATOR

Jyoti Sastry

Master of Science in Electrical Engineering

The development of the model of series and parallel rectifiers and the operation of these rectifiers at unity power factor was achieved. The method of control to achieve unity power factor operation was presented using the dq model of the rectifier topologies. This condition of operation is achieved by an in-depth steady state analysis of the converter topologies.

A novel method of steady-state analysis of an induction machine as a dc power generator is developed, where the steady-state model was obtained using the dq reference frame equivalent circuits of the induction generator system. Also, the self-excitation requirements of an induction generator were studied, in terms of the magnitude of the modulation index of the rectifier. The detailed analysis studied the system under two operating conditions, rated slip and minimum loss. The condition for minimum loss was achieved by operation of the generator at the slip calculated to satisfy this condition. The effect of magnetic saturation was also accounted for in the analysis.

A new control structure for the rotor-flux vector control of an induction machine as a dc generator was developed, where the input-output linearization method was used in separating the linear from the nonlinear terms in the system model equations. The proposed control scheme aims at regulating the dc voltage at the output of the rectifier. The robustness of the proposed control scheme was tested and verified by simulation and experimental results.

Control of an induction generator using natural variables was a new method of control put forth. The control scheme was simpler as the system model was in the stationary reference frame. The system model used included a loss-minimization loop, whereby the reference rotor flux in the control scheme was calculated such that the induction generator system operates under a condition of minimum loss.

ANALYSIS AND CONTROL OF AN AC/DC PWM RECTIFIER-
ASSISTED INDUCTION GENERATOR

A Thesis

Presented to

The Faculty of the Graduate School

Tennessee Technological University

by

Jyoti Sastry

In Partial Fulfillment

Of the Requirements of the Degree

MASTER OF SCIENCE

Electrical Engineering

August 2005

CERTIFICATE OF APPROVAL OF THESIS

**ANALYSIS AND CONTROL OF AN AC/DC PWM RECTIFIER-
ASSISTED INDUCTION GENERATOR**

by

Jyoti Sastry

Graduate Advisory Committee:

Joseph O. Ojo, Chairperson _____
date

Prit Chowdhuri _____
date

Ghadir Radman _____
date

Approved for the Faculty:

Francis Otuonye
Associate Vice President for Research
and Graduate Studies

Date

STATEMENT OF PERMISSION TO USE

In presenting this thesis in partial fulfillment of the requirements for a Master of Science degree at Tennessee Technological University, I agree that the University Library shall make it available to borrowers under rules of the Library. Brief quotations from this thesis are allowable without special permission, provided that accurate acknowledgement of the source is made.

Permission for extensive quotation from or reproduction of this thesis may be granted by my major professor when the proposed use of the material is for scholarly purposes. Any copying or use of the material in this thesis for financial gain shall not be allowed without my written permission.

Signature_____

Date_____

DEDICATION

This work is dedicated to my family.

ACKNOWLEDGEMENTS

I would sincerely like to express my gratitude to the chairperson of my committee, Dr. Joseph Ojo, for his support throughout the period of my Masters Program. I would like to thank Dr. Ghadir Radman and Dr. Prit Chowdhuri for serving as faculty members on my committee.

I would also like to thank Zhiqiao Wu, Gan Dong, Conard Murray, and L.V. Randolph for their invaluable help during the course of this project. I would also like to thank the Department of Electrical and Computer Engineering, Center for Energy Systems Research, and the Office of Naval Research (ONR) for the financial support provided during my study.

I would like to thank my parents, brother, sister, and Varghese Muthalaly for their moral support, invaluable help, and encouragement during the course of my Masters Program.

TABLE OF CONTENTS

	Page
LIST OF FIGURES	XI
LIST OF TABLES	XXV
CHAPTER	
1. INTRODUCTION	1
1.1 INTRODUCTION	1
1.1.1 Classification of Switching Power Converters	2
1.2 INDUCTION GENERATORS.....	4
1.3 RESEARCH GOALS	5
1.4 ORGANIZATION OF THESIS	6
2. LITERATURE REVIEW	9
2.1 INTRODUCTION	9
2.2 SERIES- PARALLEL BOOST RECTIFIERS.....	10
2.3 INDUCTION GENERATORS.....	13
3. MODELING OF THREE-PHASE BOOST RECTIFIER.....	19
3.1 INTRODUCTION	19
3.2 OPERATION OF THREE-PHASE BOOST RECTIFIER	20
3.3 POSSIBLE SWITCHING MODES OF THE BOOST RECTIFIER.....	25

	Page
3.4 MODULATION TECHNIQUES.....	29
3.5 RELATIONSHIP BETWEEN SWITCHING FUNCTION AND MODULATION SIGNAL	30
3.6 MODEL OF THREE-PHASE BOOST RECTIFIER.....	32
3.7 DYNAMIC SIMULATION OF THREE-PHASE BOOST RECTIFIER.....	40
3.8 STEADY – STATE ANALYSIS.....	43
4. SERIES AND PARALLEL BOOST RECTIFIERS	49
4.1 INTRODUCTION	49
4.2 PARALLEL RECTIFIERS.....	51
4.2.1 Model of Parallel Rectifiers.....	51
4.2.2 Steady State Analysis.....	58
4.2.3 Dynamic Simulation.....	64
4.3 SERIES RECTIFIER	71
4.3.1 Model of Series Rectifier.....	72
4.3.2 Steady State Analysis.....	75
4.3.3 Dynamic Simulation.....	79
4.4 PARALLEL RECTIFIERS WITH COMMON INPUT SOURCE.....	82
4.4.1 Model of Parallel Rectifiers.....	84
4.4.1 Steady State Analysis.....	88
4.4.1 Dynamic Simulation.....	90
5. MODELING OF AND PARAMETER DETERMINATION OF THREE-PHASE INDUCTION MACHINE.....	99

	Page
5.1 INTRODUCTION	99
5.2 BASIC OPERATION OF AN INDUCTION MACHINE.....	100
5.2.1 Stator-Flux Model of Induction Machine.....	107
5.2.1 Rotor-Flux Model of Induction Machine	109
5.2.1 Natural Variables Model of Induction Machine	112
6. STEADY-STATE ANALYSIS OF VSI-ASSISTED INDUCTION GENERATOR.	123
6.1 INTRODUCTION	123
6.2 SYSTEM MODEL.....	124
6.2.1 Steady-State Model of Battery.....	126
6.2.2 Overall System Model.....	127
7. MODELING OF THREE-PHASE INDUCTION GENERATOR- RECTIFIER	
SYSTEM.....	145
7.1 INTRODUCTION	145
7.2 SYSTEM MODEL.....	147
8. STEADY-STATE EXCITATION OF INDUCTION GENERATOR –RECTIFIER	
SYSTEM.....	153
8.1 INTRODUCTION	153
8.2 STEADY-STATE MODEL	154
8.3 VARIATION OF L_M WITH MAGNETIZING FLUX.....	157
8.4 ANALYSIS AT RATED SLIP	159
8.4.1 Influence of Magnetizing Flux on ‘M’	159

	Page
8.4.2 Influence of Magnetizing Flux ' λ_m ' on Output DC voltage.....	171
8.5 ANALYSIS AT MINIMUM COPPER LOSS.....	183
8.5.1 Condition of Minimum Copper Loss.....	183
8.5.2 Influence of Magnetizing Flux ' λ_m ' on 'M' under Minimum Copper Loss.....	187
8.5.3 Influence of λ_m on Output DC voltage.....	193
9. ROTOR FLUX VECTOR CONTROL OF THREE-PHASE INDUCTION GENERATOR-RECTIFIER SYSTEM.....	199
9.1 INTRODUCTION.....	199
9.2 VECTOR CONTROL OF AN INDUCTION MACHINE.....	200
9.3 PRINCIPLE OF VECTOR CONTROL.....	201
9.4 VECTOR CONTROL OF AN INDUCTION GENERATOR.....	204
9.5 CONTROLLER DESIGN FOR AN INDUCTION GENERATOR-RECTIFIER SYSTEM.....	209
9.6 DYNAMIC SIMULATION OF THE INDUCTION GENERATOR-RECTIFIER SYSTEM USING ROTOR FLUX VECTOR CONTROL.....	221
9.7 EXPERIMENTAL RESULTS FOR ROTOR FLUX VECTOR CONTROL SCHEME.....	231
10. CONTROL OF THREE-PHASE INDUCTION GENERATOR USING NATURAL VARIABLES.....	235
10.1 INTRODUCTION.....	235
10.2 NATURAL VARIABLES MODEL OF INDUCTION GENERATOR.....	236
10.2.1 Loss Minimization using Natural Variables Model.....	239
10.3 CONTROLLER DESIGN FOR NATURAL VARIABLES MODEL.....	240

	Page
10.4 DYNAMIC SIMULATION OF CONTROL SCHEME USING NATURAL VARIABLES	247
11. HARDWARE IMPLEMENTATION.....	255
11.1 INTRODUCTION	255
11.2 EXPERIMENTAL SETUP.....	255
11.2.1 Encoder.....	256
11.2.1 Sensors.....	257
11.2.2 Rectifier Design	259
12. CONCLUSION AND SCOPE FOR FUTURE WORK.....	260
12.1 SERIES-PARALLEL BOOST RECTIFIERS.....	260
12.2 INDUCTION GENERATOR-BOOST RECTIFIER SYSTEM.....	261
12.3 SCOPE FOR FUTURE WORK.....	263
REFERENCES.....	266

LIST OF FIGURES

	Page
Figure 1.1: Conversion of ac-ac	2
Figure 1.2: Conversion of ac-dc	3
Figure 1.3: Switching converter topologies	3
Figure 3.1: (a) single-phase bridge rectifier (b) three-phase bridge rectifier	19
Figure 3.2: Topology of three-phase boost rectifier	21
Figure 3.3. Modulated and unmodulated existence functions	22
Figure 3.4: Schematic illustrating KVL	24
Figure 3.5. Schematic illustrating KCL	25
Figure 3.6. Simplified schematic of boost rectifier	25
Figure 3.7 (a) to (c): Modes of operation of three-phase boost rectifier	27
Figure 3.7 (d) to (f): Modes of operation of three-phase boost rectifier	28
Figure 3.8: Sine-triangle PWM	29
Figure 3.9: Topology of three-phase boost rectifier	32
Figure 3.10: Simulation results for the rectifier, from top : (a) output dc voltage V_{dc} , (b) load current I_L , (c) dc output current I_p	41
Figure 3.11: Simulation results for the rectifier, from top: (a) phase 'a' current I_a , (b) phase 'b' current I_b , (c) phase 'c' current I_c	42
Figure 3.12: Simulation results for the rectifier, from top: (a) phase 'a' voltage V_a , (b) phase 'b' voltage V_b , (c) phase 'c' voltage V_c	42

Figure 3.13 Simulation results for the rectifier, from top: (a) modulation signal for phase ‘a’ M_a , (b) modulation signal for phase ‘b’ M_b , (c) modulation signal for phase ‘c’ M_c	43
Figure 3.14: Variation of M_q with the dc voltage with varying load resistance of $R_L = 30\Omega, 60\Omega, \text{ and } 150\Omega$,.....	47
Figure 3.15: Variation of M_d with the dc voltage with varying load resistance of $R_L = 30\Omega, 60\Omega, \text{ and } 150\Omega$	48
Figure 4.1: Topology of parallel connection of boost rectifiers with zero circulating currents.....	50
Figure 4.2: Topology of parallel connection of boost rectifiers with independent sources	52
Figure 4.3: Variation of the q-axis and d-axis modulation index with the output dc voltage varying between 300V and 100V at a constant load resistance of $R_L = 100\Omega$ for varying values of α for rectifier ‘a’	62
Figure 4.4: Variation of the q-axis and d-axis modulation index with the output dc voltage varying between 300V and 100V at a constant load resistance of $R_L = 100\Omega$ for varying values of α for rectifier ‘b’	62
Figure 4.5: Variation of the q-axis modulation index and power, with the dc voltage varying between 300V and 100V at a constant load resistance of $R_L = 100\Omega$ for varying values of α for rectifier ‘a’	63

Figure 4.6: Variation of the q-axis modulation index and power, with the dc voltage varying between 300V and 100V at a constant load resistance of $R_L = 100\Omega$ for varying values of α for rectifier 'b'	63
Figure 4.7: Simulation results for the parallel rectifier, from top : (a) output dc voltage V_{dc} , (b) load current I_L	64
Figure 4.8: Simulation results for the parallel rectifier, from top: (a) output dc current rectifier 'a' I_{p1} , (b) output dc current rectifier 'b' I_{p2}	65
Figure 4.9: Simulation results for the parallel rectifier, phase -a input voltage and current for rectifier 'a'	65
Figure 4.10: Simulation results for parallel rectifier, phase -a input voltage and current for rectifier 'b'	66
Figure 4.11: Simulation results for the parallel rectifier, phase voltages from top: (a) rectifier 'a', (b) rectifier 'b'	66
Figure 4.12: Simulation results for the parallel rectifier, phase currents from top: (a) rectifier 'a', (b) rectifier 'b'	67
Figure 4.13: Simulation results for the parallel rectifier, from top : (a) output dc voltage V_{dc} , (b) load current I_L	67
Figure 4.14: Simulation results for the parallel rectifier, from top : (a) output dc current rectifier 'a' I_{p1} , (b) output dc current rectifier 'b' I_{p2}	68
Figure 4.15: Simulation results for the parallel rectifier, phase -a input voltage and current for rectifier	68

Figure 4.16: Simulation results for the parallel rectifier, phase -a input voltage and current for rectifier69

Figure 4.17: Simulation results for the parallel rectifier, phase voltages from top: (a) rectifier ‘a’, (b) rectifier ‘b’69

Figure 4.18: Simulation results for the parallel rectifier, phase currents from top: (a) rectifier ‘a’, (b) rectifier ‘b’70

Figure 4.19: Topology for series rectifier connection72

Figure 4.20: Variation of the q and d-axis modulation signals, with the dc voltage varying between 80V and 550V for varying load resistances $R_L = 100\Omega, 150\Omega$ and 200Ω , for rectifier ‘a’78

Figure 4.21: Variation of the q and d-axis modulation signals with the dc voltage varying between 80V and 550V for varying load resistances $R_L = 100\Omega, 150\Omega$ and 200Ω ,for rectifier ‘b’78

Figure 4.22: Simulation results for the series rectifier, from top: (a) output dc voltage for rectifier ‘a’ V_{c1} , (b) output dc voltage for rectifier ‘b’ V_{c2} , (c) sum of output voltages for $V_{c1} + V_{c2}$, (c)load current I_L 79

Figure 4.23: Simulation results for the series rectifier, from top : (a) output dc current rectifier ‘a’ I_{p1} , (b) output dc current rectifier ‘b’ I_{p2} 80

Figure 4.24: Simulation results for the series rectifier, phase -a input voltage and current for rectifier ‘a’80

Figure 4.25: Simulation results for the series rectifier, phase -a input voltage and current for rectifier ‘b’81

Figure 4.26: Simulation results for the series rectifier, phase voltages from top: (a) rectifier 'a', (b) rectifier 'b'	81
Figure 4.27: Simulation results for the series rectifier, phase currents from top: (a) rectifier 'a', (b) rectifier 'b'	82
Figure 4.28: Circuit topology for parallel rectifiers with a common input source.....	83
Figure 4.29: Phase 'a' voltage and zero sequence current.....	89
Figure 4.30 Simulation results for the parallel rectifier, from top: (a) output dc voltage, (b) zero sequence currents I_{os1} and I_{os2} (c) phase 'a' voltage and current (scaled by a factor 10) for rectifier A, (d) phase 'a' voltage and current for rectifier B for $M_q = 0.7$, and $M_d = 0.07$	92
Figure 4.31: Simulation results for the parallel rectifier, from top: (a) output dc voltage, (b) zero sequence currents I_{os1} and I_{os2} (c) phase 'a' voltage and current (scaled by a factor 10) for rectifier A, (d) phase 'a' voltage and current for rectifier B for $M_q = 0.7$, and $M_d = 0.07$	94
Figure 4.32: Simulation results for the parallel rectifier, from top: (a) output dc voltage, (b) zero sequence currents I_{os1} and I_{os2} (c) phase 'a' voltage and current (scaled by a factor 10) for rectifier A, (d) phase 'a' voltage and current for rectifier B for $M_q = 0.7$, and $M_d = 0.07$	96
Figure 4.33: Simulation results for the parallel rectifier, from top: (a) output dc voltage, (b) zero sequence currents I_{os1} and I_{os2} (c) phase 'a' voltage and current (scaled by a factor 10) for rectifier A, (d) phase 'a' voltage and current for rectifier B for $M_q = 0.7$, and $M_d = 0.07$	97

Figure 5.1: Per-phase equivalent circuit for a three-phase induction machine.....	100
Figure 5.2(a) q-axis equivalent circuit in an arbitrary reference frame for the three-phase induction machine.....	106
Figure 5.2(b): d-axis equivalent circuit in an arbitrary reference frame for the three-phase induction machine.....	106
Figure 5.3: Equivalent circuit of three phase induction machine including the core loss resistance.....	116
Figure 5.4: Simplified equivalent circuit for three-phase induction machine.....	116
Figure 5.5 Equivalent circuit for short-circuit test.....	117
Figure 5.6 Equivalent circuit for no-load test.....	119
Figure 5.7: Variation of magnetizing inductance with input phase voltage.....	121
Figure 5.8: Variation of magnetizing inductance with magnetizing flux linkage.....	122
Figure 6.1: Proposed system model.....	124
Figure 6.2: Equivalent circuit model of battery.....	126
Figure 6.3: Simplified model of battery.....	127
Figure 6.4: Variation of V_d with magnetizing flux λ_m for a load resistance of $R_L=100\Omega$ and $L = 50\text{mH}$	136
Figure 6.5: Variation of I_d with magnetizing flux λ_m for a load resistance of $R_L=100\Omega$ and $L = 50\text{mH}$	137
Figure 6.6: Variation of M_q and M_d with magnetizing flux λ_m for a load resistance of 138 $R_L = 100\Omega$ and $L = 50\text{mH}$	138

Figure 6.7: Variation of M with magnetizing flux λ_m for a load resistance of $R_L=100\Omega$ and $L = 50\text{mH}$	139
Figure 6.8: Variation of V_d with magnetizing flux λ_m for a load resistance of $R_L= 10\Omega$ and $L = 5\text{mH}$	139
Figure 6.9: Variation of I_d with magnetizing flux λ_m for a load resistance of $R_L= 100\Omega$ and $L = 50\text{mH}$	140
Figure 6.10: Variation of M_q and M_d with magnetizing flux λ_m for a load resistance of $R_L= 100\Omega$ and $L = 50\text{mH}$	140
Figure 6.11: Variation of V_d with magnetizing flux λ_m for a load resistance of $R_L= 100\Omega$ and $L = 50\text{mH}$ under minimum loss condition.....	141
Figure 6.12: Variation of I_d with magnetizing flux λ_m for a load resistance of $R_L= 100\Omega$ and $L = 50\text{mH}$ under minimum loss condition.....	142
Figure 6.13: Variation of M_q and M_d with magnetizing flux λ_m for a load resistance of $R_L= 100\Omega$ and $L = 50\text{mH}$ under minimum loss condition.....	142
Figure 6.14: Variation of V_d with magnetizing flux λ_m for a load resistance of $R_L= 10\Omega$ and $L = 5\text{mH}$ under minimum loss condition.....	143
Figure 6.15: Variation of I_d with magnetizing flux λ_m for a load resistance of $R_L= 10\Omega$ and $L = 5\text{mH}$ under minimum loss condition.....	143
Figure 6.16: Variation of M_q and M_d with magnetizing flux λ_m for a load resistance of $R_L= 10\Omega$ and $L = 5\text{mH}$ under minimum loss condition.....	144

Figure 7.1: Generator modes of operation in an induction machine, from top: (a) poly-phase ac supply, (b) VSI with dc supply, (c) CSI with dc supply, (d) VSI self-excitation, (e) capacitive self-excitation, (f) CSI self-excitation.....	146
Figure 7.2: Induction generator-boost rectifier system model.....	148
Figure 8.1: System model	154
Figure 8.1: Variation of magnetizing inductance with peak magnetizing flux at a constant frequency.....	158
Figure 8.2: Variation of magnetizing inductance with peak phase voltage at a constant input frequency.....	158
Figure 8.3: Variation of modulation index with the magnetizing inductance for a constant load resistance and slip $s = -0.04$	164
Figure 8.4: Variation of modulation index with the rotor speed for fixed magnetizing flux and load resistance.....	165
Figure 8.5: Variation of modulation index with the magnetizing flux and load resistance.....	167
Figure 8.6: Variation of modulation index with the magnetizing flux and load resistance, illustrated as a contour plot.....	168
Figure 8.7: Variation of modulation index with the magnetizing flux and rotor speed ..	168
Figure 8.8: Variation of modulation index with the magnetizing flux and rotor speed ..	169
Figure 8.9: Variation of R_o with magnetizing flux linkage for varying operating slips..	169
Figure 8.10 Variation of R_o with the magnetizing flux and operating slip.....	170
Figure 8.11 Variation of R_o with the magnetizing flux and operating slip.....	170

Figure 8.12: Variation of the q-axis component of the magnetizing inductance with the peak magnetizing flux.....	173
Figure 8.13: Variation of output dc voltage with the q-axis component of the modulation index for varying load resistances for first value of magnetizing flux	175
Figure 8.14: Variation of output dc voltage with the q-axis component of the modulation index for varying load resistances for second value of magnetizing flux.....	176
Figure 8.15: Variation of output dc voltage with the d-axis component of the modulation index for varying load resistances for first value of magnetizing flux	177
Figure 8.16: Variation of output dc voltage with the d-axis component of the modulation index for varying load resistances for second value of magnetizing flux.....	177
Figure 8.17: Variation of output power with the q-axis component of the modulation index for varying load resistances for the first value of magnetizing flux	178
Figure 8.18: Variation of major axis length with the magnetizing flux for different values of 'M', for a fixed load resistance, rotor speed and slip	182
Figure 8.19: Variation of minor axis length with the magnetizing flux for different values of 'M', for a fixed load resistance, rotor speed and slip	183
Figure 8.20: Variation of the slip with magnetizing flux linkage λ_m	186
Figure 8.21: Variation of the magnitude of the modulation index with magnetizing flux linkage λ_m	188
Figure 8.22: Variation of the magnitude of the modulation index with magnetizing flux linkage λ_m and load resistance R_L	189

Figure 8.23: Variation of the magnitude of the modulation index with magnetizing flux linkage λ_m and load resistance R_L	190
Figure 8.24: Variation of the magnitude of the modulation index with magnetizing flux linkage λ_m and load resistance R_L	190
Figure 8.25: Variation of the magnitude of the modulation index with magnetizing flux linkage λ_m and load resistance R_L	191
Figure 8.26: Variation of the magnitude of the modulation index with magnetizing flux linkage λ_m and load resistance R_L	192
Figure 8.27: Variation of the magnitude of the modulation index with magnetizing flux linkage λ_m and load resistance R_L	193
Figure 8.28: Variation of output dc voltage with the q-axis component of the modulation index for varying load conditions for the λ_{m1}	194
Figure 8.29: Variation of output dc voltage with the q-axis component of the modulation index for varying load conditions for the λ_{m2}	195
Figure 8.30: Variation of output dc voltage with the d-axis component of the modulation index for varying load conditions for the λ_{m1}	195
Figure 8.31: Variation of output dc voltage with the d-axis component of the modulation index for varying load conditions for the λ_{m2}	196
Figure 8.32: Variation of output power with the q-axis component of the modulation index for varying load conditions for the λ_{m1}	196
Figure 8.33: Variation of major axis length with the magnetizing flux for different values of 'M', for a fixed load resistance, rotor speed	197

	Page
Figure 8.34: Variation of minor axis length with the magnetizing flux for different values of 'M', for a fixed load resistance, rotor speed	198
Figure 9.1: Block diagram representation of a separately excited dc motor.	200
Figure 9.2: Equivalent circuit model of induction machine in the synchronous reference frame. (a) d-axis (b) q-axis.....	202
Figure 9.3: Phasor representation of the stator currents and flux alignment	203
Figure 9.4: Schematic of a separately excited dc generator.....	205
Figure 9.5: Field orientation of the Orientation of rotor flux on d-axis	207
Figure 9.6: Generator system	209
Figure 9.7: Control Structure for machine.....	216
Figure 9.8: Control Structure	217
Figure 9.9: Pole placement using Butterworth polynomial	220
Figure 9.10: Simulation results for starting process, from top: (a) electromagnetic torque T_e (b) dc voltage V_{dc} , (c) phase 'a' voltage V_a	222
Figure 9.11: Simulation results for starting process, from top: (a) q-axis voltage V_{qs} (b) d-axis voltage V_{ds} , (c) load current I_L	223
Figure 9.12: Simulation results for starting process, from top: (a) voltage frequency ω_e (b) slip frequency ω_s , (c) rotor speed ω_r	224
Figure 9.13: Simulation results for dynamic process, from top: (a) electromagnetic torque T_e (b) dc voltage V_{dc} , (c) phase 'a' voltage V_a	225
Figure 9.14: Simulation results for dynamic process, from top: (a) q-axis voltage V_{qs} (b) d-axis voltage V_{ds} , (c) load current I_L	225

Figure 9.15: Simulation results for dynamic process, from top: (a) voltage frequency ω_e (b) slip frequency ω_s , (c) rotor speed ω_r	226
Figure 9.16: Simulation results for starting process, from top: (a) voltage frequency ω_e (b) slip frequency ω_s , (c) rotor speed ω_r	227
Figure 9.17: Simulation results for starting process, from top: (a) q-axis voltage V_{qs} (b) d-axis voltage V_{ds} , (c) load current I_L	227
Figure 9.18: Simulation results for starting process, from top: (a) electromagnetic torque T_e (b) dc voltage V_{dc} , (c) phase 'a' voltage V_a	228
Figure 9.19: Simulation results for dynamic process, from top: (a) voltage frequency ω_e (b) slip frequency ω_s , (c) rotor speed ω_r	229
Figure 9.20: Simulation results for dynamic process, from top: (a) q-axis voltage V_{qs} (b) d-axis voltage V_{ds} , (c) load current I_L	229
Figure 9.21: Simulation results for dynamic process, from top: (a) electromagnetic torque T_e (b) dc voltage V_{dc} , (c) phase 'a' voltage V_a	230
Figure 9.22: Dynamic response of the 2 hp induction generator. Reference dc voltage = 220V , rotor speed= 1320 rpm , load resistance = 80 Ω . (a) line-line voltage, V_{AC} (350 V/div); (b) line-to-line voltage V_{BC} (350 V/div); (c) phase A current (7.5 A/div); (d) phase B current (7.5A /div).....	231
Figure 9.23: Dynamic response of the 2 hp induction generator. Reference dc voltage = 220V , rotor speed= 1320 rpm , load resistance = 80 Ω . (a) dc voltage V_{dc} (137.5 V/div); (c) d-axis rotor flux (1.36/div); (d) phase A modulation signal (1.36 /div)	232

Figure 9.24: Steady-state response of the 2 hp induction generator. Reference dc voltage =220V, rotor speed= 1320 rpm , load resistance = 80 Ω . (a) line-line voltage, V_{AC} (350 V/div); (b) line-to-line voltage V_{BC} (350 V/div); (c) phase A current (7.5 A/div); (d) phase B current (7.5A /div).....	233
Figure 9.25: Dynamic response of the 2 hp induction generator. Reference dc voltage = 220V , rotor speed= 1320 rpm , load resistance = 80 Ω . (a) dc voltage V_{dc} (137.5 V/div); (c) d-axis rotor flux (1.36/div); (d) phase A modulation signal (1.36 /div)	234
Figure 10.1: System Model.....	235
Figure 10.2: Control loops in proposed control scheme.....	241
Figure 10.3: Simulation results for starting process, from top: (a) dc voltage V_{dc} (b) Load current voltage I_L , (c) rotor speed ω_r	248
Figure 10.4: Simulation results for starting process, from top: (a) electromagnetic torque T_e (b) reactive torque T_r , (c) rotor flux λ_{rT}	249
Figure 10.5: Simulation results for dynamic process, from top: (a) dc voltage V_{dc} (b) Load current voltage I_L , (c) rotor speed ω_r	250
Fig 10.6: Simulation results for dynamic process, from top: (a) electromagnetic torque T_e (b) reactive torque T_r , (c) rotor flux λ_{rT}	250
Figure 10.7: Simulation results for starting process, from top: (a) electromagnetic torque T_e (b) reactive torque T_r , (c) rotor flux λ_{rT}	251
Figure 10.8: Simulation results for starting process, from top: (a) dc voltage V_{dc} (b) Load current voltage I_L , (c) rotor speed ω_r	252

Figure 10.9: Simulation results for starting process, from top: (a) dc voltage V_{dc} (b) Load current voltage I_L , (c) rotor speed ω_r	253
Figure 10.10: Simulation results for starting process, from top: (a) electromagnetic torque T_e (b) reactive torque T_r , (c) rotor flux λ_{r1}	253
Figure 11.1: Schematic of experimental setup.....	256
Figure 11.2: Schematic of experimental setup.....	257
Figure 11.3: Voltage sensor used in ac voltage measurement	258
Figure 11.4: Voltage sensor used in dc voltage measurement.....	258
Figure 11.5: Current sensor used in line current measurement.....	258

LIST OF TABLES

	Page
Table 3.1: Variables used for three-phase boost rectifier model.....	21
Table 3.2: Switching modes for boost-rectifier.....	23
Table 4.1: Parameters for rectifier ‘a’	52
Table 4.2: Parameters for rectifier ‘b’	54
Table 4.3: Parameters used for parallel rectifiers.....	61
Table 4.4: Parameters for rectifier ‘a’	77
Table 4.5: Parameters for rectifier ‘b’	77
Table 4.6: Parameters for rectifier ‘A’ and ‘B’.....	93
Table 5.1 Parameters of per-phase equivalent circuit.....	101
Table 5.2: Measurements for short circuit test.....	118
Table 5.3: Experimental readings for no-load test	120
Table 6.1: Parameters used in model equations	128
Table 6.2: Parameters used in analysis	144
Table 8.1: Variables used in machine equations.....	155
Table 8.2: Variables used in capacitor voltage equation	157
Table 8.3: Parameters of 2 hp induction machine used in steady state analysis.....	163
Table 9.1: Controller Parameters	220
Table 9.1: Machine parameters used in dynamic simulation.....	221
Table 9.1. Machine parameters used in dynamic simulation.....	248

CHAPTER 1

INTRODUCTION

1.1 Introduction

Electronic equipment has become an indispensable part of everyday life. An important feature of the equipment used is the low power consumption, in a range of a few watts to a few hundreds of watts. Far less familiar is the electronic equipment, which operates at power levels of interest to the industry. Such equipment, its study, design, manufacture, and utilization is known under the general heading of ‘power electronics.’

There are numerous reasons for the importance of power electronics, of which the most important is controllability. Power electronic equipment is highly controllable. The speed of operation of these devices and the comparatively low losses are the main reason for the large range of applications of power electronics.

From the history of development of power electronics, it is evident that there are a large number of switching converter topologies and composite switching converters are possible.

These possibilities are expanded in terms of the realization of all the switching functions possible with the semiconductor switching devices available at present. This adds up to a very vast array of possible solutions in applying switching power converters to AC drive problems.

The following section briefly discusses the classification of switching power converters.

1.1.1 Classification of Switching Power Converters

A switching power converter is a power electronic system, which converts one level of electrical energy into another level of electrical energy, at the load by switching action. The conversion of electrical energy can be broadly classified as

- ac-to-ac
- ac-to-dc
- dc-to-ac
- dc-to-dc

Conversion of ac-to-ac is also called cycloconversion; this involves conversion of ac power of one frequency to an ac output power of another frequency, and can be carried out by a one-step or two-step process.

The two-step process would include an intermediate step involving the conversion of ac-to-dc and then back from dc-to-ac.

Similarly, conversion of ac-to-dc, also called rectification (Figure 1.2) is the process of conversion of ac input to dc output. The conversion to dc can be carried out for both single phase as well as three-phase ac as an input. The power semiconductor devices that are used in a rectifier are varied. Thyristors, diodes, IGBT's are some of the devices that are used in rectifiers (both single phase as well as three-phase).

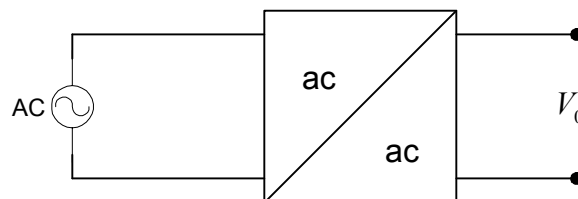


Figure 1.1: Conversion of ac-ac

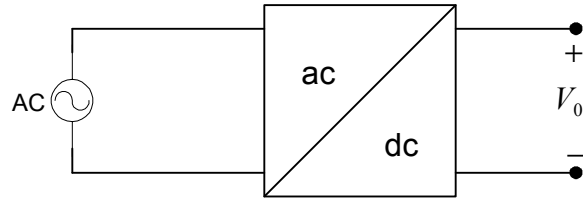


Figure 1.2: Conversion of ac-dc

The classification based on the *field of application* of switching power converters is shown in Figure 1.3 [A.8].

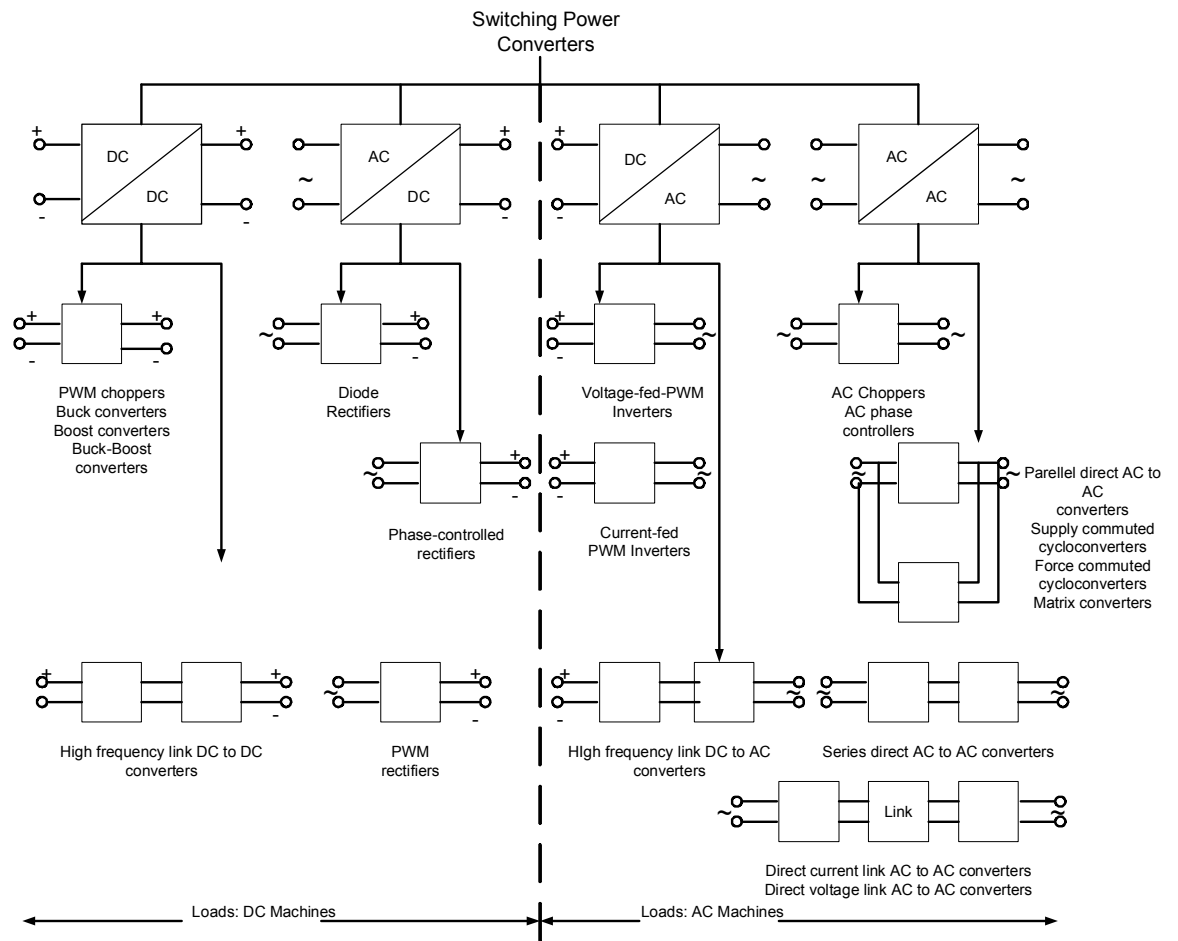


Figure 1.3: Switching converter topologies

Motion control applications with DC commutator machines use either PWM (pulse width modulated) choppers in various configurations or high-frequency link DC-DC converters in more specialized mobile applications. Therefore, the application of DC-DC coupled converters as well as high-frequency link transformer coupled converters are applied in motion control.

Converters in the AC to DC conversion field are the most widespread, and are found as input converter topologies for AC variable speed drives, whether that be as diode rectifier inputs to voltage fed inverter drives, controlled rectifier inputs to current-fed inverters, or PWM AC-to-DC converters for traction drives on locomotives.

1.2 Induction Generators

Induction motors are used extensively in the industry due to the low cost, and brushless commutator. However, the application of induction generators used to be minimal due to the lack of voltage control and stability of the generator. Therefore, the synchronous generator had taken precedence for a large period of time.

With the advent of nonconventional sources of energy, such as wind, hydro, etc., the applications of induction generators has greatly increased. Apart from the low cost and advantageous structure, the main feature of an induction generator that has led to the increase in its application in these areas is the ability for the generator to self-excite. With the connection of capacitors across the stator terminals of the machine, the build up of the air-gap flux takes place which in turn causes the voltage buildup. Other machines such as the synchronous generator require an independent source to enable excitation.

The process of self-excitation can be achieved in numerous ways, one of which is primarily used in this thesis.

1.3 Research Goals

This thesis studies in detail an induction-generator rectifier system for dc power generation. The system has been studied with the effect of saturation and under a condition of minimum copper loss.

The following are the topics addressed in this thesis.

- Development of the model of a high performance induction generator-boost rectifier system for dc power generation.
- The rectifier used in the system is studied in detail for different connection models (series and parallel), and operation at unity power factor of these models is proposed. The parallel rectifier scheme is studied for two different cases, one where each rectifier has an independent sources, and the second where the rectifiers share the same input ac source.
- Detailed analysis of the excitation requirements of the induction generator-ac/dc rectifier system is studied at steady state.
- Development of model and steady state analysis of a voltage source inverter assisted induction generator. The voltage source inverter is connected to a battery on the dc side to allow for bi-directional power flow in the system.
- Development of a rotor flux vector -control scheme for the control of the dc voltage of the boost rectifier.

- A second control scheme for the system under consideration is proposed using natural variables and loss minimization.
- Experimental verification of the rotor-flux vector control scheme.

1.4 Organization of Thesis

The organization of the thesis is as follows.

- Chapter 2 conducts a detailed literature survey on the previous work done in induction generator systems; both dynamic and steady-state operation. The chapter also includes sections on the past work done in series-parallel connections of boost rectifiers.
- Chapter 3 details the model of the boost rectifier used in the system under consideration. The simulation results and steady-state analysis are presented for the single rectifier.
- Chapter 4 proposes two topologies for the connection of boost rectifiers; each is dealt with it under unity power factor operation. The analysis verified by the dynamic simulation results for both the proposed connections of the rectifiers. Also a third scheme is detailed, where the parallel rectifier scheme is studied assuming a common input source for the two rectifiers.
- The parameter estimation and model of an induction generator is presented in chapter 5. The tests performed and the parameters calculated for the machine are presented using the equivalent circuit model of an induction

machine. Three models of the machine are derived; rotor flux, stator flux, and natural variables.

- Chapter 6 proposes a model of a voltage source inverter assisted induction generator for the generation of AC voltages. The stator windings are connected through a transformer to a three-phase boost rectifier. A battery is connected to the dc side of the boost rectifier. This scheme is modeled, and the steady-state analysis of the scheme studied in detail.
- The self-excitation process and the different methods of self-excitation of an induction generator with and without converters are discussed in the Chapter 7, following which the development of the complete model of the induction generator-rectifier system is obtained.
- Exhaustive study on the steady state-excitation conditions under various operating conditions of the system is made in Chapter 8. The effect of saturation on the performance and self-excitation requirements of the system has been studied. The system is studied under rated slip operation as well as operation under minimum copper loss.
- Chapter 9 proposes a rotor-flux vector control scheme for an induction generator-rectifier system for the control of the dc voltage of the rectifier. The model of the scheme is developed and the derivation of the controller transfer functions and parameters are dealt with. The scheme is simulated under various operating conditions.
- Chapter 10 proposes a second control scheme for the system. The scheme deals with step-by-step detailing of the model of the scheme and

derivation of the controller parameters. The dynamic simulation results are presented for the scheme to illustrate the robustness of the scheme and controller design.

- Chapter 11 discusses the overall structure of the experimental setup with each component briefly dealt with.
- Chapter 12 summarizes the work done in the thesis and concludes with suggestions for future work.

CHAPTER 2

LITERATURE REVIEW

2.1 Introduction

This chapter presents a review on the various works previously done on dc induction generators. The review includes the vast amount of work done in the area of rectifiers and the self-excitation methods of induction generators.

The first section highlights the work done on three-phase boost rectifiers and methods of control applied to different connection topologies of these rectifiers. The inherent advantages of some series and parallel connections over others are illustrated with the examples of work previously done.

The second section deals primarily with the self-excitation studies on induction generators. The vast amount of work done is discussed and the method of study of the process of self-excitation developed in this thesis is briefly put forth in contrast. Also, the different methods of control used in the dc voltage regulation of induction generators are discussed. Implementation of loss minimization in induction machines as well as application of induction generators in wind power generation is studied. The stability of an induction machine under different operating slips is also presented.

2.2 Series- Parallel Boost Rectifiers

The application of parallel and series connected converters has become more predominant. The most important feature of boost rectifiers, which increases the application areas of these rectifiers is the bi-directional current flow capability; this along with the model of the rectifier is studied in detail in [B.3]. The model of the three-phase boost rectifier is obtained using two methods; one is the 2-port circuit model, which is obtained to study the steady-state analysis of the system. The second model developed is the dq circuit model of the boost rectifier to study the transient response and open loop dynamic stability of the system.

The steady-state analysis of the boost rectifier system is studied in terms of the input current (or output power) and the output voltage. The output voltage is varied and the nature of variation of the input current for a change in the output voltage is graphically illustrated. As obtained from [B.3], a lower output voltage correspondingly decreases the possible region of output power; an increase in the input side inductor has the same effect on the possible region of output power (or input current). Also the open loop dynamic stability of the system is studied using the dq model of the boost rectifier.

The ability to control the system to obtain unity power factor operation of a boost rectifier is another important feature of the rectifier topology. Also, an increase in the current harmonics and a decrease in the displacement power factor in AC power lines produced by diode and thyristors are a serious problem, thereby highlighting the importance of the boost rectifier in minimizing these problems. The unity power factor control and the reduction in harmonics for the boost rectifier are studied in [B.4]. The

system considered in [B.4] comprises of a vector controlled induction motor with a boost rectifier and inverter. The emphasis is laid on the rectifier side of the scheme. The model of the system used treats the inverter and motor jointly and represents the two by an equivalent impedance. The controller designed uses a space vector pulse-width modulated scheme to control the rectifier operation at unity power factor with reduced harmonics.

The emphasis on paralleling converters has been made due to the inability to meet requirements such as low harmonics, high dynamic performance and high power. The method for reduction in harmonics proposed in [B.4] for a single rectifier raises issues of instability of the system due to the linearization technique employed. Another method to increase the overall power capability and reduce harmonics is to parallel converters.

The nature of the topology used in paralleling converters would mainly be application oriented. A unique feature of parallel converters is the potential zero sequence circulating current. There has been a large amount of work done in the control of this zero sequence current [B.1, B.6, B.8].

The topology of the parallel rectifiers used in [B.6] allows the path for the zero sequence circulating current, as the parallel rectifiers share the same input source.

As mentioned in [B.6], there are a number of methods of preventing the circulating current:

- Separate ac or dc power supplies.
- Inter-phase reactors used to provide high zero-sequence impedance.
- Synchronized control, this method treats the two converters connected in parallel as one converter.

There are numerous advantages and disadvantages related to the above-mentioned methods of eliminating the circulating current. The authors in [B.6, B.8] propose the same control strategy for parallel connected boost rectifiers [B.6] and parallel connected Buck rectifiers [B.8]. The control method employed is space-vector modulation. The method involves a control variable 'k' that is a function of the distribution of the time of applying the zero vectors. Using the control variable, the average model for zero sequence dynamic is obtained. The proposed control scheme is validated by simulation results for both the buck and boost parallel rectifier topologies.

Another control method proposed aims at minimizing the power rating of each rectifier in the topology of the system [B.5]. The topology comprises of two types of rectifiers, one is a PWM rectifier and the second is a diode rectifier. Connecting two rectifiers in parallel enables power distribution between the two. The author in [B.5] obtains an optimized power distribution factor for the system so as to minimize the power rating of the rectifiers in the parallel rectifier topology used. The analysis is carried out for the system with and without an input filter.

A method of current control of series and parallel-connected rectifiers is proposed in [B.1]. The method adopted is to treat each rectifier as an autonomous unit. The current control is achieved by implementing a hysteresis controller.

The two connection types considered are series connection, and parallel connection of the rectifiers. The first set of results assumes each unit to be autonomous; the second set uses one controlled unit to determine the operation of the remaining units in the system. This can be termed as a 'master and slave' method of control.

Primarily the method of control adopted as proposed in [B.1 – B.7] are dependant on the application area and hence the method of connection of the rectifiers in series and parallel.

2.3 Induction Generators

The study of the operation of induction machines as generators is well known. There has been an exhaustive amount of work done with regard to the steady-state and dynamic response of an induction generator.

The details of the use of an induction machine operating as a self-excited generator, both analytically and experimentally determined are illustrated in [C.22]. The operation of the generator with resistive and reactive loads is studied at steady state, operating at a constant terminal voltage. A given range of power ratings quantifies the amount of power that can be extracted from low-power motors for different operating loads.

It is well known that a three-phase induction machine can be made to work as a self-excited induction generator. There are different modes of operation. Each mode is discussed in [C.18]. The possible modes are:

- Polyphase AC Supply
- Voltage Source Inverter with DC Supply
- Current Source Inverter with DC Supply
- Capacitive Self-Excitation
- Voltage Source Inverter Self-Excitation

- Current Source Inverter Self-Excitation.

The study of the different modes as carried out in [C.18], is by the representation of each mode of excitation using an equivalent circuit. To study the systems, per-unit representation is used. The effect of the change in the magnetizing flux is considered. It is shown that the effect of saturation in the system is of secondary importance in the case of the regenerative modes of operation; however for the self-excitation modes of operation, saturation plays a significant role in the nature of response.

The nature of response of the system to varying operating slips and stator voltage frequency is studied. In the case of capacitive self-excitation, for a fixed load and capacitance, the self excitation at a specific flux level can occur either at two frequencies, one frequency, or not at all depending on the load parameters and the operating speed. The different possible regions of operation are illustrated for varying operating conditions.

For all three cases of self excitation, constraining equations are derived to determine the possible operating conditions and self-excitation regions.

Similarly, a large amount of work has been done on the capacitance requirements as well as the air gap flux linkage requirements for self-excitation [C.25, C.21, C.14, C.5]. In the case of [C.5] detailed analysis has been carried out with regard to two different operating conditions, loaded and no-load. Predominantly, most of the work previously done on the steady-state analysis of induction generators involves study using the conventional equivalent circuit. The effect of changing load, slip, and magnetizing flux on the system performance in terms of the possible regions of operation as well as the effect of the rotor speed on the operation of the generator is discussed. In [C.5],

expressions for the possible regions of operating slip that the system can self-excite are obtained. The minimum and maximum values of the operating slip are determined. Using these expressions, the actual region of self-excitation can be determined. In all the above-mentioned references, an equivalent resistance has represented the model of the inverter.

In [C.21] and [C.3] the effect of the operating conditions of the induction generator on the air-gap flux requirements is studied for single as well as three-phase induction generators. The variation of the air-gap flux with the load resistance is studied for fixed capacitance values. Also the variation of the capacitance requirements of the generator with the load resistance for the minimum air-gap flux required is illustrated.

Another approach to the steady-state analysis of a self-excited induction generator involves the study of the effect of the parameters of the machine on the terminal voltage of the generator [C.15]. In this case, the effect of the core-loss is neglected. The influence of the stator resistance, rotor resistance, leakage reactance, and magnetizing reactance on the terminal voltage of the generator is studied and illustrated. The method employed is a Newton-Raphson method as the solution is complicated due to the effect of magnetic saturation being considered. The nature of response of the system to changing rotor speed and capacitance is also studied.

Similarly, the steady-state analysis of the self-excited induction generator by a single capacitor is dealt with in [C.12]. The operation of the system with star and delta connected stator windings is studied, with a single capacitor connected between any two phases (in this case, phase b and c). The influence on the value of the capacitor used as well as the effect of the load on the machine currents and voltages are studied for both the star as well as delta connected stator windings.

The effect of the load on a self-excited induction generator is of importance, as shown in [C.23]. The self-excited induction generator is studied under free-running and loaded conditions. The effect of variable speed on the machine and the region of variable speed for which the induction generator can operate without loss in self-excitation is studied.

The control of induction generators has also been studied. The operation of induction generators driven by wind turbines is vastly important. Although the application of an induction generator in wind power is popular due to the ability of an induction generator to self-excite, the drawback of using an induction generator is the inability of the generator to maintain a controlled voltage. Therefore, a large number of control schemes have been proposed to overcome this drawback.

The specific interest in induction generators for wind power applications is due to the fact that because the machine can self-excite, an independent source of power is not required for excitation. Also the relative cost of an induction machine is less.

[C.2, C.10, C.8], deal with the operation of an induction generator driven by a wind turbine. This would therefore mean the system is studied under conditions of varying rotor speeds. Also effect of the operating slip on the generated voltage and frequency is studied. The importance of magnetic saturation in self-excited induction generators, discussed earlier is also included in [C.2]. An important aspect of the self-excitation process and voltage buildup with respect to the variation of the magnetizing inductance and phase voltage is detailed in [C.2]. The stability of the system during this process is highlighted as in the initial buildup of flux in the generator; a small drop in the

phase voltage would further decrease the phase voltage. This continual decrease in both could lead to no buildup of voltage in the system.

In [C.8], the induction generator system driven by a wind turbine is controlled for constant voltage at the stator terminals of the machine. The system uses a PWM inverter for control of the excitation current to thereby enable control of the generated voltage. The control methodology is verified by simulation results for operation of the system under varying rotor speeds and loads. In [C.9], the system configuration used is similar; however, the analysis carried out shows the effect of the dc side capacitor value on the time of voltage buildup in the system. Also the dc voltage ripple is determined by the capacitor value used.

Another method of control proposed utilizes a current controlled voltage source converter [C.13]. The type of controller used is a hysteresis current controller. Just like in the previous reference cited, the effectiveness of the control scheme is illustrated using varying operating conditions of load and rotor speed.

A stator flux-oriented vector control of an induction generator system is proposed in [C.4]. In this case the control scheme proposed uses stator flux as a control variable to regulate the voltage. Similar operating conditions as [C.13] are applied. The system is specifically studied for varying rotor speeds as the proposed scheme is aimed at a wind-turbine driven generator.

Some other control schemes proposed are in [C.11, C.24] where the control scheme is different from the ones described earlier; however, the operating conditions for which the system is studied under are similar.

Finally some work has been done in the area of stability of an induction machine. The system transfer function is obtained and the poles and zeros of the system are studied under pole and zero migration, where the movement of the poles under varying current command is studied. The system is shown to be unstable for high values of rotor speed.

The vast amount of work carried out in the areas of series and parallel boost rectifiers, as well as induction generators has been highlighted in this chapter. Only a small portion of the work carried out in this field has been briefed.

CHAPTER 3

MODELING OF THREE-PHASE BOOST RECTIFIER

3.1 Introduction

As explained in Chapter 1, rectifiers are power electronic systems that convert input ac power to output dc power. Rectifiers come in many types and can be classified variedly as:

- Single-phase vs. three-phase
- Half-wave vs. full-wave
- Phase controlled vs. pulse width modulated.

Single-phase vs. three-phase rectifiers is a classification based on the type of ac input to the rectifier. The rectifiers shown in Figure 3.1(a) and 3.1(b) are diode rectifiers.

The third classification relates to the type of semiconductor device used in the rectifier; uncontrolled rectifiers comprise of diodes as the switches, phase-controlled

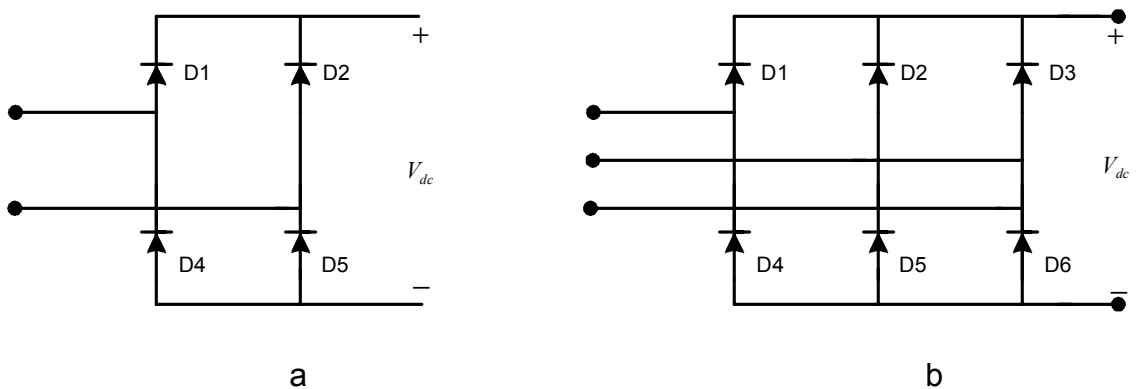


Figure 3.1: (a) single-phase bridge rectifier (b) three-phase bridge rectifier

rectifiers comprise of SCR (silicon controlled rectifiers); and in pulse_width modulated rectifiers; IGBT's (insulated gate bipolar transistors) or power MOSFET's (metal oxide field-effect transistors) are used. The rectifier is switched using pulses that are generated using sine-triangle or space vector pulse width modulation.

The pulse-width modulated rectifiers can be further divided on the basis of the relationship between the ratios of the input and output voltages. Some examples of the pulse-width modulated rectifiers are buck, 'boost', and 'buck-boost' rectifiers. In buck rectifiers, the dc output voltage is lower in magnitude than the peak value of the ac input. Similarly, the boost rectifier has an output dc voltage that is higher in magnitude than the peak value of the ac input voltage. The buck-boost rectifier can have an output voltage, either lower or higher in magnitude when compared to the ac input, with the duty ratio of the switches determining the nature of the output.

3.2 Operation of Three-Phase Boost Rectifier

The application areas of the boost rectifier are varied and exhaustive due to the efficient utilization of power in the rectification process, and the boosting of the output voltage. The topology of the three-phase boost rectifier is shown in Figure 3.2.

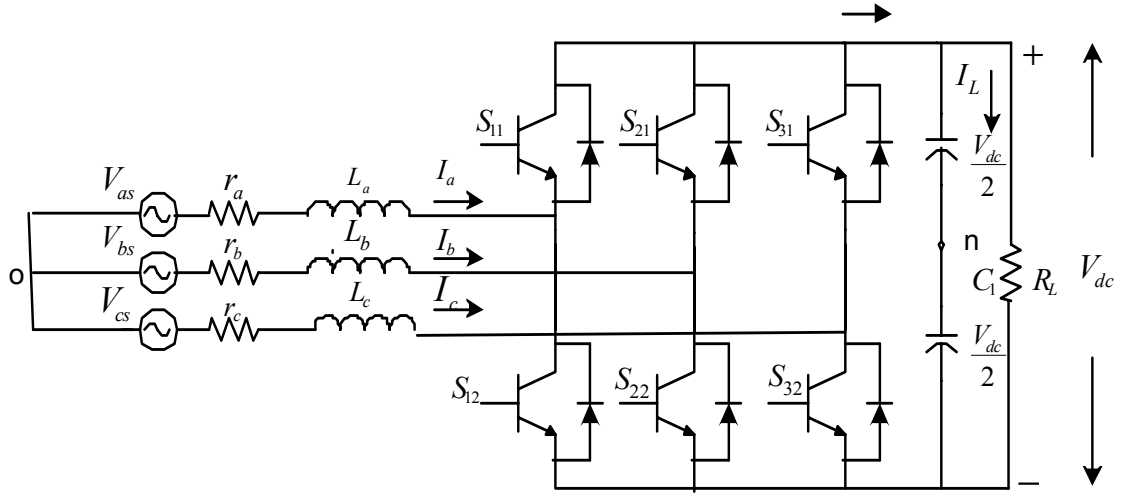


Figure 3.2: Topology of three-phase boost rectifier

The parameters of the rectifier are as defined in Table 3.1.

Table 3.1: Variables used for three-phase boost rectifier model.

V_{as}, V_{bs}, V_{cs}	Input AC-side voltages
I_a, I_b, I_c	Phase currents
r_a, r_b, r_c	Per phase resistance
L_a, L_b, L_c	Inductance per phase
I_p	DC current at the output of the rectifier
I_L	Load current
V_{dc}	Output dc voltage
S_{11}, S_{21}, S_{31}	Switching functions for top devices
S_{12}, S_{22}, S_{32}	Switching functions for bottom devices
R_L	Load resistance
C	DC- side capacitor

The three-phase boost rectifier comprises of six switches that are switched using sinusoidal pulse width modulation technique. In general, the operation of a converter can be explained in terms of the input quantities, output quantities, and the switching pattern used to obtain the desired output. The switching pattern of the switches in the converter is obtained in accordance with Kirchhoff's voltage law (KVL) and Kirchhoff's current law (KCL). The ON and 'OFF' states of a single switch are assumed to have values 0 and 1, respectively; i.e.

If the device is 'ON', the switch is assigned a value = 1.

If the device is 'OFF', the switch is assigned a value =0.

In a three-phase rectifier, the input ac voltages are defined and the output dc voltage is dependant on the input quantities as well as the switching pattern of the rectifier. The switching pattern for any converter can be expressed as a function, which is a mathematical representation of the switching pattern, called an existence function [A.1].

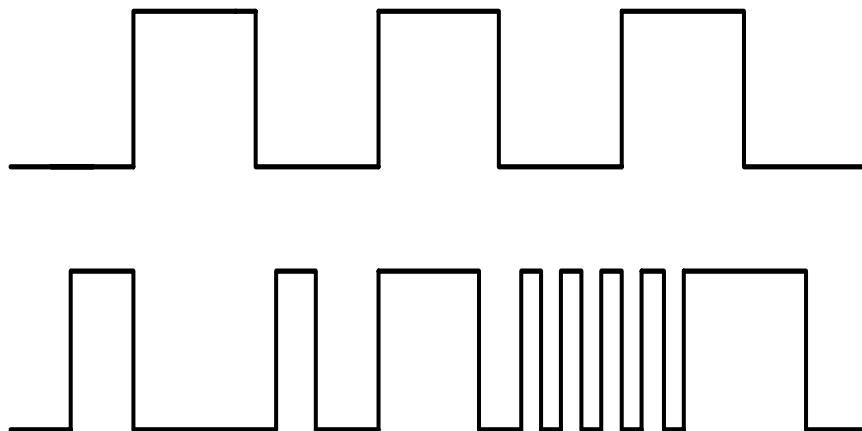


Figure 3.3. Modulated and unmodulated existence functions

The repetition of the switching patterns to obtain the desired output in a converter results in an existence function having intermittent ON and OFF periods, as the ON state is assumed to be a value 1, the pulses of the existence function have unit magnitude.

There are two different types of existence functions, modulated and unmodulated. Modulated existence functions have pulses of varying widths, and unmodulated functions have pulses of uniform width. The two types of existence functions are shown in Figure 3.3.

The operating modes of the boost rectifier are the same as that of a three-phase voltage source inverter. There are eight different switching modes for the boost rectifier. As explained earlier the ON and OFF states are assigned the values 1 and 0, respectively.

Table 3.2: Switching modes for boost-rectifier

S.No	S_{11}	S_{21}	S_{31}
1.	0	0	0
2.	0	0	1
3.	0	1	0
4.	0	1	1
5.	1	0	0
6.	1	0	1
7.	1	1	0
8.	1	1	1

From the above eight possible switching modes, only six modes can be used in synthesizing a dc voltage, and are called active states. The two states (1 and 8) are called null states as these states do not result in an output dc voltage and are thereby inactive.

This can be explained by first illustrating KVL and KCL. The first condition to be satisfied while determining the possible switching modes for the three-phase boost rectifier is KVL. Consider a circuit as shown in Figure 3.4 (a) and (b) to illustrate KVL. The circuit comprises of two voltage sources. The switch ‘S’ in Figure 3.4 has two possible states $S = 0$, when the switch is assumed to be open as shown in 3.4(a) and $S = 1$ when the switch is assumed to be closed as shown in 3.4(b).

Kirchhoff’s voltage law states that the sum of voltages in any closed path (or mesh) in a network is zero. Therefore, when the switch is open, there is no closed loop in the circuit and hence the conditions for the law to hold are not satisfied and therefore the law cannot be violated. However, in the second case, when the switch is closed, the two different sources are connected together and hence the sum of the voltages in the mesh is

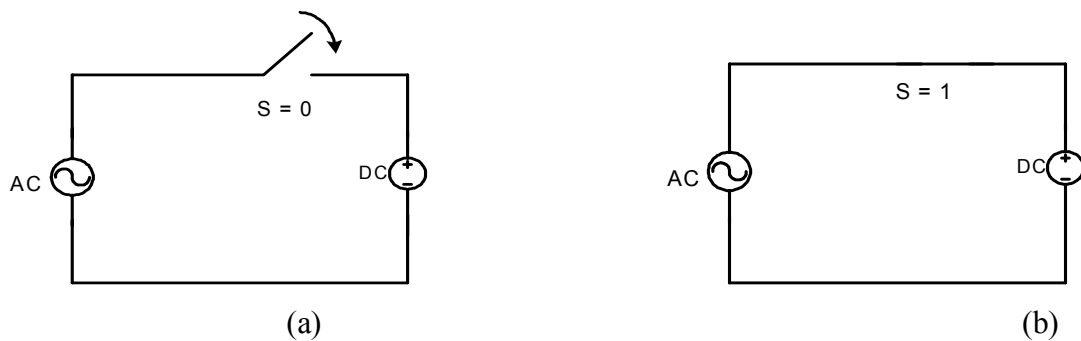


Figure 3.4: Schematic illustrating KVL

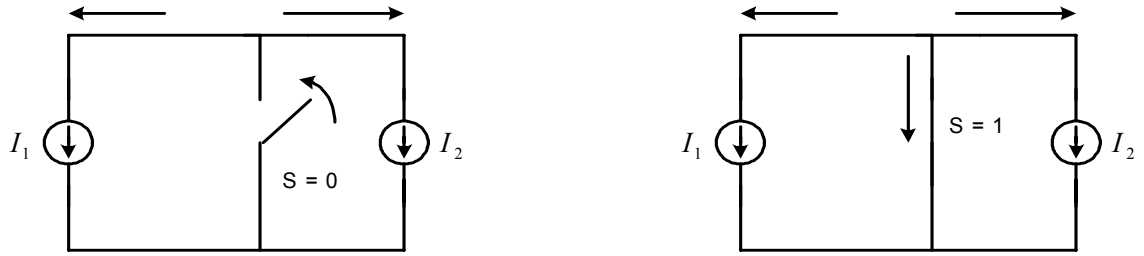


Figure 3.5. Schematic illustrating KCL

not zero thereby violating KVL. The presence of an energy-storing element in the circuit would render both states of the switch acceptable for the circuit.

Similarly Kirchhoff's current law states that the sum of currents at any node should be equal to zero. This can be explained schematically in Figure 3.5.

When the switch is closed, the sum of the currents at the node is equal to zero, and KCL is satisfied; however when the switch is open, the law is violated, as the sum of currents at the node is not equal to zero.

3.3 Possible Switching Modes of The Boost Rectifier

For the three-phase boost rectifier, the restraints on the possible modes of operation that also satisfy KVL and KCL can be mathematically expressed as

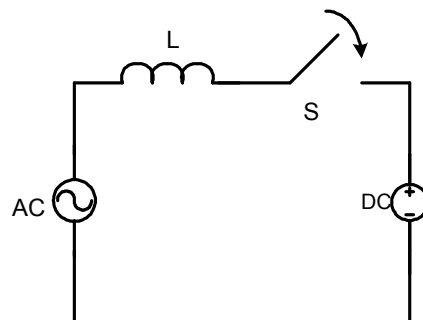


Figure 3.6. Simplified schematic of boost rectifier

$$S_{11} + S_{12} = 1 \quad (3.1)$$

$$S_{21} + S_{22} = 1 \quad (3.2)$$

$$S_{31} + S_{32} = 1. \quad (3.3)$$

Equations (3.1) to (3.3) show that at no instant of time can the top and bottom devices of the same leg be ON simultaneously, as the condition would violate KVL. Assuming one switch in the top leg and one switch in the bottom leg to be ON, the boost rectifier Figure 3.2 can be simplified as shown in Figure 3.6.

The six active states as shown in Table 3.2 can be graphically represented in Figure 3.7. For each state illustrated, the switches ON are specified, and a red line, indicating the switches 'ON' and thereby each active state, depicts the path of flow. Figure 3.7(a) illustrates the mode of operation where the top switch S_{11} and bottom switch S_{22} are ON. The switches that are ON therefore determine the path of flow of current. The second possible mode of operation is shown in Figure 3.7(b) where the switches S_{11} and S_{32} are ON. Figures 3.7(c) and (d) represent the two possible combinations for the switch S_{21} . The modes that satisfy KVL would be when S_{21} and S_{12} , and S_{21} and S_{32} are ON. The modes for the third switch are shown in Figures 3.7(e) and (f) where the top switch S_{31} and bottom switches S_{12} and S_{22} are ON, respectively.

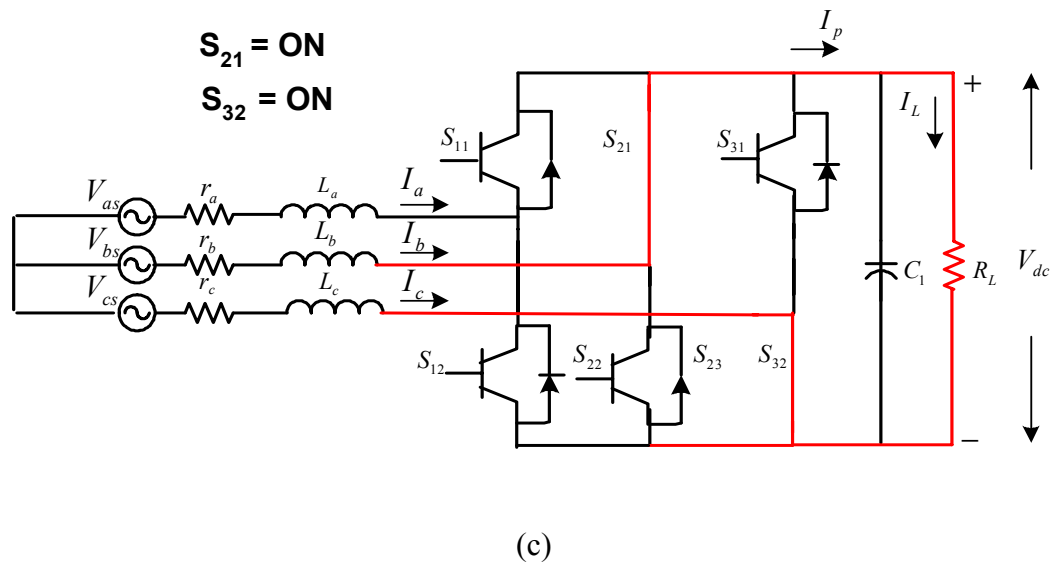
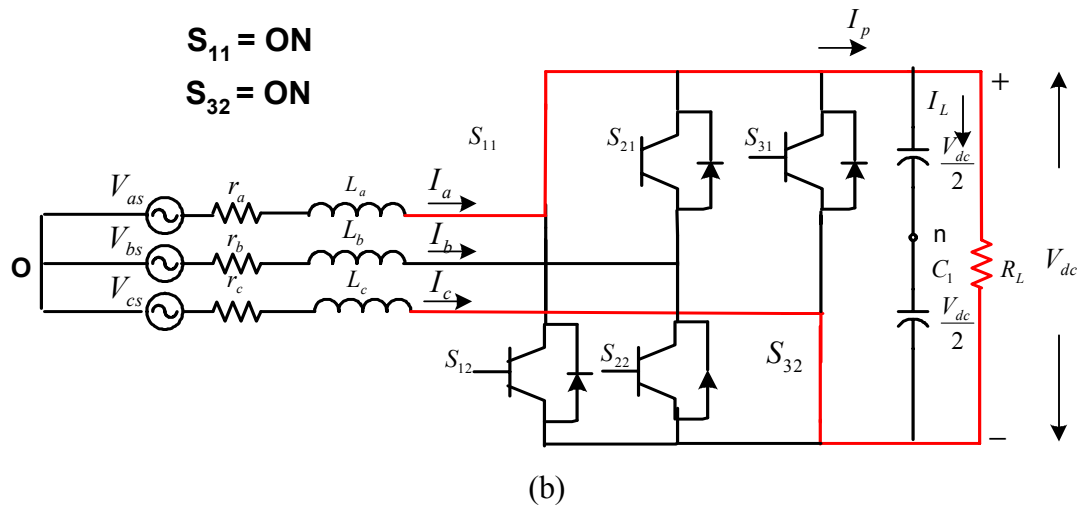
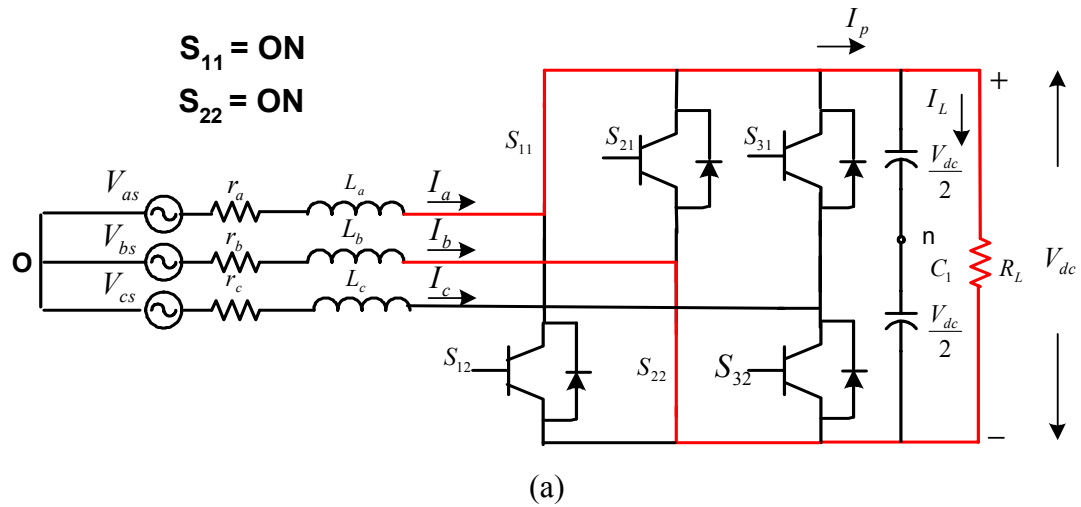


Figure 3.7 (a) to (c): Modes of operation of three-phase boost rectifier

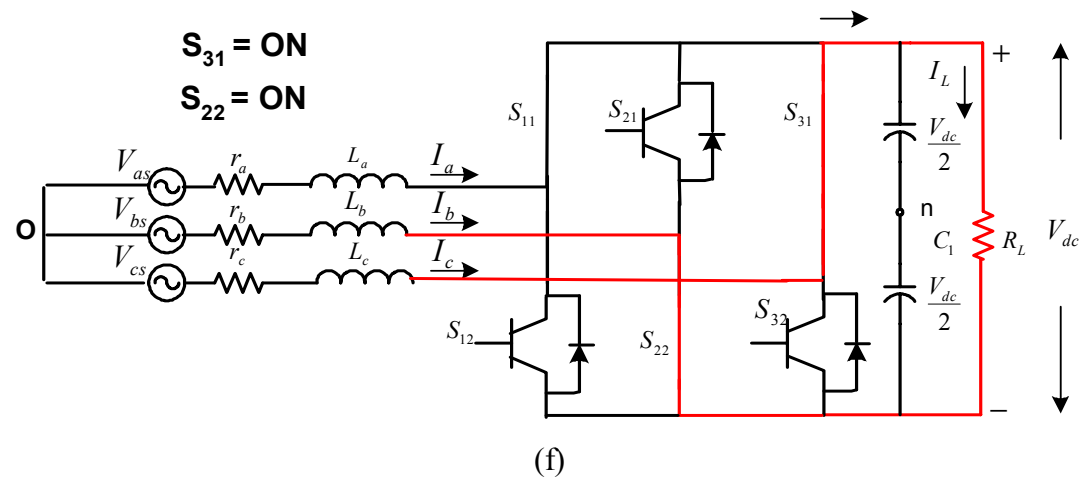
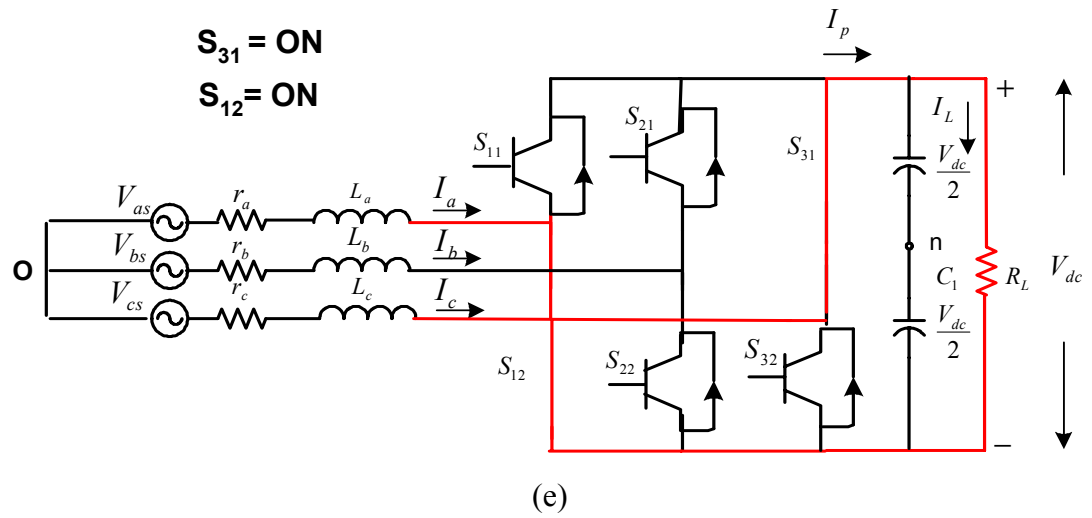
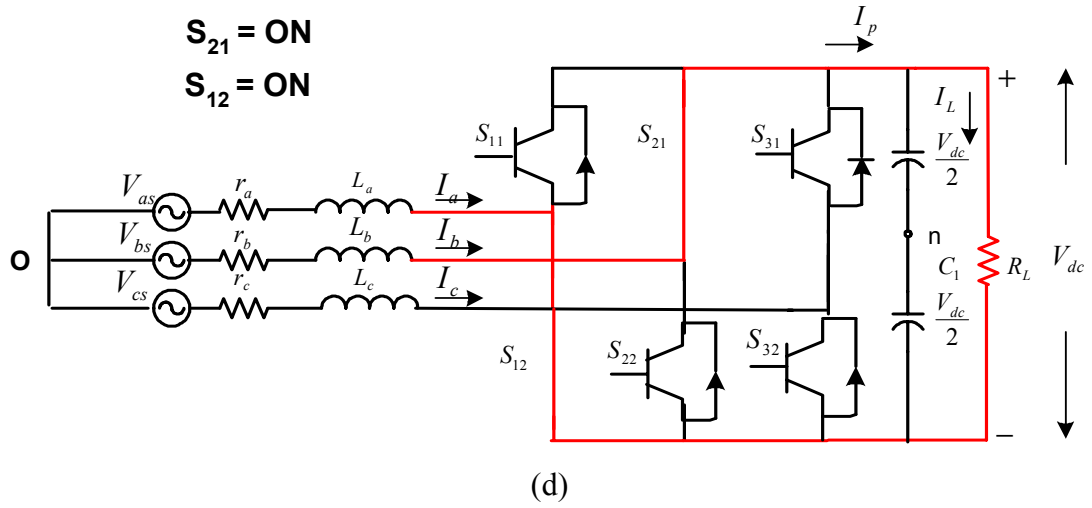


Figure 3.7 (d) to (f): Modes of operation of three-phase boost rectifier

3.4 Modulation Techniques

There are two different types of modulation techniques that are generally applied for pulse width modulation (PWM), namely:

Sinusoidal pulse width modulation

Space vector PWM.

Sinusoidal PWM is a technique employed where the sinusoidal waveform (also called the modulation signal) is compared with a very high frequency triangle (carrier signal) to obtain the switching pulses for the device. The modulation and the carrier signals are compared such that when the sine wave is higher in magnitude the corresponding value of the switching pulse is high (has a value = 1) and when the sine wave is lower than the carrier, the pulse is low (has a value = 0). This is shown graphically in Figure 3.8.

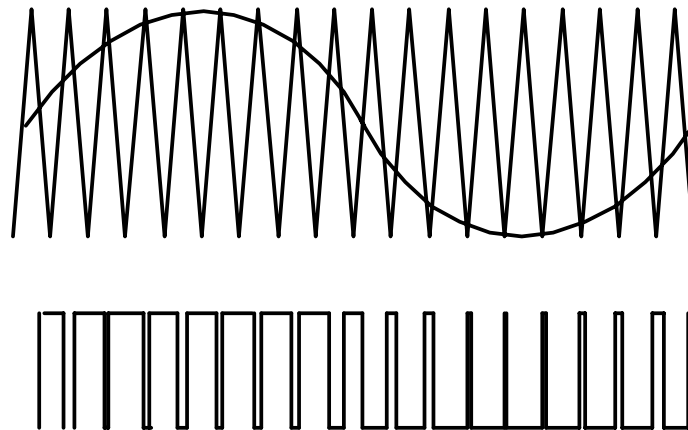


Figure 3.8: Sine-triangle PWM

The second modulation technique is also known as Generalized Discontinuous pulse width modulation (GDPWM). This method, also known as space vector modulation (SVM), represents the ac side voltages of the converter as a space vector. Each active state is represented as a vertex of a hexagon, while the null vectors are represented at the centre of the hexagon. Depending on the sector in which the reference vector lies, the switching times are calculated to generate the desired reference vector.

3.5 Relationship Between Switching Function and Modulation Signal

The switching function is a periodic waveform, i.e. it is repetitive. The function can be mathematically represented using various methods such as Laplace transforms and Z-transforms [A.1]. However if the function is represented using the above-mentioned methods of transformation, the resulting expressions cannot be easily interpreted. Therefore, the functions are represented using Fourier transforms.

The Fourier transform is obtained by setting the mid-point of one of the unit pulses as the zero point of the waveform. The frequency of repetition is defined as ‘f’ and the time period is therefore $T=1/f$. The angular frequency ω is defined as $\omega = 2\pi f$.

Assuming the angular duration of the unit value period = $2\pi/A$, the boundaries of the unit-value period are: $-\pi/A$ and π/A .

The function is expressed as

$$H_{\omega}(t) = \sum_{n=0}^{n=\infty} [C_n \cos(n\omega t) + S_n \sin(n\omega t)]. \quad (3.4)$$

Using standard Fourier expansion formulae to determine the coefficients;

$$S_n = \frac{2}{T} \int_{-T/2}^{T/2} H \sin(n\omega t) dt \quad (3.5)$$

$$= \frac{1}{\pi} \int H \sin(n\omega t) d\omega t = 0$$

$$C_o = \frac{1}{T} \int_{-T/2}^{T/2} H dt \quad (3.6)$$

$$= \frac{1}{2\pi} \int H d\omega t = 1/A$$

$$C_n (n \neq 0) = \frac{2}{T} \int_{-T/2}^{T/2} H \cos(n\omega t) dt \quad (3.7)$$

$$= \frac{1}{\pi} \int_{-\pi/A}^{\pi/A} \cos(n\omega t) d\omega t$$

$$= \frac{2}{\pi} \sin(n\pi/A) / n.$$

Having derived the coefficients for the Fourier expansion, the expression for the existence function can be represented as a summation:

$$H(\omega t) = \frac{1}{A} + \frac{2}{\pi} \sum_{n=1}^{n=\infty} [\sin(n\pi/A)] \cos(n\omega t). \quad (3.8)$$

The variable 'A' can take a range of values varying from rational, irrational, integer, etc. However with 'A' as an integer, the components for which 'n' is an integral multiple of 'A' are equal to zero. Hence the expression would reduce to a fundamental component and a time varying term as shown in Equation (3.10).

$$H(\omega t) = \frac{1}{A} + \frac{2}{\pi} \sum_{n=1}^{n=\infty} [\sin(n\pi/A)] \cos(n(\omega t - 2k\pi/A)) \quad (3.9)$$

$$S = \frac{1}{A} + M \quad (3.10)$$

where M is the time varying component also called the modulation signal, the fundamental component of which can be expressed as:

$$M = M_i \cos(\omega t - \alpha).$$

M_i is the modulation index.

3.6 Model of Three-Phase Boost Rectifier

The model of the three-phase rectifier is shown in Figure 3.9. The switching modes and the different types of modulation schemes have been discussed in sections 3.3 and 3.4. The next step in the analysis is the derivation of the model equations of the boost rectifier. In this section, the model equations of the boost rectifier are derived in the abc reference frame and then transformed to the qd reference frame.

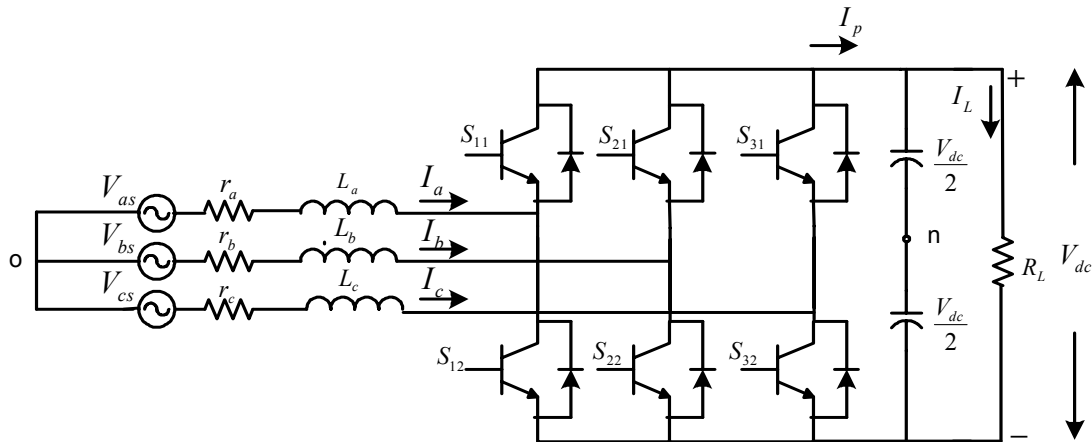


Figure 3.9: Topology of three-phase boost rectifier

The voltage equations for the boost rectifier in the abc reference frame are

$$V_{as} = I_a Z + (S_{11} - S_{21}) \frac{V_{dc}}{2} + V_{no} \quad (3.11)$$

$$V_{bs} = I_b Z + (S_{21} - S_{22}) \frac{V_{dc}}{2} + V_{no} \quad (3.12)$$

$$V_{cs} = I_c Z + (S_{31} - S_{32}) \frac{V_{dc}}{2} + V_{no} . \quad (3.13)$$

The phase resistances and inductances are assumed to be balanced i.e. $r_a = r_b = r_c$ and $L_a = L_b = L_c$, where the phase impedance is

$$Z = r_i + jL_i p \quad i = a, b, c \quad (3.14)$$

$$p = \frac{d}{dt} .$$

The phase voltages are assumed to be balanced and have a peak value of V_m .

Hence the phase voltages can be defined as

$$V_{as} = V_m \cos(\omega t + \phi_v) \quad (3.15)$$

$$V_{bs} = V_m \cos\left(\omega t + \phi_v - \frac{2\pi}{3}\right) \quad (3.16)$$

$$V_{cs} = V_m \cos\left(\omega t + \phi_v + \frac{2\pi}{3}\right). \quad (3.17)$$

ϕ_v is the voltage phase angle and ω is the frequency of the voltage in rad/sec.

V_{no} is the neutral voltage.

Substituting Equations (3.1) – (3.3) in (3.11) – (3.13), the voltage equations for the boost rectifier can be expressed in terms of the switching functions of the top devices

as

$$V_{as} = I_a Z + (2S_{11} - 1) \frac{V_{dc}}{2} + V_{no} \quad (3.18)$$

$$V_{bs} = I_b Z + (2S_{21} - 1) \frac{V_{dc}}{2} + V_{no} \quad (3.19)$$

$$V_{cs} = I_c Z + (2S_{31} - 1) \frac{V_{dc}}{2} + V_{no} . \quad (3.20)$$

The phase impedance Z can be substituted for in Equations (3.18) to (3.20) by substituting Equation (3.14).

$$V_{as} = rI_a + LpI_a + (2S_{11} - 1) \frac{V_{dc}}{2} + V_{no} \quad (3.21)$$

$$V_{bs} = rI_b + LpI_b + (2S_{21} - 1) \frac{V_{dc}}{2} + V_{no} \quad (3.22)$$

$$V_{cs} = rI_c + LpI_c + (2S_{31} - 1) \frac{V_{dc}}{2} + V_{no} \quad (3.23)$$

$$p = \frac{d}{dt} .$$

The final state equation that completes the system model for the boost rectifier is the capacitor voltage equation. The capacitor voltage equation for the boost rectifier is expressed in terms of the load current I_L and the dc current at the output of the rectifier.

$$CpV_{dc} = I_p - \frac{V_{dc}}{R_L} \quad (3.24)$$

where I_p the output is current defined in terms of the switching functions of the top devices as

$$I_p = S_{11}I_a + S_{21}I_b + S_{31}I_c . \quad (3.25)$$

Substituting equation (3.25) in (3.24)

$$CpV_{dc} = S_{11}I_a + S_{21}I_b + S_{31}I_c - \frac{V_{dc}}{R_L}. \quad (3.26)$$

The next step in the analysis is the elimination of the neutral voltage in Equations 3.21 to 3.23. The neutral voltage is eliminated by adding Equations (3.21) to (3.23). As the system voltages V_{as} , V_{bs} and V_{cs} are balanced,

$$V_{as} + V_{bs} + V_{cs} = 0$$

hence the neutral voltage can be expressed in terms of the switching functions as

$$V_{no} = -\frac{V_{dc}}{3}[2S_{11} + 2S_{21} + 2S_{31} - 3]. \quad (3.27)$$

Using Equation (3.27), the neutral voltage can be eliminated in the voltage equations 3.21 to 3.23 resulting in

$$V_{as} = rI_a + LpI_a + V_{dc}\left[\frac{2}{3}S_{11} - \frac{1}{3}S_{21} - \frac{1}{3}S_{31}\right] \quad (3.28)$$

$$V_{bs} = rI_b + LpI_b + V_{dc}\left[-\frac{1}{3}S_{11} + \frac{2}{3}S_{21} - \frac{1}{3}S_{31}\right] \quad (3.29)$$

$$V_{cs} = rI_c + LpI_c + V_{dc}\left[-\frac{1}{3}S_{11} - \frac{1}{3}S_{21} + \frac{2}{3}S_{31}\right]. \quad (3.30)$$

The switching functions for each phase can be expressed in terms of the modulation signals as

$$S_{11} = \left(\frac{1 + M_a}{2}\right) \quad (3.31)$$

$$S_{12} = \left(\frac{1 + M_b}{2} \right) \quad (3.32)$$

$$S_{13} = \left(\frac{1 + M_c}{2} \right). \quad (3.33)$$

Substituting for the modulation signals, the voltage equations can be rewritten

$$V_{as} = rI_a + LpI_a + V_{dc} \left[\frac{2}{3}M_a - \frac{1}{3}M_b - \frac{1}{3}M_c \right] \quad (3.34)$$

$$V_{bs} = rI_b + LpI_b + V_{dc} \left[-\frac{1}{3}M_a + \frac{2}{3}M_b - \frac{1}{3}M_c \right] \quad (3.35)$$

$$V_{cs} = rI_c + LpI_c + V_{dc} \left[-\frac{1}{3}M_a - \frac{1}{3}M_b + \frac{2}{3}M_c \right]. \quad (3.36)$$

Similarly, the switching functions in the capacitor voltage equations are replaced by the modulation signals using Equations (3.31) to (3.33)

For further analysis, the equations in this form can be simplified by the transformation to another frame of reference. The equations of the rectifier are time varying, and hence the reference frame chosen is one that rotates at the same frequency as that of the supply voltages. This reference frame is called the synchronous reference frame, and transformation to this reference frame is achieved as shown.

Assume the parameters to be transformed are V_{as} , V_{bs} , and V_{cs} . The time-invariant variables are V_{qs} , V_{ds} , and V_{os} . The transformation matrix, $K_s(\theta_s)$ is defined as:

$$K_s(\theta_s) = \frac{2}{3} \begin{bmatrix} \cos(\theta_s) & \cos\left(\theta_s - \frac{2\pi}{3}\right) & \cos\left(\theta_s + \frac{2\pi}{3}\right) \\ \sin(\theta_s) & \sin\left(\theta_s - \frac{2\pi}{3}\right) & \sin\left(\theta_s + \frac{2\pi}{3}\right) \\ \frac{1}{2} & \frac{1}{2} & \frac{1}{2} \end{bmatrix}. \quad (3.37)$$

The angle θ is defined as

$$\theta = \int \omega_e t + \psi_m \quad (3.38)$$

ω_e is the frequency of the supply voltages

Ψ_m is the initial angle of the reference frame.

The transformation to the desired reference (in this case the synchronous reference frame) frame is obtained by Equation (3.39).

$$f_{qds0} = (K_s(\theta_s))f_{abc} \quad (3.39)$$

$$V_{qds0} = (K_s(\theta_s))V_{abc} \quad (3.40)$$

$$V_{qds0} = [V_q \quad V_d \quad V_o]^T \quad (3.41)$$

$$V_{abc} = [V_a \quad V_b \quad V_c]^T \quad (3.42)$$

The voltage equations expressed in the matrix form:

$$\begin{bmatrix} V_{as} \\ V_{bs} \\ V_{cs} \end{bmatrix} = r \begin{bmatrix} I_a \\ I_b \\ I_c \end{bmatrix} + L p \begin{bmatrix} I_a \\ I_b \\ I_c \end{bmatrix} + \frac{V_{dc}}{3} \begin{bmatrix} 2M_a - M_b - M_c \\ -M_a + 2M_b - M_c \\ -M_a - M_b + 2M_c \end{bmatrix}. \quad (3.43)$$

Multiplying the above equation by the transformation matrix $K_s(\theta_s)$

$$\begin{bmatrix} V_{qs} \\ V_{ds} \\ V_{os} \end{bmatrix} = r \begin{bmatrix} I_q \\ I_d \\ I_o \end{bmatrix} + L p \begin{bmatrix} I_q \\ I_d \\ I_o \end{bmatrix} + \begin{bmatrix} \omega & 0 & 0 \\ 0 & -\omega & 0 \\ 0 & 0 & 0 \end{bmatrix} \times \begin{bmatrix} I_q \\ I_d \\ I_o \end{bmatrix} + \frac{V_{dc}}{2} \begin{bmatrix} M_q \\ M_d \\ M_o \end{bmatrix}. \quad (3.44)$$

The voltages for the boost rectifier in the qd reference frame from Equation (3.44),

$$V_{qs} = rI_{qs} + LpI_{qs} + \omega LI_{ds} + \frac{M_q V_{dc}}{2} \quad (3.45)$$

$$V_{ds} = rI_{ds} + LpI_{ds} - \omega LI_{qs} + \frac{M_d V_{dc}}{2} \quad (3.46)$$

$$V_o = rI_{os} + LpI_o \quad (3.47)$$

V_{qs} , V_{ds} are the q and d-axis voltages

I_{qs} , I_{ds} are the q and d-axis currents

M_{qs} , M_{ds} are the q and d-axis modulation signals.

As the system is balanced, the zero sequence voltage is zero. However if there were some unbalance in the system the zero sequence voltage would reflect the unbalance in the system. Equations (3.45) to (3.47) are the voltage equations for the boost rectifier in the synchronous reference frame. The capacitor voltage equation (3.26) needs to be transformed to obtain the complete model of the boost rectifier.

The voltage equations are transformed by multiplying the equations by the transformation matrix, Equation (3.37). However, the transformation of the capacitor voltage equation is done by replacing the currents in the abc reference frame in terms of the qdo currents (synchronous reference frame) using the inverse transformation.

$$I_{abc}^T = I_{qdo}^T (K_s^T)^{-1} \quad (3.48)$$

$$K_s(\theta_s)^{-1} = \begin{bmatrix} \cos(\theta_s) & \sin(\theta_s) & 1 \\ \cos\left(\theta_s - \frac{2\pi}{3}\right) & \sin\left(\theta_s - \frac{2\pi}{3}\right) & 1 \\ \cos\left(\theta_s + \frac{2\pi}{3}\right) & \sin\left(\theta_s + \frac{2\pi}{3}\right) & 1 \end{bmatrix} \quad (3.49)$$

Similarly, the modulation signals in the abc reference frame are expressed in terms of the qdo modulation signals using the same method as above.

$$M_{abc}^T = M_{qdo}^T (K_s^T)^{-1} \quad (3.50)$$

The capacitor voltage equation expressed in terms of the modulation signals in the abc reference frame (Equation (3.26)) is

$$Cp V_{dc} = (M_a I_a + M_b I_b + M_c I_c) - \frac{V_{dc}}{R_L} \quad (3.51)$$

$$Cp V_{dc} = (I_{abc}^T M_{abc}) \quad (3.52)$$

$$I_{abc}^T = [I_a \quad I_b \quad I_c] \quad (3.53)$$

$$M_{abc} = \begin{bmatrix} M_a \\ M_b \\ M_c \end{bmatrix}. \quad (3.54)$$

Substituting for the abc reference frame current and modulation signals using equations (3.48) and (3.50)

$$Cp V_{dc} = (I_{qdo}^T (K_s^T)^{-1} (K_s)^{-1} M_{abc}). \quad (3.55)$$

Equation (3.55) is simplified by evaluating $(K_s^T)^{-1} (K_s)^{-1}$

$$K_s(\theta_s)^{-1} = \begin{bmatrix} 1.5 & 0 & 0 \\ 0 & 1.5 & 0 \\ 0 & 0 & 3 \end{bmatrix}. \quad (3.56)$$

Substituting Equation (3.56) in (3.51)

$$Cp V_{dc} = \frac{3}{2} (M_{qs} I_{qs} + M_{ds} I_{ds} + 2M_o I_o) - \frac{V_{dc}}{R_L}. \quad (3.57)$$

As the system is balanced, the capacitor voltage equation consists of only the q and d axis components, as the three phase currents add up to zero.

$$Cp V_{dc} = \frac{3}{2} (M_{qs} I_{qs} + M_{ds} I_{ds}) - \frac{V_{dc}}{R_L} \quad (3.58)$$

The system equations for the boost rectifier in the synchronous reference frame are given by Equations (3.45) to (3.47) and (3.58). The next section illustrates the dynamic simulation of the system. The steady-state analysis, and unity power factor operation of the boost rectifier are dealt with in section 3.8.

3.7 Dynamic Simulation of Three-Phase Boost Rectifier

The dynamic simulation of the three-phase boost rectifier is carried out using the following equations (Section 3.6).

$$V_{as} = rI_a + LpI_a + V_{dc} \left[\frac{2}{3}S_{11} - \frac{1}{3}S_{21} - \frac{1}{3}S_{31} \right] \quad (3.59)$$

$$V_{bs} = rI_b + LpI_b + V_{dc} \left[-\frac{1}{3}S_{11} + \frac{2}{3}S_{21} - \frac{1}{3}S_{31} \right] \quad (3.60)$$

$$V_{cs} = rI_c + LpI_c + V_{dc} \left[-\frac{1}{3}S_{11} - \frac{1}{3}S_{21} + \frac{2}{3}S_{31} \right] \quad (3.61)$$

$$CpV_{dc} = S_{11}I_a + S_{21}I_b + S_{31}I_c - \frac{V_{dc}}{R_L}. \quad (3.62)$$

The switching functions for the rectifier are obtained by sine-triangle PWM. The modulation signals are chosen to have a magnitude of 0.5 and the frequency of the modulation signals (which is equal to the frequency of the supply voltages) is taken as 60Hz. The load resistance is assumed to be 100Ω and the three-phase balanced voltages (on the input side) are

$$V_{as} = 180 \cos\left(377t - \frac{\pi}{6}\right) \quad r = 0.1 \Omega$$

$$V_{bs} = 180 \cos\left(377t - \frac{\pi}{6} - \frac{2\pi}{3}\right) \quad C = 150 \mu\text{F}$$

$$V_{cs} = 180 \cos\left(377t - \frac{\pi}{6} + \frac{2\pi}{3}\right). \quad L = 6.4 \text{ mH}$$

$$R_L = 50 \Omega$$

Figure 3.10 shows the output voltage V_{dc} , load current I_L , and the dc output current I_p . The waveforms show the starting as well as the steady state response of the rectifier. Figures 3.11, 3.12, and 3.13 show the phase current, phase voltage, and modulation signals for all three phases, 'a', 'b', and 'c'. The plots show that the voltage, currents, and modulation signals to be balanced.

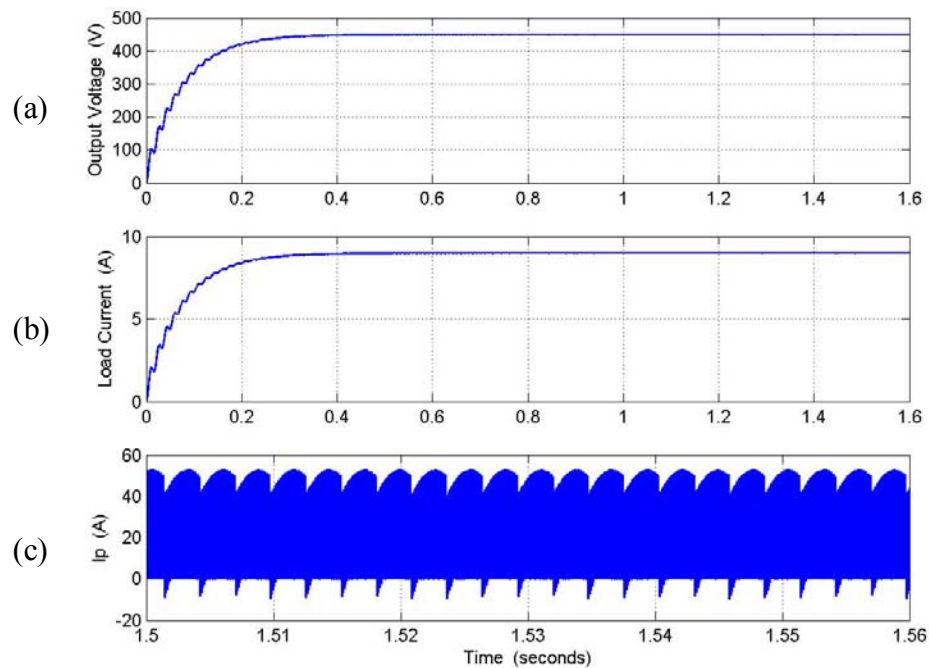


Figure 3.10: Simulation results for the rectifier, from top : (a) output dc voltage V_{dc} , (b) load current I_L , (c) dc output current I_p .

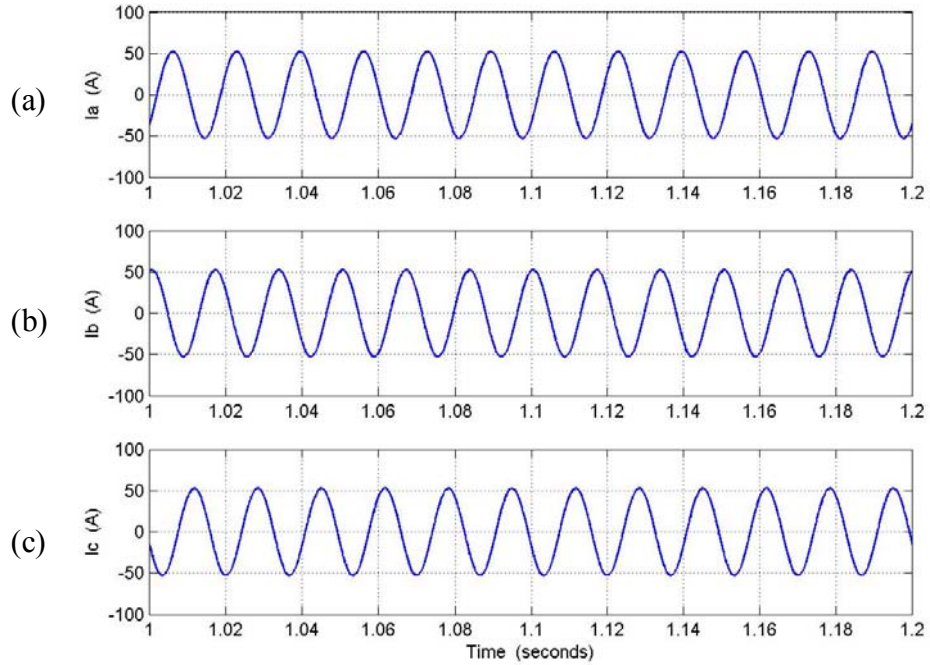


Figure 3.11: Simulation results for the rectifier, from top: (a) phase 'a' current I_a , (b) phase 'b' current I_b , (c) phase 'c' current I_c .

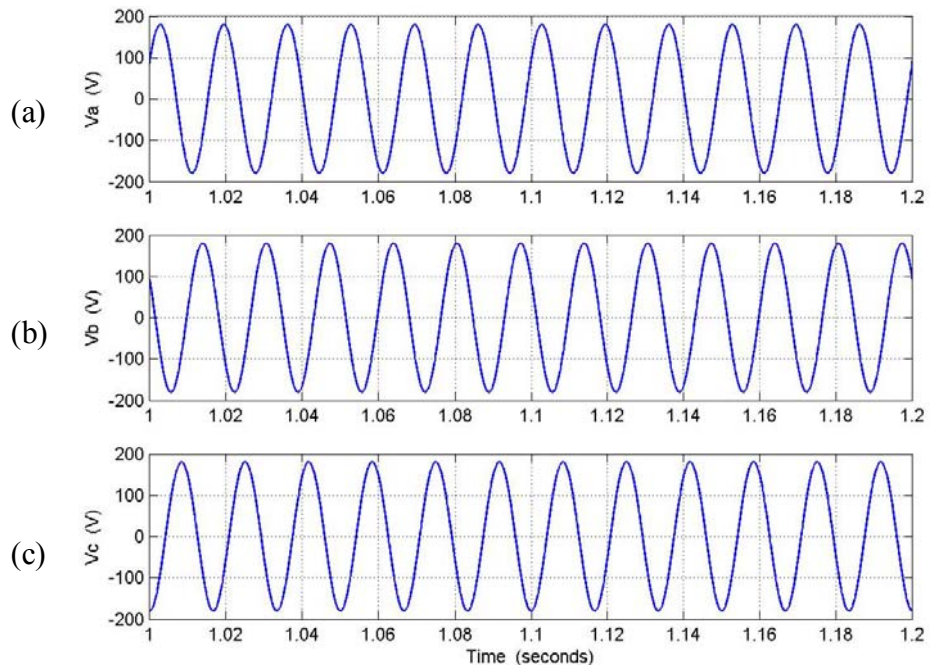


Figure 3.12: Simulation results for the rectifier, from top: (a) phase 'a' voltage V_a , (b) phase 'b' voltage V_b , (c) phase 'c' voltage V_c .

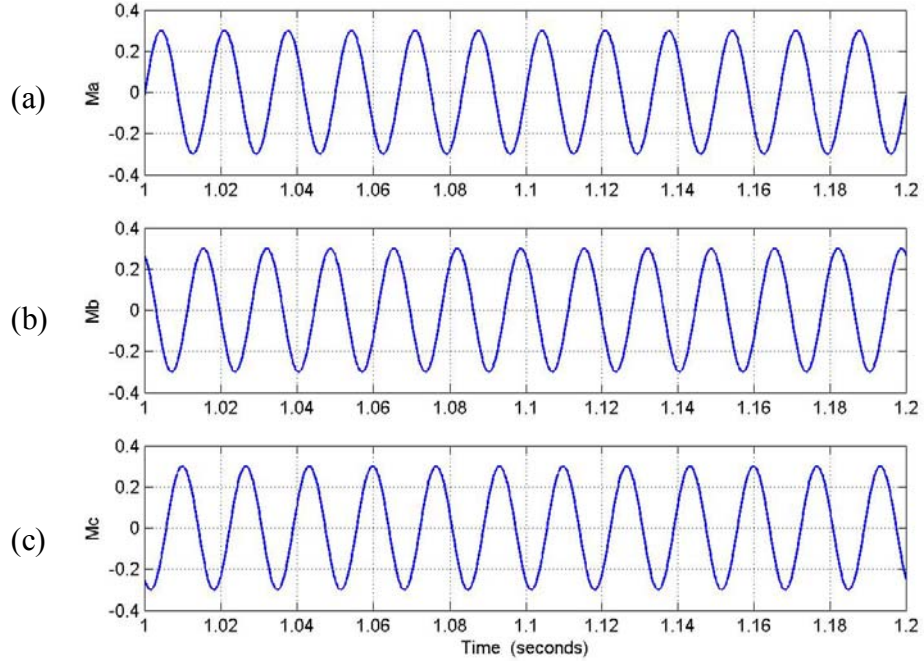


Figure 3.13 Simulation results for the rectifier, from top: (a) modulation signal for phase ‘a’ M_a , (b) modulation signal for phase ‘b’ M_b , (c) modulation signal for phase ‘c’ M_c .

3.8 Steady – State Analysis

The steady-state analysis of the system is done using the state equations of the system in the synchronous reference frame, as the variables in the equation are time-invariant with respect to the frame of reference. The steady-state analysis of any system is carried out to study the nature of the system at steady state and use the analysis to control the response of the system.

$$V_{qs} = rI_{qs} + LpI_{qs} + \omega_e LI_{ds} + \frac{M_{qs}V_{dc}}{2} \quad (3.63)$$

$$V_{ds} = rI_{ds} + LpI_{ds} - \omega_e LI_{qs} + \frac{M_{ds}V_{dc}}{2} \quad (3.64)$$

$$CpV_{dc} = \frac{3}{2}(M_{qs}I_{qs} + M_{ds}I_{ds}) - \frac{V_{dc}}{R_L} \quad (3.65)$$

The steady state equations of the system are obtained by setting the differential terms to zero.

$$pI_{qs} = pI_{ds} = pV_o = 0$$

$$V_{qs} = rI_{qs} + \omega_e LI_{ds} + \frac{M_{qs}V_{dc}}{2} \quad (3.66)$$

$$V_{ds} = rI_{ds} - \omega_e LI_{qs} + \frac{M_{ds}V_{dc}}{2} \quad (3.67)$$

$$V_o = rI_{os} \quad (3.68)$$

$$0 = \frac{3}{2}(M_{qs}I_{qs} + M_{ds}I_{ds} + 2M_oI_o) - \frac{V_{dc}}{R_L} \quad (3.69)$$

As the system is balanced, the zero sequence voltage is equal to zero (3.68) and the zero sequence component of the current in Equation (3.69) is equal to zero. Therefore, the equations used in the steady state analysis are

$$V_{qs} = RI_{qs} + \omega LI_{ds} + \frac{M_q V_o}{2} \quad (3.70)$$

$$V_{ds} = RI_{ds} - \omega LI_{qs} + \frac{M_d V}{2} \quad (3.71)$$

$$0 = \frac{3}{2}(M_{qs}I_{qs} + M_{ds}I_{ds}) - \frac{V_{dc}}{R_L} \quad (3.72)$$

The boost rectifier system is studied under a condition of unity power factor. The power factor angle is the angle between the input voltage and current, and for unity power factor the angle is equal to zero. The importance of a system operating under unity

power factor lies in the fact that under this condition the system outputs maximum power.

The condition for unity power factor is for the reactive power 'Q' of the system to be equal to zero. The expression for the reactive power of the system can be derived from the apparent power equation given by

$$S = \frac{3}{2}(V_{qds} I_{qds}^*) \quad (3.73)$$

$$V_{qds} = V_{qs} + jV_{ds} \quad (3.74)$$

$$I_{qds} = I_{qs} + jI_{ds} \quad (3.75)$$

Therefore,

$$S = \frac{3}{2}(V_{qs} + jV_{ds}) \times (I_{qs} + jI_{ds}) \quad (3.76)$$

Separating the real and imaginary parts, the expressions for real and reactive power can be obtained as

$$P = \frac{3}{2}(V_{qs} I_{qs} + V_{ds} I_{ds}) \quad (3.77)$$

$$Q = \frac{3}{2}(V_{qs} I_{ds} - V_{ds} I_{qs}) \quad (3.78)$$

Alignment of the voltage vector with the q-axis sets the d-axis component of the voltage to be equal to zero; therefore the d-axis current is also equal to zero.

$$V_{ds} = 0, I_{ds} = 0 \quad (3.79)$$

Applying the above condition, the equations for the rectifier (3.70) to (3.72) are expressed as

$$V_{qs} = rI_{qs} + \frac{M_{qs} V_{dc}}{2} \quad (3.80)$$

$$0 = -\omega_e L I_{qs} + \frac{M_{ds} V_{dc}}{2} \quad (3.81)$$

$$\frac{2}{3} \times \frac{V_{dc}}{R_L} = (M_{qs} I_{qs}). \quad (3.82)$$

Having derived the equations for the system to operate under unity power factor, to obtain the operating condition, the range of values of M_q and M_{ds} are expressed as a function of the output dc voltage of the system. Using the relationship between the q and d-axis modulation signals and the dc voltage, the operating point can be determined for the system to operate at a certain output dc voltage under a condition of unity power factor between the input currents and voltages.

From Equation (3.81)

$$I_{qs} = \frac{M_{ds} V_{dc}}{2\omega_e L}. \quad (3.83)$$

Substituting for I_q in Equation (3.80)

$$V_{qs} = \frac{rM_{ds} V_{dc}}{\omega_e L} + \frac{M_{qs} V_{dc}}{2}. \quad (3.84)$$

Rearranging Equation (3.84)

$$M_{qs} = \frac{2V_{qs}}{V_{dc}} - \frac{rM_{ds} V_{dc}}{2\omega_e L}. \quad (3.85)$$

Also, eliminating the q-axis current (3.83) in equation (3.82)

$$M_{qs} = \frac{4\omega_e L}{3M_{ds} R_L}. \quad (3.86)$$

Using Equations (3.85) and (3.86) the q and d-axis modulation signals can be solved for as functions of the output dc voltage.

Solving Equations (3.85) and (3.86) results in a quadratic equation in M_q and M_d . The steady state plots in Figures 3.14 and 3.15 show the variation of one of the solutions of both the q and d-axis modulation indexes as a function of the dc voltage. The load resistance is varied and the frequency is assumed to be constant at $\omega_e = 377$ rad/sec. The load resistance is varied as $R_L = 30\Omega$, 60Ω , and 150Ω . The calculated values of the q and d-axis modulation index for the dc voltage varying between 300V and 1000V are plotted in Figures 3.14 and 3.15, respectively. As can be seen from Figure 3.14, the varying of the load resistance does not have too much of an effect on the variation of the q-axis modulation signal; however, the d-axis modulation signal varies significantly with changing load resistance.

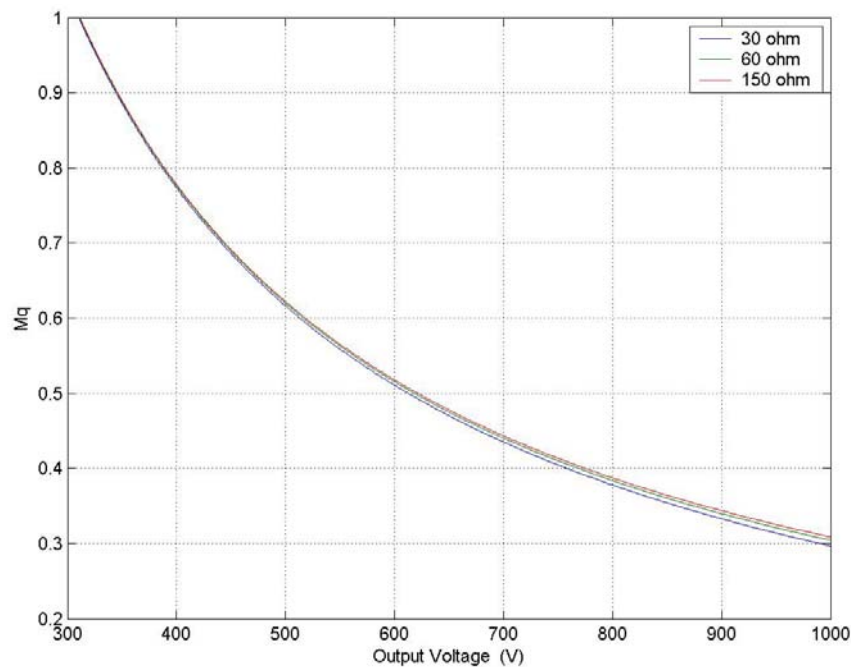


Figure 3.14: Variation of M_q with the dc voltage with varying load resistance of $R_L = 30\Omega$, 60Ω , and 150Ω ,

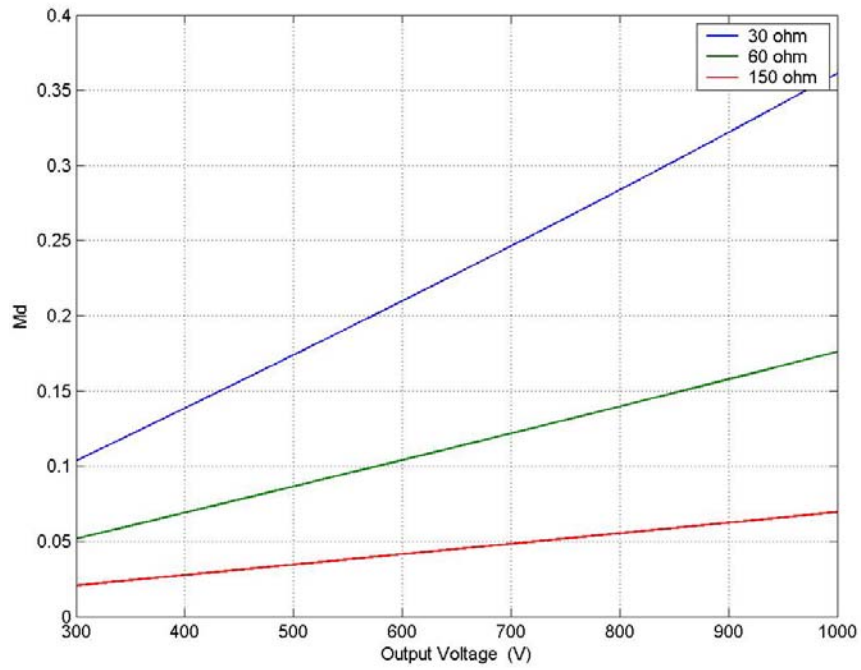


Figure 3.15: Variation of M_d with the dc voltage with varying load resistance of $R_L = 30\Omega$, 60Ω , and 150Ω .

CHAPTER 4

SERIES AND PARALLEL BOOST RECTIFIERS

4.1 Introduction

The use of parallel power converters, parallel dc-dc converters have become more common in the past decade. However the use of parallel three-phase converters has not yet been explored extensively. One unique feature with parallel three-phase converters is the potential zero-sequence circulating current [B.3]. The zero-sequence circulating current exists when the parallel connection of the rectifiers share the same input source, as shown in Figure 4.1. However the parallel rectifier connection considered in this chapter assumes independent sources for the two rectifiers. The analysis in this chapter shows a degree of freedom in the parallel connection of rectifiers that is used for power partitioning between the rectifiers. The effect of the power-partitioning factor α is studied under the steady state operation of the rectifiers.

The series connection of boost rectifiers considered in this chapter allows three output voltages that can be used in various applications. However, unlike the case of the parallel connection of the rectifiers, the series connection does not have the degree of freedom that allows for the power partitioning.

The first section lays out the modeling of the parallel connection of the rectifiers using the model of the boost rectifier developed in Chapter 3. The steady state analysis and the condition for unity power factor operation for the parallel connection of the boost

rectifiers is presented in section 4.2.2, and section 4.2.3 shows the dynamic simulation results

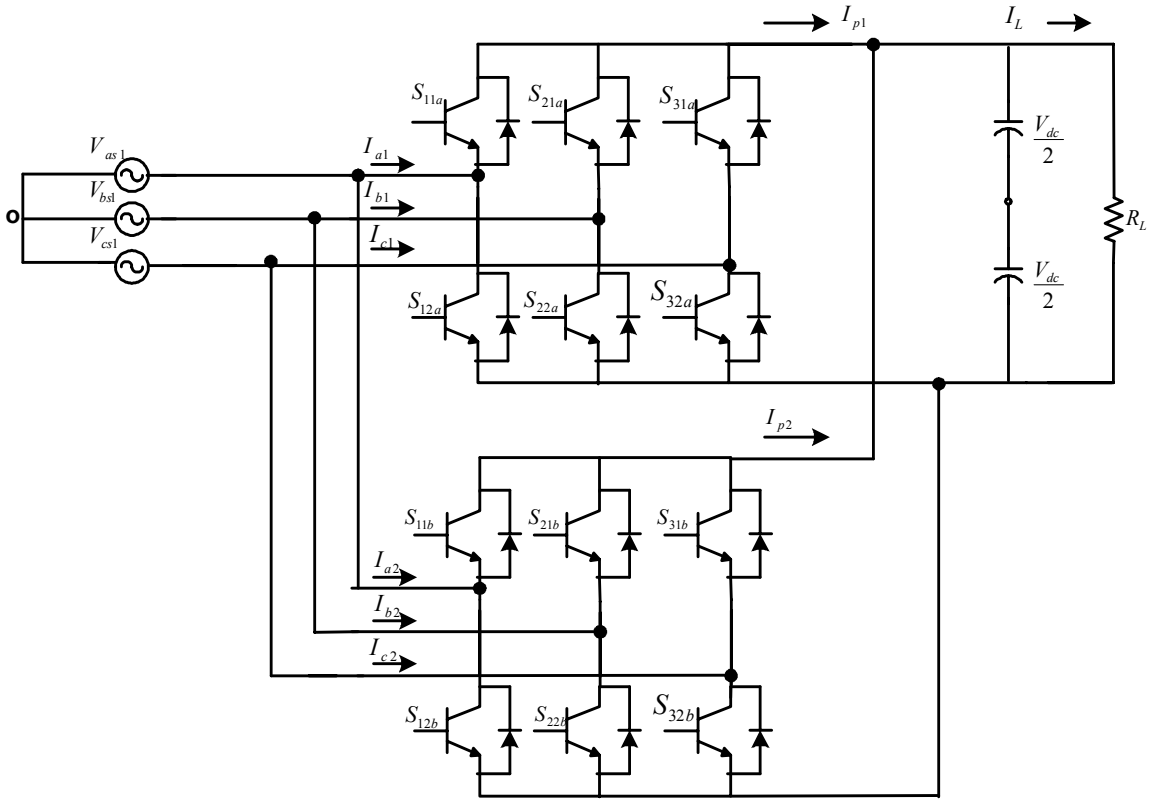


Figure 4.1: Topology of parallel connection of boost rectifiers with zero circulating currents

for the parallel rectifier connection with sources of same and different frequencies operating at unity power factor. The analysis carried out for the parallel rectifiers in sections 4.2 to 4.4 is repeated for the series connection of the rectifier in sections 4.3.

A unique feature of paralleling rectifiers, as mentioned earlier is the zero circulating current in the circuit. The circulating current is present because at any instant of time two devices in each converter are ‘ON’, thereby creating a path for current through two devices in the first converter and two devices in the second converter.

4.2 Parallel Rectifiers

4.2.1 Model of Parallel Rectifiers

The parallel connection of boost rectifiers used in this chapter is shown in Figure 4.2. The modeling of the rectifier follows the modeling of the single boost rectifier developed in Chapter 3.

For the parallel configuration, the boost rectifiers are connected in parallel at the output, i.e. the two rectifiers share the same output capacitor and load resistance. The method of modeling of the parallel rectifiers is to derive the voltage equations for each rectifier independently and then develop the equation at the output capacitor of the system by combining the output dc currents. This is explained in detail in the ensuing sections.

The model equations of each rectifier are exactly the same as that for the single boost rectifier derived in Chapter 3. The switching functions for each rectifier satisfy the same conditions as explained for the single boost rectifier, i.e. at no instant of time should two switches be ON' simultaneously as it would short-circuit the capacitor at the output. The model equations for each rectifier are presented separately following which the complete model of the parallel rectifiers will be presented. The conditions satisfied by the switching functions for rectifier A are shown in Equations (4.1) to (4.3).

$$S_{11a} + S_{12a} = 1 \quad (4.1)$$

$$S_{21a} + S_{22a} = 1 \quad (4.2)$$

$$S_{31a} + S_{32a} = 1 \quad (4.3)$$

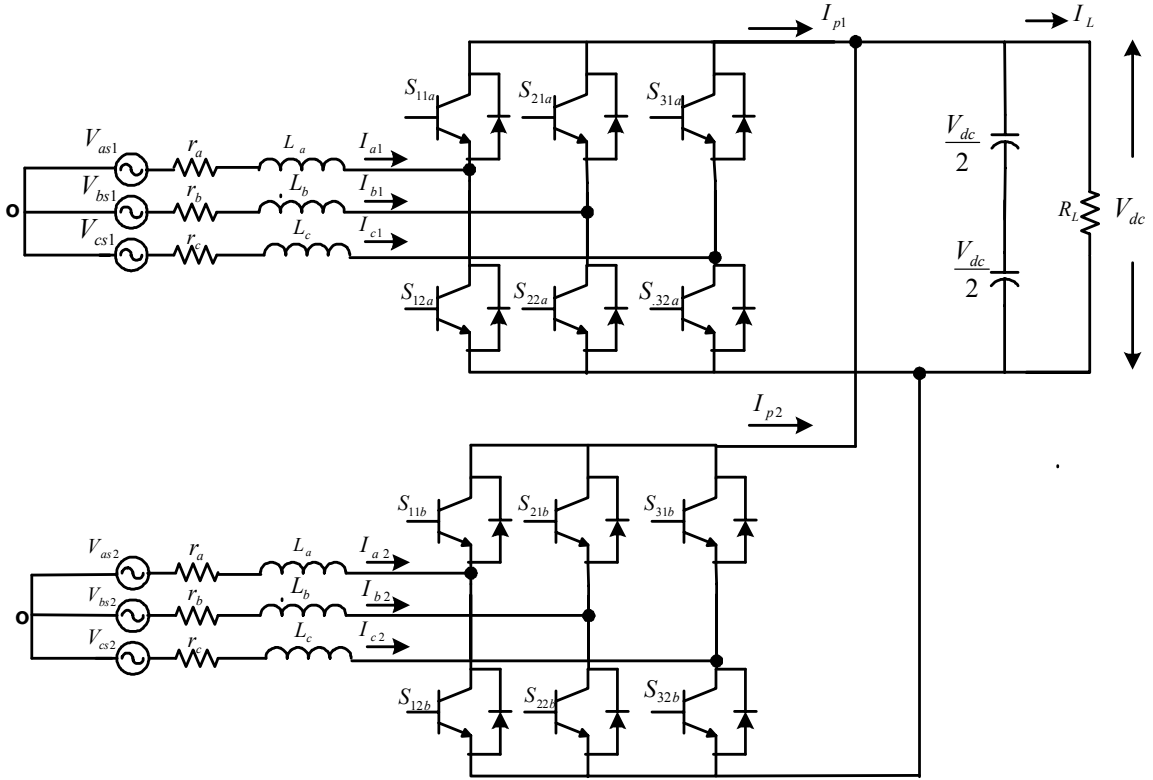


Figure 4.2: Topology of parallel connection of boost rectifiers with independent sources

The parameters for rectifier ‘A’ are shown in Table 4.1.

Table 4.1: Parameters for rectifier ‘a’

$V_{as1}, V_{bs1}, V_{cs1}$	Voltages on AC-side
I_{a1}, I_{b1}, I_{c1}	Phase currents
r_a, r_b, r_c	Resistance per phase
L_a, L_b, L_c	Inductance per phase
I_{p1}	Dc current at the output of the rectifier
I_L	Load current
V_{dc}	Output dc voltage
$S_{11a}, S_{21a}, S_{31a}$	Switching functions for top devices
$S_{12a}, S_{22a}, S_{32a}$	Switching functions for bottom devices

The equations are presented for each rectifier separately as

Rectifier ‘A’

The phase voltages for rectifier A can be expressed in terms of the switching functions for the rectifier as

$$V_{as1} = rI_{a1} + LpI_{a1} + (2S_{11a} - 1)\frac{V_{dc}}{2} + V_{no} \quad (4.4)$$

$$V_{bs1} = rI_{b1} + LpI_{b1} + (2S_{21a} - 1)\frac{V_{dc}}{2} + V_{no} \quad (4.5)$$

$$V_{cs1} = rI_{c1} + LpI_{c1} + (2S_{31a} - 1)\frac{V_{dc}}{2} + V_{no} \quad (4.6)$$

The neutral voltage, (Equation 4.7), solved for using Equations (4.4) to (4.6) is expressed in terms of the switching functions of the top devices for Rectifier ‘a’.

$$V_{no} = -\frac{V_{dc}}{3}[2S_{11a} + 2S_{21a} + 2S_{31a} - 3] \quad (4.7)$$

Substituting for the neutral voltage in Equations 4.4 to 4.6 in terms of the switching functions, the phase voltages can be expressed in terms of the switching functions as

$$V_{as1} = rI_{a1} + LpI_{a1} + V_{dc} \left[\frac{2}{3}S_{11a} - \frac{1}{3}S_{21a} - \frac{1}{3}S_{31a} \right] \quad (4.8)$$

$$V_{bs1} = rI_{b1} + LpI_{b1} + V_{dc} \left[-\frac{1}{3}S_{11a} + \frac{2}{3}S_{21a} - \frac{1}{3}S_{31a} \right] \quad (4.9)$$

$$V_{cs1} = rI_{c1} + LpI_{c1} + V_{dc} \left[-\frac{1}{3}S_{11a} - \frac{1}{3}S_{21a} + \frac{2}{3}S_{31a} \right] \quad (4.10)$$

The dc current at the output of the rectifier is expressed in terms of the switching functions of the top devices and the phase currents.

$$I_{p1} = S_{11a}I_{a1} + S_{21a}I_{b1} + S_{31a}I_{c1} \quad (4.11)$$

Equations (4.8) to (4.11) are the state equations for rectifier ‘a’ in the parallel rectifier. Similarly, the model equations for the second rectifier, rectifier ‘b’ can be derived as below.

Rectifier ‘b’

The switching functions for rectifier ‘b’ satisfy the same conditions as described for ‘a’,

$$S_{11b} + S_{12b} = 1 \quad (4.12)$$

$$S_{21b} + S_{22b} = 1 \quad (4.13)$$

$$S_{31b} + S_{32b} = 1 \quad (4.14)$$

The parameters for this rectifier are defined in Table 4.2.

Table 4.2: Parameters for rectifier ‘b’

$V_{as2}, V_{bs2}, V_{cs2}$	Voltages on AC-side
I_{a2}, I_{b2}, I_{c2}	Phase currents
r_a, r_b, r_c	Resistance per phase
L_a, L_b, L_c	Inductance per phase
I_{p2}	Dc current at the output of the rectifier
I_L	Load current
V_{dc}	Output dc voltage
$S_{11b}, S_{21b}, S_{31b}$	Switching functions for top devices
$S_{12b}, S_{22b}, S_{32b}$	Switching functions for bottom devices

The phase voltage equations for rectifier ‘b’ and the dc current at the output of the rectifier are expressed in Equations (4.15) to (4.18). The equations are exactly the same as that derived for the single boost rectifier as well as ‘rectifier ‘a’,

$$V_{as2} + V_{no} = rI_{a2} + LpI_{a2} + (2S_{11b} - 1)\frac{V_{dc}}{2} + V_{no} \quad (4.15)$$

$$V_{bs2} = rI_{b2} + LpI_{b2} + (2S_{21b} - 1)\frac{V_{dc}}{2} + V_{no} \quad (4.16)$$

$$V_{cs2} = rI_{c2} + LpI_{c2} + (2S_{31b} - 1)\frac{V_{dc}}{2} + V_{no} \quad (4.17)$$

$$I_{p2} = S_{11b}I_{a2} + S_{21b}I_{b2} + S_{31b}I_{c2}. \quad (4.18)$$

Eliminating the term for the neutral voltage in Equations (4.15) to (4.17) , the phase voltages are

$$V_{as2} = rI_{a2} + LpI_{a2} + V_{dc} \left[\frac{2}{3}S_{11b} - \frac{1}{3}S_{21b} - \frac{1}{3}S_{31b} \right] \quad (4.19)$$

$$V_{bs2} = rI_{b2} + LpI_{b2} + V_{dc} \left[-\frac{1}{3}S_{11b} + \frac{2}{3}S_{21b} - \frac{1}{3}S_{31b} \right] \quad (4.20)$$

$$V_{cs2} = rI_{c2} + LpI_{c2} + V_{dc} \left[-\frac{1}{3}S_{11b} - \frac{1}{3}S_{21b} + \frac{2}{3}S_{31b} \right] \quad (4.21)$$

$$I_{p2} = S_{11b}I_{a2} + S_{21b}I_{b2} + S_{31b}I_{c2}. \quad (4.22)$$

As the two rectifiers, ‘a’ and ‘b’ are connected in parallel at the output, the capacitor voltage equation for the parallel rectifiers is modified from that derived for the single three-phase boost rectifier. The capacitor voltage equation is the nodal equation, and expresses the current flowing through the capacitor at the output of the rectifiers as the difference of the dc current I_p and the load current I_L . For the rectifiers connected in parallel the current through the capacitor is the difference of the sum of the dc currents

and the load current of rectifier ‘a’ and ‘b’. Therefore, the capacitor voltage equation for the parallel rectifiers can be expressed as

$$C_p V_{dc} = [I_{p1} + I_{p2} - I_L], \quad (4.23)$$

with the load current defined as

$$I_L = \frac{V_{dc}}{R_L} \quad (4.24)$$

$$C_p V_{dc} = (S_{11a} I_{a1} + S_{21a} I_{b1} + S_{31a} I_{c1} + S_{11b} I_{a2} + S_{21b} I_{b2} + S_{31b} I_{c2}) - \frac{V_{dc}}{R_L}. \quad (4.25)$$

The switching functions are expressed in terms of the modulation signals using the following general equation.

$$S = \frac{1 + M}{2} \quad (4.26)$$

Substituting for the switching functions in terms of the modulation signals, the capacitor voltage equation:

$$C_p V_{dc} = (M_{a1} I_{a1} + M_{b1} I_{b1} + M_{c1} I_{c1} + M_{a2} I_{a2} + M_{b2} I_{b2} + M_{c2} I_{c2}) - \frac{V_{dc}}{R_L} \quad (4.27)$$

M_{a1} , M_{b1} , and M_{c1} are the modulation signals for rectifier ‘a’ and M_{a2} , M_{b2} , and M_{c2} are the modulation signals for rectifier ‘b’.

Transformation of the state equations to the qd (synchronous) reference frame simplifies the analysis, as the variables are then time invariant with respect to the reference frame. Also transformation would allow the steady state analysis of the parallel connection of the rectifiers to be studied.

The voltage equations for the system are transformed by multiplying using the transformation matrix given in Equation (4.29).

$$f_{qds0} = (K_s(\theta_s))f_{abc} \quad (4.28)$$

$$K_s(\theta_s) = \frac{2}{3} \begin{bmatrix} \cos(\theta_s) & \cos\left(\theta_s - \frac{2\pi}{3}\right) & \cos\left(\theta_s + \frac{2\pi}{3}\right) \\ \sin(\theta_s) & \sin\left(\theta_s - \frac{2\pi}{3}\right) & \sin\left(\theta_s + \frac{2\pi}{3}\right) \\ \frac{1}{2} & \frac{1}{2} & \frac{1}{2} \end{bmatrix} \quad (4.29)$$

Applying the above transformation (4.28), the voltage equations for the parallel rectifier expressed in the synchronous reference frame are

$$V_{qs1} = rI_{qs1} + LpI_{qs1} + \omega_{e1}LI_{ds1} + \frac{M_{q1}V_{dc}}{2} \quad (4.30)$$

$$V_{ds1} = rI_{ds1} + LpI_{ds1} - \omega_{e1}LI_{qs1} + \frac{M_{d1}V_{dc}}{2} \quad (4.31)$$

$$V_{o1} = rI_{os1} + LpI_{os1} \quad (4.32)$$

$$V_{qs2} = rI_{qs2} + LpI_{qs2} + \omega_{e2}LI_{ds2} + \frac{M_{q2}V_{dc}}{2} \quad (4.33)$$

$$V_{ds2} = rI_{ds2} + LpI_{ds2} - \omega_{e2}LI_{qs2} + \frac{M_{d2}V_{dc}}{2} \quad (4.34)$$

$$V_{o2} = rI_{os2} + LpI_{os2} \quad (4.35)$$

V_{qs1} , V_{qs2} , V_{ds1} , V_{ds2} are q and d axis voltages for rectifier 'a' and 'b', respectively.

I_{qs1} , I_{qs2} , I_{ds1} , I_{ds2} are q and d axis currents for rectifier 'a' and 'b', respectively, and V_{os1} and V_{os2} are the zero sequence voltages for each rectifier.

M_{qs1} , M_{ds1} , M_{qs2} , and M_{ds2} are the q and d axis components of the modulation signals for rectifier 'a' and 'b', respectively.

As the system is assumed to have balanced voltages, the zero sequence voltages for both rectifier ‘a’ and ‘b’ are equal to zero. Therefore, the voltage equations for the parallel rectifier system are Equations (4.30), (4.31), (4.33), and (4.34).

The capacitor voltage equation for the system (4.27) is transformed to the synchronous reference frame by replacing the abc components of the currents and modulation signals with the q and d-axis components using the inverse transformation matrix K_s^{-1} .

$$CpV_{dc} = \left(I_{qdo}^T (K_s^T)^{-1} (K_s)^{-1} M_{abc} \right) \quad (4.36)$$

$$CpV_{dc} = \frac{3}{2} \left(M_{qs1} I_{qs1} + M_{ds1} I_{ds1} + 2M_{o1} I_{o1} + M_{qs2} I_{qs1} + M_{ds2} I_{ds2} + 2M_{o2} I_{o2} \right) - \frac{V_{dc}}{R_L} \quad (4.37)$$

Since the system is balanced, the zero sequence components of the currents are equal to zero.

$$CpV_{dc} = \frac{3}{2} \left(M_{qs1} I_{qs1} + M_{ds1} I_{ds1} + M_{qs2} I_{qs1} + M_{ds2} I_{ds2} \right) - \frac{V_{dc}}{R_L} \quad (4.38)$$

4.2.2 Steady State Analysis

Setting the differential terms in the dynamic equation to zero results in the steady state equations for the system. The analysis is performed to obtain the values of the q and d-axis modulation signals for each rectifier to operate the rectifiers at unity power factor.

$$V_{qs1} = rI_{qs1} + \omega_{e1} LI_{ds1} + \frac{M_{q1} V_{dc}}{2} \quad (4.39)$$

$$V_{ds1} = rI_{ds1} - \omega_{e1} LI_{qs1} + \frac{M_{d1} V_{dc}}{2} \quad (4.40)$$

$$V_{qs2} = rI_{qs2} + \omega_{e2}LI_{ds2} + \frac{M_{q2}V_{dc}}{2} \quad (4.41)$$

$$V_{ds2} = rI_{ds2} - \omega_{e2}LI_{qs2} + \frac{M_{d2}V_{dc}}{2} \quad (4.42)$$

$$0 = \frac{3}{2} \left(M_{qs1}I_{qs1} + M_{ds1}I_{ds1} + M_{qs2}I_{qs1} + M_{ds2}I_{ds2} \right) - \frac{V_{dc}}{R_L} \quad (4.43)$$

As in the case of the single boost rectifier system, the parallel rectifiers are studied under a condition of unity power factor. The need to operate any system at unity power factor arises from the fact losses are minimum at this point of operation. This is because the current and voltage on the input side of the rectifier are in phase. This condition is applied when the reactive power is equal to zero.

$$Q = \frac{3}{2} (V_{qs}I_{ds} - V_{ds}I_{qs}) \quad (4.44)$$

Setting the d-axis voltage and currents to be equal to zero in Equations (4.39) to (4.43)

$$V_{qs1} = rI_{qs1} + \frac{M_{q1}V_{dc}}{2} \quad (4.45)$$

$$0 = -\omega_{e1}LI_{qs1} + \frac{M_{d1}V_{dc}}{2} \quad (4.46)$$

$$V_{qs2} = rI_{qs2} + \frac{M_{q2}V_{dc}}{2} \quad (4.47)$$

$$0 = -\omega_{e2}LI_{qs2} + \frac{M_{d2}V_{dc}}{2} \quad (4.48)$$

$$0 = \frac{3}{2} \left(M_{qs1}I_{qs1} + M_{qs2}I_{qs1} \right) - \frac{V_{dc}}{R_L}. \quad (4.49)$$

To determine the operating point for each rectifier under unity power factor, for a specific value of dc voltage, the q and d-axis modulation signals for each rectifier need to be determined. From Equations (4.45) to (4.49) it can be seen that the number of variables are greater than the number of equations, i.e. the variables to be determined are I_{qs1} , I_{qs2} , M_{qs1} , M_{qs2} , M_{ds1} , and M_{ds2} (six variables) and the number of equations are five. To solve for the variables, an additional constraint is applied to the parallel rectifier system. The constraint applied is power partitioning between the rectifiers. The total power of the two rectifiers is partitioned by considering a factor α , where α denotes the ratio in which the power total power is distributed between the two rectifiers.

Considering the power equations for each rectifier:

$$P_1 = \frac{3}{2} (V_{qs1} I_{qs1} + V_{ds1} I_{ds1}) \quad (4.50)$$

$$P_2 = \frac{3}{2} (V_{qs2} I_{qs2} + V_{ds2} I_{ds2}). \quad (4.51)$$

Let the total power be P ,

$$\text{where } P = P_1 + P_2. \quad (4.52)$$

Applying the condition for unity power factor, $V_{ds1} = V_{ds2} = 0$

$$\frac{P_1}{P_2} = \frac{\alpha}{(1-\alpha)} = \frac{V_{qs1} I_{qs1}}{V_{qs2} I_{qs2}}. \quad (4.53)$$

Therefore,

$$(1-\alpha)V_{q1}I_{q1} = \alpha V_{q2}I_{q2}. \quad (4.54)$$

Therefore, using the additional equation describing the power partitioning of the system, the variables can be calculated.

Using the above equations (4.45) – (4.49) and (4.54) the steady state plots for the parallel rectifier system are presented. The system has been studied under varying dc voltages and power partitioning factors. The load resistance has been kept constant and the dc voltage has been varied between 300V and 1000V. The power for each rectifier has been calculated considering the factor α and has been plotted as a function of the q-axis modulation index for each rectifier.

The effect of alpha on the output power of each rectifier is evident from the steady-state plots as an increase in alpha for one rectifier decreases the power and vice versa for the second rectifier.

The parameters used for each rectifier are the same and are shown in Table 4.3.

Table 4.3: Parameters used for parallel rectifiers

$V_{as} = 180 \cos\left(377t - \frac{\pi}{6}\right)$
$V_{bs} = 180 \cos\left(377t - \frac{\pi}{6} - \frac{2\pi}{3}\right)$
$V_{cs} = 180 \cos\left(377t - \frac{\pi}{6} + \frac{2\pi}{3}\right)$
$r = 0.1 \Omega$
$L = 6.4 \text{ mH}$
$C = 150 \mu\text{F}$
$R_L = 30 \Omega$

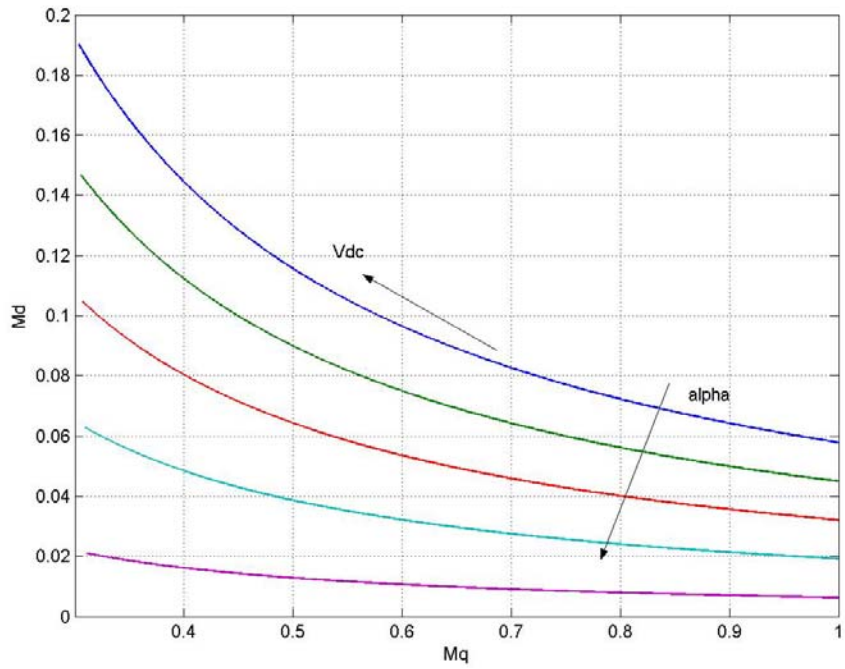


Figure 4.3: Variation of the q-axis and d-axis modulation index with the output dc voltage varying between 300V and 100V at a constant load resistance of $R_L = 100\Omega$ for varying values of α for rectifier 'a'

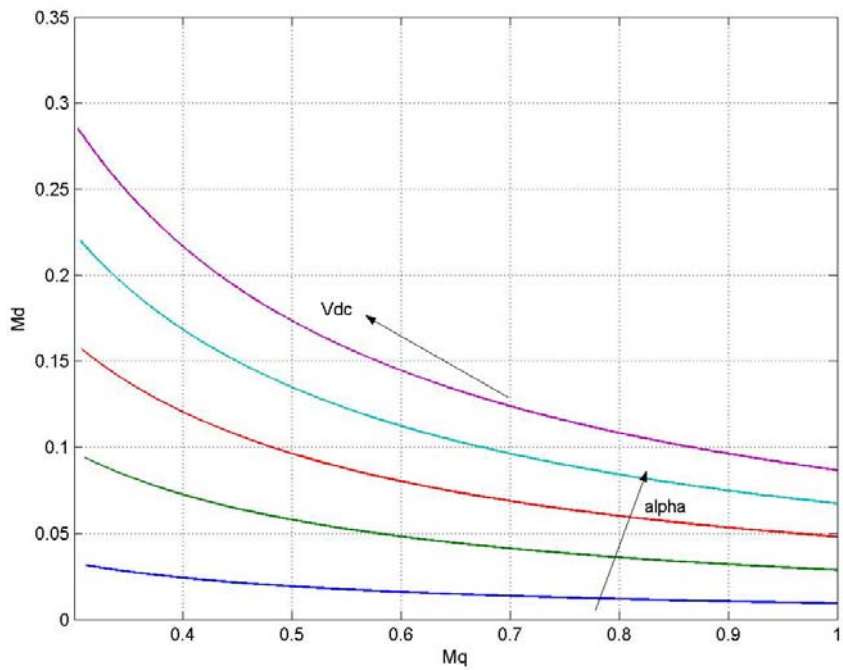


Figure 4.4: Variation of the q-axis and d-axis modulation index with the output dc voltage varying between 300V and 100V at a constant load resistance of $R_L = 100\Omega$ for varying values of α for rectifier 'b'

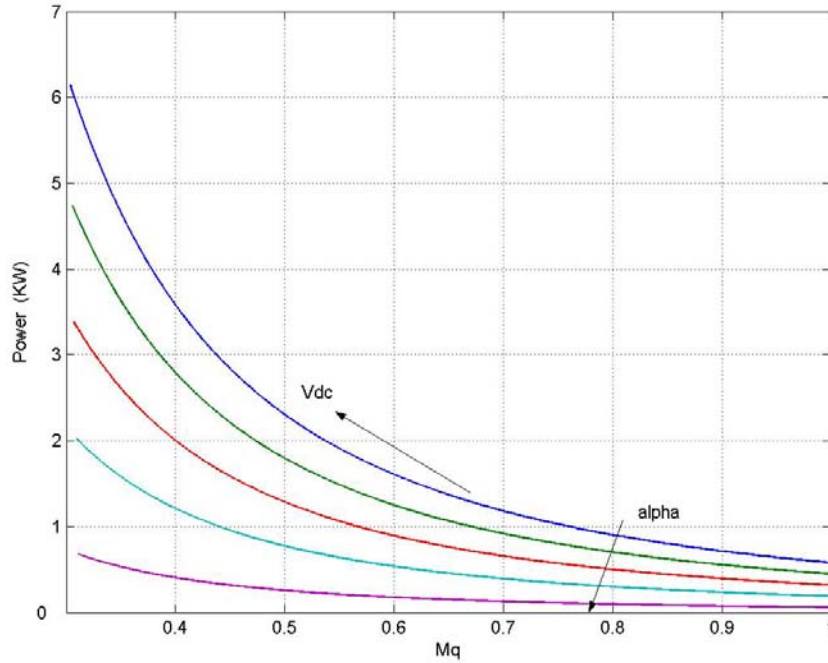


Figure 4.5: Variation of the q-axis modulation index and power, with the dc voltage varying between 300V and 100V at a constant load resistance of $R_L = 100\Omega$ for varying values of α for rectifier 'a'

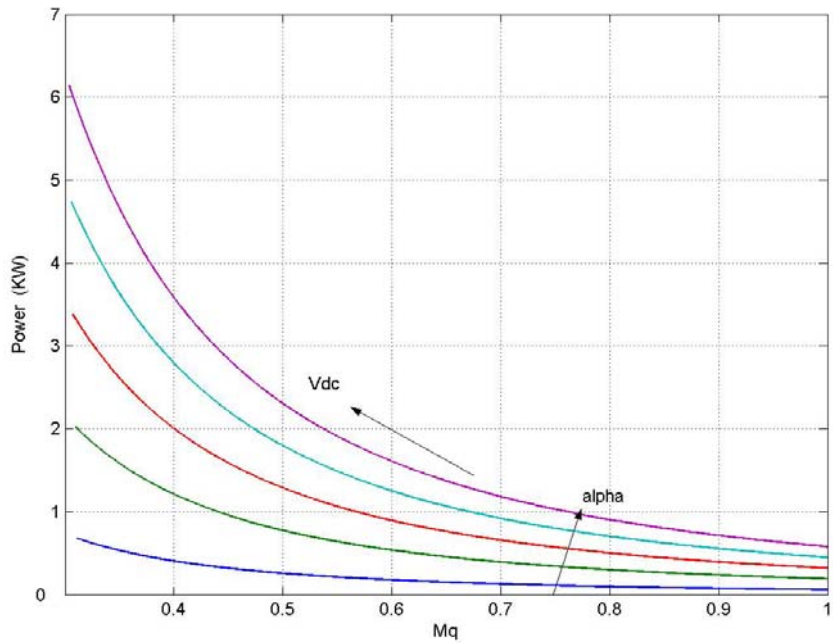


Figure 4.6: Variation of the q-axis modulation index and power, with the dc voltage varying between 300V and 100V at a constant load resistance of $R_L = 100\Omega$ for varying values of α for rectifier 'b'

From Figures 4.3 to 4.6, for a constant load resistance and power, an increase in the dc voltage increases the value of the q-axis modulation index, and a decrease in the d-axis modulation index. Also for an increase in the power partitioning factor, the value of the q-axis modulation signal decreases.

The steady state analysis enables the determination of the operating point by selection of the dc voltage and the corresponding values of the q and d-axis modulation signals. The dynamic simulation in the next section shows one such operating point on the steady state curve chosen to operate the system at unity power factor.

4.2.3 Dynamic Simulation

The dynamic simulation of the parallel boost rectifiers has been carried out under two different conditions. The first assumes both the independent sources to operate with the same supply frequency. The second considers the sources to have different frequencies. The parameters used in the simulation are the same as in Table 4.3.

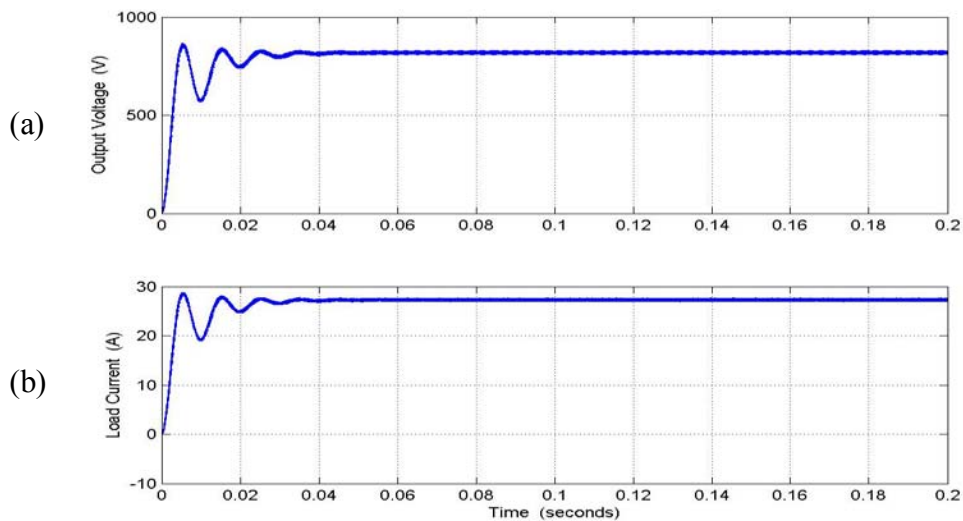


Figure 4.7: Simulation results for the parallel rectifier, from top : (a) output dc voltage V_{dc} ,
(b) load current I_L

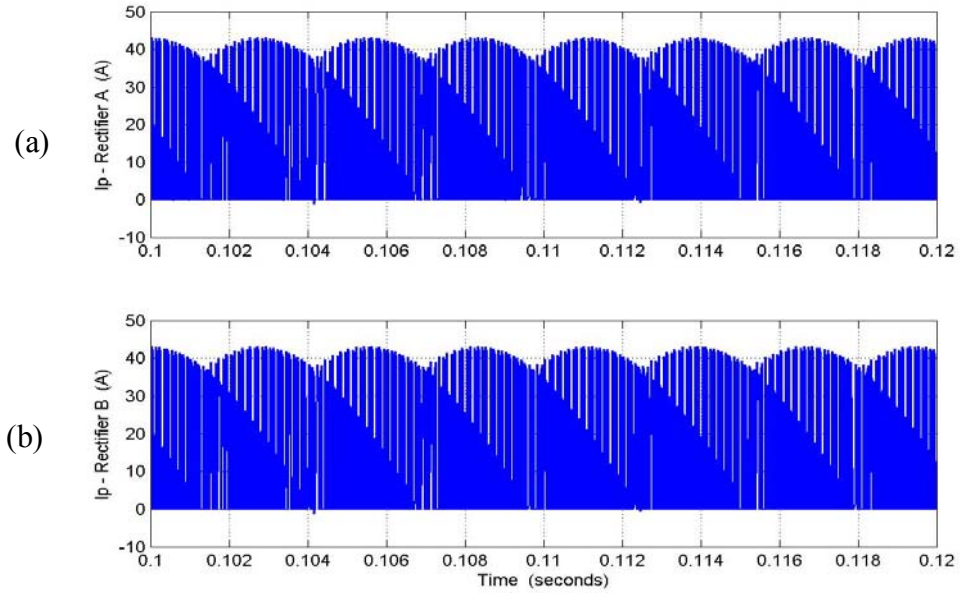


Figure 4.8: Simulation results for the parallel rectifier, from top: (a) output dc current rectifier 'a' I_{p1} , (b) output dc current rectifier 'b' I_{p2}

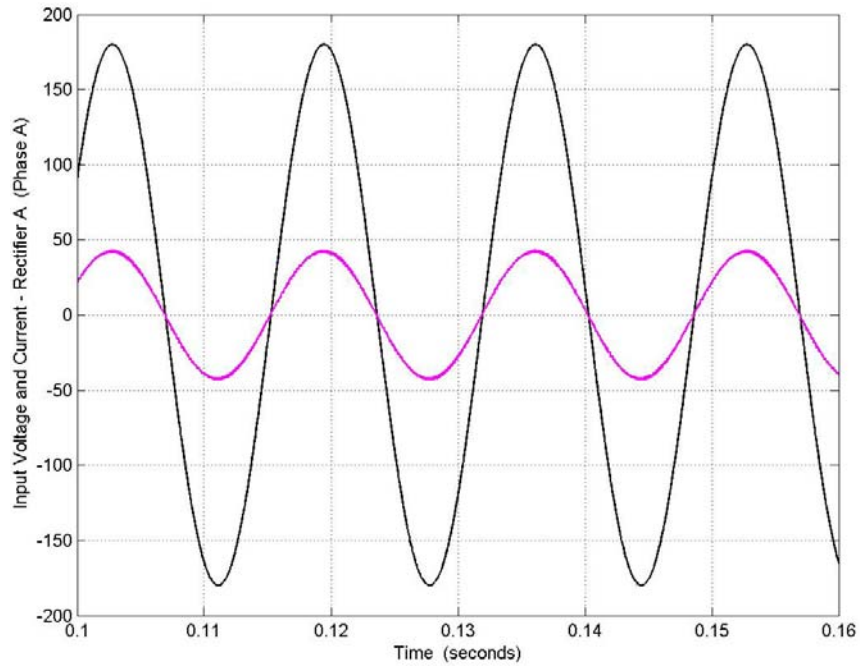


Figure 4.9: Simulation results for the parallel rectifier, phase -a input voltage and current for rectifier 'a'

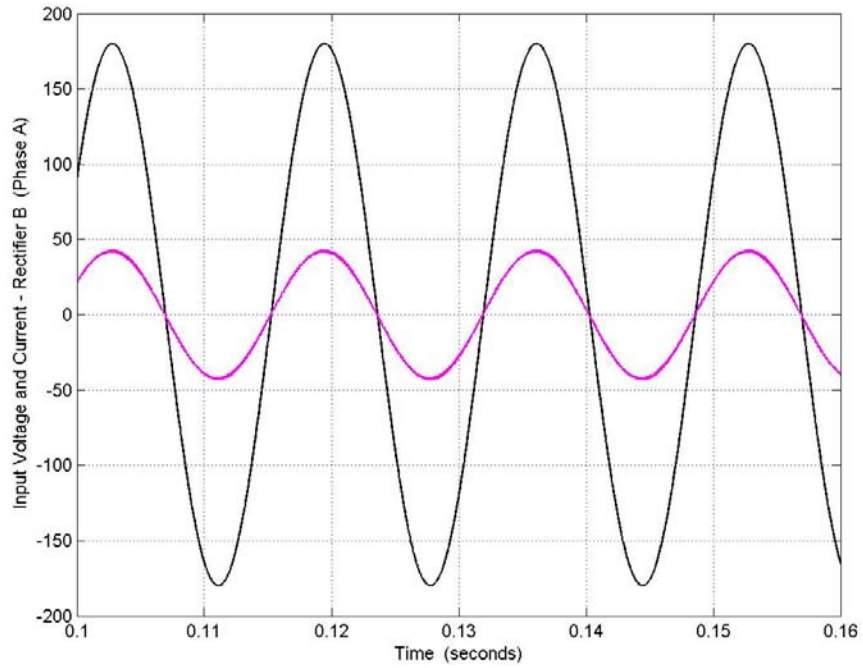


Figure 4.10: Simulation results for parallel rectifier, phase -a input voltage and current for rectifier 'b'

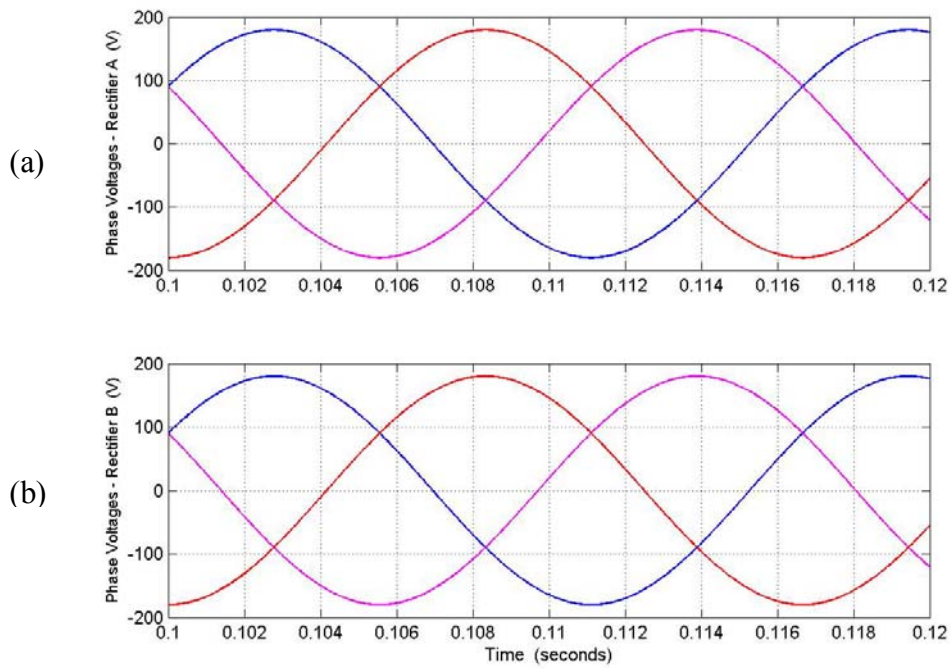


Figure 4.11: Simulation results for the parallel rectifier, phase voltages from top: (a) rectifier 'a', (b) rectifier 'b'

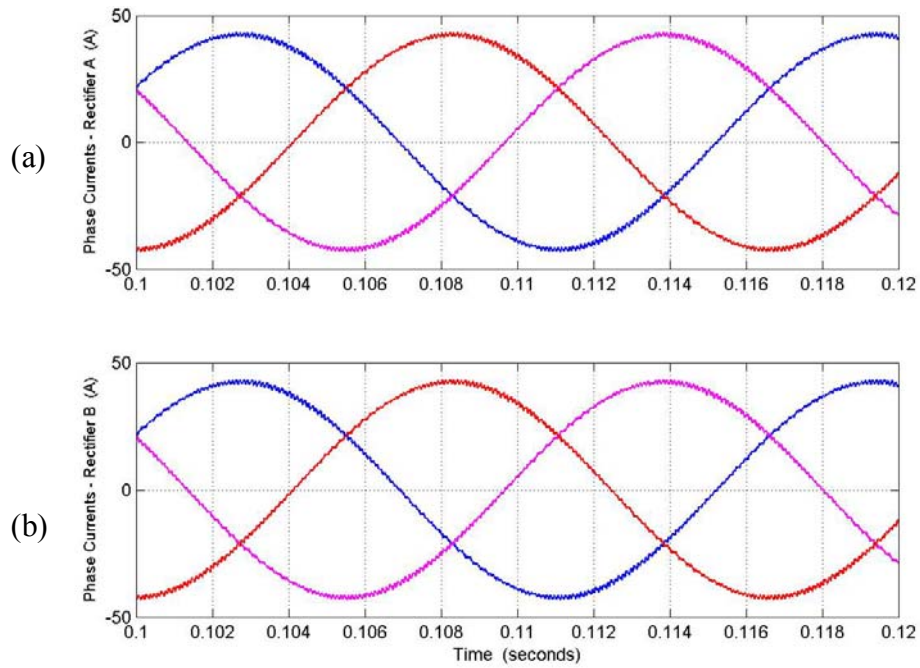


Figure 4.12: Simulation results for the parallel rectifier, phase currents from top: (a) rectifier 'a', (b) rectifier 'b'

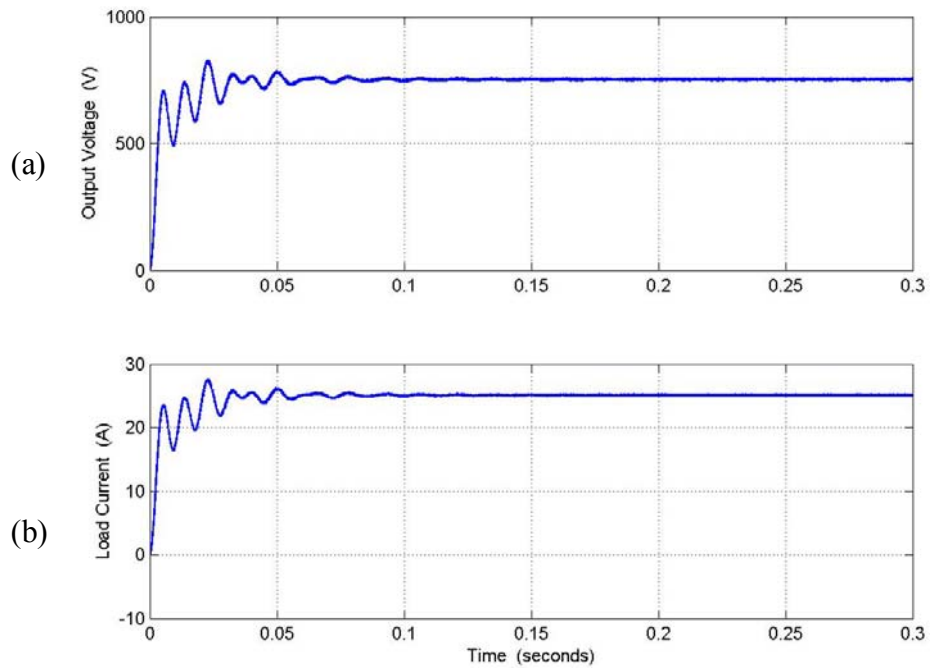


Figure 4.13: Simulation results for the parallel rectifier, from top : (a) output dc voltage V_{dc} , (b) load current I_L

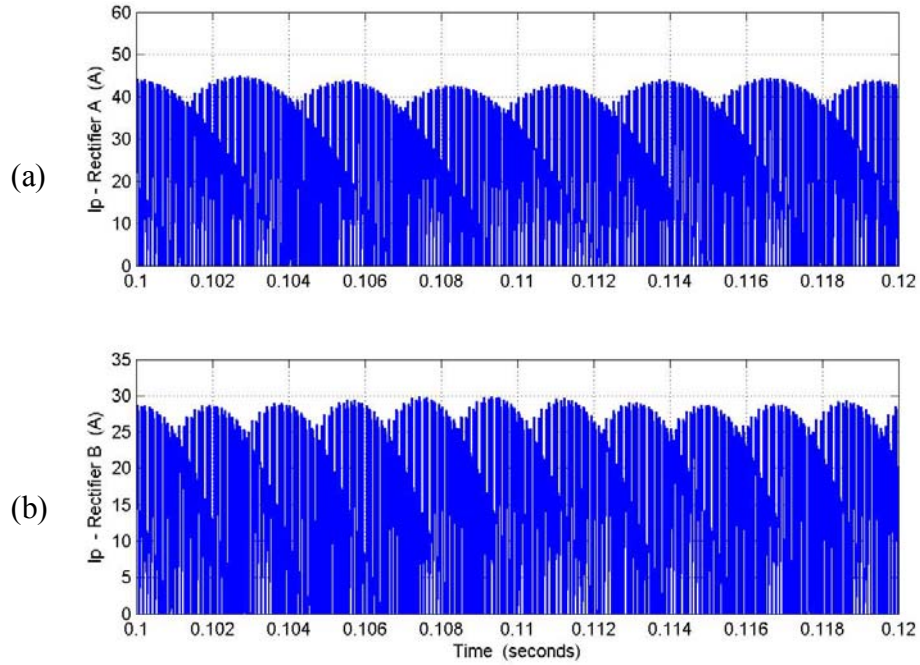


Figure 4.14: Simulation results for the parallel rectifier, from top : (a) output dc current rectifier 'a' I_{p1} , (b) output dc current rectifier 'b' I_{p2}

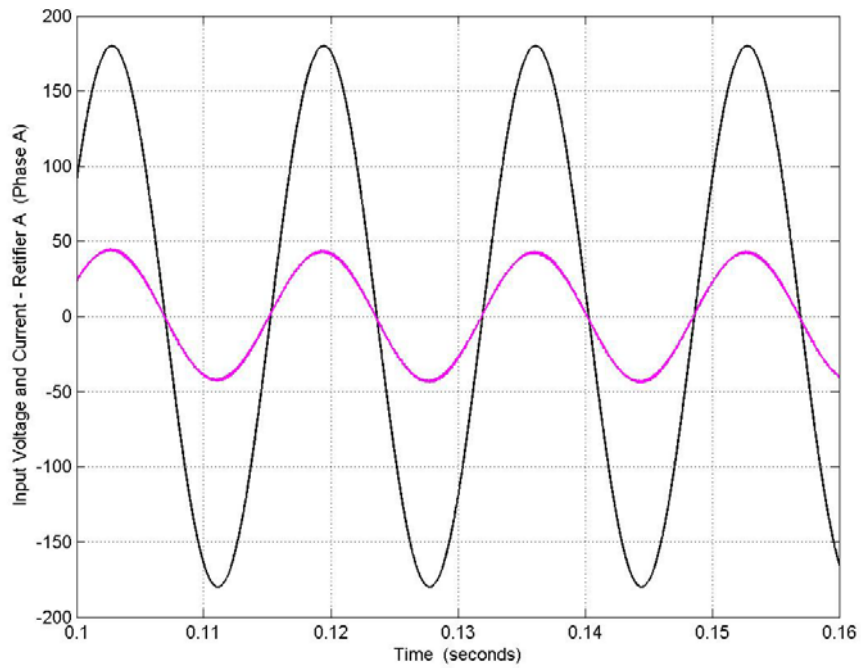


Figure 4.15: Simulation results for the parallel rectifier, phase -a input voltage and current for rectifier

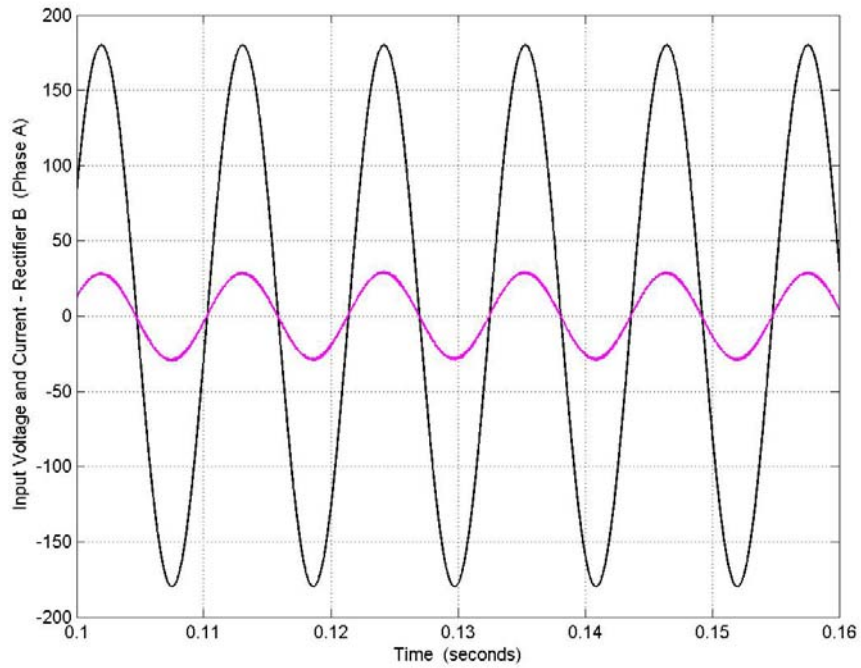


Figure 4.16: Simulation results for the parallel rectifier, phase-a input voltage and current for rectifier

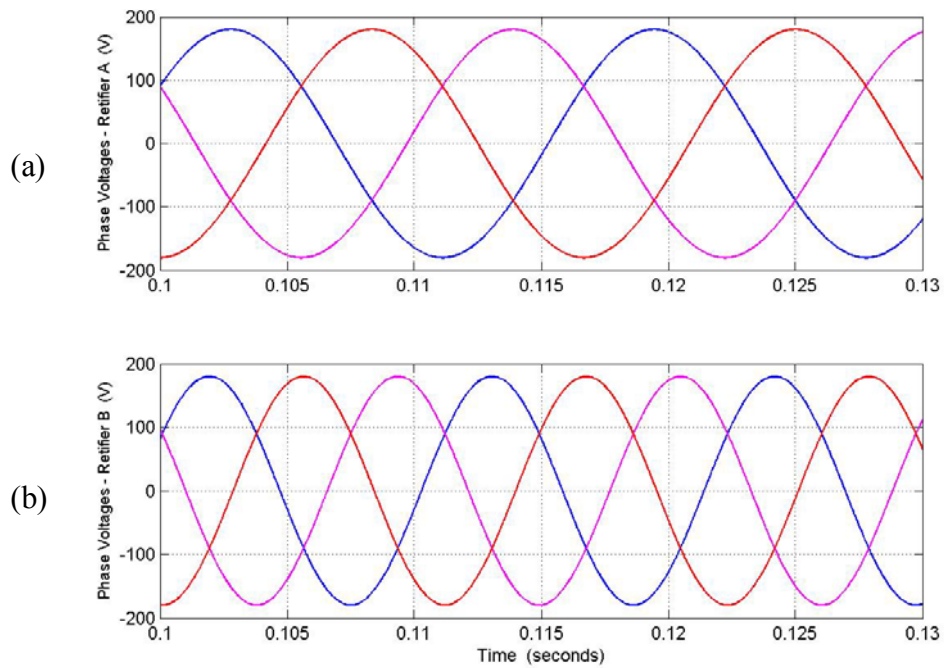


Figure 4.17: Simulation results for the parallel rectifier, phase voltages from top: (a) rectifier 'a', (b) rectifier 'b'

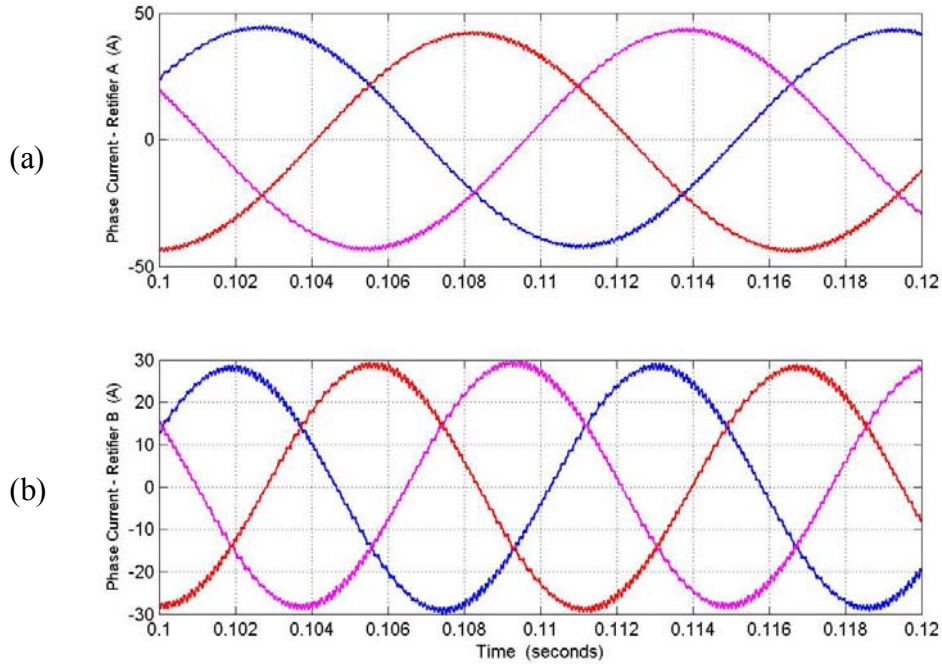


Figure 4.18: Simulation results for the parallel rectifier, phase currents from top: (a) rectifier 'a', (b) rectifier 'b'.

The simulation for the parallel rectifier system has been performed and the results are as shown in Figures 4.7 to 4.18. The first set of figures, Figures 4.7 to 4.12 show the response of the parallel rectifier system when the sources on the input side of the rectifier have the same supply frequency of $\omega_{e1} = \omega_{e2} = 377$ rad/sec. Figure 4.7 shows the output voltage of the parallel rectifier system and the load current. Figure 4.8 shows the dc current at the output of both rectifier 'a' and 'b'. The nature of the dc current waveform is evident from Equations 4.18 and 4.22. Figures 4.9 and 4.10 show the input voltage and current (phase-'a') for each rectifier to be in phase i.e. the operation of the rectifiers at unity power factor. The input voltages and currents for both rectifiers are shown in Figures 4.11 and 4.12.

The second set of Figures 4.13 to 4.18 is obtained by taking the input sources of the two rectifiers to be of different frequencies generates, $\omega_{e1} = 377$ rad/sec and $\omega_{e2} = 565$ rad/sec. The output voltage and load current are shown in Figure 4.13; the dc current for each rectifier is shown in Figure 4.14. Figures 4.15 and 4.16 show the unity power factor operation and Figures 4.17 and 4.18 show the phase voltages and currents for each rectifier.

4.3 Series Rectifier

Series boost rectifiers can be applied to a large range of applications based on the specific area of application required. The series connection of the rectifiers can be use as three independent voltage sources, assuming the accessibility of the voltages depending on the configuration of the system.

In present day systems, due to the increased complexity of system models, the requirements for more dc sources has increased. Therefore a scheme where for the same system configuration, multiple supplies can be drawn is very advantageous.

The system configuration studied in this section allows the voltage across each of the series connected rectifiers as each rectifier has a capacitor at the output as shown in Figure 4.19.

The circuit configuration considered involves the sharing of one load resistance for both the rectifiers; however, the system can be operated with independent load resistances for each rectifier.

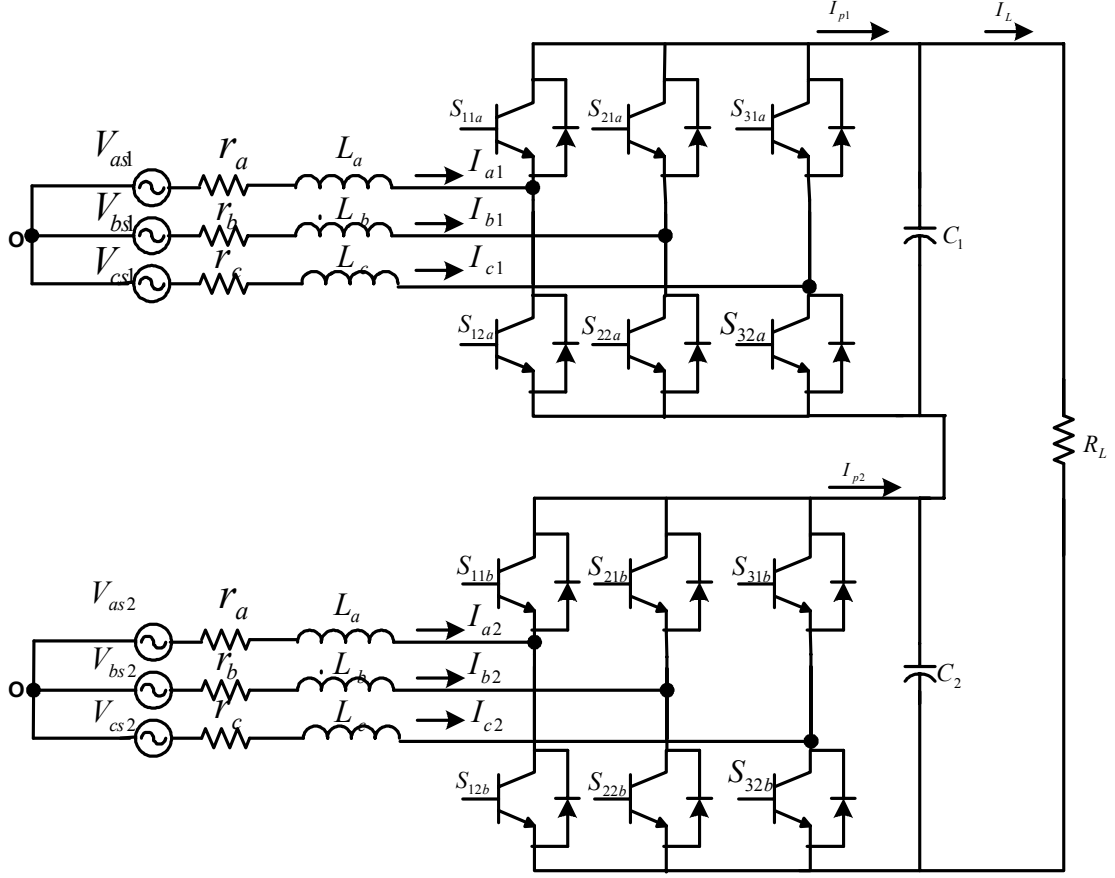


Figure 4.19: Topology for series rectifier connection

4.3.1 Model of Series Rectifier

The method of modeling of the series connection of the boost rectifiers is exactly the same as that adopted for the parallel rectifiers in section 4.2. Each rectifier is modeled independently and as the rectifiers are connected in series at the output, modeling series connection of the rectifiers is included on the output side of the rectifiers. As the model of each rectifier is exactly the same as the model derived in Chapter 3 the model equations for the rectifier in the abc reference frame are repeated below

$$V_{as1} = rI_{a1} + LpI_{a1} + V_{dc} \left[\frac{2}{3}S_{11a} - \frac{1}{3}S_{21a} - \frac{1}{3}S_{31a} \right] \quad (4.55)$$

$$V_{bs1} = rI_{b1} + LpI_{b1} + V_{dc} \left[-\frac{1}{3}S_{11a} + \frac{2}{3}S_{21a} - \frac{1}{3}S_{31a} \right] \quad (4.56)$$

$$V_{cs1} = rI_{c1} + LpI_{c1} + V_{dc} \left[-\frac{1}{3}S_{11a} - \frac{1}{3}S_{21a} + \frac{2}{3}S_{31a} \right] \quad (4.57)$$

$$I_{p1} = S_{11a}I_{a1} + S_{21a}I_{b1} + S_{31a}I_{c1} \quad (4.58)$$

$$V_{as2} = rI_{a2} + LpI_{a2} + V_{dc} \left[\frac{2}{3}S_{11b} - \frac{1}{3}S_{21b} - \frac{1}{3}S_{31b} \right] \quad (4.59)$$

$$V_{bs2} = rI_{b2} + LpI_{b2} + V_{dc} \left[-\frac{1}{3}S_{11b} + \frac{2}{3}S_{21b} - \frac{1}{3}S_{31b} \right] \quad (4.60)$$

$$V_{cs2} = rI_{c2} + LpI_{c2} + V_{dc} \left[-\frac{1}{3}S_{11b} - \frac{1}{3}S_{21b} + \frac{2}{3}S_{31b} \right] \quad (4.61)$$

$$I_{p2} = S_{11b}I_{a2} + S_{21b}I_{b2} + S_{31b}I_{c2} \quad (4.62)$$

Equations (4.55) to (4.58) are the model equations for rectifier ‘a’ and (4.59) to (4.62) are the model equations for rectifier ‘b’.

The parameters used in the equations for each rectifier are the same as in Tables 4.1 and 4.2.

The capacitor voltage equations for each rectifier are

$$CpV_{c1} = Ip_1 - \frac{V_{dc}}{R_L} \quad (4.63)$$

$$CpV_{c2} = Ip_2 - \frac{V_{dc}}{R_L} \quad (4.64)$$

V_{c1} is the voltage across the capacitor for rectifier ‘a’.

V_{c2} is the voltage across the capacitor for rectifier ‘b’.

As the rectifiers are connected in series at the output, the output voltage is the sum of the individual voltages of the boost rectifiers, and can be expressed as

$$V_{dc} = V_{e1} + V_{e2} \quad (4.65)$$

To perform the steady state analysis, the model equations for the system are transformed to the synchronous reference frame using the transformation matrix: The method of transformation is as explained in the previous section.

$$K_s(\theta_s) = \frac{2}{3} \begin{bmatrix} \cos(\theta_s) & \cos\left(\theta_s - \frac{2\pi}{3}\right) & \cos\left(\theta_s + \frac{2\pi}{3}\right) \\ \sin(\theta_s) & \sin\left(\theta_s - \frac{2\pi}{3}\right) & \sin\left(\theta_s + \frac{2\pi}{3}\right) \\ \frac{1}{2} & \frac{1}{2} & \frac{1}{2} \end{bmatrix} \quad (4.66)$$

The capacitor voltage equations for each rectifier are transformed to the synchronous reference frame by substituting for the abc reference frame currents and modulation signals in terms of the inverse transformation matrix and the qdo currents and modulation signals, as explained in Chapter 3.

Hence the model equations for the series boost rectifiers in the synchronous reference frame are

$$V_{qs1} = rI_{qs1} + LpI_{qs1} + \omega_{e1}LI_{ds1} + \frac{M_{q1}V_{dc}}{2} \quad (4.67)$$

$$V_{ds1} = rI_{ds1} + LpI_{ds1} - \omega_{e1}LI_{qs1} + \frac{M_{d1}V_{dc}}{2} \quad (4.68)$$

$$V_{o1} = rI_{os1} + LpI_{os1} \quad (4.69)$$

$$V_{qs2} = rI_{qs2} + LpI_{qs2} + \omega_{e2}LI_{ds2} + \frac{M_{q2}V_{dc}}{2} \quad (4.70)$$

$$V_{ds2} = rI_{ds2} + LpI_{ds2} - \omega_{e2}LI_{qs2} + \frac{M_{d2}V_{dc}}{2} \quad (4.71)$$

$$V_{o2} = rI_{os2} + LpI_{os2} \quad (4.72)$$

V_{qs1} , V_{qs2} , V_{ds1} , V_{ds2} are q and d axis voltages for rectifier ‘a’ and ‘b’ respectively.

I_{qs1} , I_{qs2} , I_{ds1} , I_{ds2} are q and d axis currents for rectifier ‘a’ and ‘b’, respectively, and V_{os1} and V_{os2} are the zero sequence voltages for each rectifier.

M_{qs1} , M_{ds1} , M_{qs2} , and M_{ds2} are the q and d axis components of the modulation signals for rectifier ‘a’ and ‘b’, respectively.

The capacitor voltage equations in the synchronous reference frame are

$$CpV_{c1} = \frac{3}{2} \left(M_{qs1} I_{qs1} + M_{ds1} I_{ds1} + M_{o1} I_{o1} \right) - \frac{V_{dc}}{R_L} \quad (4.73)$$

$$CpV_{c2} = \frac{3}{2} \left(M_{qs2} I_{qs2} + M_{ds2} I_{ds2} + M_{o2} I_{o2} \right) - \frac{V_{dc}}{R_L}. \quad (4.74)$$

Assuming the voltages and currents to be balanced, the zero sequence currents and voltages are equal to zero.

4.3.2 Steady State Analysis

Setting the differential terms in the equation to be equal to zero results in the steady state equations for the system.

$$V_{qs1} = rI_{qs1} + \omega_{e1} LI_{ds1} + \frac{M_{q1} V_{dc}}{2} \quad (4.75)$$

$$V_{ds1} = rI_{ds1} - \omega_{e1} LI_{qs1} + \frac{M_{d1} V_{dc}}{2} \quad (4.76)$$

$$V_{qs2} = rI_{qs2} + \omega_{e2} LI_{ds2} + \frac{M_{q2} V_{dc}}{2} \quad (4.77)$$

$$V_{ds2} = rI_{ds2} - \omega_{e2} LI_{qs2} + \frac{M_{d2} V_{dc}}{2} \quad (4.78)$$

$$0 = \frac{3}{2} (M_{qs1} I_{qs1} + M_{ds1} I_{ds1}) - \frac{V_{dc}}{R_L} \quad (4.79)$$

$$0 = \frac{3}{2} (M_{qs2} I_{qs2} + M_{ds2} I_{ds2}) - \frac{V_{dc}}{R_L} . \quad (4.80)$$

The next step in the analysis is to determine the system equations in the synchronous reference frame under unity power factor condition. The procedure followed is the same as for the parallel rectifiers; therefore, setting the d-axis current and voltage to zero, the system equations at unity power factor are

$$V_{qs1} = r I_{qs1} + \frac{M_{q1} V_{dc}}{2} \quad (4.81)$$

$$0 = -\omega_{e1} L I_{qs1} + \frac{M_{d1} V_{dc}}{2} \quad (4.82)$$

$$V_{qs2} = r I_{qs2} + \frac{M_{q2} V_{dc}}{2} \quad (4.83)$$

$$0 = -\omega_{e2} L I_{qs2} + \frac{M_{d2} V_{dc}}{2} \quad (4.84)$$

$$0 = \frac{3}{2} (M_{qs1} I_{qs1}) - \frac{V_{dc}}{R_L} \quad (4.85)$$

$$0 = \frac{3}{2} (M_{qs2} I_{qs2}) - \frac{V_{dc}}{R_L} . \quad (4.86)$$

To determine the operating point of the series rectifier for a particular value of output voltage, the q and d axis modulation signals have to be determined. The unknown parameters for the system are the q and d-axis modulation signals and the q axis voltages for both rectifiers. The total number of unknowns (6) is equal to the number of equations, hence the additional constraint applied in the case of the parallel rectifiers cannot be applied for the series connection of the boost rectifiers.

The steady state plots in Figures 4.20 and 4.21 show the variation of the q and d-axis modulation signals with varying dc voltage for a constant load resistance. The voltage across each rectifier is varied between 80 V and 550V. The parameters used for each rectifier ‘a’ and ‘b’ in the simulation as well as the steady state analysis are in Tables 4.4 and 4.5 respectively.

Table 4.4: Parameters for rectifier ‘a’

$V_{as} = 40 \cos\left(377t - \frac{\pi}{6}\right)$
$V_{bs} = 40 \cos\left(377t - \frac{\pi}{6} - \frac{2\pi}{3}\right)$
$V_{cs} = 40 \cos\left(377t - \frac{\pi}{6} + \frac{2\pi}{3}\right)$
$r = 0.1\Omega$
$L = 6.4 \text{ mH}$
$C_1 = 135\mu\text{F}$
$R_L = 100 \Omega$

Table 4.5: Parameters for rectifier ‘b’

$V_{as} = 40 \cos\left(377t - \frac{\pi}{6}\right)$
$V_{bs} = 40 \cos\left(377t - \frac{\pi}{6} - \frac{2\pi}{3}\right)$
$V_{cs} = 40 \cos\left(377t - \frac{\pi}{6} + \frac{2\pi}{3}\right)$
$r = 0.1\Omega$
$L = 6.4 \text{ mH}$
$C = 150 \mu\text{F}$
$R_L = 30 \Omega$

The plots shown below, illustrate the variation of the q and d-axis modulation signals with the varying values of dc voltage. The load resistance and operating frequency are assumed to be constant.

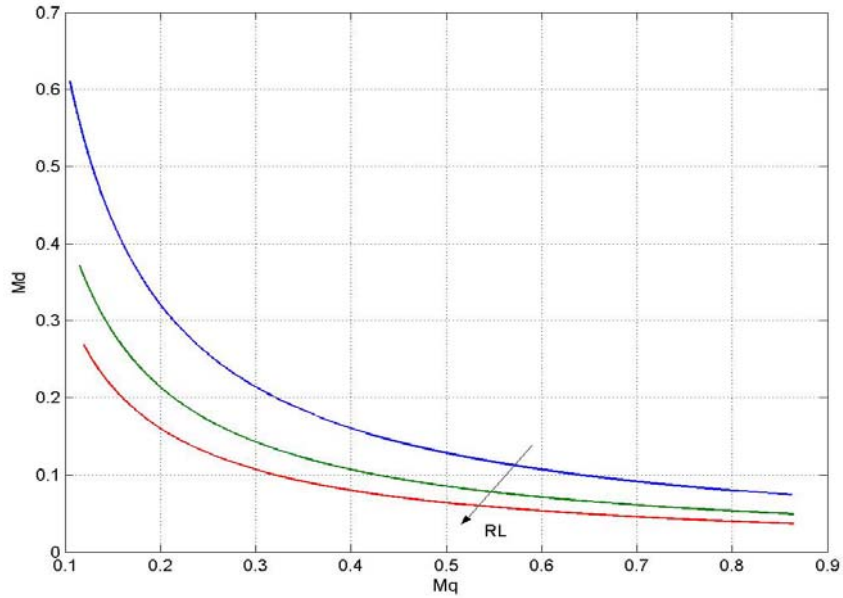


Figure 4.20: Variation of the q and d-axis modulation signals, with the dc voltage varying between 80V and 550V for varying load resistances $R_L = 100\Omega$, 150Ω and 200Ω , for rectifier ‘a’

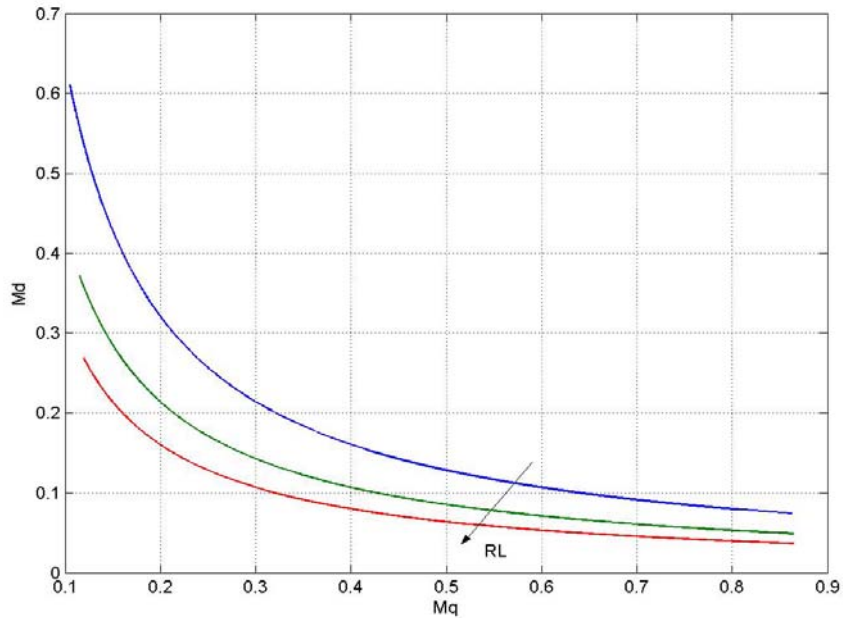


Figure 4.21: Variation of the q and d-axis modulation signals with the dc voltage varying between 80V and 550V for varying load resistances $R_L = 100\Omega$, 150Ω and 200Ω , for rectifier ‘b’

4.3.3 Dynamic Simulation

The dynamic simulation of the series rectifier has been performed for a given operating point to achieve unity power factor operation for both the rectifiers. The sources are assumed to have the same frequency and hence the modulation signals have the same frequency $\omega_{e1} = \omega_{e2} = 377$ rad/sec.

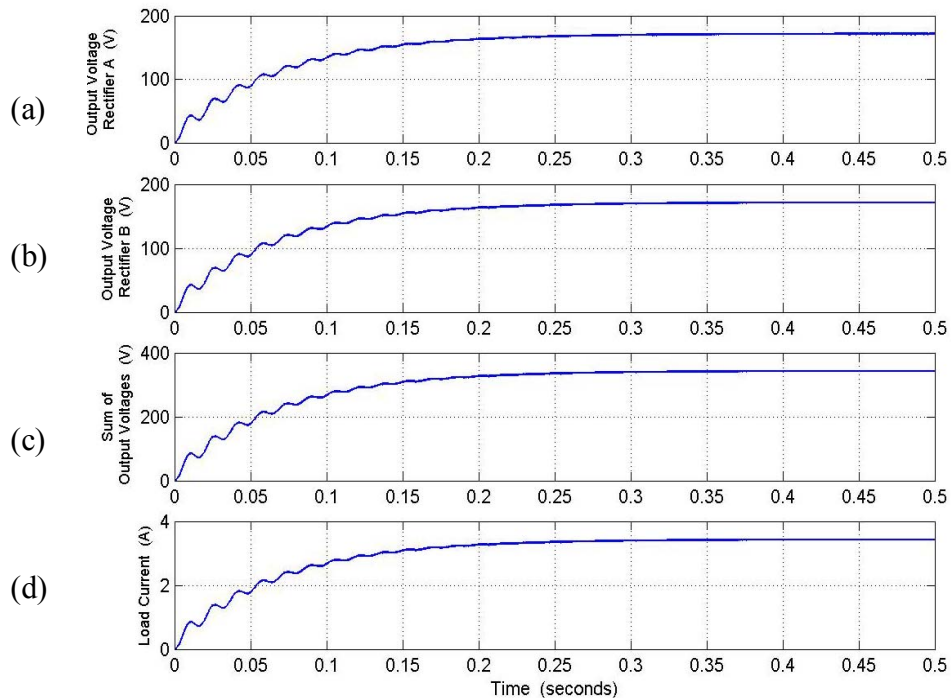


Figure 4.22: Simulation results for the series rectifier, from top: (a) output dc voltage for rectifier 'a' V_{c1} , (b) output dc voltage for rectifier 'b' V_{c2} , (c) sum of output voltages for $V_{c1} + V_{c2}$, (d) load current I_L

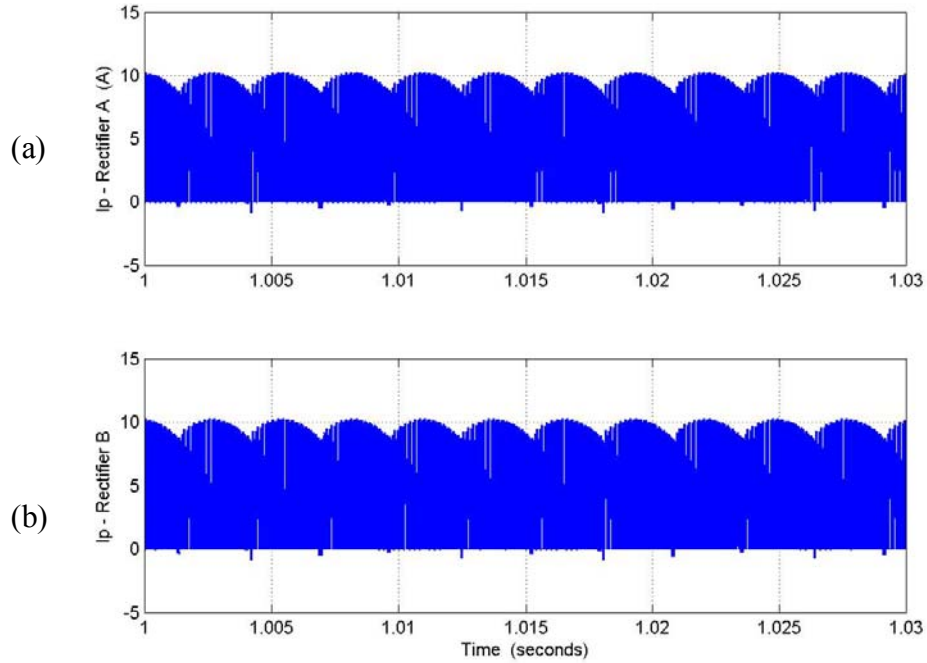


Figure 4.23: Simulation results for the series rectifier, from top : (a) output dc current rectifier 'a' I_{p1} , (b) output dc current rectifier 'b' I_{p2}

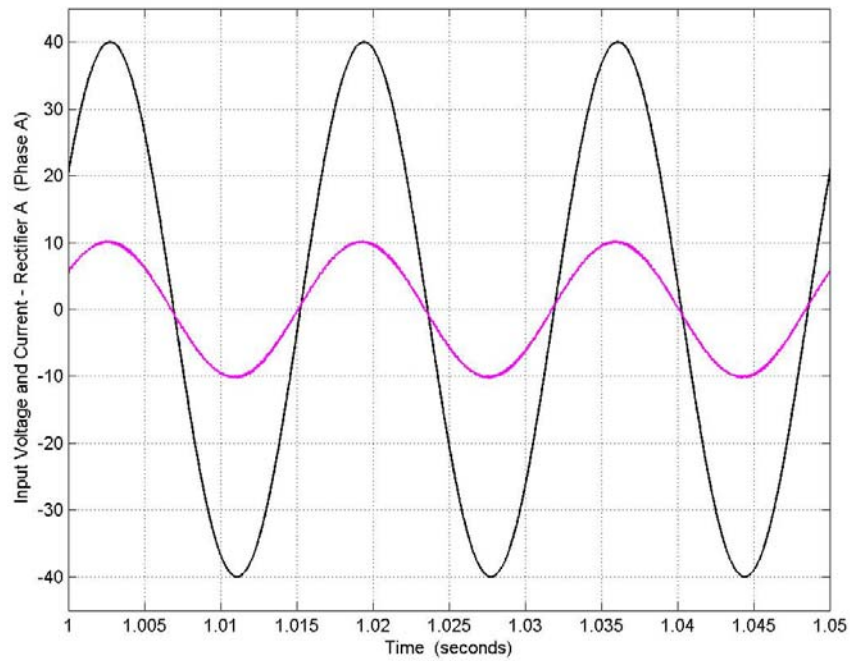


Figure 4.24: Simulation results for the series rectifier, phase -a input voltage and current for rectifier 'a'

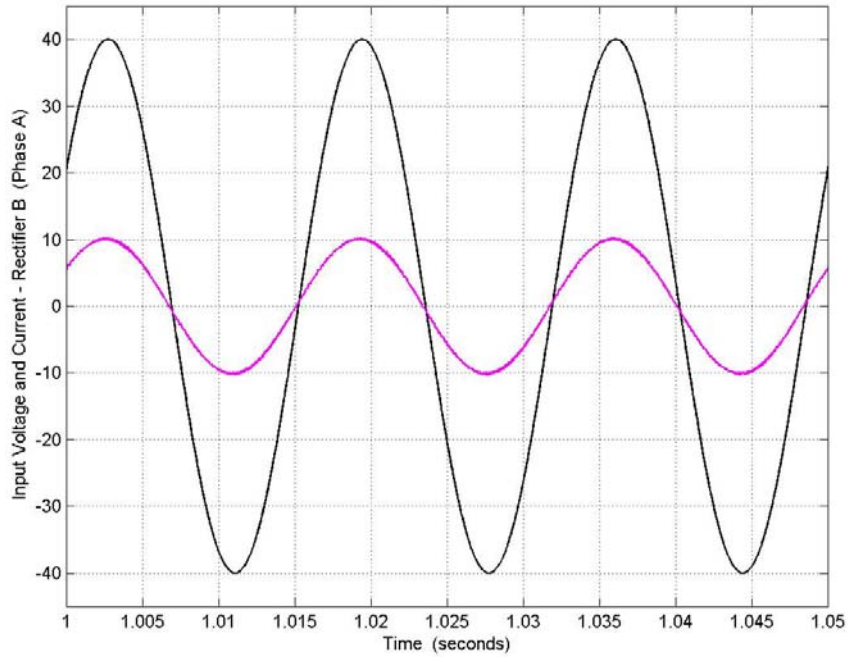


Figure 4.25: Simulation results for the series rectifier, phase -a input voltage and current for rectifier 'b'

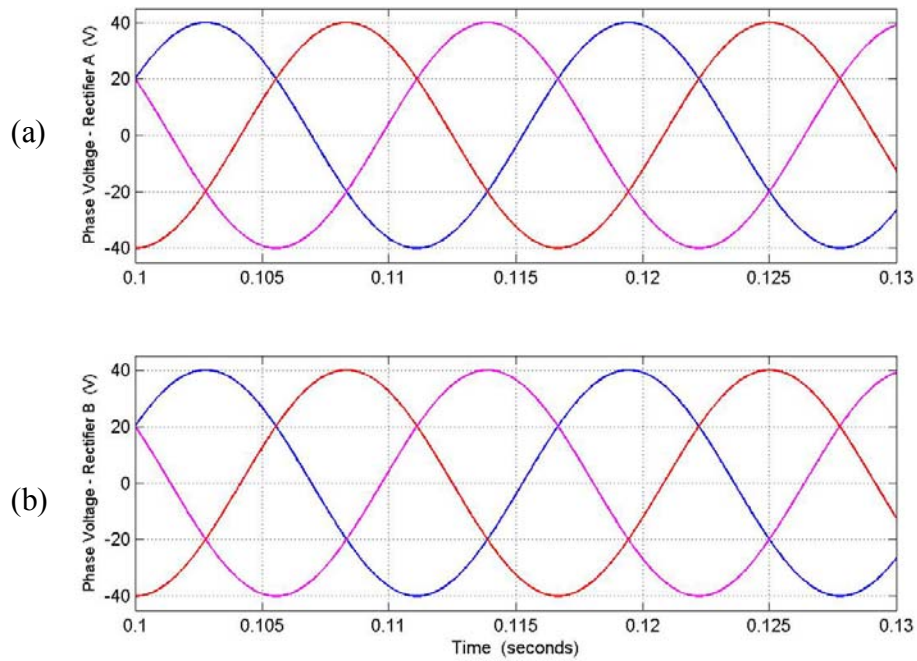


Figure 4.26: Simulation results for the series rectifier, phase voltages from top: (a) rectifier 'a', (b) rectifier 'b'

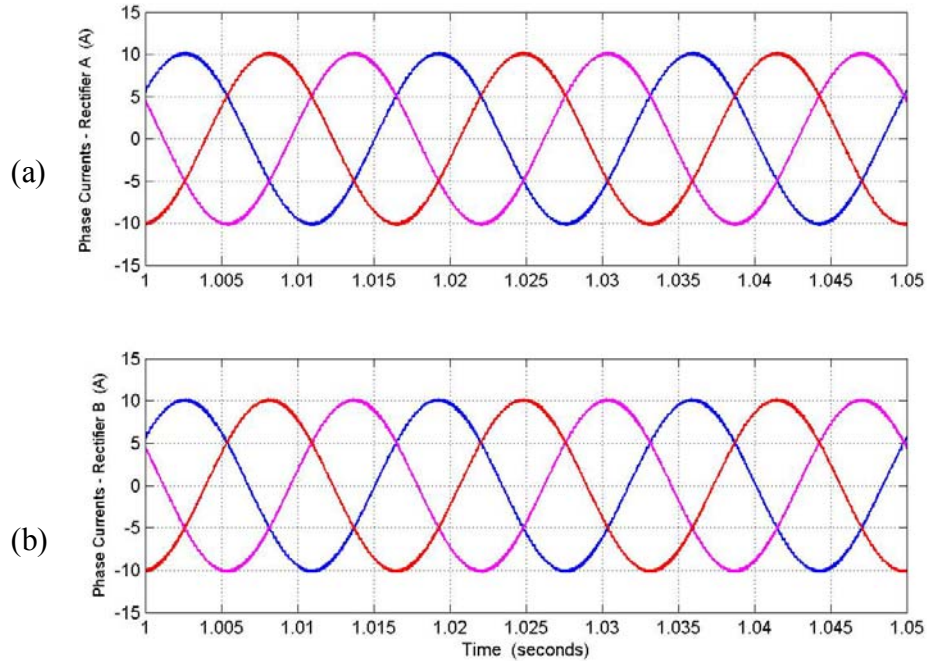


Figure 4.27: Simulation results for the series rectifier, phase currents from top: (a) rectifier 'a', (b) rectifier 'b'.

The results of the dynamic simulation are in Figures 4.22 to 4.27. Figure 4.22 shows the output voltage of each rectifier to reach a steady state value of 170V. The sum of the voltages and the load current are shown as well. Figure 4.21 shows the dc current at the output of each rectifier, and Figures 4.24 and 4.26 show the phase 'a' voltage and current to be in phase, i.e. operation of each rectifier with unity power factor. Figures 4.26 and 4.27 show the phase voltages and currents for each rectifier.

4.4 Parallel Rectifiers with Common Input Source

The model of the parallel connection of the three-phase boost rectifiers considered in section 4.2, assumes the rectifiers to have independent input sources.

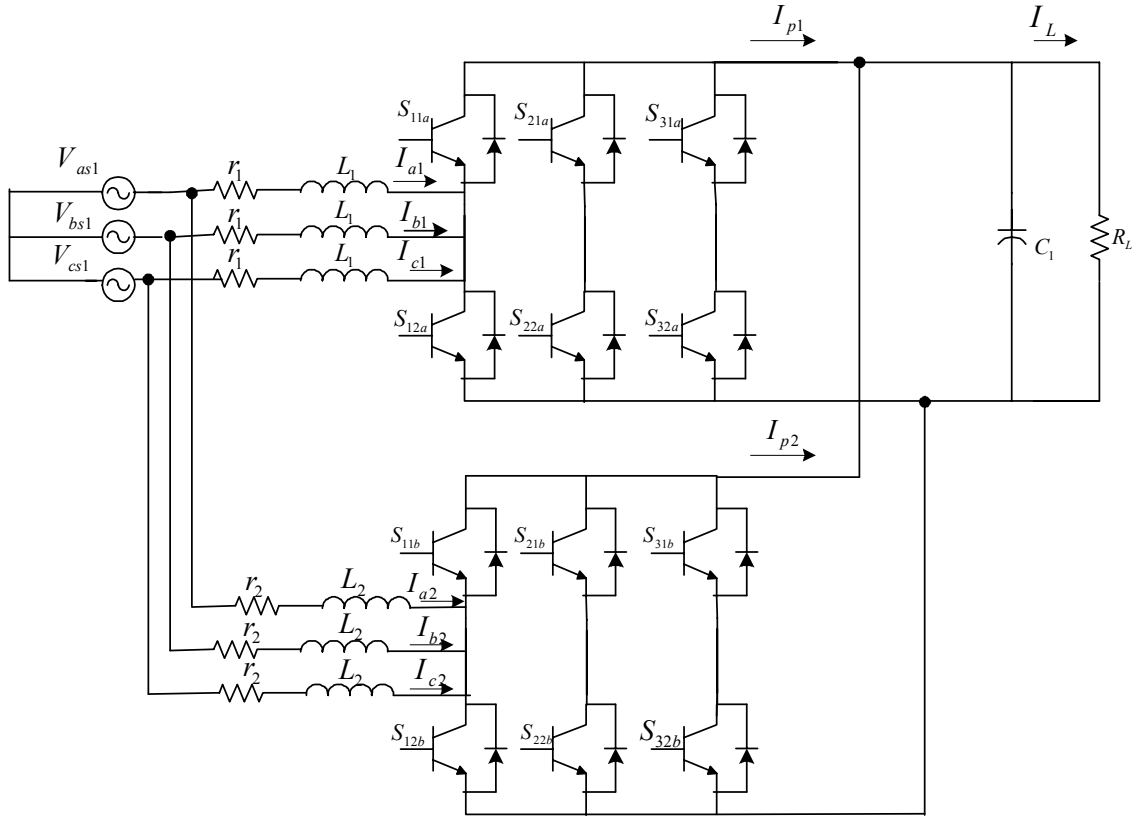


Figure 4.28: Circuit topology for parallel rectifiers with a common input source

The advantage of assuming independent sources rests in the fact that the zero sequence circulating current (a unique feature of the parallel rectifier topologies), is absent. As explained earlier, this is due to the absence of a path for the flow of the current. The topology of the parallel rectifiers considered in this section assumes a common input voltage source. In this case, as the rectifiers share the same input, a path exists for the flow of the zero sequence circulating current. The topology considered in this circuit is as shown in Figure 4.28.

4.4.1 Model of Parallel Rectifiers

The model equations for the parallel rectifiers are the same as that derived in section 4.2, however in this case, the terms for the zero sequence currents and voltages are included in the modeling.

The model equations for each rectifier in the parallel rectifier topology are defined as below. Equations 4.87 to 4.89 are the voltage equations in the abc reference frame for Rectifier A, and 4.90 to 4.92 are the voltage equations for Rectifier B in the abc reference frame.

$$V_{as1} = rI_{a1} + LpI_{a1} + (2S_{11a} - 1)\frac{V_{dc}}{2} + V_{no} \quad (4.87)$$

$$V_{bs1} = rI_{b1} + LpI_{b1} + (2S_{21a} - 1)\frac{V_{dc}}{2} + V_{no} \quad (4.88)$$

$$V_{cs1} = rI_{c1} + LpI_{c1} + (2S_{31a} - 1)\frac{V_{dc}}{2} + V_{no} \quad (4.89)$$

$$V_{as2} = rI_{a2} + LpI_{a2} + (2S_{11b} - 1)\frac{V_{dc}}{2} + V_{no} \quad (4.90)$$

$$V_{bs2} = rI_{b2} + LpI_{b2} + (2S_{21b} - 1)\frac{V_{dc}}{2} + V_{no} \quad (4.91)$$

$$V_{cs2} = rI_{c2} + LpI_{c2} + (2S_{31b} - 1)\frac{V_{dc}}{2} + V_{no} \quad (4.92)$$

The parameters used in the above equations are defined in Tables 4.1 and 4.2. The capacitor voltage equation for the parallel rectifiers is the same as Equation 4.25, as in both cases the rectifiers are connected in parallel at the output.

$$CpV_{dc} = (S_{11a}I_{a1} + S_{21a}I_{b1} + S_{31a}I_{c1} + S_{11b}I_{a2} + S_{21b}I_{b2} + S_{31b}I_{c2}) - \frac{V_{dc}}{R_L} \quad (4.93)$$

The dc currents at the output of each rectifier can be expressed in terms of the switching functions and the phase currents as in Equations 4.94 and 4.95.

$$I_{p1} = S_{11a}I_{a1} + S_{21a}I_{b1} + S_{31a}I_{c1} \quad (4.94)$$

$$I_{p2} = S_{11b}I_{a2} + S_{21b}I_{b2} + S_{31b}I_{c2} \quad (4.95)$$

The analysis performed on the parallel rectifiers in this section has been carried out in the synchronous frame of reference, with the frequency of the reference frame being equal to the frequency of the input ac voltages. The transformation to the synchronous reference frame has been carried out using the transformation matrix defined in Equation 4.29.

The voltage equations for the parallel rectifiers in the synchronous reference frame are for Rectifiers A and B are defined in Equations 4.96 to 4.98 and 4.99 to 4.101 respectively.

$$V_{qs1} = r_1 I_{qs1} + L_1 p I_{qs1} + \omega L_1 I_{ds1} + \frac{S_{q1} V_{dc}}{2} \quad (4.96)$$

$$V_{ds1} = r_1 I_{ds1} + L_1 p I_{ds1} - \omega L_1 I_{qs1} + \frac{S_{d1} V_{dc}}{2} \quad (4.97)$$

$$V_{os1} = r_1 I_{os1} + L_1 p I_{os1} + \frac{S_{o1} V_{dc}}{2} + V_{no} \quad (4.98)$$

$$V_{qs2} = r_2 I_{qs2} + L_2 p I_{qs2} + \omega L_2 I_{ds2} + S_{q2} \frac{V_{dc}}{2} \quad (4.99)$$

$$V_{ds2} = r_2 I_{ds2} + L_2 p I_{ds2} - \omega L_2 I_{qs2} + S_{d2} \frac{V_{dc}}{2} \quad (4.100)$$

$$V_{os2} = r_2 I_{os2} + L_2 p I_{os2} + S_{o2} \frac{V_{dc}}{2} + V_{no} \quad (4.101)$$

The switching functions for the two rectifiers in the synchronous reference frame are defined by Equations 4.102 to 4.107.

$$S_{q1} = \left[2S_{11a} \cos \theta + 2S_{21a} \cos\left(\theta - \frac{2\pi}{3}\right) + 2S_{31a} \cos\left(\theta + \frac{2\pi}{3}\right) \right] \times \frac{2}{3} \quad (4.102)$$

$$S_{d1} = \left[2S_{11a} \sin \theta + 2S_{21a} \sin\left(\theta - \frac{2\pi}{3}\right) + 2S_{31a} \sin\left(\theta + \frac{2\pi}{3}\right) \right] \times \frac{2}{3} \quad (4.103)$$

$$S_{o1} = [2(S_{11a} + S_{21a} + S_{31a}) - 3] \times \frac{1}{3} \quad (4.104)$$

$$S_{q2} = \left[2S_{11b} \cos \theta + 2S_{21b} \cos\left(\theta - \frac{2\pi}{3}\right) + 2S_{31b} \cos\left(\theta + \frac{2\pi}{3}\right) \right] \times \frac{2}{3} \quad (4.105)$$

$$S_{d2} = \left[2S_{11b} \sin \theta + 2S_{21b} \sin\left(\theta - \frac{2\pi}{3}\right) + 2S_{31b} \sin\left(\theta + \frac{2\pi}{3}\right) \right] \times \frac{2}{3} \quad (4.106)$$

$$S_{o2} = \frac{1}{3} [2(S_{11b} + S_{21b} + S_{31b}) - 3] \quad (4.107)$$

S_{q1} , S_{d1} , and S_{o1} are the q, d and zero components of the switching functions for Rectifier A, and S_{q2} , S_{d2} , and S_{o2} are the q, d, and zero components of the switching functions for Rectifier B.

The capacitor voltage equation for the parallel rectifier topology in the synchronous reference frame is

$$C_p V_{dc} = \frac{3}{2} [S_{q1} I_{q1} + S_{d1} I_{d1} + 2S_{o1} I_{os1} + S_{q2} I_{q2} + S_{d2} I_{d2} + 2S_{o2} I_{os2}] - \frac{V_{dc}}{R_L} \quad (4.108)$$

In this case, as the zero sequence currents exist in the system, the terms are retained in the capacitor voltage equation.

For the system under consideration, the sum of the six phase currents are equal to zero, i.e.

$$I_{a1} + I_{b1} + I_{c1} + I_{a2} + I_{b2} + I_{c2} = 0 \quad (4.109)$$

Equation 4.109 can be rewritten as

$$\frac{1}{3}(I_{a1} + I_{b1} + I_{c1}) + \frac{1}{3}(I_{a2} + I_{b2} + I_{c2}) = 0 \quad (4.110)$$

From the definition of the zero sequence currents, equation 4.110 can be expressed in terms of the zero sequence currents of the two rectifiers as

$$I_{os1} + I_{os2} = 0 \quad (4.111)$$

$$\Rightarrow I_{os1} = -I_{os2} \quad (4.112)$$

Also, as the two rectifiers share the same input voltage source,

$$V_{os1} = V_{os2} \quad (4.113)$$

Using Equations 4.98 and 4.101, in Equation 4.113

$$V_{os1} = V_{os2} = r_1 I_{os1} - r_2 I_{os2} + L_1 p I_{os1} - L_2 p I_{os2} + (S_{o1} - S_{o2}) \frac{V_{dc}}{2} \quad (4.114)$$

$$\Rightarrow (S_{o1} - S_{o2}) \frac{V_{dc}}{2} = r_1 I_{os1} - r_2 I_{os2} + L_1 p I_{os1} - L_2 p I_{os2} \quad (4.115)$$

Substituting Equation 4.113 in 4.115

$$(S_{o1} - S_{o2}) \frac{V_{dc}}{2} = (r_1 + r_2) I_{os1} + (L_1 + L_2) p I_{os1} \quad (4.116)$$

Therefore, using Equation 4.116, the zero sequence circulating currents for each rectifier I_{os1} and I_{os2} can be determined.

4.4.1 Steady State Analysis

The steady state analysis of the parallel rectifiers has been performed. The q and d-axis voltage equations at steady state are the same as Equations 4.39 to 4.42. The difference in the analysis of the parallel rectifier topology is the determination of an expression for the zero sequence current at steady state.

The qd voltage equations for the rectifiers at steady state are

$$V_{qs1} = r_1 I_{qs1} + \omega L_1 I_{ds1} + \frac{S_{q1} V_{dc}}{2} \quad (4.117)$$

$$V_{ds1} = r_1 I_{ds1} - \omega L_1 I_{qs1} + \frac{S_{d1} V_{dc}}{2} \quad (4.118)$$

$$V_{qs2} = r_2 I_{qs2} + \omega L_2 I_{ds2} + S_{q2} \frac{V_{dc}}{2} \quad (4.119)$$

$$V_{ds2} = r_2 I_{ds2} - \omega L_2 I_{qs2} + S_{d2} \frac{V_{dc}}{2} \quad (4.120)$$

The capacitor voltage equation at steady state is

$$0 = \frac{3}{2} [S_{q1} I_{q1} + S_{d1} I_{d1} + S_{q2} I_{q2} + S_{d2} I_{d2} + 2(S_{o1} - S_{o2}) I_{os1}] - \frac{V_{dc}}{R_L} \quad (4.121)$$

The Equation for the zero sequence circulating current can be determined at steady state using the harmonic balance technique. Harmonic balance technique for a linear system states that, for a given system, for example the output (current) will have the same form as the input (voltage). For example, if the voltage (input) has the form as in Equation 4.122, then the current (output) has the same form as the input as in Equation 4.123. The current may be shifted in phase with respect to the voltage.

$$V_a = V \cos(\omega t + \theta_v) = \text{Re}[\bar{V}e^{j\omega t}]$$

$$\bar{V} = V \angle \theta_v \tag{4.122}$$

$$I_a = I \cos(\omega t + \theta_i) = \text{Re}[\bar{I}e^{j\omega t}]$$

$$\bar{I} = I \angle \theta_i \tag{4.123}$$

The zero sequence current, which is a function of the difference of the zero sequence switching functions for each rectifier, is third harmonic, i.e. the frequency of the zero sequence current is three times the frequency of the input voltage, and this property of the zero sequence current is illustrated in Figure 4.29. Using Equation 4.116, the difference of the fundamental component of the zero sequence switching signals can be expressed as

$$S_{o1} - S_{o2} = S_3 \cos(3\omega_e t - \psi) = \text{Re}[\bar{S}_3 e^{j\theta}]$$

$$\bar{S}_3 = S_3 \angle -\psi, \theta = 3\omega_e t \tag{4.124}$$

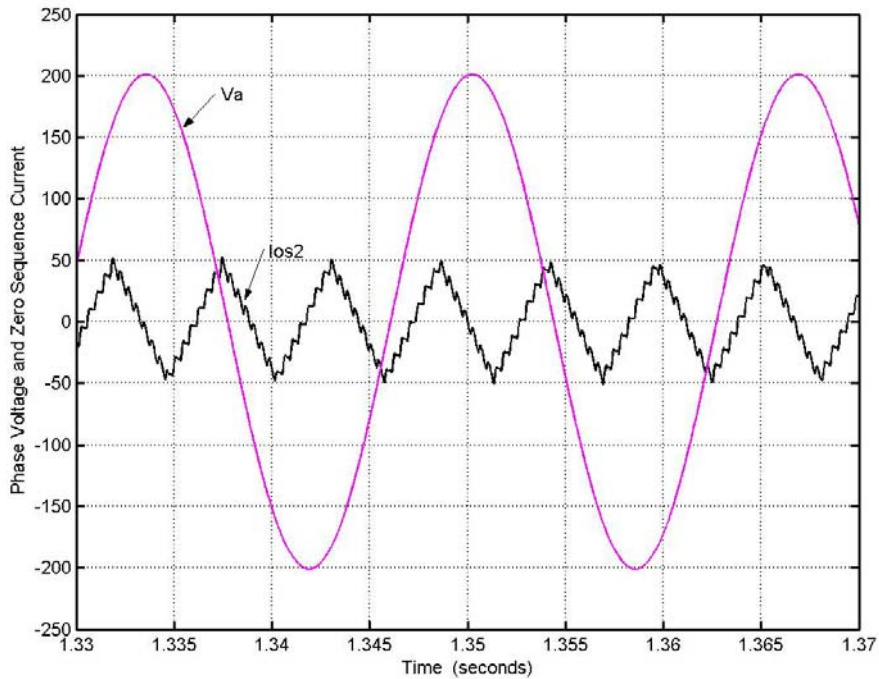


Figure 4.29: Phase 'a' voltage and zero sequence current

As the zero sequence current has the same form as $S_{o1} - S_{o2}$, it can be expressed as

$$I_o = \text{Re}[\bar{I}_o e^{j\theta}] \quad (4.125)$$

Substituting Equation 4.124 and 4.125 in 4.116.

$$(r_1 + r_2)\text{Re}[\bar{I}_o e^{j\theta}] + (L_1 + L_2)p \text{Re}[\bar{I}_o e^{j\theta}] = \frac{V_{dc}}{2} \text{Re}[\bar{S}_3 e^{j\theta}] \quad (4.126)$$

Applying Harmonic balance technique, the peak current in the equation 4.126 can be expressed as [A.12].

$$(r_1 + r_2)\bar{I}_o + (L_1 + L_2)p\bar{I}_o + j3\omega_e(L_1 + L_2)\bar{I}_o = \frac{V_{dc}}{2}\bar{S}_3 \quad (4.127)$$

The steady state equation for the zero sequence current can then be determined as

$$(r_1 + r_2)\bar{I}_o + j3\omega_e(L_1 + L_2)\bar{I}_o = \frac{V_{dc}}{2}\bar{S}_3 \quad (4.126)$$

Therefore

$$\bar{I}_o = \frac{V_{dc}}{2} \frac{\bar{S}_3}{(r_1 + r_2) + j3\omega_e(L_1 + L_2)} \quad (4.127)$$

4.4.1 Dynamic Simulation

The dynamic simulation for the parallel rectifier topology has been carried out under different conditions. The effect of the neutral voltage on the nature of the zero sequence current has been illustrated, as well as the effect of the zero sequence voltage (V_{pn}), on the magnitude of the dc voltage. Certain conditions that have been simulated

illustrate the large effect of the zero sequence circulating current on the waveform of the phase current of the rectifiers.

The method of determination of the modulation signals for the parallel rectifier scheme implemented is the discontinuous pulse-width modulation [B.10]. In this method of PWM, the generalized expression for the neutral voltage has been used, Equation 4.128. The modulation signals have been determined using the expression for the generalized neutral voltage, Equation 4.129.

$$V_{pn} = 0.5V_d(1 - 2\alpha) - \alpha V_{\min} + V_{\max}(\alpha - 1) \quad (4.128)$$

$$M_{ip} = V_{ip} / 0.5V_d + (1 - 2\alpha) - \alpha V_{\min} / 0.5V_d + V_{\max}(\alpha - 1) / 0.5V_d \quad (4.129)$$

The simulation results shown in Figures 4.30 and 4.31 illustrate the operation of the parallel rectifiers assuming the neutral voltage to be equal to zero, i.e. V_{pn} is assumed to be equal to zero. The dc voltage shown in Figure 4.30(a) reaches a steady state value of 500V. The switching frequencies for the two rectifiers are taken to be equal to 10 kHz and 5 kHz respectively. As the frequencies are different there is a zero sequence circulating current as shown in Figure 4.30(b). The relationship between the zero sequence currents as defined in Equation 4.112 is illustrated in Figure 4.30(b). The parameters used in the simulation are defined in Table 4.6.

The second set of Figures for this simulation 4.30(c) and 4.30(d) illustrate the phase 'a' voltage and current for each rectifier. The effect of the zero sequence current on the phase current can be seen from the plots.

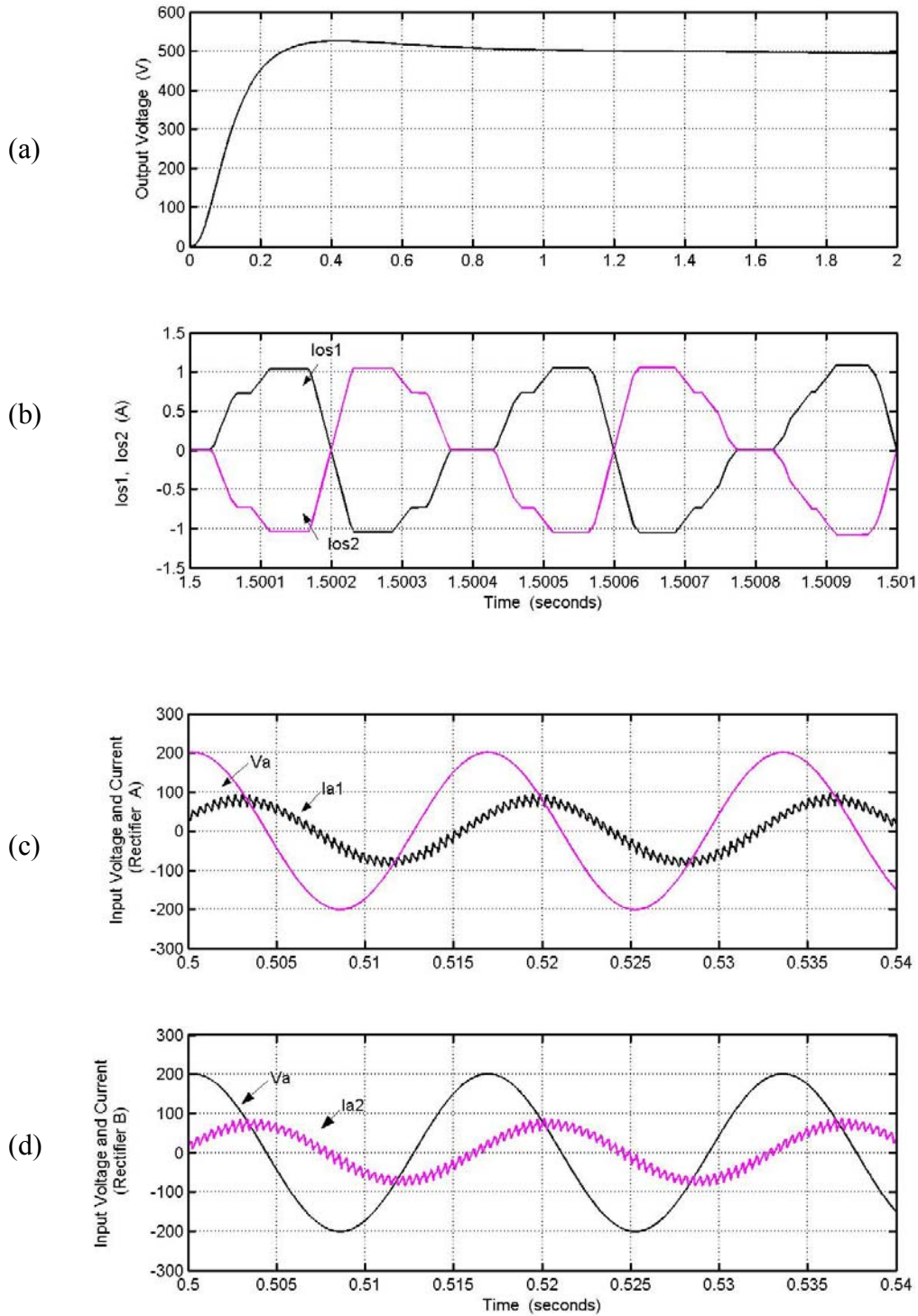


Figure 4.30 Simulation results for the parallel rectifier, from top: (a) output dc voltage, (b) zero sequence currents I_{os1} and I_{os2} (c) phase 'a' voltage and current (scaled by a factor 10) for rectifier A, (d) phase 'a' voltage and current for rectifier B for $M_d = 0.7$, and $M_d = 0.07$

Table 4.6: Parameters for rectifier ‘A’ and ‘B’

Parameter	Rectifier A	Rectifier B
V_{as}	$200\cos(377t)$	$200\cos(377t)$
V_{bs}	$200\cos\left(377t - \frac{2\pi}{3}\right)$	$200\cos\left(377t - \frac{2\pi}{3}\right)$
V_{cs}	$200\cos\left(377t + \frac{2\pi}{3}\right)$	$200\cos\left(377t + \frac{2\pi}{3}\right)$
r	0.1Ω	0.2Ω
L	6.4 mH	8.0 mH
C_1	1200 μ F	1200 μ F
R_L	50 Ω	50 Ω
f_s	10 kHz	5 kHz

The phase currents in both Figures 4.30(a) and 4.30(b) have been scaled by a factor 10 to better illustrate the nature of the waveform, therefore the values of the phase currents when compared to the value of the zero sequence currents are not very large, hence the effect of I_{os1} and I_{os2} on the phase currents is evident.

The second set of simulation results, Figure 4.31(a) and 4.31(b) assume α to be equal to 0.5 for each of the rectifiers, which corresponds to the classical space vector PWM.

For the condition of α to be equal to 0.5, the output dc voltage reaches a steady state value of 500V, similar to the case when the neutral voltage is assumed to be equal to zero. The zero sequence currents in this case are illustrated in Figures 4.31(b). In this case, the peak value of the zero sequence currents is slightly smaller as compared to the previous case. Figures 4.31(c) and 4.31(d) show the input phase voltage and current for each rectifier. In this case as well the current has been scaled in the plot to illustrate the effect of the zero sequence current.

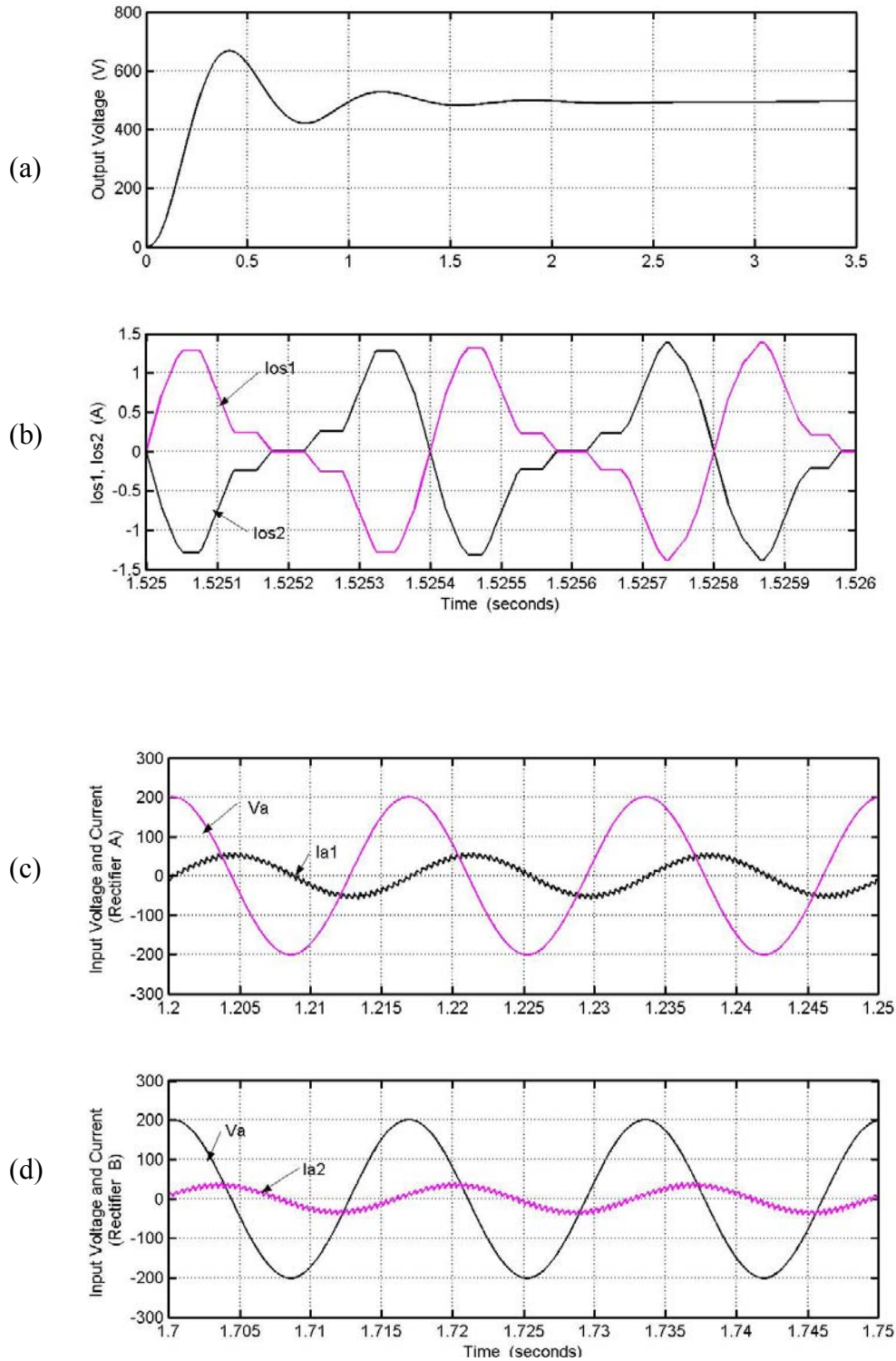


Figure 4.31: Simulation results for the parallel rectifier, from top: (a) output dc voltage, (b) zero sequence currents I_{os1} and I_{os2} (c) phase 'a' voltage and current (scaled by a factor 10) for rectifier A, (d) phase 'a' voltage and current for rectifier B for $M_q = 0.7$, and $M_d = 0.07$

The third set of results have been obtained assuming two different values of α for the rectifiers, $\alpha = 0.5$, and $\alpha = 0.4$ respectively. In this case, the output voltage is slightly less than the previous two cases. The major difference however lays in the nature of the zero sequence currents of the rectifiers. In this case the currents have a dc offset equal to the dc value of the zero sequence currents. The phase currents have been scaled in magnitude as in the previous cases in Figures 4.32(c) and 4.32(d).

The final simulation performed is performed using generalized discontinuous pulse-width modulation. In this method, the α is determined using Equation 4.130.

$$\alpha = 1 - \beta \tag{4.130}$$

$$\beta = 0.5[1 + \text{Sgn} \cos 3(\alpha t + \delta)]$$

The value of δ used in the simulation is $-\pi/3$ for rectifier B, and rectifier A is assumed to have $\alpha = 0.5$. As can be seen from the simulation, the zero sequence current is almost equal in magnitude to the phase current. Therefore the effect of the zero sequence currents on the phase currents is large. The nature of the phase current is illustrated in Figures 4.33(c) and 4.33(d). The dc voltage is close to the values that were obtained in the previous simulations, 500V.

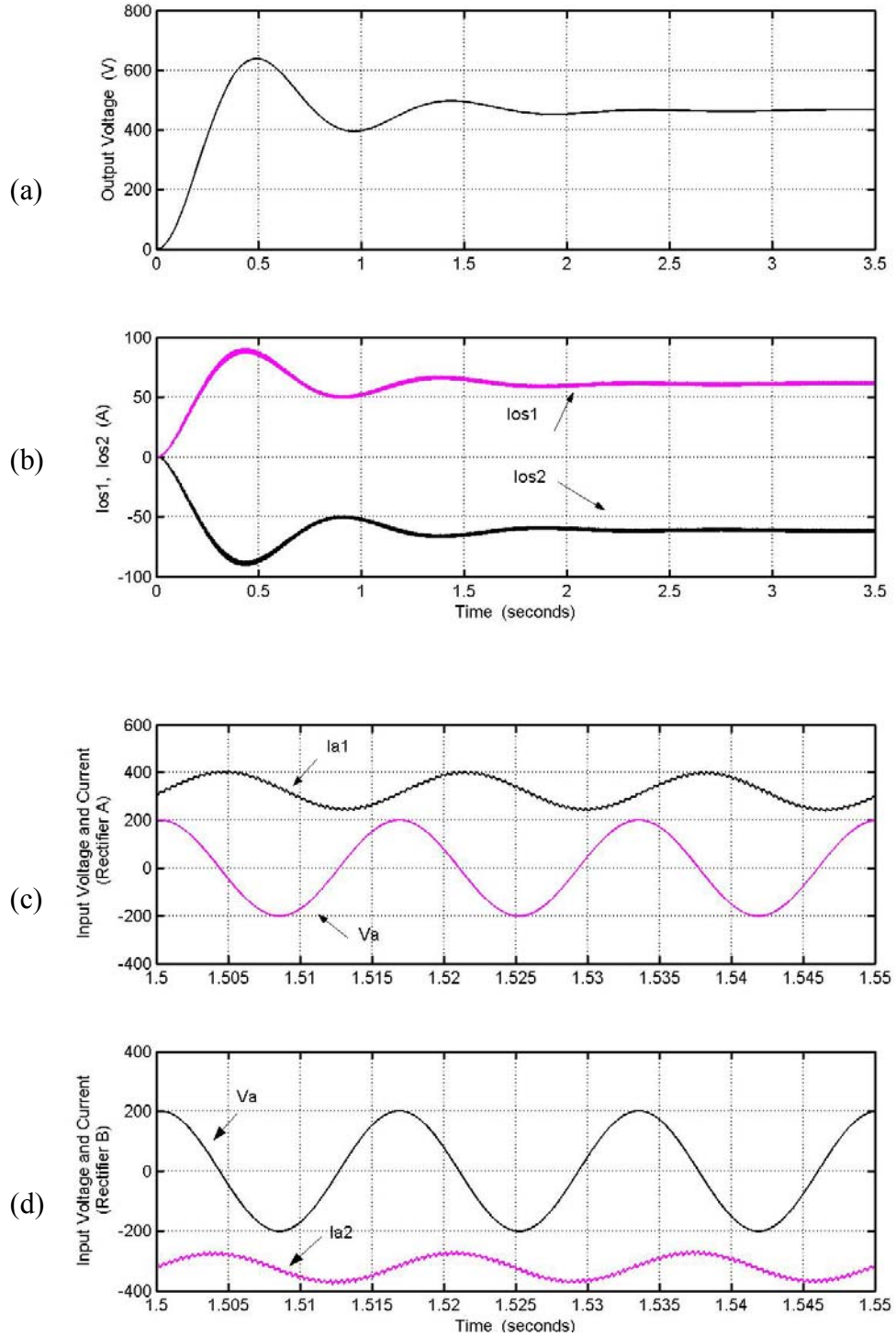


Figure 4.32: Simulation results for the parallel rectifier, from top: (a) output dc voltage, (b) zero sequence currents I_{os1} and I_{os2} (c) phase 'a' voltage and current (scaled by a factor 10) for rectifier A, (d) phase 'a' voltage and current for rectifier B for $M_q = 0.7$, and $M_d = 0.07$

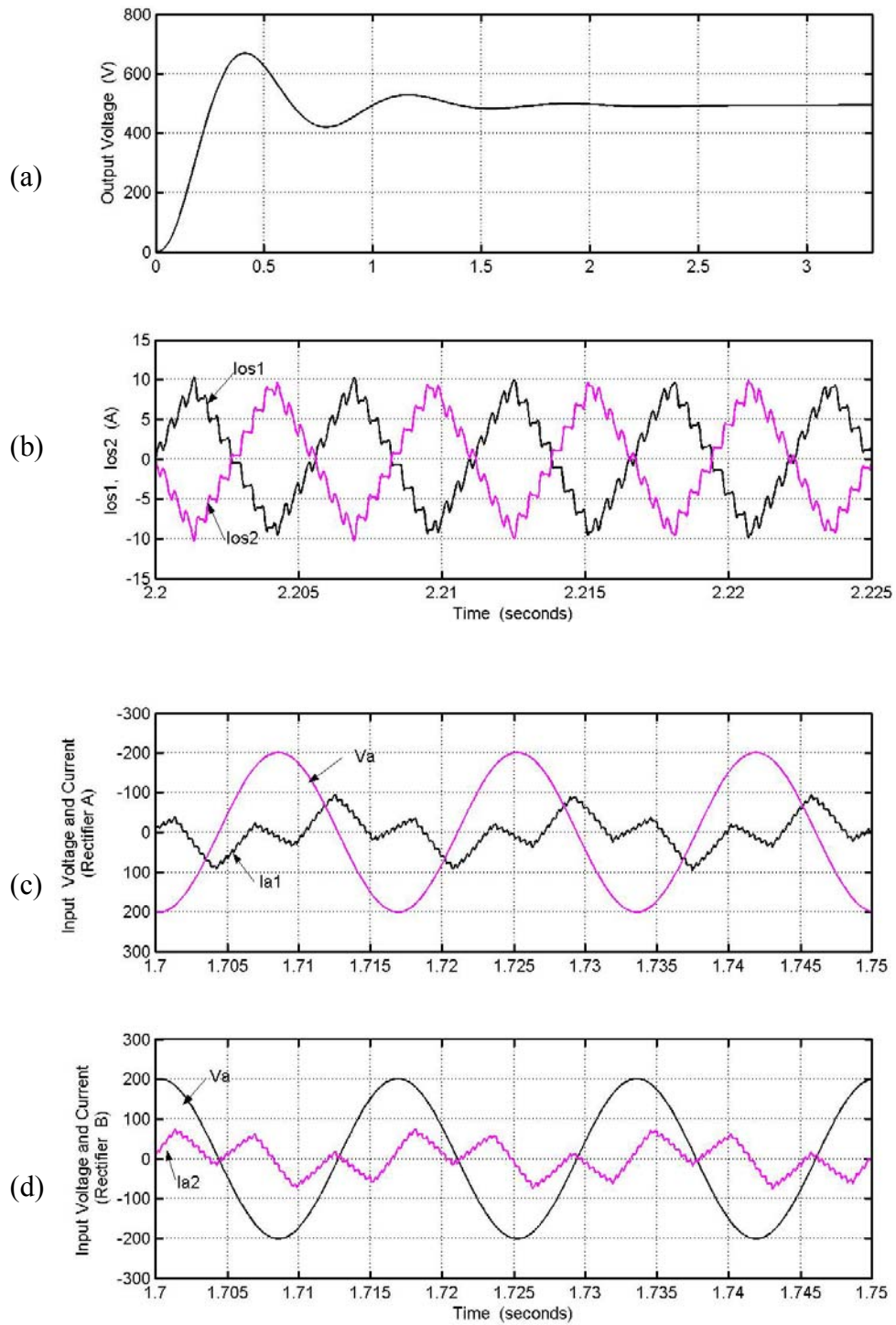


Figure 4.33: Simulation results for the parallel rectifier, from top: (a) output dc voltage, (b) zero sequence currents I_{os1} and I_{os2} (c) phase 'a' voltage and current (scaled by a factor 10) for rectifier A, (d) phase 'a' voltage and current for rectifier B for $M_q = 0.7$, and $M_d = 0.07$

The analysis in this section aims at illustrating the effect of the neutral voltage V_{pn} on the magnitude of the zero sequence currents in the circuit.

In the first set of results, the zero sequence voltage is assumed to be equal to zero. The zero sequence current at this condition has a value slightly larger than the case where V_{pn} is calculated assuming α equal to 0.5 for both the rectifiers.

To illustrate the nature of the change in α on the zero sequence currents, the third simulation is performed with α set equal to 0.5 for rectifier A and 0.4 for rectifier B. In this case the zero sequence currents are dc and the effect of the currents on the waveform of the phase currents is seen in the form of a dc offset of the phase currents equal to the magnitude of the zero sequence currents.

The generalized discontinuous pulse width modulation is used in calculating the neutral voltage. The zero sequence currents in this case are very large values and have a large effect on the phase currents, thereby illustrating the drawbacks of the GDPWM method in this scheme. Other possible cases of δ have not been simulated due to the huge effect of the zero sequence current on the system when considering generalized discontinuous pulse-width modulation.

CHAPTER 5

MODELING OF AND PARAMETER DETERMINATION OF THREE-PHASE INDUCTION MACHINE

5.1 Introduction

With almost universal adoption of an a.c. system of distribution of electric energy for light and power, the field of application of a.c. motors has widened considerably during recent years.

The three-phase induction machine is widely used in a variety of applications as a means of converting electrical power to mechanical work.

The application of the induction machine as a generator has grown in the recent years specifically in areas of non-conventional energy sources, e.g wind power. The increase in the use of the induction machine as a generator is due to the inherent advantages of the machine such as low cost, reduced maintenance, rugged and simple construction, brushless rotor (squirrel cage), and so on.

This chapter discusses the basic operation and the model of a three-phase induction machine. As the model of the machine in the abc and the qd reference frame are fairly familiar, the basic equations are defined and the equivalent circuit of the machine is developed in the synchronous reference frame. Three different models of the induction machine are derived based on the model equations of the system in the qd reference frame.

Following the derivation of the different models is the parameter determination of the induction machine with a detailed description of the various tests performed.

5.2 Basic Operation of an Induction Machine

In a three-phase induction machine, alternating current is supplied to the stator winding directly and to the rotor bars by induction from the stator. Balanced three-phase stator and rotor currents create stator and rotor component mmf waves of constant amplitude rotating in the air-gap at synchronous speed and therefore stationary with respect to each other regardless of the mechanical speed of the rotor. The resultant of these mmf waves creates the resultant air-gap flux density wave. Interaction of the flux wave and the rotor mmf wave gives rise to the torque.

The operation of an induction machine as a motor or a generator is governed by the operating slip of the machine. With a positive operating slip, the machine operates as a motor and converts electrical to mechanical energy. With a negative slip, the machine operates as a generator and converts mechanical to electrical energy. The model equations for a generator and motor are the same except for the direction of current flow.

The equivalent circuit of a three-phase induction machine is given in Figure 5.1.

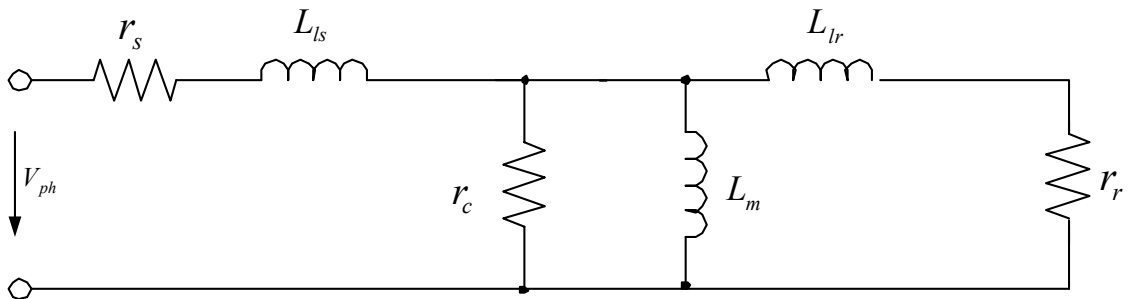


Figure 5.1: Per-phase equivalent circuit for a three-phase induction machine

Table 5.1 Parameters of per-phase equivalent circuit

V_{ph} = per phase voltage
r_s = stator resistance per phase
r_r = rotor resistance per phase
L_{ls} = per phase stator leakage inductance
L_{lr} = per phase rotor leakage inductance
r_c = core loss resistance
L_m = magnetizing inductance

The parameters in the equivalent circuit are defined in Table 5.1. The model of the three-phase induction machine in the abc and qd reference are explained in detail in the next section.

5.2 Model of Induction Machine

The model of a three-phase induction machine is developed assuming the three phase stator windings to be identical sinusoidally distributed windings, displaced by 120° with N_s equivalent turns per phase. For the modeling of the machine, the rotor windings are also assumed to be identical and sinusoidally distributed windings 120° apart with N_r turns. For the analysis and also the transformation to the synchronous reference frame, the positive direction of the magnetic axes coincides with the direction of the vectors used in transformation.

The voltage equations of the machine in the abc reference frame are

$$V_{abc_s} = r_s i_{abc_s} + p \lambda_{abc_s} \quad (5.1)$$

$$V_{abc_r} = r_r i_{abc_r} + p \lambda_{abc_r} \quad (5.2)$$

Equation (5.1) is the stator voltage equation for the induction machine in terms of the stator flux linkages λ_{abc_s} , the stator resistance r_s and the stator currents i_{abc_s}

$$\text{where } i_{abc_s}^T = [i_{as} \quad i_{bs} \quad i_{cs}]$$

$$\lambda_{abc_s}^T = [\lambda_{as} \quad \lambda_{bs} \quad \lambda_{cs}].$$

Similarly the rotor voltage equation, expressed in Equations (5.2) has parameters referred to the rotor. λ_{abc_r} is the rotor flux linkage and i_{abc_r} is the rotor current in the complex form.

The flux linkages for the stator and the rotor can be defined in terms of the stator and rotor currents. Equation (5.3) shows the relationship between the fluxes and currents for the stator and rotor.

$$\begin{bmatrix} \lambda_{abc_s} \\ \lambda_{abc_r} \end{bmatrix} = \begin{bmatrix} L_s & L_{sr} \\ (L_{sr})^T & L_r \end{bmatrix} \begin{bmatrix} i_{abc_s} \\ i_{abc_r} \end{bmatrix} \quad (5.3)$$

The inductance matrices are defined in Equations (5.4) [A.3]

$$L_s = \begin{bmatrix} L_{ls} + L_{ms} & -\frac{1}{2} L_{ms} & -\frac{1}{2} L_{ms} \\ -\frac{1}{2} L_{ms} & L_{ls} + L_{ms} & -\frac{1}{2} L_{ms} \\ -\frac{1}{2} L_{ms} & -\frac{1}{2} L_{ms} & L_{ls} + L_{ms} \end{bmatrix}$$

$$L_r = \begin{bmatrix} L_{lr} + L_{mr} & -\frac{1}{2} L_{mr} & -\frac{1}{2} L_{mr} \\ -\frac{1}{2} L_{mr} & L_{lr} + L_{mr} & -\frac{1}{2} L_{mr} \\ -\frac{1}{2} L_{mr} & -\frac{1}{2} L_{mr} & L_{lr} + L_{mr} \end{bmatrix}$$

$$\mathbf{L}_{sr} = L_{sr} \begin{bmatrix} \cos\theta_r & \cos\left(\theta_r + \frac{2\pi}{3}\right) & \cos\left(\theta_r - \frac{2\pi}{3}\right) \\ \cos\left(\theta_r - \frac{2\pi}{3}\right) & \cos\theta_r & \cos\left(\theta_r + \frac{2\pi}{3}\right) \\ \cos\left(\theta_r + \frac{2\pi}{3}\right) & \cos\left(\theta_r - \frac{2\pi}{3}\right) & \cos\theta_r \end{bmatrix} \quad (5.4)$$

L_{ls} and L_{ms} are the stator leakage and magnetizing inductances, respectively, L_{lr} and L_{mr} are the rotor leakage and magnetizing inductances and L_{sr} is the amplitude of the mutual inductances between the stator and rotor windings.

Equations (5.1) and (5.2) can be expressed with respect to the stator. This is achieved by referring the rotor parameters to the stator using the turn's ratio for the stator and rotor.

The voltage equations for the induction machine with respect to the stator side are given in Equation (5.5).

$$\begin{bmatrix} v_{abcs} \\ v_{abcr} \end{bmatrix} = \begin{bmatrix} r_s + pL_s & pL'_{sr} \\ p(L'_{sr})^T & r'_r + pL'_r \end{bmatrix} \begin{bmatrix} i_{abcs} \\ i'_{abcr} \end{bmatrix} \quad (5.5)$$

$$\text{where } r'_r = \left(\frac{N_s}{N_r}\right)^2 r_r.$$

As can be seen from the nature of the equations defined for the induction machine in the abc reference frame, the inductances are time varying with respect to the rotor speed, hence reference frame transformation is performed to render the variables time invariant.

The transformation of the equations in the abc reference frame to the qdo reference frame, in this case the synchronous reference frame renders the variables time invariant. The transformation to a reference frame of arbitrary speed ω is carried out using the following transformation matrix.

$$f_{qds0} = (K_s(\theta_s))f_{abc} \quad (5.6)$$

$$K_s(\theta_s) = \frac{2}{3} \begin{bmatrix} \cos(\theta_s) & \cos\left(\theta_s - \frac{2\pi}{3}\right) & \cos\left(\theta_s + \frac{2\pi}{3}\right) \\ \sin(\theta_s) & \sin\left(\theta_s - \frac{2\pi}{3}\right) & \sin\left(\theta_s + \frac{2\pi}{3}\right) \\ \frac{1}{2} & \frac{1}{2} & \frac{1}{2} \end{bmatrix} \quad (5.7)$$

where θ_s is defined as

$$\theta_s = \int \omega t + \psi_m$$

$$(5.8)$$

Ψ_m is the initial angle of the reference frame.

The frame of reference chosen is the synchronous reference frame where $\omega = \omega_e$ i.e. the frequency of the reference frame is the same as the frequency of the stator voltages.

The voltage equations for the induction machine after transformation to the synchronous reference frame are

$$V_{qs} = r_s I_{qs} + p\lambda_{qs} + \omega_e \lambda_{ds} \quad (5.9)$$

$$V_{ds} = r_s I_{ds} + p\lambda_{ds} - \omega_e \lambda_{qs} \quad (5.10)$$

$$V_{os} = r_s I_{os} + p\lambda_{os} \quad (5.11)$$

$$V_{qr} = r_r I_{qr} + p\lambda_{qr} + (\omega_e - \omega_r)\lambda_{dr} \quad (5.12)$$

$$V_{dr} = r_r I_{dr} + p\lambda_{dr} - (\omega_e - \omega_r)\lambda_{qr} \quad (5.13)$$

$$V_{or} = r_r I_{or} + p\lambda_{or} \quad (5.14)$$

V_{qs} , V_{ds} are the stator q and d-axis voltages.

I_{qs} , I_{ds} are the stator q and d-axis currents.

V_{qr} , V_{dr} are the rotor q and d-axis voltages.

I_{qr} , I_{dr} are the rotor q and d-axis currents.

The q and d-axis stator and rotor flux linkages λ_{qs} , λ_{ds} , λ_{qr} , and λ_{dr} can be expressed in terms of the stator and rotor q and d-axis currents as

$$\begin{bmatrix} \lambda_{qr} \\ \lambda_{qs} \end{bmatrix} = \begin{bmatrix} L_r & L_m \\ L_m & L_s \end{bmatrix} \begin{bmatrix} I_{qr} \\ I_{qs} \end{bmatrix} \quad (5.15)$$

$$\begin{bmatrix} \lambda_{dr} \\ \lambda_{ds} \end{bmatrix} = \begin{bmatrix} L_r & L_m \\ L_m & L_s \end{bmatrix} \begin{bmatrix} I_{dr} \\ I_{ds} \end{bmatrix}. \quad (5.16)$$

Expanding the above equations,

$$\lambda_{qs} = L_r I_{qr} + L_m I_{qs} \quad (5.17)$$

$$\lambda_{qr} = L_m I_{qr} + L_s I_{qs} \quad (5.18)$$

$$\lambda_{ds} = L_s I_{ds} + L_m I_{dr} \quad (5.19)$$

$$\lambda_{dr} = L_m I_{ds} + L_r I_{dr}. \quad (5.20)$$

As the induction machine is assumed to have balanced three-phase voltages, the zero sequence components of the stator and rotor voltages are equal to zero. Therefore Equations (5.11) and (5.14) are set to zero.

The torque equation for the induction machine [A.3] expressed in terms of the stator and rotor currents is given by

$$T_e = \frac{3P}{4} (i_{qs} i_{dr} - i_{ds} i_{qr}). \quad (5.21)$$

Using the model equations for the induction machine, the equivalent circuit for the machine in the synchronous reference frame can be developed as shown in Figure 5.2(a) and 5.2(b).

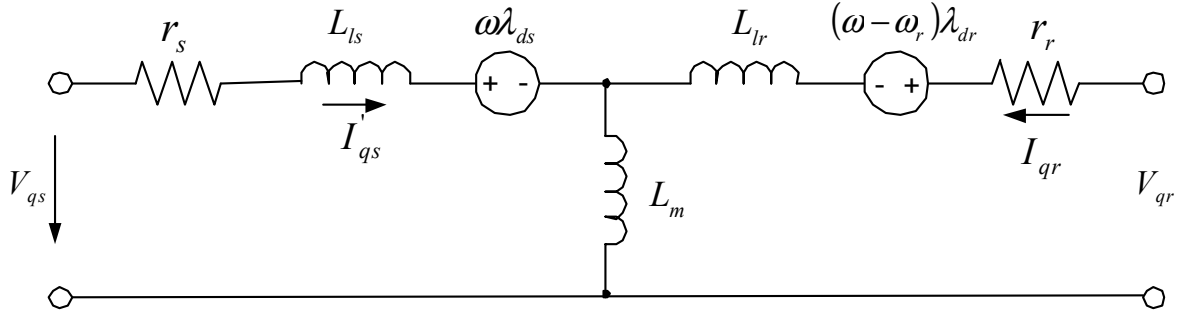


Figure 5.2(a) q-axis equivalent circuit in an arbitrary reference frame for the three-phase induction machine

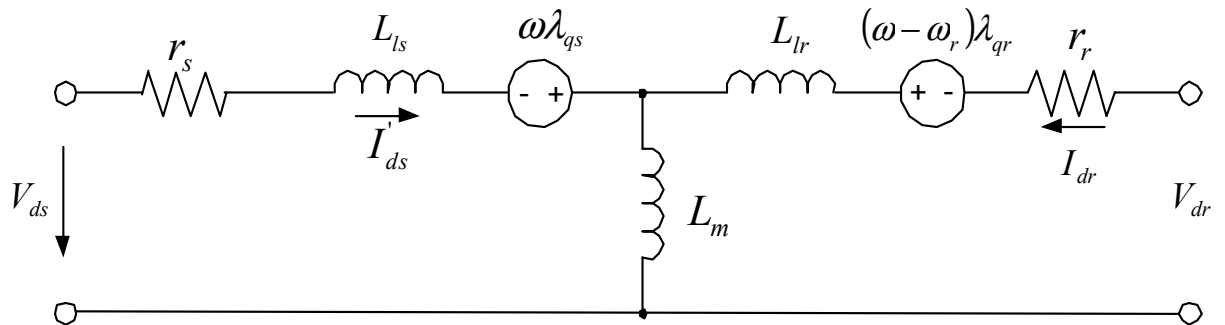


Figure 5.2(b): d-axis equivalent circuit in an arbitrary reference frame for the three-phase induction machine

Figure 5.2(a) shows the equivalent circuit for the q-axis in an arbitrary reference frame with a speed equal to ω . Similarly the d-axis equivalent circuit is shown in Figure 5.2(b).

The model equations of the machine have been expressed in terms of the stator q and d-axis currents, stator q and d-axis fluxes, and the rotor q and d-axis fluxes. Using the model equations of the induction generator in terms of all six variables involves large amounts of calculations. Therefore, the model is simplified and expressed in terms of four out of the six variables.

To design any control system using the model equations of an induction machine would involve expressing the equations in terms of the desired state variables. This reduces the steps in calculation and thereby simplifies the entire scheme.

There are three different models of the induction machine discussed in this chapter for which the derivation for each will be detailed:

Rotor flux model

Stator flux model

Natural variables model.

5.2.1 Stator-Flux Model of Induction Machine

The stator-flux model of the induction machine is the representation of the machine model equations in terms of the stator currents and stator fluxes of the induction machine. The model equations of the induction machine are

$$V_{qs} = r_s I_{qs} + p\lambda_{qs} + \omega_e \lambda_{ds} \quad (5.21)$$

$$V_{ds} = r_s I_{ds} + p\lambda_{ds} - \omega_e \lambda_{qs} \quad (5.22)$$

$$V_{qr} = r_r I_{qr} + p\lambda_{qr} + (\omega_e - \omega_r) \lambda_{dr} \quad (5.23)$$

$$V_{dr} = r_r I_{dr} + p\lambda_{dr} - (\omega_e - \omega_r) \lambda_{qr} \quad (5.24)$$

To obtain the stator flux model of the induction machine, the rotor fluxes and currents are expressed in terms of the stator fluxes and currents. As Equations (5.21) and (5.22) are already expressed in terms of the desired variables, the rotor equations are modified as follows.

Equations (5.17) to (5.20) express the q and d-axis stator and rotor flux linkages in terms of the currents. Rearranging Equation (5.17)

$$I_{qr} = \frac{1}{L_m} \lambda_{qs} - \frac{L_s}{L_m} I_{qs}. \quad (5.25)$$

Substituting for the rotor q-axis currents in Equation (5.18)

$$\lambda_{qr} = \frac{L_r}{L_m} \lambda_{qs} + L_1 I_{qs} \quad (5.26)$$

$$\text{where } L_1 = \left(L_m - \frac{L_s L_r}{L_m} \right).$$

Similarly, the d-axis rotor fluxes and currents can be expressed in terms of the d-axis stator currents and fluxes as by first expressing the d-axis rotor current in terms of the stator currents and fluxes using Equation (5.19) and then eliminating the d-axis rotor current in Equation (5.20) resulting in Equations (5.27) and (5.28).

$$I_{dr} = \frac{1}{L_m} \lambda_{ds} - \frac{L_s}{L_m} I_{ds} \quad (5.27)$$

$$\lambda_{dr} = \frac{L_r}{L_m} \lambda_{ds} + L_1 I_{ds} \quad (5.28)$$

Using Equations (5.25), (5.26), (5.27), and (5.28) the q and d-axis rotor fluxes and currents can be eliminated in Equations (5.23) and (5.24).

As the induction machine has a squirrel cage rotor, the q and d-axis rotor voltages are equal to zero. Therefore Equations (5.23) and (5.34) are

$$0 = r_r I_{qr} + p \lambda_{qr} + (\omega_e - \omega_r) \lambda_{dr} \quad (5.29)$$

$$0 = r_r I_{dr} + p \lambda_{dr} - (\omega_e - \omega_r) \lambda_{qr}. \quad (5.30)$$

Substituting for the rotor fluxes and currents in Equation (5.29)

$$0 = r_r \left(\frac{1}{L_m} \lambda_{qs} - \frac{L_s}{L_m} I_{qs} \right) + p \left(\frac{L_r}{L_m} \lambda_{qs} + L_1 I_{qs} \right) + (\omega_e - \omega_r) \left(\frac{L_r}{L_m} \lambda_{ds} + L_1 I_{ds} \right). \quad (5.31)$$

Simplifying the above equation results in the state equation for the q-axis stator current for the stator flux model of the machine

$$L_1 p I_{qs} = r I_{qs} - \frac{r_r}{L_m} \lambda_{qs} - \frac{L_r}{L_m} V_{qs} - (\omega_e - \omega_r) L_1 I_{ds} + \frac{\omega_r L_r}{L_m} \lambda_{ds} \quad (5.32)$$

$$r = \frac{1}{L_m} (r_r L_s + r_s L_r).$$

Similarly to obtain the state equation for the d-axis stator current for the stator flux model of the machine, Equations (5.26), (5.27), and (5.28) are substituted in the d-axis rotor Equation (5.30).

$$0 = r_r \left(\frac{1}{L_m} \lambda_{ds} - \frac{L_s}{L_m} I_{ds} \right) + p \left(\frac{L_r}{L_m} \lambda_{ds} + L_1 I_{ds} \right) - (\omega_e - \omega_r) \left(\frac{L_r}{L_m} \lambda_{qs} + L_1 I_{qs} \right) \quad (5.33)$$

Simplifying the above equation:

$$L_1 p I_{ds} = r I_{ds} - \frac{r_r}{L_m} \lambda_{ds} - \frac{L_r}{L_m} V_{ds} + (\omega_e - \omega_r) L_1 I_{qs} - \frac{\omega_r L_r}{L_m} \lambda_{qs}. \quad (5.34)$$

Therefore, the stator flux model equations for the induction machine are given by Equations (5.21), (5.22), (5.32), and (5.33).

5.2.1 Rotor-Flux Model of Induction Machine

The second model considered in this chapter is the rotor flux model of the induction machine. This model uses the stator currents and the rotor fluxes as state variables in the model equations for the machine.

Using the equations for the induction machine in the synchronous reference frame the machine equations can be modified in terms of the desired state variables.

The q-axis rotor current can be expressed in terms of the currents and the rotor fluxes using Equation (5.18)

$$I_{qr} = \frac{1}{L_r} \lambda_{qr} - \frac{L_m}{L_r} I_{qs} \quad (5.35)$$

The desired model requires the stator q and d-axis fluxes and currents to be expressed in terms of the rotor fluxes and stator currents.

From Equation (5.20) the d-axis rotor current is

$$I_{dr} = \frac{\lambda_{dr}}{L_r} - \frac{L_m}{L_r} I_{ds} \quad (5.36)$$

Eliminating the rotor currents in Equations (5.17) and (5.19) results in expressions for the stator q and d axis fluxes in terms of the desired state variables for the system.

$$\lambda_{qs} = L_s I_{qs} + L_m \left[\frac{1}{L_r} \lambda_{qr} - \frac{L_m}{L_r} I_{qs} \right] \quad (5.37)$$

Simplifying Equation (5.37)

$$\lambda_{qs} = L_\sigma I_{qs} + \frac{L_m}{L_r} I_{qr} \quad (5.38)$$

$$\text{where } L_\sigma = L_s - \frac{L_m^2}{L_r}$$

Following the same method as described for the q-axis stator flux, the d-axis stator flux can be expressed in terms of the desired state variables as

$$\lambda_{ds} = L_\sigma I_{ds} + \frac{L_m}{L_r} I_{dr} \quad (5.39)$$

Substituting Equations (5.38) and (5.39) in (5.21)

$$V_{qs} = rI_{qs} + L_{\sigma} pI_{qs} + \omega_e L_{\sigma} I_{ds} - \frac{r_r L_m}{L_r^2} \lambda_{qr} + \frac{\omega_r L_m}{L_r} \lambda_{dr} \quad (5.40)$$

where $r = r_s + \frac{r_r L_m^2}{L_r^2}$.

Similarly the d-axis voltage equation,

$$V_{ds} = rI_{ds} + L_{\sigma} pI_{ds} - \omega_e L_{\sigma} I_{qs} - \frac{r_r L_m}{L_r^2} \lambda_{dr} + \frac{\omega_r L_m}{L_r} \lambda_{qr} \quad (5.41)$$

The terms for the rotor currents in equations in (5.29) and (5.30) are eliminated using Equations (5.35) and (5.36), respectively.

$$0 = \frac{r_r}{L_r} \lambda_{qr} - \frac{r_r L_m}{L_r} I_{qs} + p\lambda_{qr} + (\omega_e - \omega_r) \lambda_{dr} \quad (5.42)$$

$$0 = \frac{r_r}{L_r} \lambda_{dr} - \frac{r_r L_m}{L_r} I_{ds} + p\lambda_{dr} - (\omega_e - \omega_r) \lambda_{qr} \quad (5.43)$$

Rearranging Equations (5.40), (5.41), and (5.42) and (5.43), the state equations for the induction generator can be expressed in terms of the desired state variables.

$$L_{\sigma} pI_{qs} = V_{qs} - rI_{qs} - \omega_e L_{\sigma} I_{ds} + \frac{r_r L_m}{L_r^2} \lambda_{qr} - \frac{\omega_r L_m}{L_r} \lambda_{dr} \quad (5.44)$$

$$L_{\sigma} pI_{ds} = V_{ds} - rI_{ds} + \omega_e L_{\sigma} I_{qs} + \frac{r_r L_m}{L_r^2} \lambda_{dr} + \frac{\omega_r L_m}{L_r} \lambda_{qr} \quad (5.45)$$

$$p\lambda_{qr} = \frac{-r_r}{L_r} \lambda_{qr} + \frac{r_r L_m}{L_r} I_{qs} - (\omega_e - \omega_r) \lambda_{dr} \quad (5.46)$$

$$p\lambda_{dr} = \frac{-r_r}{L_r} \lambda_{dr} + \frac{r_r L_m}{L_r} I_{ds} + (\omega_e - \omega_r) \lambda_{qr} \quad (5.47)$$

The final model discussed in this chapter is the model of the induction machine in terms of the natural variables, discussed in the next section.

5.2.1 Natural Variables Model of Induction Machine

The natural variables of the machine are the electromagnetic torque, reactive torque, and the rotor flux. The terms natural variables arises from the fact that these variables can be easily related to and also these terms are reference frame independent. Therefore the model of the machine in this form can be used in implementing various types of control schemes. One such scheme is illustrated in [C.1].

The equations for the natural variables are as follows:

$$T_e = k(\lambda_{dr}I_{qs} - \lambda_{qr}I_{ds}) \quad (5.48)$$

$$T_r = k(\lambda_{dr}I_{ds} + \lambda_{qr}I_{qs}) \quad (5.49)$$

$$\lambda_{rr} = \lambda_{qr}^2 + \lambda_{dr}^2 \quad (5.50)$$

where $\frac{3P}{4} \frac{L_m}{L_r}$.

The first step in obtaining the model of the machine in terms of the natural variables is differentiating Equations (5.48) to (5.50).

$$pT_e = k(\lambda_{dr}pI_{qs} + I_{qs}p\lambda_{dr} - \lambda_{qr}pI_{ds} - I_{ds}p\lambda_{qr}) \quad (5.51)$$

$$pT_r = k(\lambda_{dr}pI_{ds} + I_{ds}p\lambda_{dr} + \lambda_{qr}pI_{qs} + I_{qs}p\lambda_{qr}) \quad (5.52)$$

$$p\lambda_{rr} = 2\lambda_{qr}p\lambda_{qr} + 2\lambda_{dr}p\lambda_{dr} \quad (5.53)$$

To express Equations (5.51) to (5.53) in terms of the natural variables, Equations (5.21) to (5.24) are modified. The method followed is detailed below.

Rearranging Equations (5.44) and (5.45) results in the desired state equation for the stator currents.

$$pI_{qs} = \frac{1}{L_\sigma}V_{qs} - rI_{qs} + \frac{r_r L_m}{L_\sigma L_r} \lambda_{qr} - \frac{L_m}{L_r L_\sigma} \omega_r \lambda_{dr} - \omega_e I_{ds} \quad (5.54)$$

$$pI_{ds} = \frac{1}{L_\sigma}V_{ds} - rI_{ds} + \frac{r_r L_m}{L_\sigma L_r} \lambda_{dr} + \frac{L_m}{L_r L_\sigma} \omega_r \lambda_{qr} + \omega_e I_{qs} \quad (5.55)$$

$$r = \frac{r_s}{L_\sigma} + \frac{r_r L_r^2}{L_\sigma L_r^2}$$

The equations for the rotor q and d-axis fluxes are

$$p\lambda_{qr} = -\frac{r_r}{L_r} \lambda_{qr} + \frac{r_r L_m}{L_r} I_{qs} - (\omega_e - \omega_r) \lambda_{dr} \quad (5.56)$$

$$p\lambda_{dr} = -\frac{r_r}{L_r} \lambda_{dr} + \frac{r_r L_m}{L_r} I_{ds} + (\omega_e - \omega_r) \lambda_{qr} \quad (5.57)$$

Substituting Equations (5.54) to (5.57) in(5.51) to (5.53)

$$pT_e = \frac{k}{L_\sigma} (\lambda_{dr} V_{qs} - \lambda_{qr} V_{ds}) - \left(r + \frac{r_r}{L_r} \right) T_e - \omega_r T_r - \frac{kL_m}{L_\sigma L_r} \omega_r \lambda_{rr} \quad (5.58)$$

$$pT_r = \frac{k}{L_\sigma} (\lambda_{qr} V_{qs} + \lambda_{dr} V_{ds}) - \left(r + \frac{r_r}{L_r} \right) T_r + \omega_r T_e + \frac{kL_m}{L_\sigma L_r} \omega_r \lambda_{rr} + \frac{r_r L_m}{kL_r \lambda_{rr}} (T_e^2 + T_r^2) \quad (5.59)$$

$$p\lambda_{rr} = 2 \left[\frac{-r_r}{L_r} \lambda_{rr} + \frac{r_r L_m}{kL_r} T_r \right] \quad (5.60)$$

Therefore the model equations for the induction machine in terms of the natural variables are given by Equations (5.58) to (5.60).

The natural variables model of the induction machine can also be expressed in terms of the stator flux in place of the rotor flux. The model equations are derived as below. The method used in the derivation is the same as that used for the model of the natural variables in terms of the rotor flux.

The second model of the induction machine in terms of the natural variables has the electromagnetic torque, reactive torque, and the stator flux defined as follows:

$$T_e = k(\lambda_{ds} I_{qs} - \lambda_{qs} I_{ds}) \quad (5.61)$$

$$T_r = -k(\lambda_{qs} I_{qs} + \lambda_{ds} I_{ds}) \quad (5.62)$$

$$\lambda_{ss} = \lambda_{qs}^2 + \lambda_{ds}^2. \quad (5.63)$$

To obtain the desired model, Equations (5.61) to (5.63) are differentiated.

$$\frac{1}{k} T_e = (\lambda_{ds} p I_{qs} + I_{qs} p \lambda_{ds} - \lambda_{qs} p I_{ds} - I_{ds} p \lambda_{qs}) \quad (5.64)$$

$$\frac{-1}{k} p T_r = (\lambda_{qs} p I_{qs} + I_{qs} p \lambda_{qs} + \lambda_{ds} p I_{ds} + I_{ds} p \lambda_{ds}) \quad (5.65)$$

$$p \lambda_{ss} = 2(\lambda_{qs} p \lambda_{qs} + \lambda_{ds} p \lambda_{ds}) \quad (5.66)$$

Rearranging Equations (5.21) and (5.22) results in the state equation for the q and d-axis stator fluxes.

$$p \lambda_{qs} = V_{qs} - r_s I_{qs} - \omega_e \lambda_{ds} \quad (5.67)$$

$$p \lambda_{ds} = V_{ds} - r_s I_{ds} + \omega_e \lambda_{qs} \quad (5.68)$$

Rearranging Equations (5.32) and (5.34)

$$p I_{qs} = \frac{1}{L_\sigma} V_{qs} - \frac{1}{L_\sigma} \left(\frac{L_s r_r}{L_r} + r_s \right) I_{qs} - \omega_s I_{ds} + \frac{r_r}{L_r L_\sigma} \lambda_{qs} - \frac{\omega_r}{L_\sigma} \lambda_{ds} \quad (5.69)$$

$$pI_{ds} = \frac{1}{L_\sigma}V_{ds} - \frac{1}{L_\sigma}\left(\frac{L_s r_r}{L_r} + r_s\right)I_{ds} + \omega_s I_{qs} + \frac{r_r}{L_r L_\sigma}\lambda_{ds} + \frac{\omega_r}{L_\sigma}\lambda_{qs}. \quad (5.70)$$

Substituting Equations (5.66) to (5.69) in Equations (5.64) to (5.66).

$$pT_e = k\left[\left(\frac{\lambda_{ds} - L_\sigma I_{ds}}{L_\sigma}\right)V_{qs} - \left(\frac{\lambda_{qs} - L_\sigma I_{qs}}{L_\sigma}\right)V_{ds} - \frac{1}{L_\sigma}\left(r_s + \frac{r_r L_s}{L_r}\right)T_e - \omega_r T_r - \frac{k\omega_r}{L_\sigma}\lambda_{ss}\right] \quad (5.71)$$

$$pT_e = k\left[-\left(\frac{\lambda_{qs} + L_\sigma I_{qs}}{L_\sigma}\right)V_{qs} - \left(\frac{\lambda_{ds} + L_\sigma I_{ds}}{L_\sigma}\right)V_{ds} - \frac{r_r}{L_\sigma L_r}\lambda_{ss}\right] - \frac{1}{L_\sigma}\left(r_s + \frac{r_r L_s}{L_r}\right)T_r + \omega_r T_e + \frac{r_s}{k\lambda_{ss}}(T_e^2 + T_r^2) \quad (5.72)$$

$$p\lambda_{ss} = 2(\lambda_{qs}V_{qs} + \lambda_{ds}V_{ds}) - \frac{2r_s}{k}T_r \quad (5.73)$$

Equations (5.71) to (5.73) are the model equations for the induction machine in terms of the natural variables T_e , T_r , and λ_{ss} .

Having derived the model of the induction machine using three different state variables, the next section illustrates the method of determination of the parameters of the induction machine.

5.2 Parameter Determination of an Induction Machine

The determination of the parameters of an induction machine involves three different tests, namely the blocked rotor test, no-load test, and dc test. The equivalent circuit of a three-phase squirrel cage induction machine is shown in Figure 5.3 [A.2].

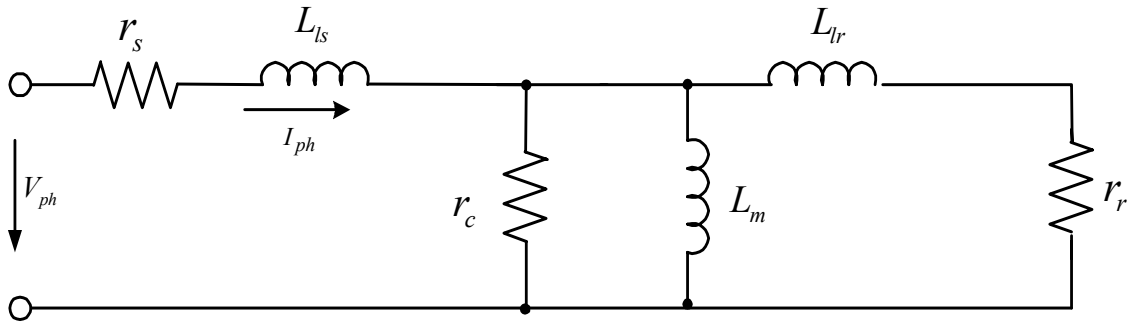


Figure 5.3: Equivalent circuit of three phase induction machine including the core loss resistance

The calculation of the different parameters of the equivalent circuit involves making the following assumptions:

The stator and rotor leakage inductances are assumed to be equal i.e.

$$L_{ls} = L_{lr}.$$

The core loss resistance r_c is neglected.

The simplified equivalent circuit of the three-phase induction machine is shown in Figure 5.4.

The dc test is used to determine the stator resistance. The test involves applying a dc voltage across any of the two of the three terminals of the induction machine. The

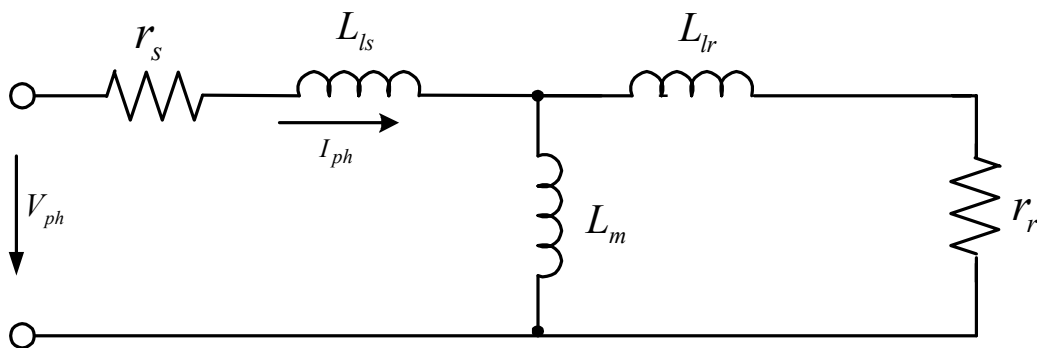


Figure 5.4: Simplified equivalent circuit for three-phase induction machine.

voltage applied divided by the current flowing through the two windings gives the sum of the resistance for each winding. Therefore on a per-phase basis,

$$r_s = \frac{1}{2} \frac{V_{dc}}{I_{dc}}. \quad (5.74)$$

The second test performed is the blocked rotor test, sometimes referred to as the short circuit test. This test is performed by blocking the rotor so it cannot rotate. A three-phase balanced voltage is applied to the stator windings and the rotor is held stationary. The voltage applied is usually low as the input impedance of the machine is very low thereby giving rise to very high stator currents. The voltage applied is increased until the current through the stator windings reaches the rated current, as applying a higher current can cause overheating of the stator windings. The test involves measuring the power, voltage and current flowing through the induction machine when the rotor is prevented from spinning. For this case the slip is equal to one and the equivalent circuit is as in Figure 5.5.

As can be seen from Figure 5.5, the magnetizing inductance is neglected as the test is performed at low voltages. At low voltages the core loss resistance and

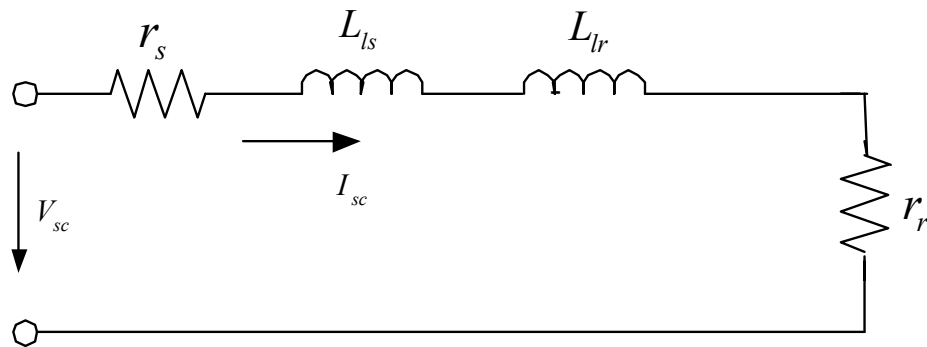


Figure 5.5 Equivalent circuit for short-circuit test

magnetizing inductances are very small, and can therefore be neglected in the calculations. Therefore the equivalent short-circuit impedance is

$$Z_{sc} = (r_s + r_r) + j(X_1 + X_2) \quad (5.75)$$

$$= (r_s + r_r) + j2X_1$$

$$R_{sc} = (r_s + r_r) \quad (5.76)$$

$$X_{sc} = 2X_1 \quad (5.77)$$

$$= 2X_2.$$

As the stator resistance is calculated using the dc voltage test, the rotor resistance and stator and rotor leakage inductances are calculated using the short-circuit test.

The rotor resistance is calculated as

$$r_r = R_{sc} - r_s \quad (5.78)$$

where R_{sc} is calculated using the measured values as in Table 5.2.

The stator and rotor leakage impedances, which are assumed to be equal are calculated by calculating the equivalent reactance of the equivalent circuit for the short circuit test, as expressed in Equation (5.78).

Table 5.2: Measurements for short circuit test

Voltage (Volts)	Current (Amps)	Power (Watts)
3.47	6.2	94.13

The third test performed is the no-load test. This test is performed to calculate the magnetizing inductance.

For the no load test, the symmetrical three phase induction machine is supplied by a system of symmetrical three-phase voltages and the machine is uncoupled from its load. Thus, the speed is close to the synchronous speed and it follows that the slip is very small ($s \approx 0$) and it is assumed that there are no rotor currents. Readings are taken of the stator currents and the input power at various input voltages and rated supply frequency. The equivalent circuit for the no-load test is in Figure 5.6. The equivalent impedance for the no load test is

$$\begin{aligned}
 Z_{nl} &= \frac{V_{nl}}{I_{nl}} \\
 &= R_{nl} + jX_{nl}.
 \end{aligned}
 \tag{5.79}$$

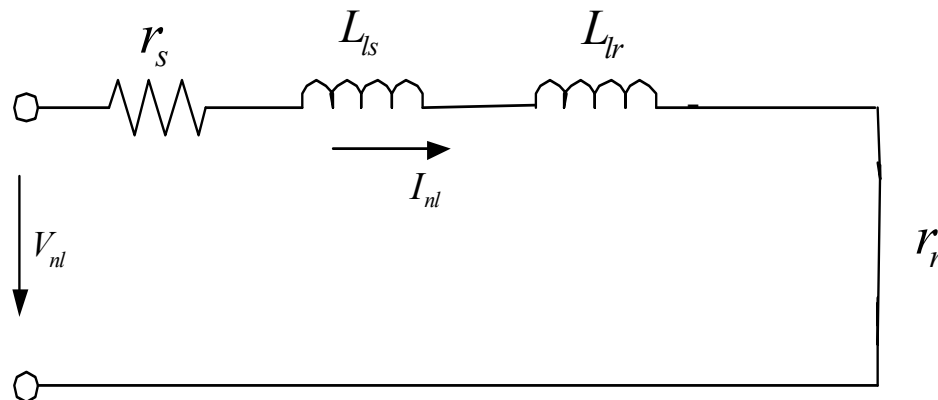


Figure 5.6 Equivalent circuit for no-load test

As can be seen from the equivalent circuit, the no-load resistance is equal to the stator resistance and the reactance is equal to the sum of the stator leakage reactance and magnetizing reactance. As the stator leakage reactance and resistance have been calculated from the other two tests performed, the magnetizing reactance is calculated.

$$R_{nl} = r_s \quad (5.80)$$

$$X_{nl} = X_1 + X_m \quad (5.81)$$

$$X_m = X_{nl} - X_1 \quad (5.82)$$

$$L_m = \frac{X_m}{2\pi f} \quad (5.83)$$

f = supply frequency = 60 Hz

The results for the no-load test are in Table 5.3.

Table 5.3: Experimental readings for no-load test

Voltage (Volts)	Current (Amps)
10.36	2.31
20.03	1.06
23	0.96
27.1	0.964
30	0.979
40	1.17
50.04	1.39
52.7	1.46

56.5	1.54
60.9	1.66
70.32	1.917
80.99	2.19
90.01	2.463
100.15	2.785
109.65	3.11
119	3.5
121.96	3.66

For a given operating frequency, the magnetizing inductance varies substantially as the supply voltage changes. Therefore the no load test is performed for terminal voltages ranging from small to large. The magnetizing inductance is then calculated for each value of voltage and current measured. The variation of the magnetizing inductance with changing input voltage is plotted in Figure 5.7, and the variation of the magnetizing inductance with the magnetizing flux linkage is given in Figure 5.8.

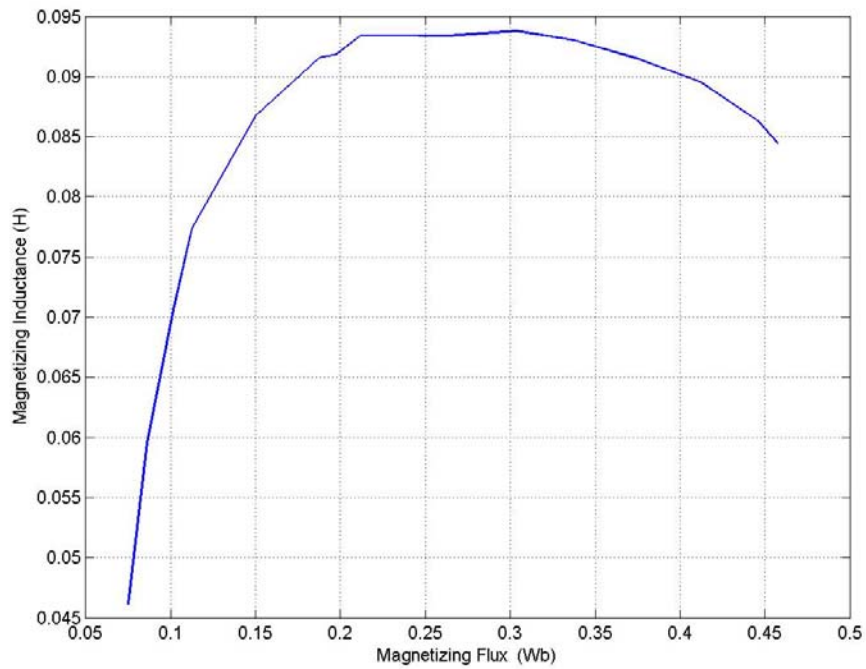


Figure 5.7: Variation of magnetizing inductance with input phase voltage

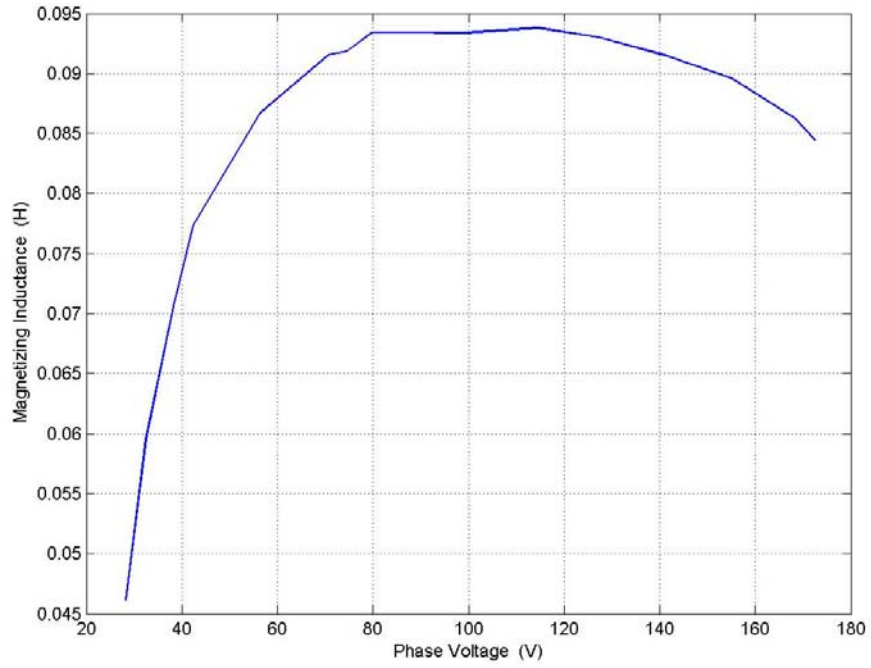


Figure 5.8: Variation of magnetizing inductance with magnetizing flux linkage

CHAPTER 6

STEADY-STATE ANALYSIS OF VSI-ASSISTED INDUCTION GENERATOR

6.1 Introduction

The induction generator-rectifier system dealt with so far is used for the generation of dc power has been illustrated in Chapter 5. The system proposed is an induction generator connected to a boost rectifier, which uses the dc side capacitor of the boost rectifier for self-excitation. Further analysis on the proposed model will be discussed in the later chapters.

The scheme studied in this Chapter is a ‘voltage-source inverter assisted’ induction generator. The converter is connected to a battery to enable bi-directional flow of power. The direction of flow would be dependant on the load condition. The type of power generated in this scheme is ‘ac’.

This chapter proposes a model, which has three-phase capacitors, connected across the stator windings of the machine. The capacitors are used to maintain a consistent load voltage. Steady-state analysis of is studied for the different conditions of the system to illustrate the bi-directional flow of power.

6.2 System Model

The system model used in the analysis is as shown in Figure 6.1. The system includes a boost rectifier. The main feature of the boost rectifier in the operation of this model is the bi-directional power flow capability of the rectifier.

The operation of the system is such that the capacitors connected at the terminals of the generator are used for maintaining a constant voltage across the load, and the generator is self-excited by the voltage-source converter connected to the stator windings through a three-phase transformer. Depending on the load condition, the system can either absorb power or supply power for charging of the battery.

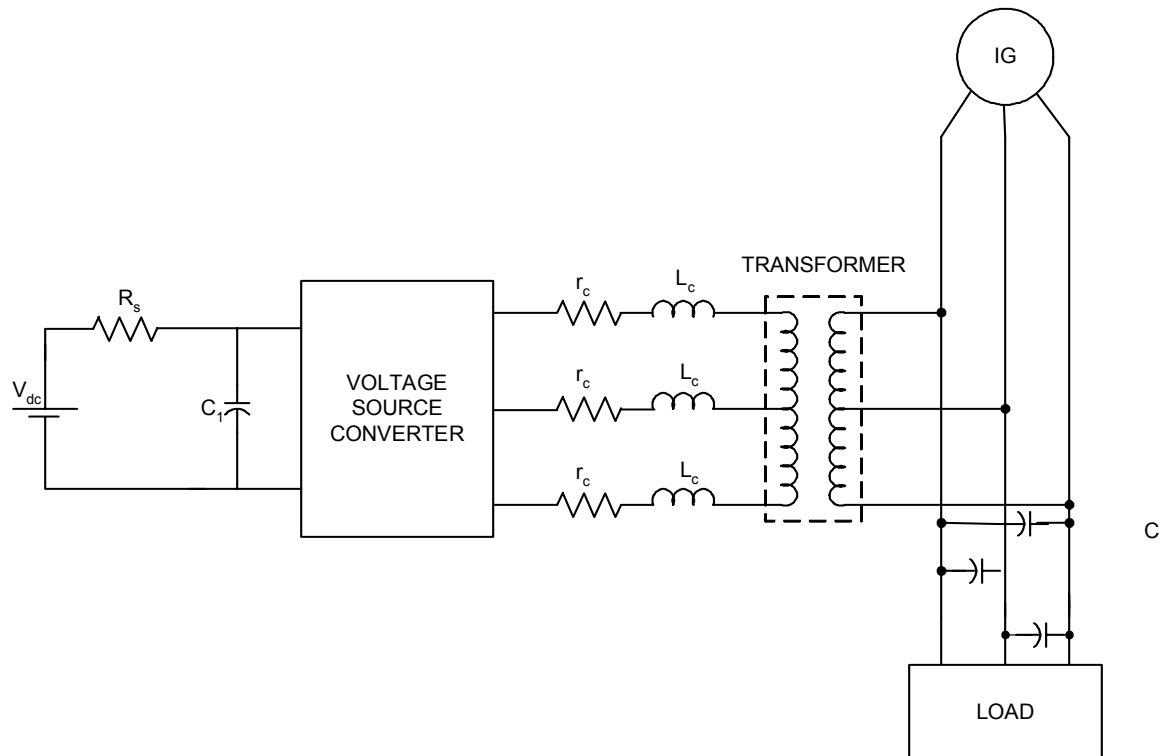


Figure 6.1: Proposed system model

During the process of self-excitation, the voltage-source inverter provides the required reactive power. This is provided by the capacitor on the dc-side of the converter. However, it has been shown that the voltage stability of the induction generator is poor when the rotor speed and load conditions vary. Therefore there have been some schemes proposed whereby the required active power by the load, if in excess of the input rotor mechanical power is supplied by a battery connected to the dc side of a three-phase rectifier. One such scheme has been proposed for a dual-winding generator [C.26].

The advantage of using a boost rectifier is the bidirectional flow of power. When the generated power is in excess, the power flow is towards the battery, thereby the charging of the battery takes place. However, when the active power required by the load is in excess of the mechanical power of the rotor, the difference is supplied by the battery on the dc side of the rectifier. The inclusion of a battery allows for the bi-directional flow of power. There are schemes proposed that do not include the battery [C.26]. However in the case where there is no battery, an additional switch is used in the capacitor leg of the converter for control of the dc voltage across the capacitor.

The model also includes a transformer which provides isolation between the two parts of the system, i.e. the rectifier side and generator side. The transformer is also used in appropriate matching of the current on the two sides. As the battery voltage determines the value of the voltages at the output of the converter, the matching of the two sides is essential.

The following section illustrates the model of the battery used. The proposed model is illustrated and the model equations derived.

6.2.1 Steady-State Model of Battery

The model of the battery used is illustrated in Figure 6.2. The voltage at the output of the battery is the voltage input to the converter for the proposed scheme.

At steady state, the model of the battery can be represented as in Figure 6.3. This is because at steady state the current through the capacitor is equal to zero, hence the capacitor is an open circuit. The dynamic equations for the battery are

$$CpV = I_b - \frac{V_o}{r_1} \quad (6.1)$$

$$CpV_1 = I_b - \frac{V_{c1}}{r_2} \quad (6.2)$$

$$V_d = V + V_{c1} + I_b r_s \quad (6.3)$$

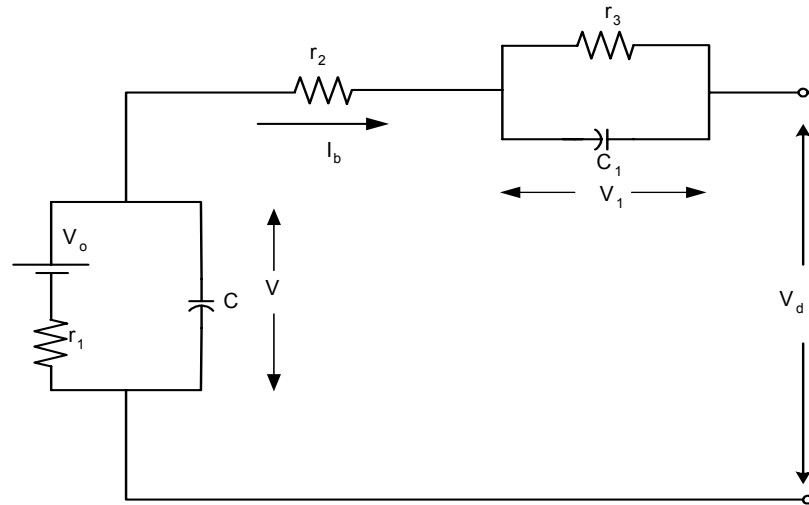


Figure 6.2: Equivalent circuit model of battery

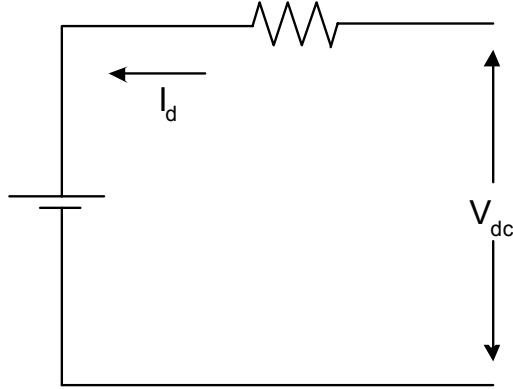


Figure 6.3: Simplified model of battery

Therefore, the model equations for the battery at steady state are

$$V_o = R_s I_b + V_{dc}$$

where $R_s = r_1 + r_2 + r_3$, is equal to the sum of the resistances in the circuit.

The simplified equivalent circuit is shown in Figure 6.3.

6.2.2 Overall System Model

The overall system model is obtained by using the equations of the induction generator and boost rectifier derived in the previous chapters. The model equations of the induction generator are

$$V_{qs} = r_s I_{qs} + p\lambda_{qs} + \omega_e \lambda_{ds} \quad (6.3)$$

$$V_{ds} = r_s I_{ds} + p\lambda_{ds} - \omega_e \lambda_{qs} \quad (6.4)$$

$$0 = r_r I_{qr} + p\lambda_{qr} + (\omega_e - \omega_r) \lambda_{dr} \quad (6.5)$$

$$0 = r_r I_{dr} + p\lambda_{dr} - (\omega_e - \omega_r) \lambda_{qr} . \quad (6.6)$$

The parameters used in the qd model equations for the induction machine have been derived in Chapter 5, and are therefore not repeated here.

The model equations for the boost rectifier have been derived in Chapter 3. The equations are

$$V_{qs} = r_c I_{qc} + \omega_e L_c I_{dc} + \frac{M_{qs} V_{dc}}{2} \quad (6.7)$$

$$V_{ds} = r_c I_{dc} - \omega_e L_c I_{qc} + \frac{M_{ds} V_{dc}}{2} \quad (6.8)$$

$$0 = \frac{3}{2} (M_{qs} I_{qs} + M_{ds} I_{ds}) - \frac{V_{dc}}{R_L} \quad (6.9)$$

The parameters used in the above model equations are defined in Table 6.1.

Table 6.1: Parameters used in model equations

I_{qc}	q-axis primary side current
I_{dc}	d-axis primary side current
I_{qf}	q-axis secondary side current
I_{df}	d-axis secondary side current
I_{qL}	q-axis load current
I_{dL}	d-axis load current
N	Transformer turns ratio
Z_o	Load impedance
Z_c	Line impedance

Having defined the parameters used in the model equations, the model equations for the overall system are derived.

The first step is the determination of the state equations for the currents on the machine side of the system. The dynamic equations expressed in the qd reference frame are

$$CpV_{qs} + \omega_e CV_{ds} = -I_{qs} - I_{qf} - I_{qL} \quad (6.10)$$

$$CpV_{ds} - \omega_e CV_{qs} = -I_{ds} - I_{df} - I_{dL} \quad (6.11)$$

$$V_{qs} = r_o I_{qL} + L_o p I_{ql} + \omega_e L_o I_{dL} \quad (6.12)$$

$$V_{ds} = r_o I_{dL} + L_o p I_{dl} - \omega_e L_o I_{qL} \quad (6.13)$$

$$\frac{M_q V_d}{2} = -(r_c I_{qc} + L_c p I_{qc} + \omega_e L_c I_{dc}) + n V_{qs} \quad (6.14)$$

$$\frac{M_d V_d}{2} = -(r_c I_{dc} + L_c p I_{dc} - \omega_e L_c I_{qc}) + n V_{ds} \quad (6.15)$$

$$C_1 p V_d = I_b - \frac{3}{2} (M_{qs} I_{qc} + M_{dc} I_{dc}) \quad (6.16)$$

To simplify the analysis, the system equations (6.10) to (6.16) are expressed using the complex form. The complex form is as defined by Equation (6.17). The complex form of the q and d-axis voltage is expressed and the same method is applied to the remaining variables in the model equations.

$$V_{qds} = V_{qs} + jV_{ds} \quad (6.17)$$

Using the above definition, the complex form model equations are as expressed in Equations (6.18) to (6.21).

$$C_p V_{qds} - j\omega_e C V_{qds} = I_{qds} + I_{qdf} - I_{qdL} \quad (6.18)$$

$$V_{qds} = r_o I_{qdL} + L_o p I_{qdL} - j\omega_e L_o I_{qdL} \quad (6.19)$$

$$\frac{M_{qd} V_d}{2} = (r_c I_{qdc} + L_c p I_{qdc} - j\omega_e L_c I_{qdc}) + n V_{qds} \quad (6.20)$$

$$C_1 p V_d = I_b - \frac{3}{2} \text{Re al}(M_{qd}^* I_{qdc}) \quad (6.21)$$

Using the equations in (6.18) to (6.21), the steady state analysis of the system is performed. The analysis is carried out by setting the terms with the differential operator to be equal to zero. Applying this condition, the model equations of the system at steady state are as in 6.22 to 6.25.

$$-j\omega_e C V_{qds} = -I_{qds} - I_{qdf} - I_{pdL} \quad (6.22)$$

$$V_{qds} = Z_o I_{qdL} \quad (6.23)$$

$$\frac{M_{qd} V_d}{2} = Z_c I_{qdc} + n V_{qds} \quad (6.24)$$

$$I_b = -\frac{3}{2} \text{Re al}(M_{qd}^* I_{qdc}) \quad (6.25)$$

The steady state analysis aims at studying the nature of variation of the dc voltage and the battery current for varying load conditions and operating slips. Also the magnitude of the modulation index of the rectifier and the q and d-axis modulation

signals are calculated for specific conditions. The derivation of the expressions to determine the parameters is detailed.

The primary side currents can be expressed in terms of the secondary side current and the turns ration as

$$I_{qdf} = nI_{qdc} . \quad (6.26)$$

The method of simplification of the model equations at steady state involves expressing the stator voltages in terms of the current on the primary side.

The stator currents can be expressed in terms of the stator voltages and the machine parameters. The derivation is dealt with in detail in Chapter 8, and is repeated in Equation 6.27.

$$I_{qds} = \frac{V_{qds}}{k} \quad (6.27)$$

where k is defined by the parameters of the induction machine.

$$V_{qds} = \left[(T_s - j\omega_e) - \frac{B_s B_r}{(T_r - j\omega_s)} \right] \cdot \frac{1}{\left[\frac{L_r}{D} + \frac{B_r L_m}{D(T_r + j\omega_s)} \right]} I_{qds}$$

$$k = \frac{1}{\left[(T_s - j\omega_e) - \frac{B_s B_r}{(T_r - j\omega_s)} \right]} \cdot \left[\frac{L_r}{D} + \frac{B_r L_m}{D(T_r + j\omega_s)} \right] \quad (6.28)$$

The variables used in Equation 6.28 are defined in Chapter 8.

Also from Equation 6.23, the load current can be expressed in terms of the stator voltages and load impedance as

$$I_{qdL} = \frac{V_{qds}}{Z_o} . \quad (6.29)$$

Substituting Equations (6.28) and (6.29) in (6.23) a relationship between the stator voltages and I_{qdc} can be determined.

$$I_{qdf} = nI_{qdc} = \left(j\omega_e C - \frac{1}{k} - \frac{1}{Z_o} \right) V_{qds} \quad (6.30)$$

$$\Rightarrow \frac{nI_{qdc}}{Y_1} = V_{qds} \quad (6.31)$$

$$Y_1 = j\omega_e C - \frac{1}{k} - \frac{1}{Z_o} \quad (6.32)$$

Using Equations 6.31 in 6.34, the relationship between I_{qdc} and in terms of the q and d-axis modulation signals is obtained.

$$\frac{M_{qd}V_d}{2} = \left(Z_c + \frac{n^2}{Y_1} \right) I_{qdc} \quad (6.33)$$

$$I_{qdc} = \frac{M_{qd}V_d}{2 \left(Z_c + \frac{n^2}{Y_1} \right)} \quad (6.34)$$

Therefore, the relationship between the magnitude of the modulation index and the dc voltage can be determined by substituting Equations 6.34 in 6.25.

$$I_b = -\frac{3}{2} \text{Re al} \left(M_{qd}^* \frac{M_{qd}V_d}{2 \left(Z_c + \frac{n^2}{Y_1} \right)} \right) \quad (6.35)$$

$$I_b = -\frac{3}{4}|M|^2 V_d \operatorname{Real} \left(\frac{1}{Z_c + \frac{n^2}{Y_1}} \right) \quad (6.36)$$

The method of analysis assumes the variables $\frac{|M|^2 V_d}{I_b}$ to be equal to a constant

σ_1 , where σ_1 is known for a fixed value of saturation in the machine.

$$\frac{|M|^2 V_d}{I_b} = -\frac{4}{3} \times \frac{1}{\operatorname{Real} \left(\frac{1}{Z_c + \frac{n^2}{Y_1}} \right)} = \sigma_1 \quad (6.37)$$

$$\sigma_1 = -\frac{4}{3} \times \frac{1}{\operatorname{Real} \left(\frac{1}{Z_c + \frac{n^2}{Y_1}} \right)} \quad (6.38)$$

Having determined the equation for the modulation index, dc voltage, and battery current in terms of known parameters, the following analysis is performed to obtain an expression for the dc voltage.

Dividing Equation 6.24 by 6.37

$$\frac{M_{qd} I_b}{2|M|^2} = \frac{r_c I_{qdc} - j\omega_e L_c I_{qdc} + nV_{qds}}{\sigma_1} \quad (6.39)$$

Separating the real and imaginary terms in equation 6.24, i.e. expressing the q and d-axis components of the modulation signals separately,

$$\frac{M_q V_d}{2} = r_c I_{qc} + \omega_e L_c I_{dc} + nV_{qs} = k_1 \quad (6.40)$$

$$\frac{M_d V_d}{2} = r_c I_{dc} - \omega_e L_c I_{qc} + nV_{ds} = k_2 \quad (6.41)$$

Dividing Equations (6.40) by (6.41) results in an equation relating the q and d-axis modulation signals in terms of known quantities for a fixed condition of magnetizing flux.

$$\frac{M_q}{M_d} = \frac{(r_c I_{qc} + \omega_e L_c I_{dc}) + nV_{qs}}{(r_c I_{dc} - \omega_e L_c I_{qc}) + nV_{ds}} = z \quad (6.42)$$

$$M_q = zM_d \quad (6.43)$$

From Equation (6.40)

$$\gamma_1 = \frac{2(r_c I_{qc} + \omega_e L_c I_{dc} + nV_{qs})}{\sigma_1} \quad (6.44)$$

Therefore, substituting 6.43 in 6.37

$$M_q = \frac{I_b}{\gamma_1 \left(1 + \frac{1}{z^2}\right)} \quad (6.45)$$

Substituting the expression for the q-axis modulation index in 6.40,

$$\frac{I_b}{\gamma_1 \left(1 + \frac{1}{z^2}\right)} \times \frac{V_d}{2} = k_1 \quad (6.46)$$

From the model of the battery derived in section 6.2.1, the battery current can be expressed as

$$I_b = \frac{V_d - V_o}{R_s}. \quad (6.47)$$

Using Equations 6.46 and 6.47, a quadratic equation in terms of the dc voltage V_{dc} is obtained which is used to calculate the dc voltage across the capacitor.

$$(V_d - V_o)V_d = 2\gamma_1 k_1 \left(1 + \frac{1}{z^2}\right) R_s \quad (6.48)$$

$$V_d^2 - V_o V_d - 2\gamma_1 k_1 \left(1 + \frac{1}{z^2}\right) R_s = 0 \quad (6.49)$$

Using the above equations, the steady state analysis is performed for the system. In this case, the main feature of the system is studied, whereby the dc current from the battery can flow in both directions. This also illustrates the bidirectional power flow capability of a boost converter.

The plots illustrated are obtained for varying load conditions. The effect of saturation is considered in the induction generator. For a particular value of magnetizing flux, the corresponding values of the stator q and d-axis voltages as well as the stator currents are fixed. Correspondingly, from Equation 6.29 the load current is fixed. Therefore, the current on the secondary side and hence the primary side of the transformer are fixed. Using these conditions and values, the corresponding values of the dc voltage as well as the battery current are determined. The variables are plotted as functions of the magnetizing flux. Also the load is varied to show the positive and negative values (bi-directional) flow of the battery current.

As the equation obtained to calculate the dc voltage is a quadratic equation, there are two possible solutions for the values of the dc voltage. However, only one is possible

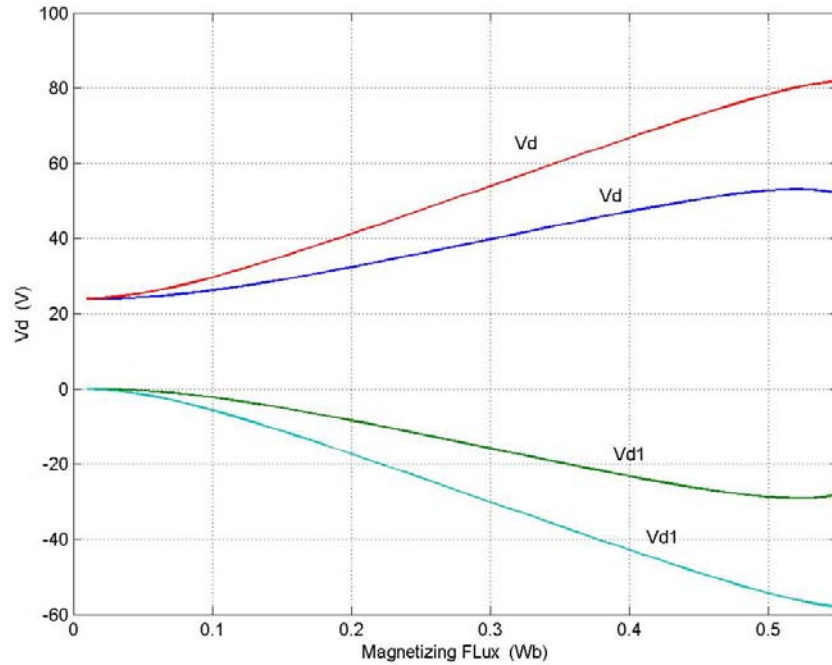


Figure 6.4: Variation of V_d with magnetizing flux λ_m for a load resistance of $R_L=100\Omega$ and $L = 50\text{mH}$

given the operating conditions. This is illustrated graphically and explained in detail with respect to the plots obtained. The parameters used in the analysis are in Table 6.2.

Figures 6.4 to 6.10 are obtained by calculating the dc voltage V_d under two specified conditions of slip. The plots obtained illustrate the two extreme conditions, one when the active power required by the load is lower than the rotor mechanical power; in this case, the surplus power is supplied to the battery, charging the battery. This condition is illustrated in Figure 6.4. From the model of the battery, the internal voltage is set to 24V. Therefore the charging of the battery is shown by the increasing value of V_d in Figure 6.4. Corresponding to the charging of the battery is the direction of flow of the battery current. The current convention used in this model is assuming a positive

direction to be the flow of current into the battery. Therefore, Figure 6.5 illustrates the battery current corresponding to the charging of the battery.

Figures 6.6 and 6.7 are the q and d-axis modulation signals and the magnitude of the modulation index, respectively. As the load determines the operating condition, only one root of the quadratic equation results in a possible point of operation. Using the calculated values of V_d the q and d-axis modulation signals and the magnitude of the modulation index are calculated.

In the first case, the load is assumed to be really large; therefore the load current drawn is very small, $R_L = 100\Omega$, and $L = 50\text{mH}$. The plots are obtained for two different operating slips, $s = -0.04$, and $s = -0.08$.

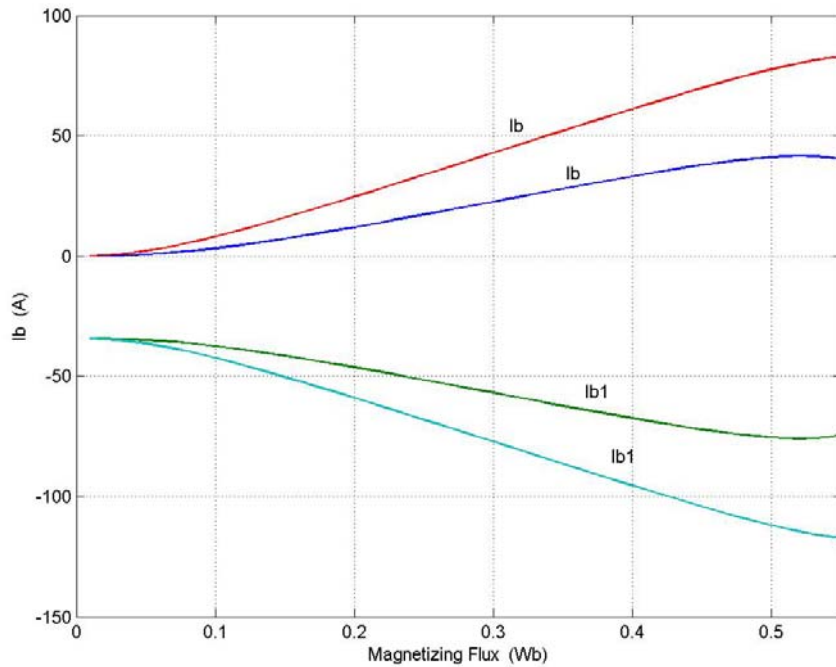


Figure 6.5: Variation of I_d with magnetizing flux λ_m for a load resistance of $R_L=100\Omega$ and $L = 50\text{mH}$

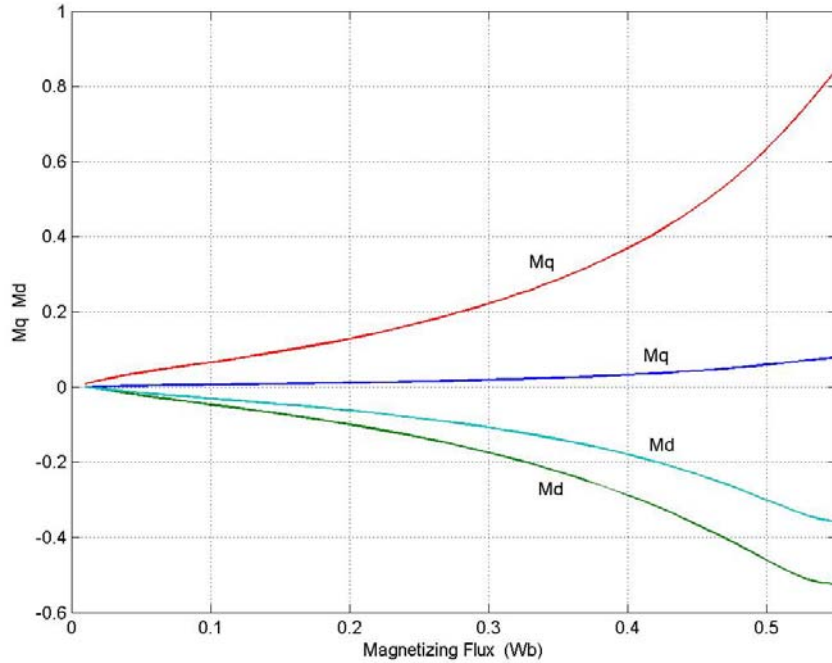


Figure 6.6: Variation of M_q and M_d with magnetizing flux λ_m for a load resistance of $R_L = 100\Omega$ and $L = 50\text{mH}$

Figures 6.8 to 6.10 illustrate the second operating condition, i.e. discharge of the battery. For this operating condition, the load connected to the induction generator is assumed to be very small; therefore the active power requirement is greater than the rotor mechanical power. This corresponds to a condition of discharging of the battery. As in the previous case, the internal battery voltage is assumed to be equal to 24V. The plots are obtained for two operating slip conditions, $s = -0.04$, and $s = -0.08$. The load in the case if assumed to be $R_L = 10\Omega$, and $L = 5\text{mH}$.

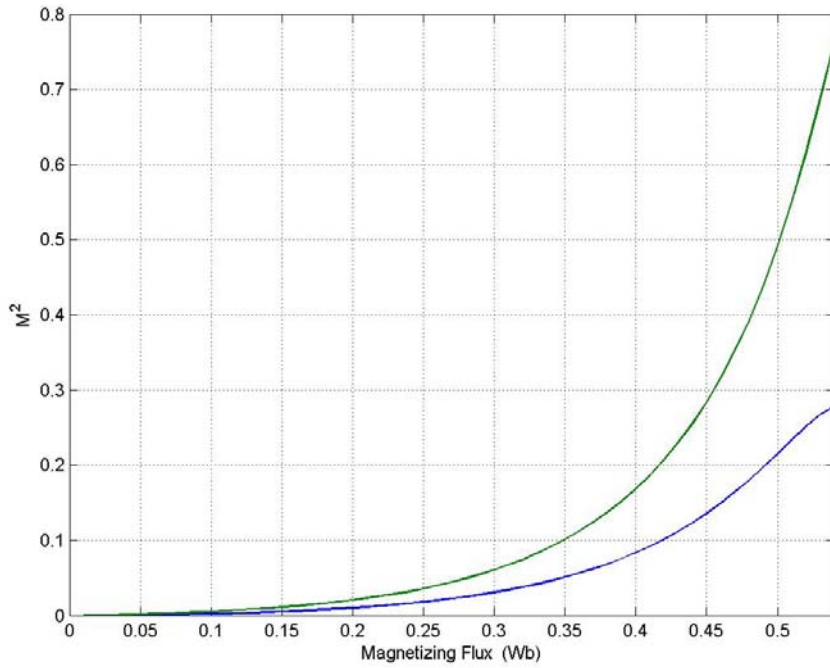


Figure 6.7: Variation of M with magnetizing flux λ_m for a load resistance of $R_L=100\Omega$ and $L = 50\text{mH}$

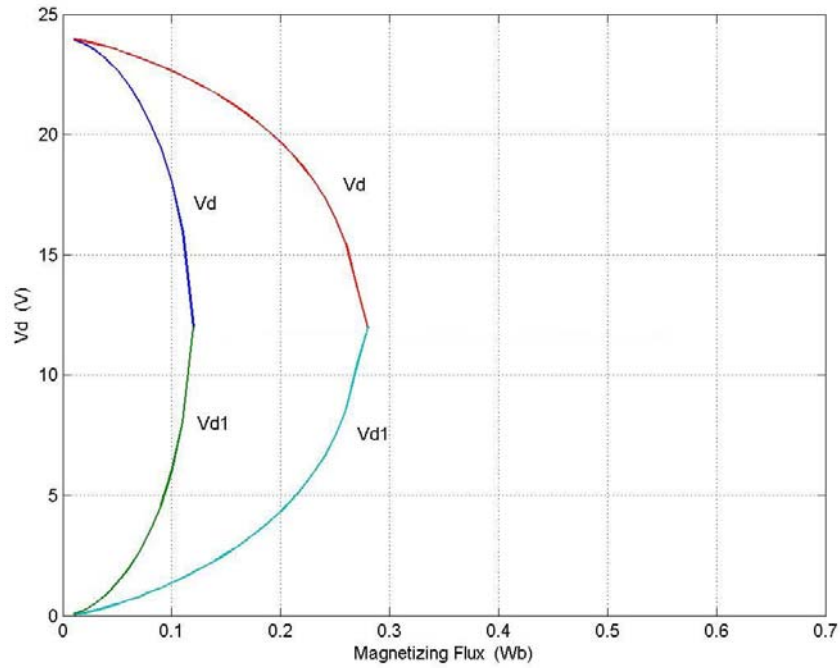


Figure 6.8: Variation of V_d with magnetizing flux λ_m for a load resistance of $R_L= 10\Omega$ and $L = 5\text{mH}$

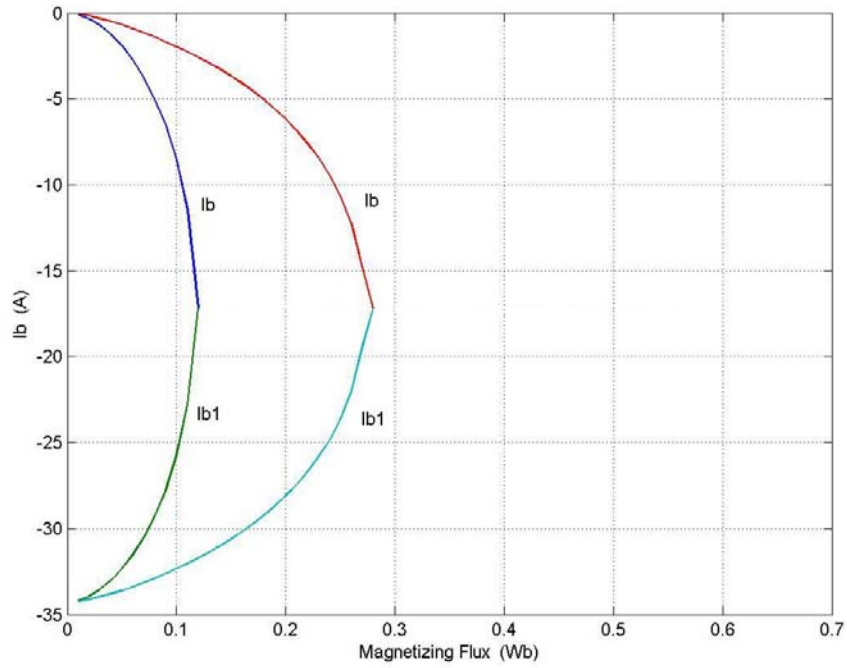


Figure 6.9: Variation of I_d with magnetizing flux λ_m for a load resistance of $R_L = 100\Omega$ and $L = 50\text{mH}$

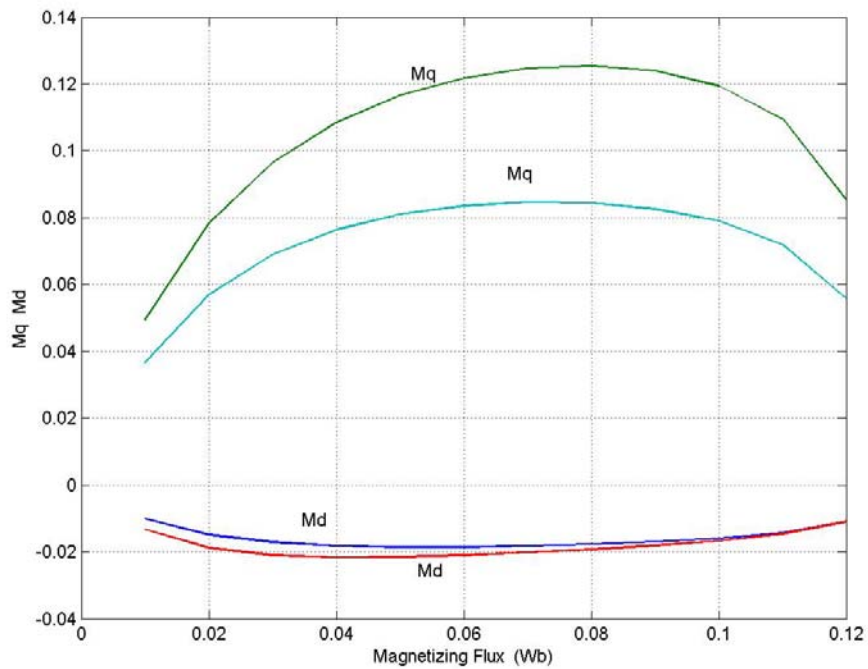


Figure 6.10: Variation of M_q and M_d with magnetizing flux λ_m for a load resistance of $R_L = 100\Omega$ and $L = 50\text{mH}$

Figures 6.11 to 6.16 are obtained assuming the machine to be operating under a condition of minimum copper loss. The condition of minimum copper loss is derived in Chapter 8, and is determined by the operating slip satisfying the condition, shown in Equation 6.50. In this case as well the analysis is carried out for two extreme operating conditions, causing both charging and discharging of the battery. Figure 6.11 illustrates the charging of the battery from 24V to 55V. The corresponding battery currents are plotted in Figure 6.12. The loads for both the conditions are assumed to be the same as in Figures 6.4 to 6.10.

$$s = -\frac{1}{\sqrt{\frac{\omega_r^2}{r_s r_r^2} (r_s L_r^2 + r_r L_m^2) - 1}} \quad (6.50)$$

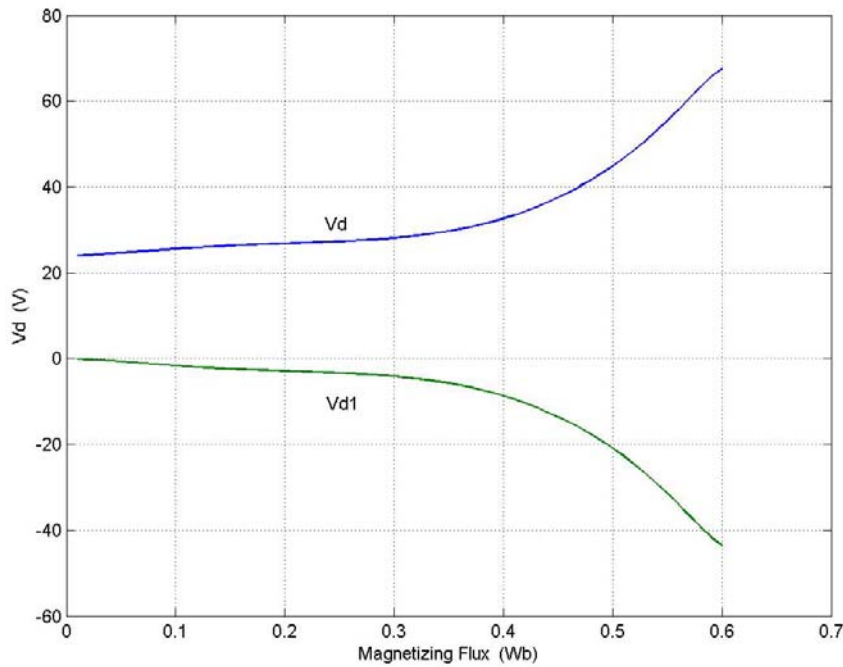


Figure 6.11: Variation of V_d with magnetizing flux λ_m for a load resistance of $R_L = 100\Omega$ and $L = 50\text{mH}$ under minimum loss condition.

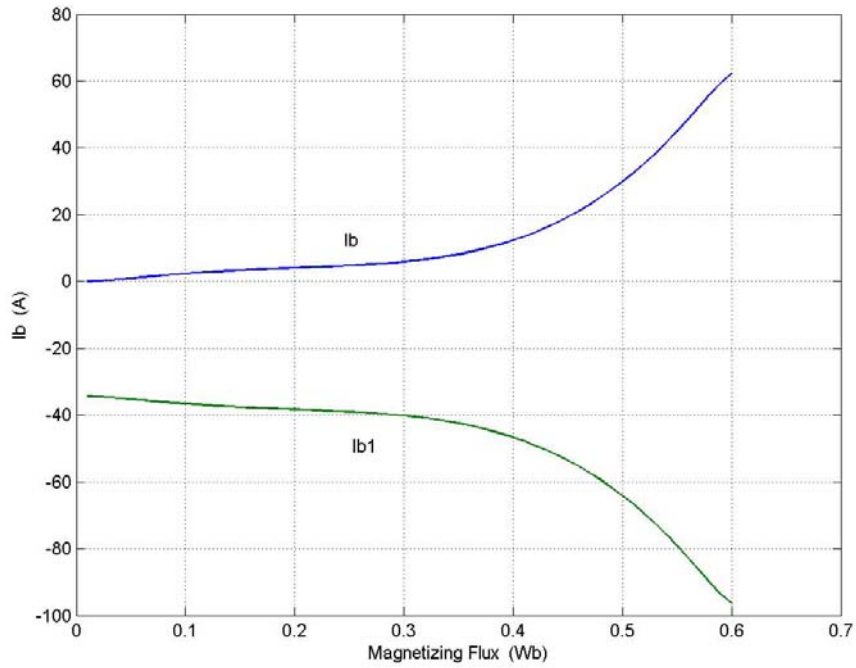


Figure 6.12: Variation of I_d with magnetizing flux λ_m for a load resistance of $R_L = 100\Omega$ and $L = 50\text{mH}$ under minimum loss condition.

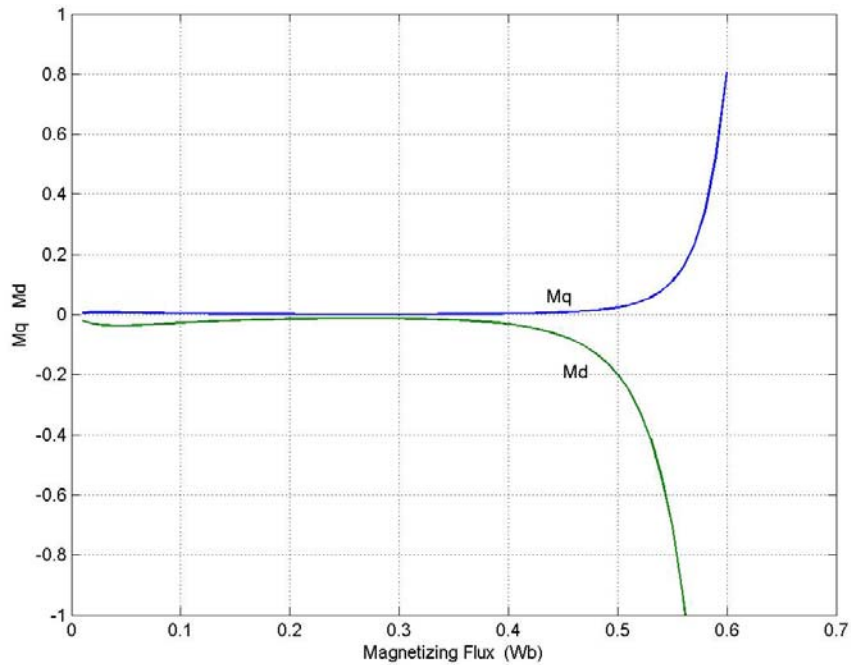


Figure 6.13: Variation of M_q and M_d with magnetizing flux λ_m for a load resistance of $R_L = 100\Omega$ and $L = 50\text{mH}$ under minimum loss condition.

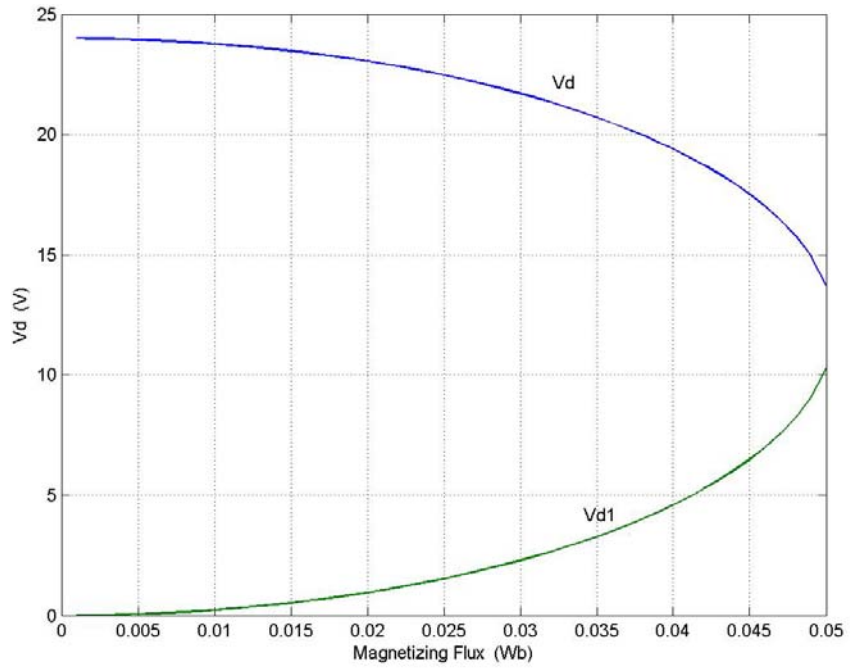


Figure 6.14: Variation of V_d with magnetizing flux λ_m for a load resistance of $R_L = 10\Omega$ and $L = 5\text{mH}$ under minimum loss condition.

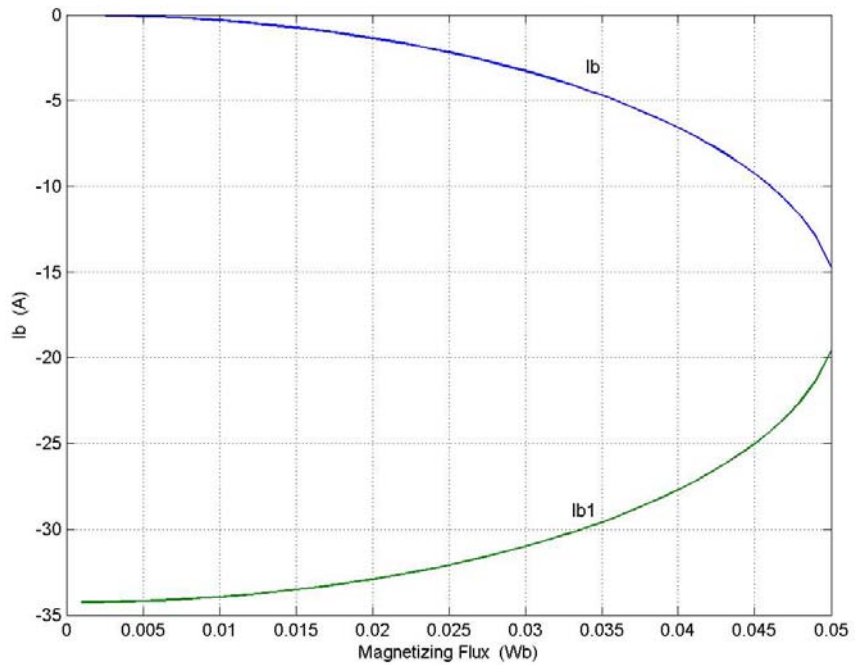


Figure 6.15: Variation of I_d with magnetizing flux λ_m for a load resistance of $R_L = 10\Omega$ and $L = 5\text{mH}$ under minimum loss condition.

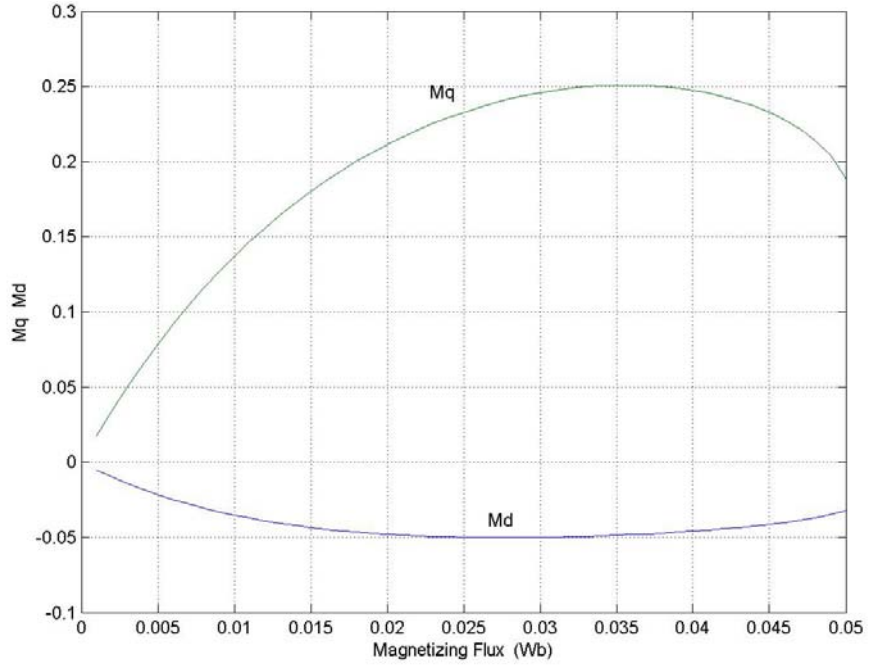


Figure 6.16: Variation of M_q and M_d with magnetizing flux λ_m for a load resistance of $R_L = 10\Omega$ and $L = 5mH$ under minimum loss condition.

Figures 6.14 to 6.16 show the discharging conditions of the battery. The dc voltage, battery current, and corresponding values of the q and d-axis modulation signals are plotted. The analysis performed show the two extreme operating conditions of the proposed system.

Table 6.2: Parameters used in analysis

$r_s = 1.54\Omega$	$r_c = 0.2\Omega$
$r_r = 0.9088\Omega$	$\omega_r = 300rad/sec$
$L_{ls} = 0.004H$	$V_o = 24V$
$L_{lr} = 0.004H$	$R_s = 0.7\Omega$
$L_c = 5mH$	

CHAPTER 7

MODELING OF THREE-PHASE INDUCTION GENERATOR- RECTIFIER SYSTEM

7.1 Introduction

Induction generators are used in a large number of applications in the area of non-conventional energy sources e.g. wind-powered electricity. The primary reason for the increase in the use of induction generators in wind power generation is the fact that induction machine can be made to work as a self- excited induction generator, and thereby does not require an independent source to produce the excitation magnetic field.

The different methods of operation of an induction generator are [C.18]:

- Polyphase AC Supply
- VSI Inverter with DC Supply
- CSI Inverter with DC Supply
- Capacitive Self-Excitation
- VSI Self-Excitation
- CSI Self-Excitation.

Each mode of operation is schematically represented in Figure 7.1.

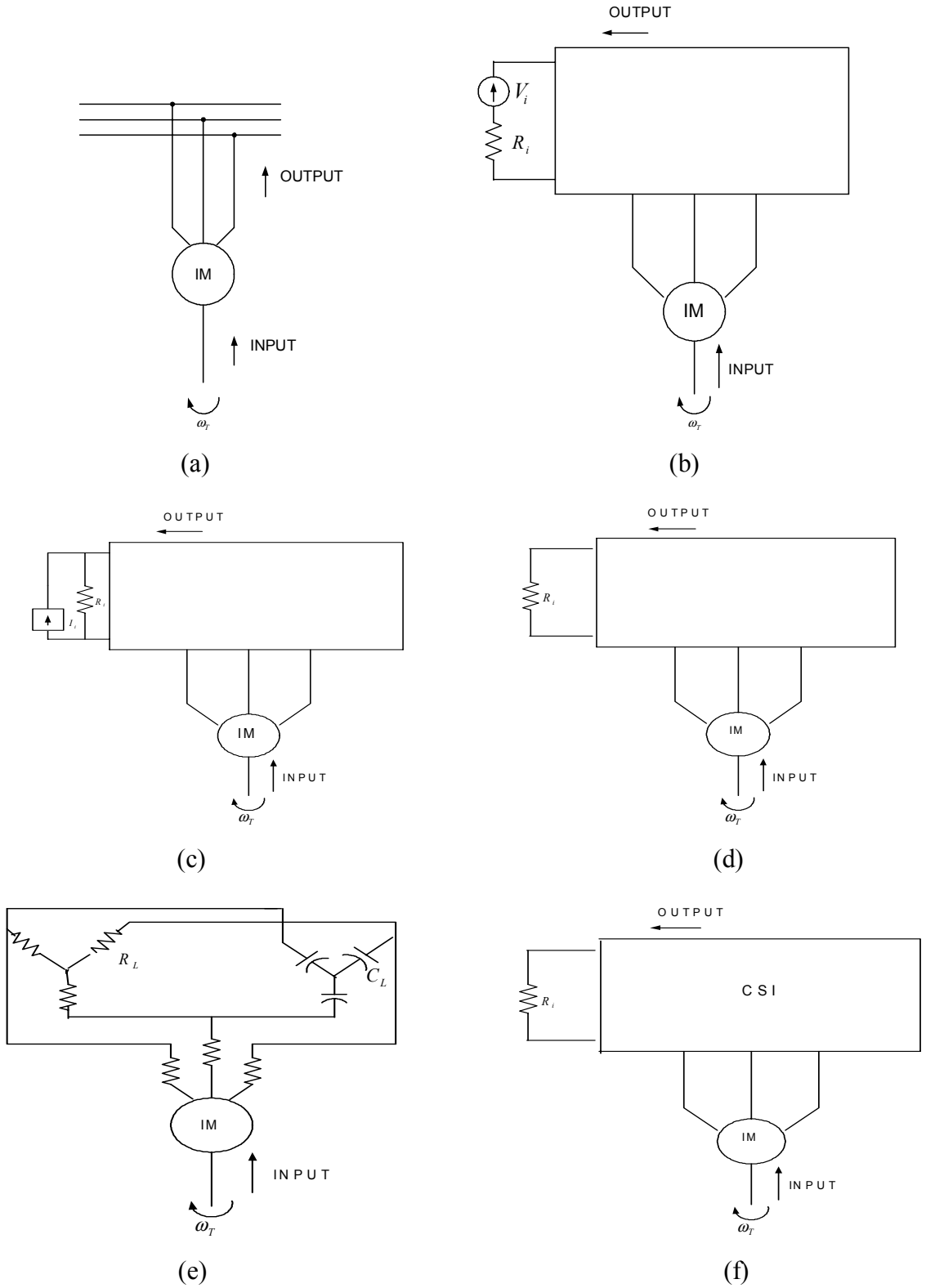


Figure 7.1: Generator modes of operation in an induction machine, from top: (a) poly-phase ac supply, (b) VSI with dc supply, (c) CSI with dc supply, (d) VSI self-excitation, (e) capacitive self-excitation, (f) CSI self-excitation

Operation of the induction generator can be obtained by the connection of the machine to a poly-phase supply. When the machine is driven at a speed greater than the synchronous speed of the machine, the direction of active power is reversed. Similarly for the connection of a voltage source inverter to a dc supply, the reversal in the direction of the dc current indicates a change in the direction of active power flow. For the connection of the CSI to a dc supply, the dc voltage changes direction when the machine is operating as a generator.

An important feature of induction machines, as mentioned earlier, is the ability for the machine to self-excite. There are two possible methods, both illustrated in Figure 7.1 (d) and 7.1(f). In the case shown in Figure 7.1(d), the reactive power supplied by the poly-phase source in Figure 7.1 9(a) is now supplied by the capacitor

7.2 System Model

The method of self -excitation studied in detail is the converter-driven method. In this method, the capacitor on the dc side of the rectifier acts like a three-phase capacitor connected across the terminals of the stator windings, the system configuration is shown in Figure 7.2. During the startup process of the generator, the converter provides the required excitation (with the dc capacitor), and as the generator voltage builds up the converter operates as a rectifier, rectifying the ac power from the generator to dc power.

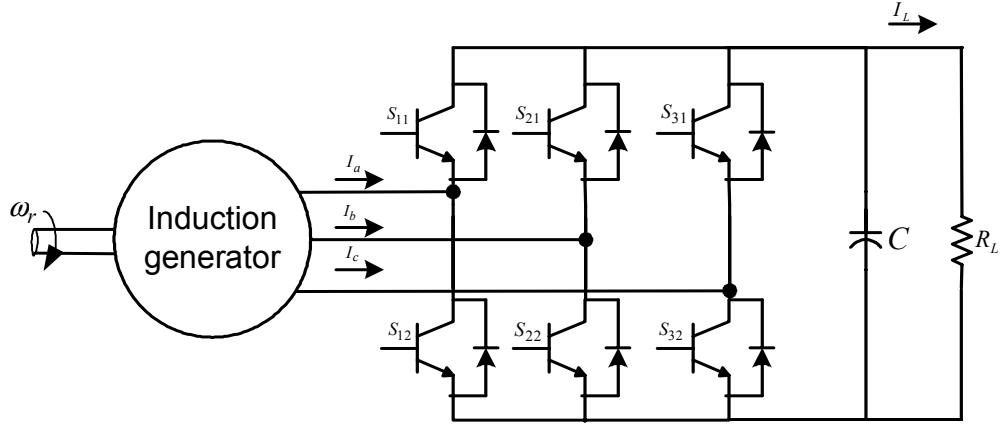


Figure 7.2: Induction generator-boost rectifier system model

The first step in the development of the scheme is the generator model, following which the model, the boost rectifier model is summarized and finally the combined model developed.

The model of a three-phase induction generator is the same as the induction motor detailed in Chapter 5. The model equations for the machine derived in Chapter 5 assumes a positive direction of current for the operation of the machine as a motor; therefore, the machine equations for the generator operation are exactly the same as the motor except for the direction of current. The induction generator model equations are given by Equations (7.1) to (7.4).

$$V_{qs} = r_s I_{qs} + p\lambda_{qs} + \omega_e \lambda_{ds} \quad (7.1)$$

$$V_{ds} = r_s I_{ds} + p\lambda_{ds} - \omega_e \lambda_{qs} \quad (7.2)$$

$$0 = r_r I_{qr} + p\lambda_{qr} + (\omega_e - \omega_r) \lambda_{dr} \quad (7.3)$$

$$0 = r_r I_{dr} + p\lambda_{dr} - (\omega_e - \omega_r) \lambda_{qr} \quad (7.4)$$

$$T_e = \frac{3P}{4} (i_{qs} i_{dr} - i_{ds} i_{qr}) \quad (7.5)$$

V_{qs} , V_{ds} are the stator q and d-axis voltages

I_{qs} , I_{ds} are the stator q and d-axis currents

V_{qr} , V_{dr} are the rotor q and d-axis voltages

I_{qr} , I_{dr} are the rotor q and d-axis currents

λ_{qs} , λ_{ds} , λ_{qr} and λ_{dr} are the stator and rotor q and d-axis flux linkages.

The model equations expressed in terms of the stator currents and rotor fluxes are used in the control scheme formulated in Chapter 9. The system equations for the generator are therefore expressed in terms of the desired variables. The model equations derived in Chapter 5, Equations (5.44) to (5.47) are repeated below.

$$L_\sigma p I_{qs} = V_{qs} - r I_{qs} - \omega_e L_\sigma I_{ds} + \frac{r_r L_m}{L_r^2} \lambda_{qr} - \frac{\omega_r L_m}{L_r} \lambda_{dr} \quad (7.6)$$

$$L_\sigma p I_{ds} = V_{ds} - r I_{ds} + \omega_e L_\sigma I_{qs} + \frac{r_r L_m}{L_r^2} \lambda_{qr} + \frac{\omega_r L_m}{L_r} \lambda_{dr} \quad (7.7)$$

$$p \lambda_{qr} = \frac{-r_r}{L_r} \lambda_{qr} + \frac{r_r L_m}{L_r} I_{qs} - (\omega_e - \omega_r) \lambda_{dr} \quad (7.8)$$

$$p \lambda_{dr} = \frac{-r_r}{L_r} \lambda_{dr} + \frac{r_r L_m}{L_r} I_{ds} + (\omega_e - \omega_r) \lambda_{qr} \quad (7.9)$$

The torque equation for the generator in terms of the desired state variables is

$$T_e = k (\lambda_{dr} I_{qs} - \lambda_{qr} I_{ds}) \quad (7.10)$$

$$k = \frac{3P L_m}{4 L_r}$$

The model equations for the boost rectifier system have been derived in Chapter 3; the equations are repeated in 7.11 to 7.14.

$$V_{qs} = rI_{qs} + LpI_{qs} + \omega_e LI_{ds} + \frac{M_q V_{dc}}{2} \quad (7.11)$$

$$V_{ds} = rI_{ds} + LpI_{ds} - \omega_e LI_{qs} + \frac{M_d V_{dc}}{2} \quad (7.12)$$

$$V_o = rI_{os} + LpI_o + V_{dc} \quad (7.13)$$

$$CpV_{dc} = \frac{3}{2} (M_{qs} I_{qs} + M_{ds} I_{ds} + 2M_o I_o) - \frac{V_{dc}}{R_L} \quad (7.14)$$

V_{qs} , V_{ds} are the q and d-axis voltages

I_{qs} , I_{ds} are the q and d-axis currents

M_{qs} , M_{ds} are the q and d-axis modulation signals

R_L = Load resistance

C = dc side capacitor

r = resistance per phase

ω_e = frequency of input voltages

L = inductance per phase

V_{dc} = output dc voltage.

The expression for the q and d-axis voltages in terms of the q and d-axis components of the modulation signals has been derived in Chapter 3 and is repeated below in Equations 7.15 and 7.16.

$$V_{qs} = \frac{M_q V_{dc}}{2} \quad (7.15)$$

$$V_{ds} = \frac{M_d V_{dc}}{2} \quad (7.16)$$

$$CpV_{dc} = \frac{3}{2} (M_{qs} I_{qs} + M_{ds} I_{ds}) - \frac{V_{dc}}{R_L} \quad (7.17)$$

From Figure 7.2, the q and d-axis voltages of the boost rectifier Equations (7.15) and (7.16) are equal to the q and d-axis stator voltages for the induction generator.

Using Equations (7.6) to (7.9) and (7.15) to (7.17), the combined model of the induction generator-boost rectifier system is derived.

As explained earlier, the model equations for the induction generator should incorporate a reversal in the current direction. This is included in the capacitor voltage equation for the boost rectifier.

$$CpV_{dc} = -\frac{3}{2} (M_{qs} I_{qs} + M_{ds} I_{ds}) - \frac{V_{dc}}{R_L} \quad (7.18)$$

Therefore the model equations of the induction generator boost rectifier system are summarized below:

$$\frac{M_q V_{dc}}{2} = r I_{qs} L_\sigma + p I_{qs} + \omega_e L_\sigma I_{ds} - \frac{r_r L_m}{L_r^2} \lambda_{qr} + \frac{\omega_r L_m}{L_r} \lambda_{dr} \quad (7.19)$$

$$\frac{M_d V_{dc}}{2} = r I_{ds} + L_\sigma p I_{ds} - \omega_e L_\sigma I_{qs} - \frac{r_r L_m}{L_r^2} \lambda_{qr} - \frac{\omega_r L_m}{L_r} \lambda_{dr} \quad (7.20)$$

$$p \lambda_{qr} = \frac{-r_r}{L_r} \lambda_{qr} + \frac{r_r L_m}{L_r} I_{qs} - (\omega_e - \omega_r) \lambda_{dr} \quad (7.21)$$

$$p \lambda_{dr} = \frac{-r_r}{L_r} \lambda_{dr} + \frac{r_r L_m}{L_r} I_{ds} + (\omega_e - \omega_r) \lambda_{qr} \quad (7.22)$$

$$CpV_{dc} = -\frac{3}{2}(M_{qs}I_{qs} + M_{ds}I_{ds}) - \frac{V_{dc}}{R_L}. \quad (7.23)$$

The model equations derived for the generator-rectifier system is used in the steady-state analysis as well as the derivation of the control scheme for the induction generator-rectifier using rotor flux vector control.

CHAPTER 8

STEADY-STATE EXCITATION OF INDUCTION GENERATOR –RECTIFIER SYSTEM

8.1 Introduction

The dynamic model of a three-phase induction generator-boost rectifier system has been detailed in Chapter 7. The steady state operation of the system is studied in detail in this chapter. The effect of saturation on the performance of an induction machine has been studied extensively in [C.1]. The effect of saturation is incorporated in the model of the system by using the variation of the magnetizing inductance L_m with the magnetizing flux linkage λ_m , which is experimentally obtained.

Various studies have been made based on the response of the induction generator with respect to the change in magnetizing flux. The magnetizing flux, and its effect on the self- excitation process of an induction machine is illustrated in [C.3].

This chapter studies the excitation requirements of an induction generator, accounting for saturation in the generator. The measure of the self-excitation requirements primarily used is the magnitude of the modulation index of the three-phase boost rectifier.

To augment the detailed analysis, the operation of the induction machine is studied and the effect of minimizing the copper loss in the system is shown graphically

by numerous plots. The effect of the different parameters affecting the system is exhaustively studied and illustrated.

8.2 Steady-State Model

The model equations of the system, derived in Chapter 7 are expressed in terms of the rotor fluxes and stator currents; however, the steady state analysis performed considers the equations for an induction machine in terms of the stator currents, stator fluxes, rotor currents, and rotor fluxes in the complex form. The dynamic equations of an induction machine are

$$V_{qs} = r_s I_{qs} + p\lambda_{qs} + \omega_e \lambda_{ds} \quad (8.1)$$

$$V_{ds} = r_s I_{ds} + p\lambda_{ds} - \omega_e \lambda_{qs} \quad (8.2)$$

$$V_{qr} = r_r I_{qr} + p\lambda_{qr} + (\omega_e - \omega_r) \lambda_{dr} \quad (8.3)$$

$$V_{dr} = r_r I_{dr} + p\lambda_{dr} - (\omega_e - \omega_r) \lambda_{qr} \quad (8.4)$$

The variables used in Equations (8.1) to (8.4) are defined in Table 8.1, and the system model is shown in Figure 8.1.

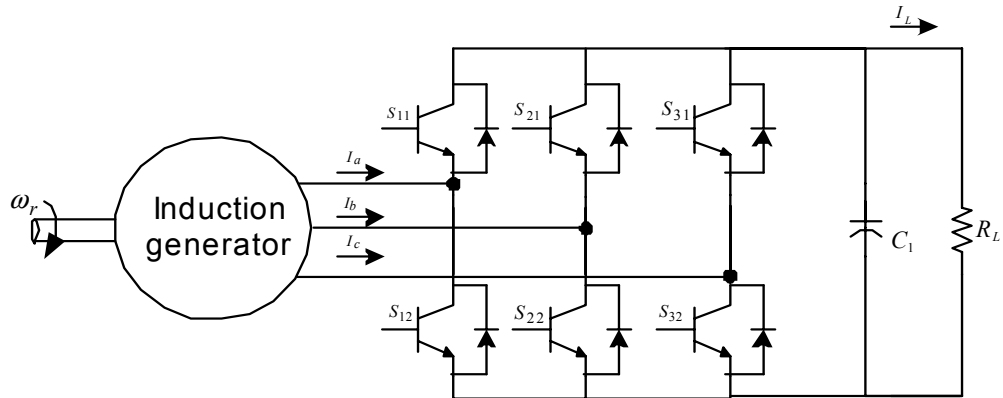


Figure 8.1: System model

Table 8.1: Variables used in machine equations

V_{qs}	Q-axis voltage (V)
V_{ds}	D-axis voltage (V)
I_{qs}	Q-axis current (A)
I_{ds}	D-axis current (A)
$\lambda_{qs}, \lambda_{qr}$	Qaxis stator and rotor fluxes (Wb)
$\lambda_{ds}, \lambda_{dr}$	D-axis stator and rotor fluxes (Wb)
r_s	Per phase stator resistance (Ω)
r_r	Per phase rotor resistance (Ω)
ω_e	Frequency of stator voltages (rad/sec)
ω_r	Rotor speed (rad/sec)

To reduce the number of Equations to simplify the analysis, equations (8.1) to (8.4) are expressed in the complex form. The complex form defines the variables using the ‘j’ operator that represents the variable as 90° apart in space. The variables of the machine are defined in the complex form as below.

$$V_{qds} = V_{qs} + jV_{ds} \quad (8.5)$$

$$V_{qdr} = V_{qr} + jV_{dr} \quad (8.6)$$

$$\lambda_{qdr} = \lambda_{qr} + j\lambda_{dr} \quad (8.7)$$

$$\lambda_{qds} = \lambda_{qs} + j\lambda_{ds} \quad (8.9)$$

Using the above definitions for the complex form currents, voltages, and fluxes, the model equations for the induction machine in the complex form are

$$V_{qds} = r_s I_{qds} + p\lambda_{qds} - j\omega_e \lambda_{qds} \quad (8.9)$$

$$V_{qdr} = r_r I_{qdr} + p \lambda_{qdr} - j \omega_s \lambda_{qds}, \quad (8.10)$$

where the slip frequency is defined as

$$\omega_s = \omega_e - \omega_r = s \omega_e \quad (8.11)$$

$$s = \frac{\omega_e - \omega_r}{\omega_e}. \quad (8.12)$$

As the generator is a squirrel cage induction generator, the rotor voltages are equal to zero, i.e.

$$V_{qdr} = 0. \quad (8.13)$$

Therefore Equation (8.10) can be rewritten as:

$$0 = r_r I_{qdr} + p \lambda_{qdr} - j \omega_s \lambda_{qds}. \quad (8.14)$$

The steady state analysis is performed by using the complex form model equations for the induction machine and setting the differential terms in the equations to be equal to zero. Therefore,

$$V_{qds} = r_s I_{qds} - j \omega_e \lambda_{qds} \quad (8.15)$$

$$V_{qdr} = r_r I_{qdr} - j \omega_s \lambda_{qds}. \quad (8.16)$$

The model equations for the boost rectifier connected to the generator is derived in Chapter 7. The capacitor voltage equation for the boost rectifier-induction generator system is given by

$$CpV_{dc} = -\frac{3}{2} (M_{qs} I_{qs} + M_{ds} I_{ds}) - \frac{V_{dc}}{R_L}. \quad (8.17)$$

Equation (8.17) can also be expressed as

$$CpV_{dc} = -\frac{3}{2} \text{Re} al (M_{qds} I_{qds}^*) - \frac{V_{dc}}{R_L} \quad (8.18)$$

The parameters for Equation (8.16) are defined in Table 8.2.

Table 8.2: Variables used in capacitor voltage equation

M_{qs}	Q-axis component of modulation index
M_{ds}	D-axis component of modulation index
I_{qs}	Q-axis current (A)
I_{ds}	D-axis current (A)
V_{dc}	Output DC voltage (V)
R_L	Load resistance (Ω)
C	DC-side capacitor (mF)

$$M_{qds} = M_{qs} + jM_{ds}. \quad (8.19)$$

The steady-state capacitor voltage equation for the boost rectifier is

$$0 = -\frac{3}{2} \text{Re}al(M_{qds} I_{qds}^*) - \frac{V_{dc}}{R_L}. \quad (8.20)$$

Therefore the model equations for the induction generator –rectifier system in the complex form are summarized below.

$$V_{qds} = r_s I_{qds} - j\omega_e \lambda_{qds} \quad (8.21)$$

$$0 = r_r I_{qdr} - j\omega_s \lambda_{qds} \quad (8.22)$$

$$0 = -\frac{3}{2} \text{Re}al(M_{qds} I_{qds}^*) - \frac{V_{dc}}{R_L} \quad (8.23)$$

8.3 Variation of L_m with Magnetizing Flux

The importance of the effect of the magnetizing flux is illustrated using Figures 8.1 and 8.2, which has been experimentally obtained as described in Chapter 5.

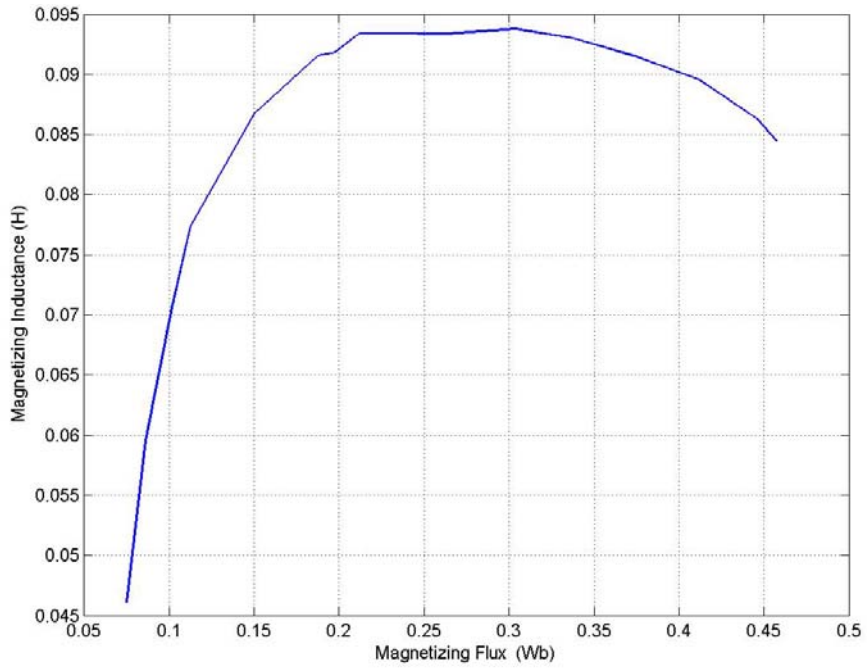


Figure 8.1: Variation of magnetizing inductance with peak magnetizing flux at a constant frequency

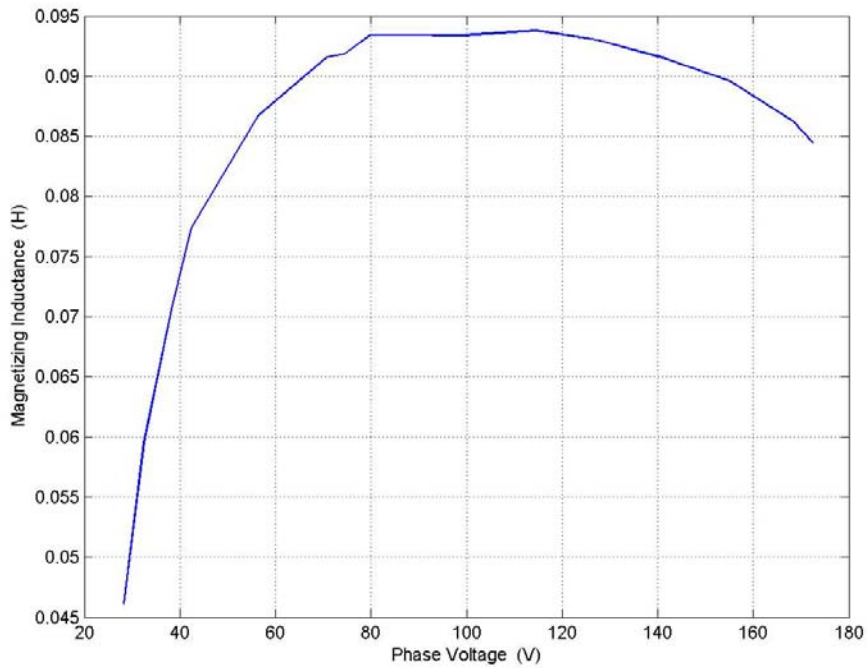


Figure 8.2: Variation of magnetizing inductance with peak phase voltage at a constant input frequency.

Figure 8.1 shows the variation of the magnetizing flux L_m with the magnetizing flux linkage and Figure 8.2 shows the variation of the magnetizing inductance with the phase voltage.

In the self-excited induction generator, the variation of the magnetizing inductance is the main factor in the dynamics of voltage buildup and stabilization. The process of voltage buildup occurs due to the remnant flux in the core.

The curve in Figure 8.2 can be expressed by Equation (8.24).

$$L_m = -0.7486\lambda_m^2 + 0.4583\lambda_m + 0.0281 \quad (8.24)$$

8.4 Analysis At Rated Slip

8.4.1 Influence of Magnetizing Flux on 'M'

Having established the effect of the magnetizing flux linkage on the magnetizing inductance, this section details the effect of the magnetizing flux linkage on the magnitude of the modulation index required for excitation of the generator.

As mentioned earlier, the steady state analysis aims at determining the value of the magnitude of the modulation index required for excitation of the generator for a constant load resistance and rotor speed. The first part of the analysis assumes a constant slip for the generator, and the second section studies the system under a condition of minimum copper loss.

Using the complex form model equations of the generator-rectifier system, (8.21) to (8.23), the stator voltage equation is expressed in terms of the stator fluxes. The derivation is laid out in detail.

The stator and rotor currents can be expressed in terms of the flux linkages using Equation (8.25).

$$\begin{bmatrix} \lambda_{qds} \\ \lambda_{qdr} \end{bmatrix} = \begin{bmatrix} L_s & L_m \\ L_m & L_r \end{bmatrix} \times \begin{bmatrix} I_{qds} \\ I_{qdr} \end{bmatrix} \quad (8.25)$$

$$\begin{bmatrix} I_{qds} \\ I_{qdr} \end{bmatrix} = \frac{1}{D} \begin{bmatrix} L_r & -L_m \\ -L_m & L_s \end{bmatrix} \times \begin{bmatrix} \lambda_{qds} \\ \lambda_{qdr} \end{bmatrix} \quad (8.26)$$

$$D = L_s L_r - L_m^2$$

From Equation (8.26), the stator and rotor currents expressed in terms of the stator and rotor fluxes are

$$I_{qds} = \frac{L_r}{D} \lambda_{qds} - \frac{L_m}{D} \lambda_{qdr} \quad (8.27)$$

$$I_{qdr} = \frac{L_s}{D} \lambda_{qdr} - \frac{L_m}{D} \lambda_{qds} \quad (8.28)$$

Substituting for I_{qds} , Equation (8.27) in Equation (8.21)

$$V_{qds} = r_s \left(\frac{L_r}{D} \lambda_{qds} - \frac{L_m}{D} \lambda_{qdr} \right) - j\omega_e \lambda_{qds} \quad (8.29)$$

Simplifying the above equation

$$V_{qds} = (T_s - j\omega_e) \lambda_{qds} + B_s \lambda_{qdr} \quad (8.30)$$

$$T_s = \frac{r_s L_r}{D}, \quad B_s = \frac{-r_s L_m}{D}.$$

Similarly, for the rotor voltage Equation, (8.28) is substituted in (8.22)

$$0 = r_r \left(\frac{L_s}{D} \lambda_{qdr} - \frac{L_m}{D} \lambda_{qds} \right) - j\omega_s \lambda_{qds} \quad (8.31)$$

$$0 = r_r (T_r - j\omega_s) \lambda_{qdr} + B_r \lambda_{qds} \quad (8.29)$$

$$T_r = \frac{r_r L_s}{D}, \quad B_s = \frac{-r_r L_m}{D}.$$

Using Equation (8.31), the rotor fluxes can be expressed in terms of the stator fluxes:

$$\lambda_{qdr} = \frac{-B_r}{(T_r - j\omega_s)} \lambda_{qds}. \quad (8.33)$$

Substituting (8.33) in (8.27) the current I_{qds} can be expressed in terms of the stator fluxes as

$$I_{qds} = \frac{L_r}{D} \lambda_{qds} - \frac{L_m}{D} \times \frac{-B_r}{(T_r - j\omega_s)} \lambda_{qds} \quad (8.34)$$

$$I_{qds} = \left[\frac{L_r}{D} + \frac{B_r L_m}{D(T_r + j\omega_s)} \right] \lambda_{qds}. \quad (8.35)$$

Also, substituting Equation (8.33) in (8.30), the stator voltage equation can be expressed in terms of the stator fluxes

$$V_{qds} = \left[(T_s - j\omega_e) - \frac{B_s B_r}{(T_r - j\omega_s)} \right] \lambda_{qds}. \quad (8.36)$$

As derived in Chapter 5, the stator voltages, which are also the input voltages to the boost rectifier, can be expressed in terms of the modulation signals and the output dc voltage.

$$V_{qds} = \frac{M_{qds} V_{dc}}{2} \quad (8.37)$$

Substituting Equation (8.37) in (8.36)

$$\frac{M_{qds} V_{dc}}{2} = \left[(T_s - j\omega_e) - \frac{B_s B_r}{(T_r - j\omega_s)} \right] \lambda_{qds}. \quad (8.38)$$

Rearranging Equation (8.38) the stator flux λ_{qds} can be expressed in terms of the modulation signal M_{qds} .

$$\lambda_{qds} = \frac{M_{qds} V_{dc}}{2 \left[(T_s - j\omega_e) - \frac{B_s B_r}{(T_r - j\omega_s)} \right]} \quad (8.39)$$

The constraining equation for the excitation of the induction generator-boost rectifier system is the capacitor voltage equation (8.23). The capacitor voltage equation at steady state relates the load current and the dc current at the output of the rectifier.

$$\frac{V_{dc}}{R_L} = -\frac{3}{2} \text{Re al} \left(M_{qds}^* I_{qds}^* \right) \quad (8.40)$$

Substituting Equation (8.35) in (8.40), the current in Equation (8.40) can be eliminated and the equation can be expressed in terms of the stator flux as

$$\frac{2 V_{dc}}{3 R_L} = -\text{Re al} \left(M_{qds}^* \times \left[\frac{L_r}{D} - \frac{B_r L_m}{D(T_r + j\omega_s)} \right] \times \lambda_{qds} \right). \quad (8.41)$$

Finally, substituting Equation (8.38) in (8.41) relates the magnitude of the modulation index 'M' with the magnetizing inductance.

$$\frac{2 V_{dc}}{3 R_L} = -\text{Re al} \left(M_{qds}^* \times \left[\frac{L_r}{D} - \frac{B_r L_m}{D(T_r + j\omega_s)} \right] \times \frac{M_{qds} V_{dc}}{2 \left[(T_s - j\omega_e) - \frac{B_s B_r}{(T_r - j\omega_s)} \right]} \right) \quad (8.42)$$

Equation (8.42) can be simplified as

$$\frac{2}{3} \frac{1}{R_L} = -|M|^2 \text{Re al} \left(\times \left[\frac{L_r}{D} - \frac{B_r L_m}{D(T_r + j\omega_s)} \right] \times \frac{1}{2 \left[(T_s - j\omega_e) - \frac{B_s B_r}{(T_r - j\omega_s)} \right]} \right) \quad (8.43)$$

$$\text{where } M = \sqrt{M_q^2 + M_d^2} \quad (8.44)$$

$$|M|^2 = -\frac{2}{3R_L} \times \frac{1}{\text{Real} \left[\left[\frac{L_r}{D} - \frac{B_r L_m}{D(T_r + j\omega_s)} \right] \times \frac{1}{2 \left[(T_s - j\omega_e) - \frac{B_s B_r}{(T_r - j\omega_s)} \right]} \right]} \quad (8.45)$$

Equation (8.45) is used to calculate the modulation index required for excitation of the generator for a fixed value of magnetizing flux, i.e. for every point on the L_m vs. λ_m curve, there is a value of ‘M’ for which the excitation of the generator would occur, for a fixed load resistance, rotor speed and slip. The variation of the magnitude of the modulation index ‘M’ with λ_m is shown on Figure 8.3.

The machine parameters used for the steady state analysis in this chapter are given in Table 8.3

As can be seen from Equation (8.45), the magnitude of the modulation index is independent of the output dc voltage; hence the variation of the modulation index is studied for different load resistances.

Table 8.3:Parameters of 2 hp induction machine used in steady state analysis

$r_s = 1.54\Omega$
$r_r = 0.9088\Omega$
$L_{ls} = 0.004H$
$L_{lr} = 0.004H$

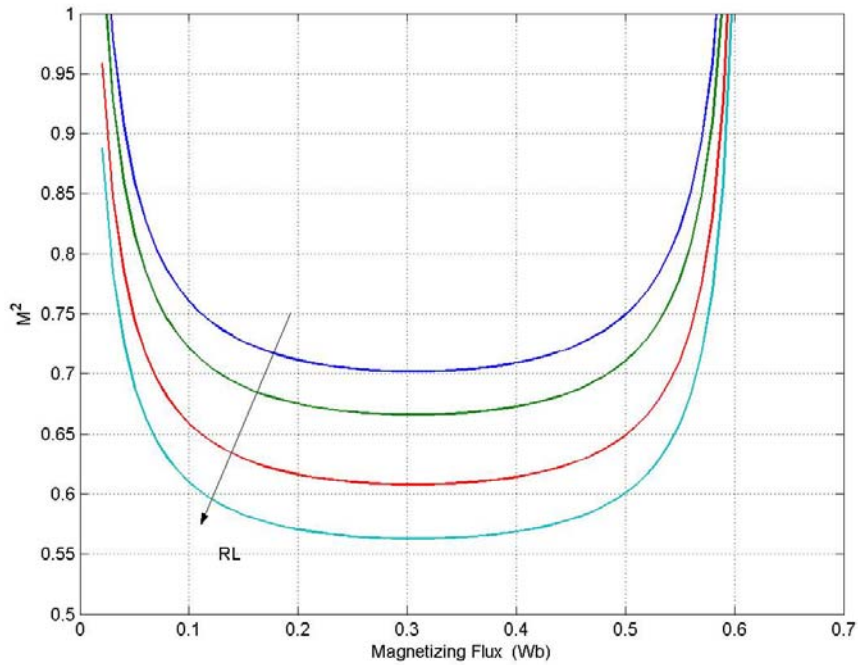


Figure 8.3: Variation of modulation index with the magnetizing inductance for a constant load resistance and slip $s = -0.04$.

Figure 8.3 is obtained by assuming the slip to be constant, the slip chosen in this case is the rated slip of the machine, $s = -0.04$. The load resistance is varied for each plot as $R_L = 45\Omega$, 50Ω , 60Ω , and 70Ω . For each value of load resistance the magnetizing inductance is varied and the corresponding values of the modulation index are calculated. As can be seen from Figure 8.3 as the load resistance increases, the range of the modulation index decreases, i.e. for a load resistance of $R_L = 45\Omega$ the modulation index required can vary up to 1, for a higher load resistance $R_L = 60\Omega$, the modulation index increases to a maximum value of 0.95.

The above set of figures assumes the rotor speed to be constant; however, at different rotor speeds, the magnitude of the modulation index required for excitation varies. This is illustrated in Figure 8.4. Figure 8.4 graphically shows the variation of the

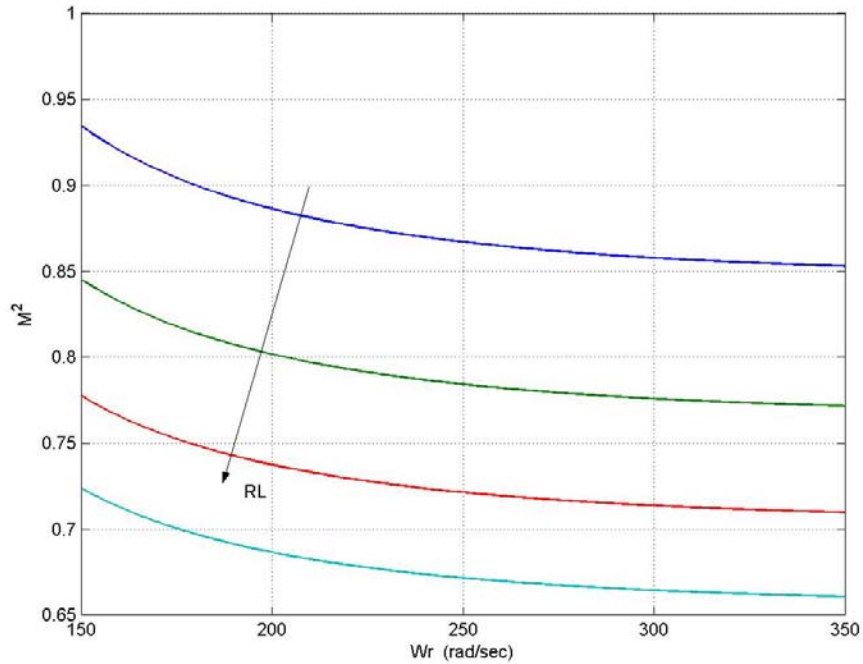


Figure 8.4: Variation of modulation index with the rotor speed for fixed magnetizing flux and load resistance.

modulation index with the rotor speed for a fixed value of magnetizing inductance ($\lambda_m=0.25\text{Wb}$). In this case the slip is chosen as in the previous case to be equal to the rated slip. The rotor speed ω_r is varied between 150 and 350 rad/sec, and the corresponding values of 'M' are calculated. The plot is repeated for different load resistances.

In the above figure, as in the previous case, with an increase in the load resistance, the modulation index values decrease. In this case, the load resistance is varied between 45Ω , 50Ω , 60Ω , and 70Ω . The rotor speed is varied between 150 rad/sec and 300 rad/sec.

Figures 8.3 and 8.4 are represented as three-dimensional plots as well as contour plots to better illustrate the nature of variation.

Figure 8.5 shows the variation of the modulation index with changing load resistance and magnetizing flux as a three-dimensional plot. The load resistance is varied between 30 and 150Ω. The magnetizing flux is varied between 0 and 0.6 Wb.

The variation of the magnitude of the modulation index with the rotor speed and load resistance is shown in Figure 8.7. The range of load resistances plotted for are 30 to 150Ω, and the rotor speed is varied between 150 and 350 rad/sec.

Another parameter used in the analysis is defined as

$$R_o = \frac{3}{2}|M|^2 R_L. \quad (8.46)$$

Assuming a constant rotor speed and load resistance, the two parameters $|M|^2$ and R_o are constant. However, as expressed in Equation 8.45, $|M|^2$ is dependant on the magnetizing flux. Therefore, the parameter R_o can also be expressed as a function of λ_m .

The parameter can be used as a measure of the load resistance that the system can be operated with for a fixed value of rotor speed and slip. The effect of the different operating slips on R_o is shown in Figure 8.9 as a three-dimensional plot and in Figure 8.10 as a contour plot.

Similarly, the variation of the parameter R_o with the operating slip and magnetizing flux is shown in Figure 8.9, and in Figure 8.10 as a three-dimensional plot. Figure 8.11 is a contour plot of the same. In the analysis, the operating slip is varied from $s = -0.02$ to $s = -0.08$.

The graphical representation of the variables in the analysis has been done as two-dimensional, three-dimensional and contour plots to fully illustrate the nature of variation.

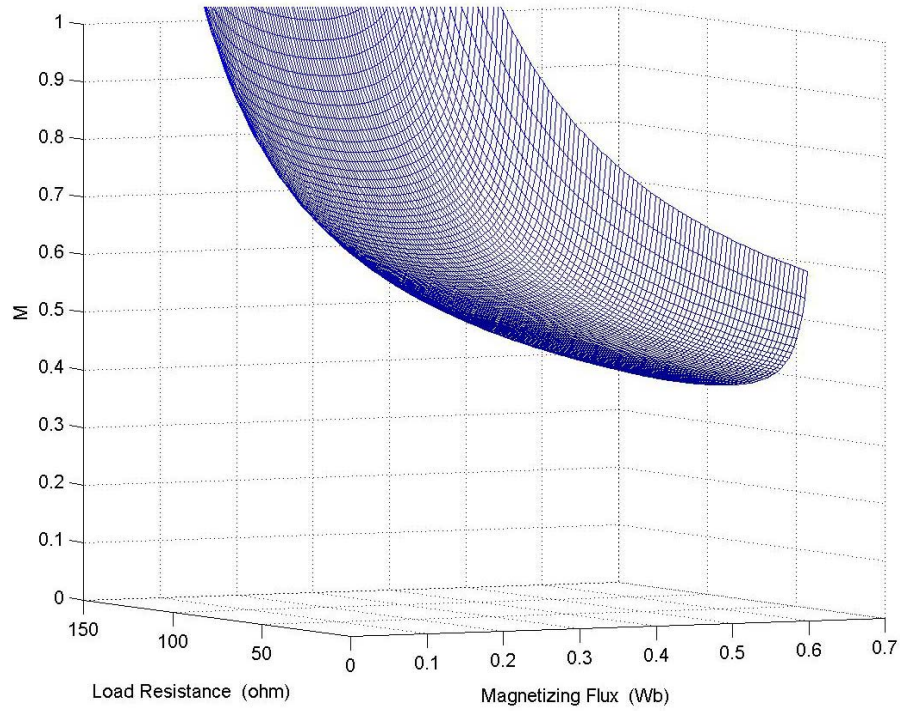


Figure 8.5: Variation of modulation index with the magnetizing flux and load resistance.

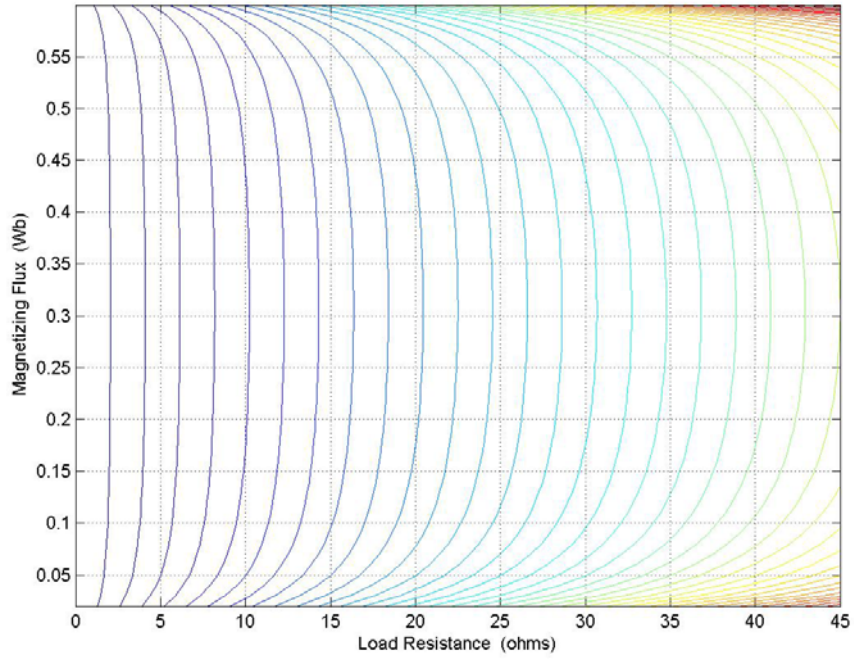


Figure 8.6: Variation of modulation index with the magnetizing flux and load resistance, illustrated as a contour plot.

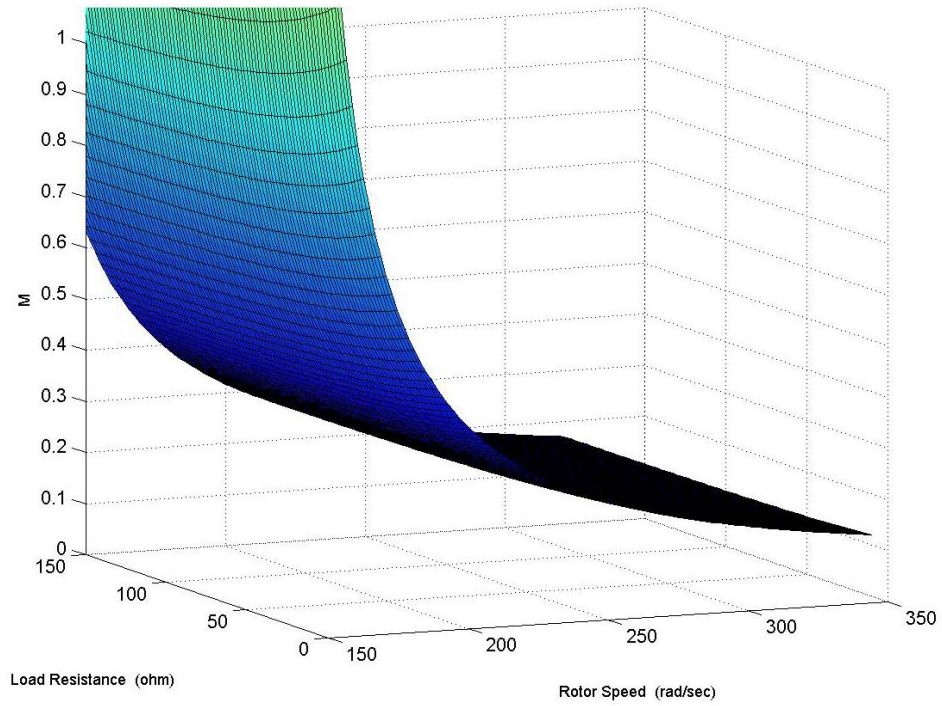


Figure 8.7: Variation of modulation index with the magnetizing flux and rotor speed

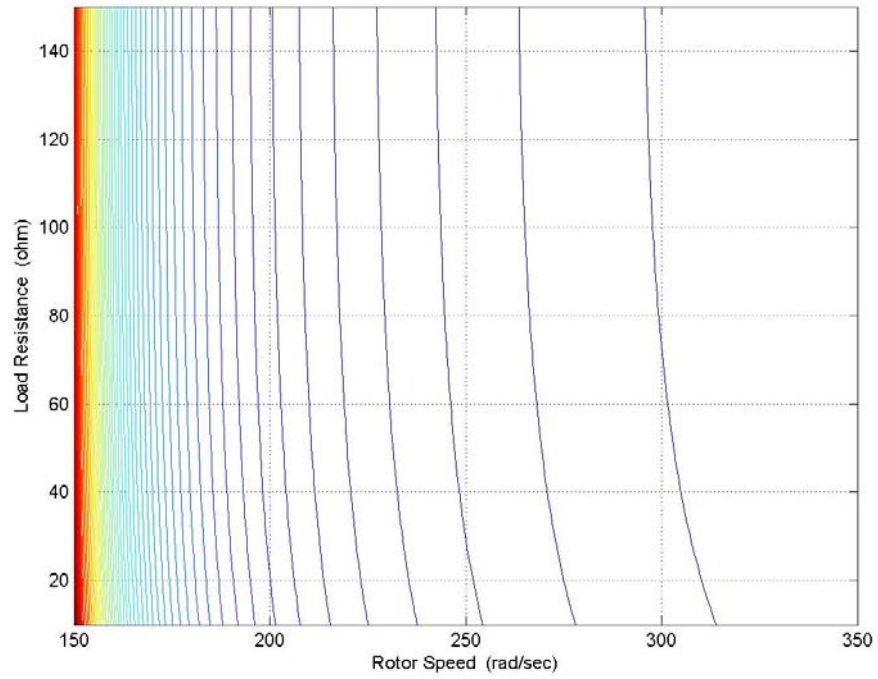


Figure 8.8: Variation of modulation index with the magnetizing flux and rotor speed

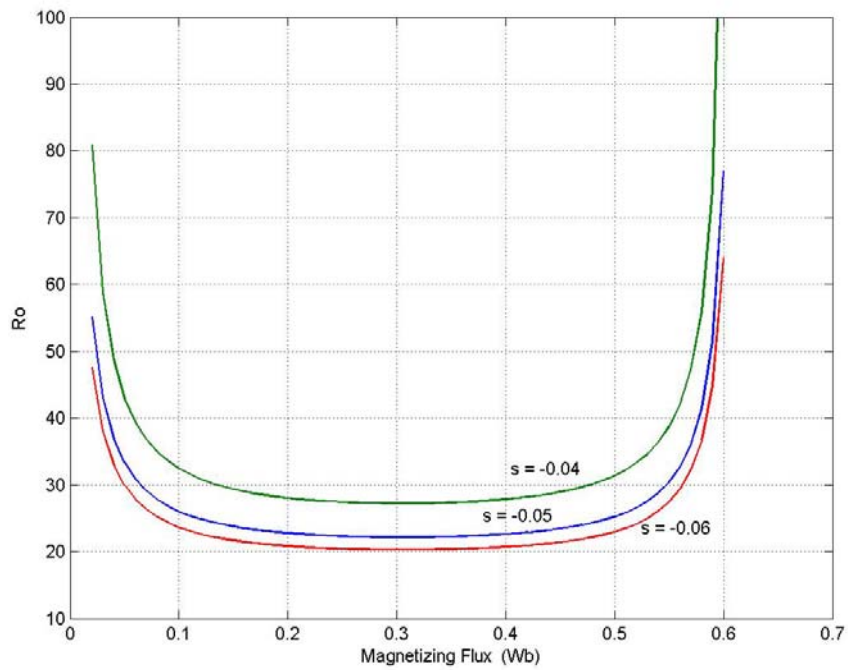


Figure 8.9: Variation of R_o with magnetizing flux linkage for varying operating slips

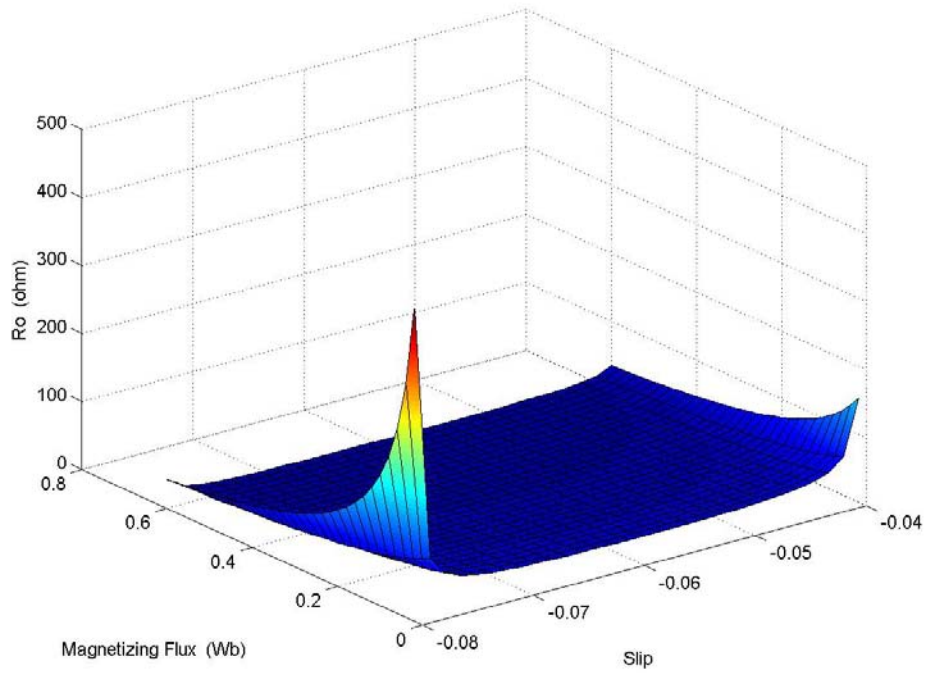


Figure 8.10 Variation of R_o with the magnetizing flux and operating slip

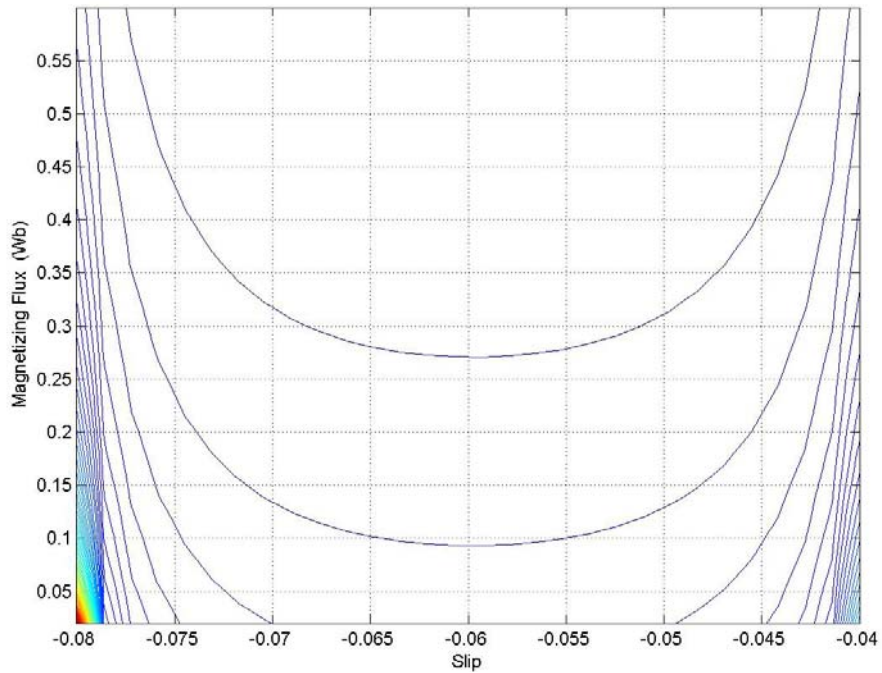


Figure 8.11 Variation of R_o with the magnetizing flux and operating slip

8.4.2 Influence of Magnetizing Flux ‘ λ_m ’ on Output DC voltage

The previous section illustrated the effect of the magnetizing flux on the modulation index. As can be seen from Figure 8.3, there are two different points on the M vs. λ_m curve that satisfy the same value of the modulation index for two different values of magnetizing flux linkage. Therefore, theoretically at a constant load, rotor speed, and operating slip, there are generators that can be excited at the same value of the modulation index for two different values of magnetizing flux.

This section studies the effect of the two operating points having the same modulation index and different values of magnetizing flux, on the output dc voltage of the rectifier.

From the analysis in the previous section, Equation (8.45) is independent of the output dc voltage; therefore, the capacitor voltage equation at steady state is expressed in terms of the magnetizing flux without eliminating the term for the dc voltage. The derivation of the equation follows expressing the stator flux λ_{qds} in terms of the magnetizing flux.

The magnetizing flux can be expressed in terms of the stator and rotor currents as

$$\lambda_{qdm} = L_m (I_{qds} + I_{qdr}) \quad (8.47)$$

Substituting for the stator and rotor currents using Equations (8.27) and (8.28) in Equation (8.47),

$$\lambda_{qdm} = \frac{L_m}{D} [(L_s - L_m)\lambda_{qds} + (L_r - L_m)\lambda_{qdr}] \quad (8.48)$$

$$\lambda_{qdm} = \frac{L_m}{D} [L_{ls}\lambda_{qds} + L_{lr}\lambda_{qdr}]. \quad (8.49)$$

Eliminating λ_{qdr} using Equation (8.33), the magnetizing flux can be expressed in terms of the stator fluxes:

$$\lambda_{qdm} = \frac{L_m}{D} \left[L_{ls} - \frac{B_r L_{lr}}{(T_r + j\omega_s)} \right] \lambda_{qds}. \quad (8.50)$$

The magnetizing flux linkage has a q-axis and a d-axis component. The reference frame transformation angle of the voltage equations assumes the alignment of the q-axis with the magnetizing flux linkage. Hence, the d-axis magnetizing flux is assumed to be zero, and the d-axis magnetizing inductance is constant. However the q-axis magnetizing inductance is a function of the magnetizing flux, which is approximated by a polynomial given in Equation (8.24), also repeated below.

$$\frac{1}{L_{mq}} = \frac{1}{-0.7486\lambda_m^2 + 0.4583\lambda_m + 0.0281} \quad (8.51)$$

The function in Equation (8.51) is illustrated in Figure 8.10. In this plot the reciprocal of the magnetizing inductance is plotted as a function of the magnetizing flux linkage. The magnetizing flux is varied between 0 and 0.6 Wb, and the corresponding values of $(1/L_{mq})$ are calculated.

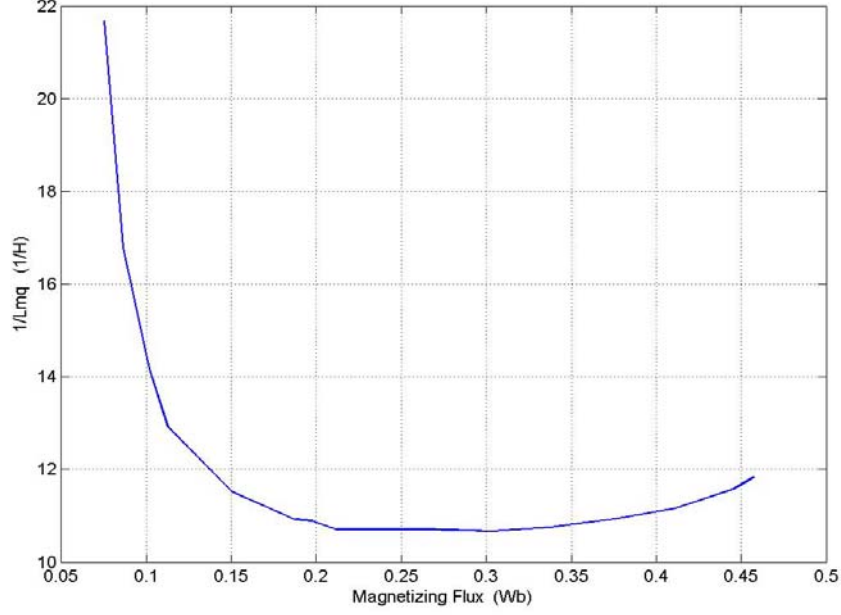


Figure 8.12: Variation of the q-axis component of the magnetizing inductance with the peak magnetizing flux.

$$\lambda_m = \lambda_{qm} = \frac{L_m}{D} \left[L_{ls} - \frac{B_r L_{lr}}{(T_r + j\omega_s)} \right] \lambda_{qds} \quad (8.52)$$

$$\lambda_{qds} = \frac{\lambda_m}{\frac{L_m}{D} \left[L_{ls} - \frac{B_r L_{lr}}{(T_r + j\omega_s)} \right]} \quad (8.53)$$

Substituting Equation (8.53) in (8.41) results in an expression that can be used to calculate the range of dc voltages that the system can operate at for a fixed value of the modulation index.

$$\frac{2 V_{dc}}{3 R_L} = -\text{Real} \left(M_{qds}^* \times \left[\frac{L_r}{D} - \frac{B_r L_m}{D(T_r + j\omega_s)} \right] \times \frac{\lambda_m}{\frac{L_m}{D} \left[L_{ls} - \frac{B_r L_{lr}}{(T_r + j\omega_s)} \right]} \right) \quad (8.54)$$

Rearranging Equation (8.54),

$$V_{dc} = -\frac{3}{2} \times R_L \times \text{Real} \left(M_{qds}^* \times \left[\frac{L_r}{D} - \frac{B_r L_m}{D(T_r + j\omega_s)} \right] \times \frac{\lambda_m}{\frac{L_m}{D} \left[L_{ls} - \frac{B_r L_{lr}}{(T_r + j\omega_s)} \right]} \right). \quad (8.55)$$

The method of determining the range of dc voltages is explained below.

For a fixed value of magnetizing flux, the corresponding value of the modulation index is calculated (as illustrated in section 8.4.1). For every value of ‘M’, the dc voltage contour is plotted by varying the q-axis component of the modulation index M_q and calculating the corresponding value of the d-axis modulation index to satisfy the value of M by Equation (8.56) to (8.58).

$$-M \leq M_q \leq M \quad (8.56)$$

$$M = \sqrt{M_q^2 + M_d^2} \quad (8.57)$$

$$\text{Hence } M_d = \pm \sqrt{M^2 - M_q^2}. \quad (8.58)$$

Figures 8.11 to 8.14 illustrate the dc voltage contour for different load resistances ($R_L = 45\Omega, 50\Omega, 60\Omega, \text{ and } 70\Omega$). By choosing a value of M the corresponding contours considering both the values of the magnetizing flux that satisfy the same value of ‘M’ are plotted. As can be seen from Figure 8.13, the variation of the dc voltage with the q-axis modulation index is in the form of an ellipse. The voltages vary between positive and negative values as shown. The maximum value of the dc voltage that can be obtained with a modulation index of 0.85 at a load resistance of R_L is close to 100V. However, considering the second (larger) value of the magnetizing flux that satisfies the same value of the modulation index, the maximum output dc voltage is almost 400V. The machine

parameters used in the steady state analysis is for a 2 hp induction machine and hence the second set of dc voltages is impractical. Therefore, the set of voltages considered are corresponding to the lower value of the magnetizing fluxes. As the dc voltages vary between positive and negative values, it would indicate the bidirectional flow of current. When the dc voltage is positive, current is flowing into the dc capacitor at the output of the rectifier, however when the dc voltage is negative it would indicate the reverse flow of current in the converter. The values of the q and d-axis modulation signals chosen for operation would determine the nature of the dc voltage, for a fixed level of saturation and load on the system.

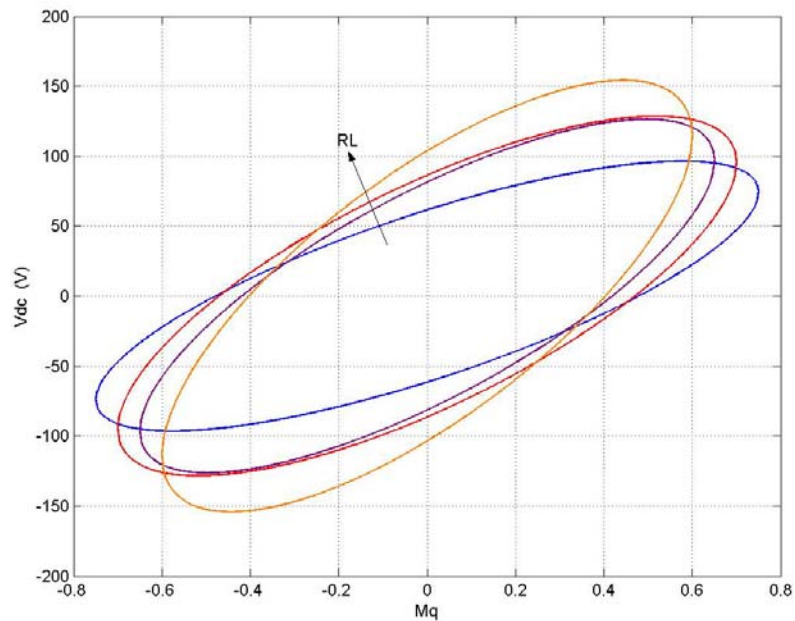


Figure 8.13: Variation of output dc voltage with the q-axis component of the modulation index for varying load resistances for first value of magnetizing flux

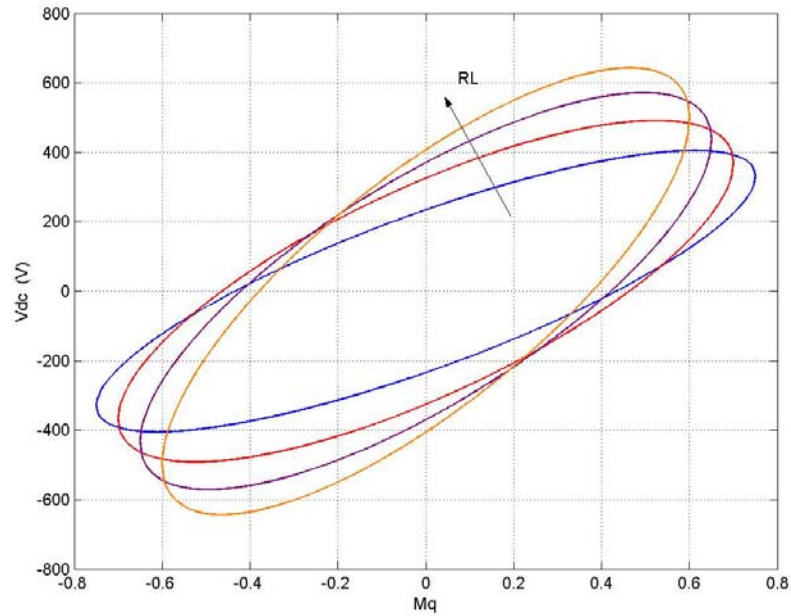


Figure 8.14: Variation of output dc voltage with the q-axis component of the modulation index for varying load resistances for second value of magnetizing flux

Figures 8.13 and 8.14 show the variation of the output voltage with the q-axis component of the modulation index.

Therefore the system under rated slip, at a fixed load resistance and magnetizing flux linkage, corresponds to a single operating point on the M vs. λ_m curve. Using the value of the modulation index required for excitation of the generator, the range of dc voltages that the system can operate with can be obtained.

Figures 8.15 and 8.16 illustrate the variation of the dc voltage with the d-axis component of the modulation index. The d-axis component of the modulation index is calculated using Equation (8.58).

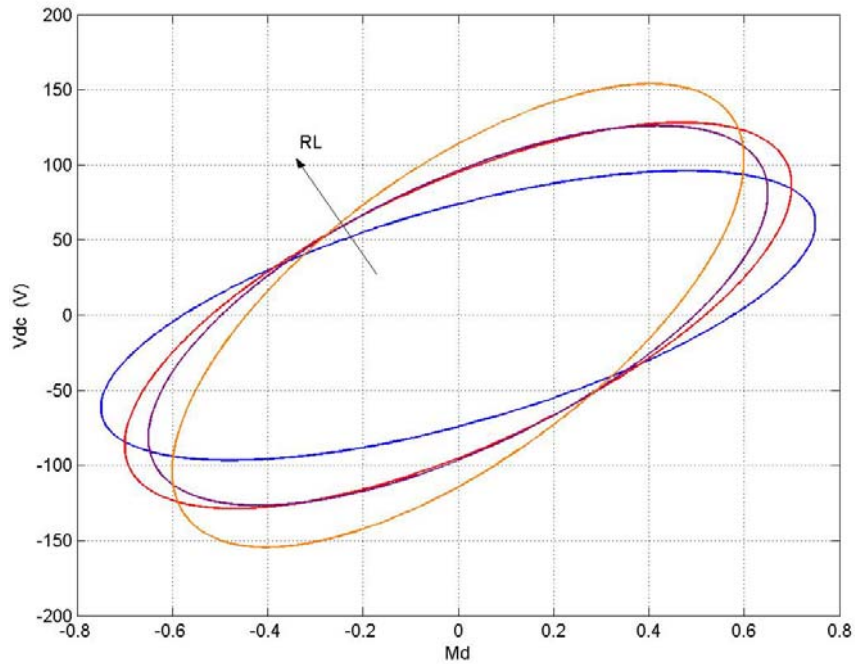


Figure 8.15: Variation of output dc voltage with the d-axis component of the modulation index for varying load resistances for first value of magnetizing flux

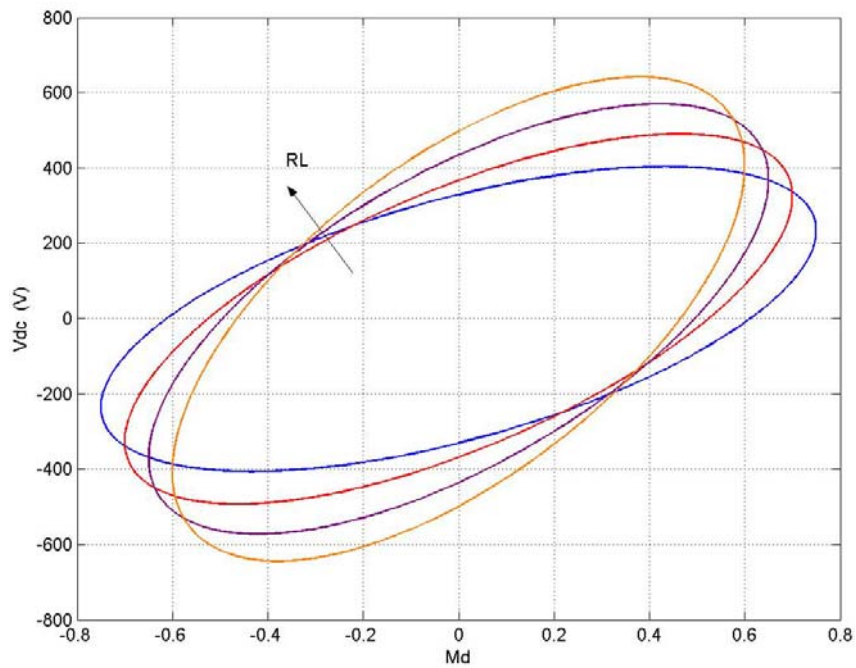


Figure 8.16: Variation of output dc voltage with the d-axis component of the modulation index for varying load resistances for second value of magnetizing flux

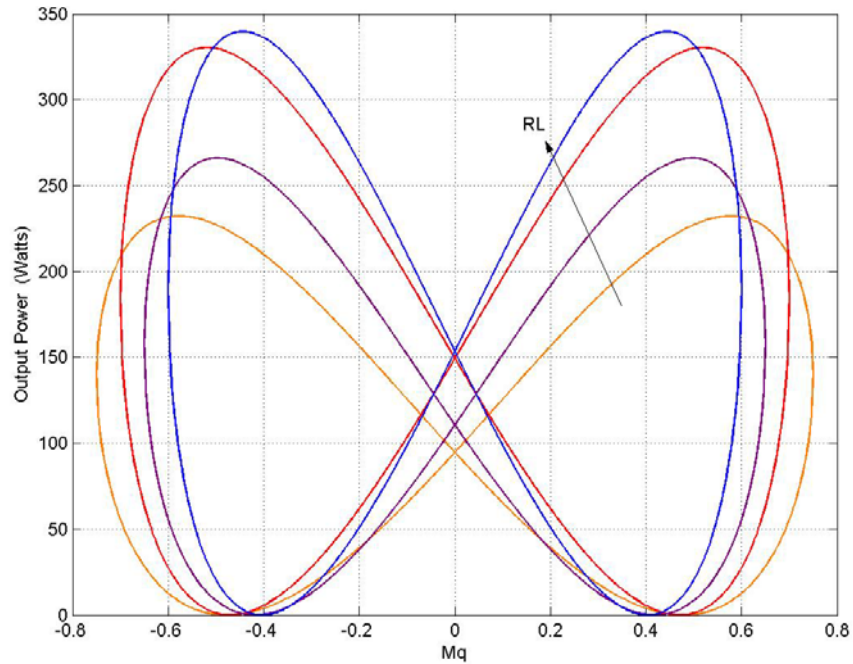


Figure 8.17: Variation of output power with the q-axis component of the modulation index for varying load resistances for the first value of magnetizing flux

The variation of the output power with the q-axis modulation signal is shown in Figure 8.17. The effect of changing load resistance is illustrated, and the plot obtained is based on the dc voltages calculated using the lower of the two values of the magnetizing fluxes for one value of the modulation index.

As can be seen from Figures 8.13 to 8.16, the nature of the variation of the dc voltage with the q-axis modulation signal is an ellipse. To further the analysis, the properties of an ellipse are applied to the analysis to obtain a simpler method of determination of the main characteristics of the dc voltage plot.

The standard equation of an ellipse is a second order equation given by Equation 8.59 as

$$A_1x^2 + B_1y^2 + C_1xy + D_1x + E_1y + F_1 = 0. \quad (8.59)$$

The equation can be further simplified assuming the major and minor axes of the ellipse parallel to the x and y-axes. Under such an assumption, the standard equation of the ellipse can be expressed as

$$\frac{x^2}{p^2} + \frac{y^2}{q^2} = 1. \quad (8.60)$$

2*p = length of major axis

2*q = length of minor axis

Expressing Equation (8.59) as (8.60) involves transformation of the x and y coordinates, which is dependent on the nature of Equation (8.59) for the system. For Equation 8.55, as can be seen in Figures 8.13 to 8.16, the major and minor axes of the ellipse are inclined at an angle α with respect to the x and y axes. Therefore the first step in expressing Equation 8.55 in the form of 8.60 is expressing the dc voltage in terms of the q-axis modulation index. This is obtained by eliminating the d-axis modulation index in the equation using Equation 8.58.

Simplifying Equation 8.55 results in Equation 8.61.

$$-\frac{2}{3R_L}V_{dc} = \frac{M_q(a \cdot b + L_r L_m L_{ls} \lambda_m \omega_s^2) + M_d(a L_m L_{ls} \omega_s + L_r \lambda_m \omega_s b)}{b^2 - L_m^2 L_{ls}^2 \omega_s^2} \quad (8.61)$$

$$a = L_r \lambda_m T_r - L_m \lambda_m B_r$$

$$b = L_m L_{ls} T_r - L_{ls} B_r$$

Equation 8.56 can be simplified as

$$M_d^2 = \frac{4k_3^2}{9R_L^2 k_2^2} V_{dc}^2 + \frac{k_1^2}{k_3^2} M_q^2 + \frac{4k_3 k_1}{3R_L k_2^2} M_q V_{dc} \quad (8.62)$$

$$k_1 = (a \cdot b + L_r L_m L_{ls} \lambda_m \omega_s^2)$$

$$k_2 = (aL_m L_{ls} \omega_s + L_r \lambda_m \omega_s b)$$

$$k_3 = b^2 - L_m^2 L_{ls}^2 \omega_s^2.$$

Substituting Equation 8.53, the dc voltage equation in 8.50 can be expressed in the form of a general equation for an ellipse as given in 8.54

$$AV_{dc}^2 + (B+1)M_q^2 + CM_q V_{dc} + M^2 = 0 \quad (8.63)$$

$$A = \frac{4k_3^2}{9R_L^2 k_2^2} \quad B = \frac{k_1^2}{k_3^2} \quad C = \frac{4k_3 k_1}{3R_L k_2^2}.$$

To obtain Equation 8.58 in the form of Equation 8.55, the x and y coordinates are transformed by an angle α so as to eliminate the 'xy' term in the equation. To obtain this, the angle is calculated using the following equation [A.11].

$$\tan \alpha = \frac{C}{A - B - 1} = a_1 \quad (8.64)$$

$$\cos \alpha = \sqrt{\frac{1 + \frac{1}{\sqrt{1 + a_1^2}}}{2}} = b_1 \quad (8.65)$$

$$\sin \alpha = \sqrt{\frac{1 - \frac{1}{\sqrt{1 + a_1^2}}}{2}} = c_1 \quad (8.66)$$

The relationship between the transformed coordinates and the x and y coordinates are given by Equations 8.67 and 8.68.

$$x = x_1 \cos \alpha - y_1 \sin \alpha \quad (8.67)$$

$$y = x_1 \sin \alpha + y_1 \cos \alpha \quad (8.68)$$

Using the above equations, 8.63 to 8.68, in Equation 8.58 where V_{dc} is the y coordinate and M_q is the x coordinate, the equation 8.55 can be represented in the standard form of equation of an ellipse.

$$M_{q1}^2 (Ab_1^2 + Bc_1^2 + c_1^2 + Cb_1c_1) + V_{dc1}^2 (Ac_1^2 + Bb_1^2 + b_1^2) + b_1c_1 - M^2 = 0 \quad (8.69)$$

$$\frac{M_{q1}^2}{\left(\frac{-b_1c_1 + M^2}{T}\right)} + \frac{V_{dc}^2}{\left(\frac{-b_1c_1 + M^2}{V}\right)} = 1 \quad (8.70)$$

$$T = (Ab_1^2 + Bc_1^2 + c_1^2 + Cb_1c_1)$$

$$V = (Ac_1^2 + Bb_1^2 + b_1^2).$$

Therefore, using Equation 8.70, the nature of the ellipse can be determined.

Comparing Equations 8.60 and 8.70, the major and minor axes lengths can be determined as

$$2p = 2\sqrt{\left(\frac{-b_1c_1 + M^2}{T}\right)} \quad (8.71)$$

$$2q = 2\sqrt{\left(\frac{-b_1c_1 + M^2}{V}\right)}. \quad (8.72)$$

The length of the major axis gives the peak value of the dc voltage that can be obtained for a fixed saturation level in the induction generator, and a fixed load resistance.

The eccentricity of the ellipse can be determined using Equation 8.70 as

$$\varepsilon = \frac{p^2 + q^2}{p}. \quad (8.73)$$

Therefore, using Equation 8.70, the peak value of the dc voltage and the point of intersection of the ellipse with the x and y axes can be determined by calculating the

major and minor axes lengths. This method of analysis can prove useful in determining the dc voltage for a given magnetizing flux and load resistance in the induction generator-rectifier system.

Figures 8.18 to 8.19 illustrate the possible values of V_{dc} that the system can achieve assuming different values of magnetizing fluxes. The major and minor axes lengths are determined from equations 8.71 and 8.72. The value of the magnetizing flux is varied between 0 and 0.6 Wb, and corresponding to three values of 'M', for a fixed load resistance and slip, $R_L = 40\Omega$ and $s = -0.06$ the major and minor axes lengths are obtained as shown in Figures 8.18 and 8.19.

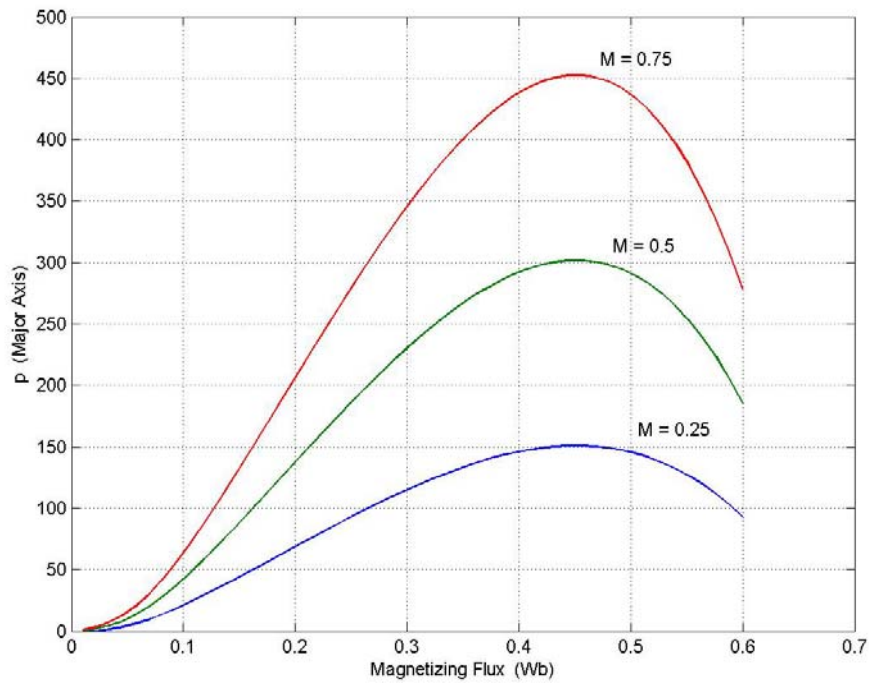


Figure 8.18: Variation of major axis length with the magnetizing flux for different values of 'M', for a fixed load resistance, rotor speed and slip

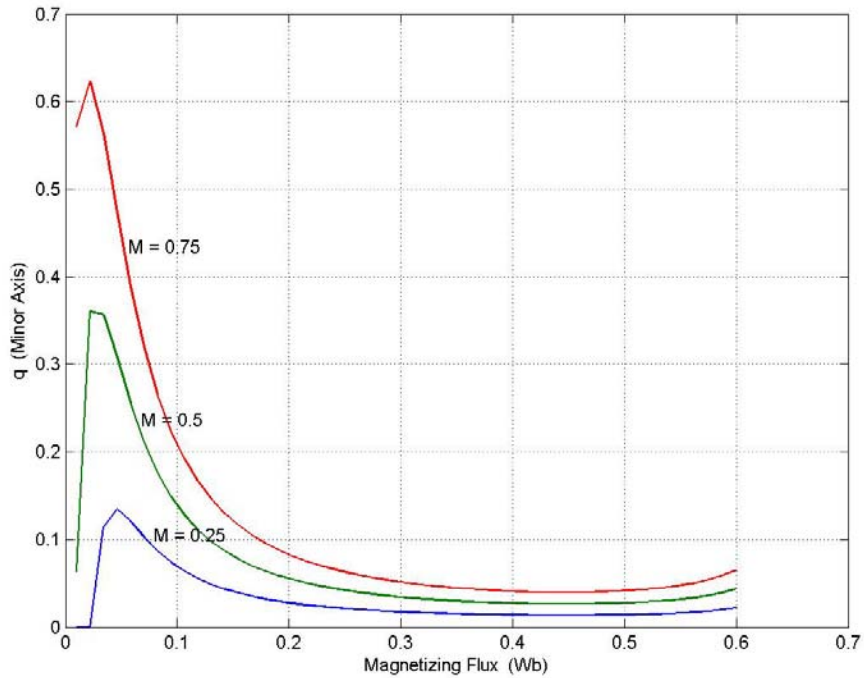


Figure 8.19: Variation of minor axis length with the magnetizing flux for different values of 'M', for a fixed load resistance, rotor speed and slip

The next section studies the nature of response of the system at steady state, considering the effect of saturation and also under a condition of minimum copper loss in the machine. The condition of minimum copper loss is obtained and the analysis is detailed for the desired condition of operation of the machine.

8.5 Analysis At Minimum Copper Loss

8.5.1 Condition of Minimum Copper Loss

The condition for minimum copper loss is obtained by minimizing the stator and rotor currents. This is achieved by first expressing the rotor currents in terms of the stator currents using the rotor voltage equations.

$$0 = r_r I_{qr} + p \lambda_{qr} + (\omega_e - \omega_r) \lambda_{dr} \quad (8.74)$$

$$0 = r_r I_{dr} + p \lambda_{dr} - (\omega_e - \omega_r) \lambda_{qr} \quad (8.75)$$

Using Equations (8.11) and (8.12),

$$\omega_s = s \omega_e = \frac{s}{1-s} \omega_r. \quad (8.76)$$

Substituting (8.76) in (8.74) and (8.75),

$$0 = r_r I_{qr} + p \lambda_{qr} + s \omega_e \lambda_{dr} \quad (8.77)$$

$$0 = r_r I_{dr} + p \lambda_{dr} - s \omega_e \lambda_{qr}. \quad (8.78)$$

The rotor fluxes are expressed in terms of the currents as

$$\lambda_{qr} = L_m I_{qs} + L_r I_{qr} \quad (8.79)$$

$$\lambda_{dr} = L_m I_{ds} + L_r I_{dr}. \quad (8.80)$$

Substituting Equations (8.79) and (8.80) in (8.77) and (8.78), and solving for the q and d-axis rotor currents in terms of the q and d-axis stator fluxes,

$$I_{qr} = \frac{s \omega_e L_m}{r_r^2 + (s \omega_e L_r)^2} (-r_r I_{ds} - s \omega_e L_r I_{qs}) \quad (8.80)$$

$$I_{dr} = \frac{s \omega_e L_m}{r_r^2 + (s \omega_e L_r)^2} (r_r I_{qs} - s \omega_e L_r I_{ds}). \quad (8.81)$$

The torque equation for the induction machine (from Chapter 5) expressed in terms of the stator and rotor currents is

$$T_e = \frac{3P}{4} (I_{qs} I_{dr} - I_{ds} I_{qr}). \quad (8.82)$$

Substituting Equations (8.80) and (8.81) in (8.82),

$$T_e = \frac{3P}{4} \frac{s \omega_e L_m^2 r_r}{r_r^2 + (s \omega_e L_r)^2} (I_{qs}^2 + I_{ds}^2). \quad (8.83)$$

The equations for the stator and rotor copper losses are given by (8.84) and (8.85)

$$P_{\text{stator_copper loss}} = \frac{3}{2} r_s (I_{qs}^2 + I_{ds}^2) \quad (8.84)$$

$$P_{\text{rotor_copper loss}} = \frac{3}{2} r_r (I_{qr}^2 + I_{dr}^2). \quad (8.85)$$

The total copper loss in the machine is the sum of the stator and rotor copper loss:

$$P_{\text{copper loss}} = \frac{3}{2} (r_s (I_{qs}^2 + I_{ds}^2) + r_r (I_{qr}^2 + I_{dr}^2)). \quad (8.86)$$

To minimize Equation (8.86), the expressions for the rotor currents in terms of the stator currents, Equations (8.80) and (8.81) are substituted in Equation (8.86) resulting in

$$P_{\text{copper loss}} = \frac{3}{2} \left(r_s (I_{qs}^2 + I_{ds}^2) + \frac{r_r (s\omega_e L_m)^2}{r_r^2 + (s\omega_e L_r)^2} (I_{qs}^2 + I_{ds}^2) \right). \quad (8.87)$$

Simplifying Equation (8.87)

$$P_{\text{copper loss}} = \frac{3}{2} \left(r_s + \frac{r_r (s\omega_e L_m)^2}{r_r^2 + (s\omega_e L_r)^2} \right) (I_{qs}^2 + I_{ds}^2). \quad (8.88)$$

Rearranging Equation (8.88)

$$T_e \times \frac{1}{\frac{3P}{4} \frac{s\omega_e L_m^2 r_r}{r_r^2 + (s\omega_e L_r)^2}} = (I_{qs}^2 + I_{ds}^2). \quad (8.89)$$

Eliminating ω_e in (8.89) and substituting Equation (8.89) in (8.87)

$$P_{\text{copper_loss}} = \frac{2}{P} \frac{T_e}{r_r L_m^2} \left[\frac{r_s r_r^2}{\omega_r} \cdot \frac{1-s}{s} + \frac{s}{1-s} \cdot (r_s \omega_r L_r^2 + r_r \omega_r L_m^2) \right]. \quad (8.90)$$

The copper loss is minimized when

$$\frac{r_s r_r^2}{\omega_r} \cdot \frac{1-s}{s} = \frac{s}{1-s} \cdot (r_s \omega_r L_r^2 + r_r \omega_r L_m^2). \quad (8.91)$$

Simplifying equation (8.91)

$$\left[\frac{\omega_r^2}{r_s r_r} (r_s L_r^2 + r_r L_m^2) - 1 \right] s^2 + 2s - 1 = 0. \quad (8.92)$$

Solving the above quadratic equation in terms of the slip

$$s = -\frac{1}{\sqrt{\frac{\omega_r^2}{r_s r_r} (r_s L_r^2 + r_r L_m^2) - 1}}. \quad (8.93)$$

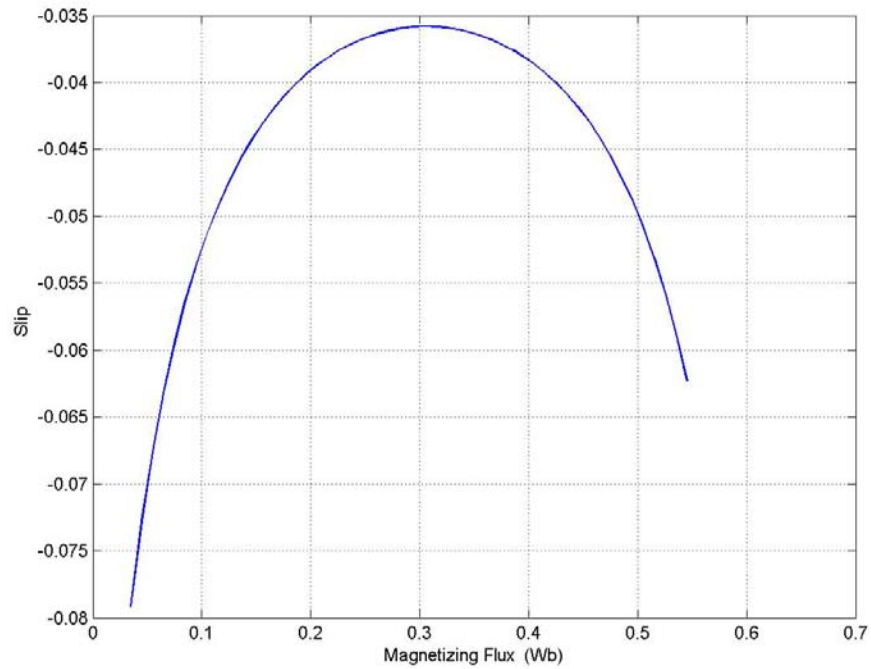


Figure 8.20: Variation of the slip with magnetizing flux linkage λ_m .

Therefore to operate the induction generator at minimum copper loss, the operating slip of the machine is calculated using equation (8.93).

From equation (8.93), it can be seen that the slip 's' is a function of the magnetizing inductance and therefore a function of the magnetizing flux linkage. Figure 8.20 illustrates the response of the slip to varying magnetizing flux linkage.

As the magnetizing flux is increased from 0 to 0.6 Wb, the slip (calculated under a condition of minimum copper loss) increases up to a point and then decreases, this is obtained for a fixed rotor speed ω_r , in this case the rotor speed $\omega_r = 200$ rad/sec. The nature of response of the slip to changing magnetizing flux linkage is similar to the response of the magnetizing inductance to varying magnetizing flux (Figure 8.1).

8.5.2 Influence of Magnetizing Flux ' λ_m ' on 'M' under Minimum Copper Loss

Just as in the case of the analysis in section 8.4.1, the influence of the magnetizing flux on the magnitude of the modulation index is studied in this section. However unlike in section 8.4.1, the generator is operated under a condition of minimum copper loss. This is included by using the slip equation (8.76) to calculate the operating slip of the machine, unlike the analysis in section 8.4.1 where the rated slip is used as the operating slip of the generator.

The method of determining the variation of the modulation index with the magnetizing flux is exactly the same as in section 8.4.1. The equation used to calculate the values of 'M' for varying values of the magnetizing flux is

$$|M|^2 = -\frac{2}{3R_L} \times \frac{1}{\text{Real} \left\{ \left[\frac{L_r}{D} - \frac{B_r L_m}{D(T_r + j\omega_s)} \right] \times \frac{1}{2 \left[(T_s - j\omega_e) - \frac{B_s B_r}{(T_r - j\omega_s)} \right]} \right\}}. \quad (8.94)$$

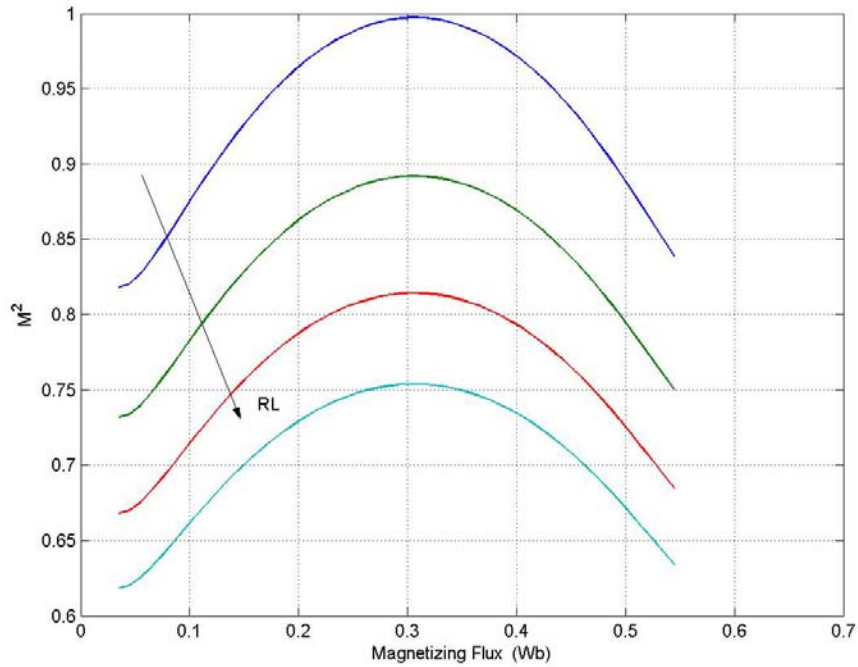


Figure 8.21: Variation of the magnitude of the modulation index with magnetizing flux linkage λ_m .

By varying the magnetizing flux, the slip as well as the modulation index needs to be calculated, i.e. for every value of magnetizing flux, the operating slip (under minimum copper loss) is calculated using Equation (8.93). Using the calculated operating slip, for a fixed load resistance, the modulation index is calculated using Equation (8.94). The parameters of the machine are the same as in Table 8.3.

Figure 8.21 is obtained for four different load resistance, $R_L = 40$ to 70Ω . The magnetizing flux linkage is varied between 0 and 0.6 Wb, and the corresponding values of the magnitude of the modulation index are calculated for a constant rotor speed of, $\omega_r = 200$ rad/sec.

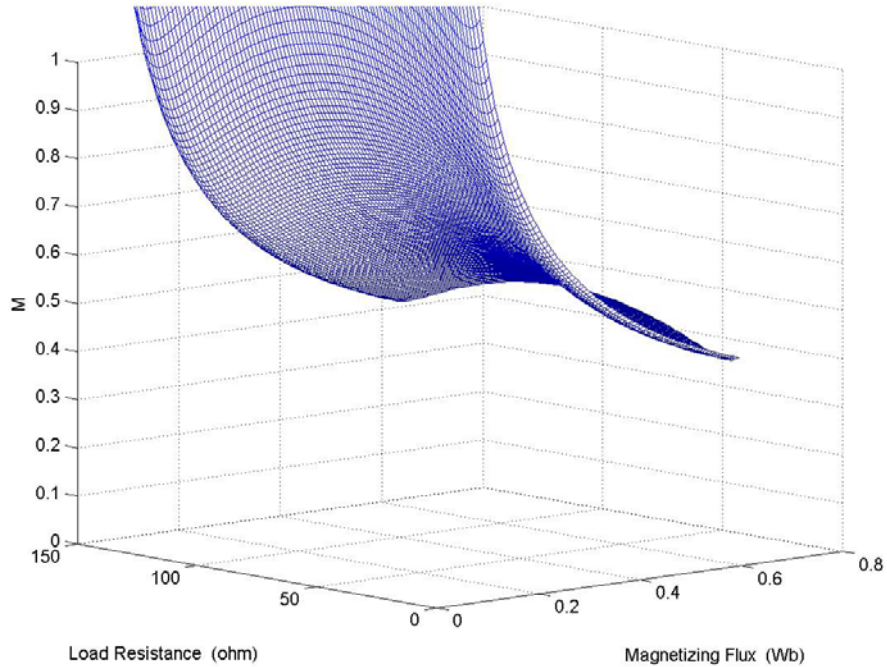


Figure 8.22: Variation of the magnitude of the modulation index with magnetizing flux linkage λ_m and load resistance R_L

The nature of the plot is different from the ‘M’ vs. λ_m plot obtained for the case assuming constant rotor slip (rated slip). In this case, the modulation index calculation is dependant on the slip calculated for minimum loss, hence the nature of variation of the modulation index follows the same pattern as the variation of the slip for minimum loss (Figure 8.20). The plot in Figure 8.21 is obtained as a three-dimensional plot, as shown in Figure 8.22 and as a contour plot shown in Figure 8.23.

The contour plot clearly illustrates the nature of variation of the modulation index with the varying magnetizing flux and load resistance.

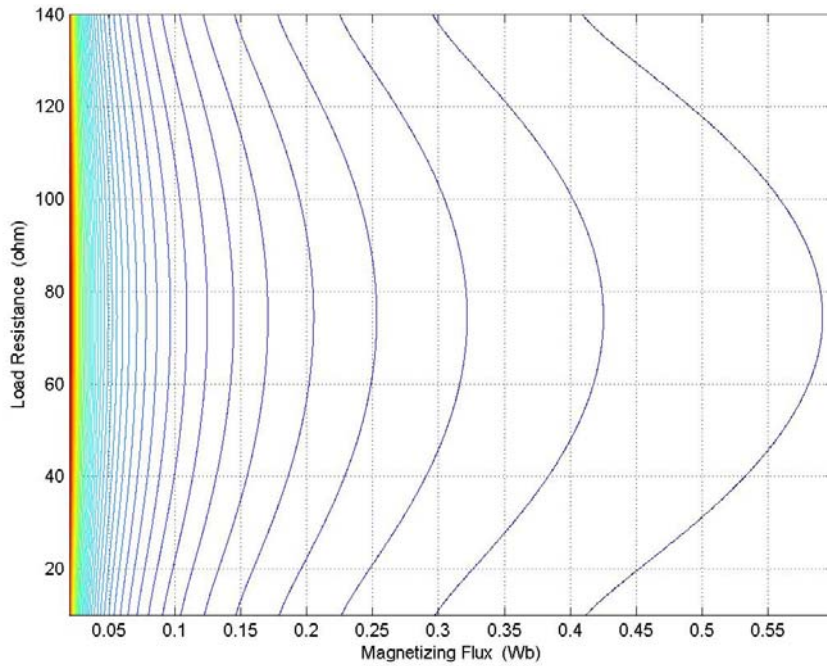


Figure 8.23: Variation of the magnitude of the modulation index with magnetizing flux linkage λ_m and load resistance R_L

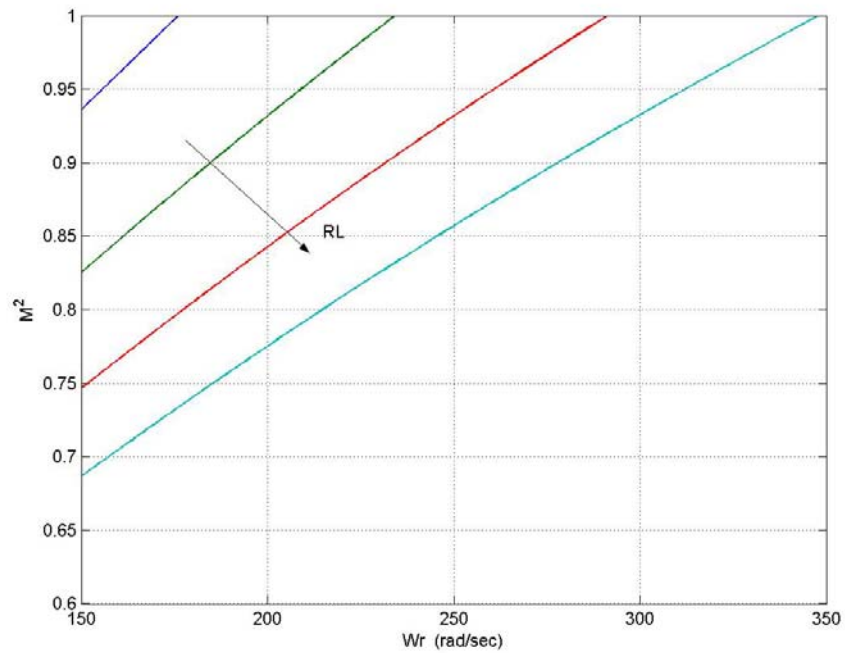


Figure 8.24: Variation of the magnitude of the modulation index with magnetizing flux linkage λ_m and load resistance R_L

In Figure 8.23 and 8.24, the load resistance is varied between 30 and 150Ω. The magnetizing flux λ_m is varied between 0 and 0.6 Wb.

The variation of the magnitude of the modulation index with the rotor speed is important, and therefore illustrated for the operation of the generator under minimum copper loss in Figures 8.24, 8.25 and 8.26. Figure 8.24 illustrates the variation under four different load conditions, and Figure 8.25 illustrates the variation of 'M' with the rotor speed for a larger range of load resistances (10 Ω to 80Ω) as a three-dimensional plot. A contour plot of the same is shown in Figure 8.26.

In Figure 8.25 and 8.26, the load resistances used are $R_L = 35\Omega, 45\Omega, 55\Omega,$ and 65Ω . The rotor speed is varied between 150 and 350 rad/sec.

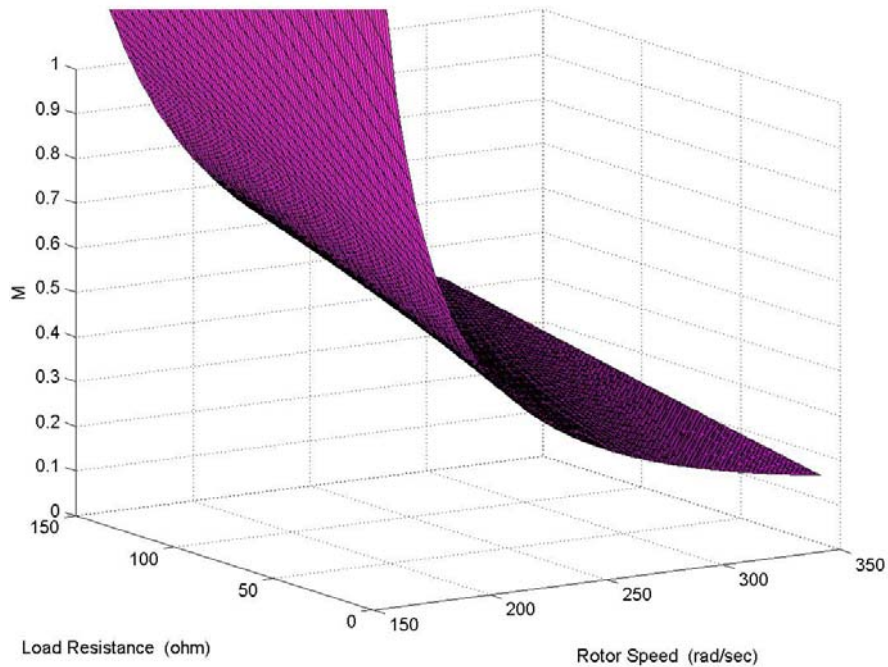


Figure 8.25: Variation of the magnitude of the modulation index with magnetizing flux linkage λ_m and load resistance R_L

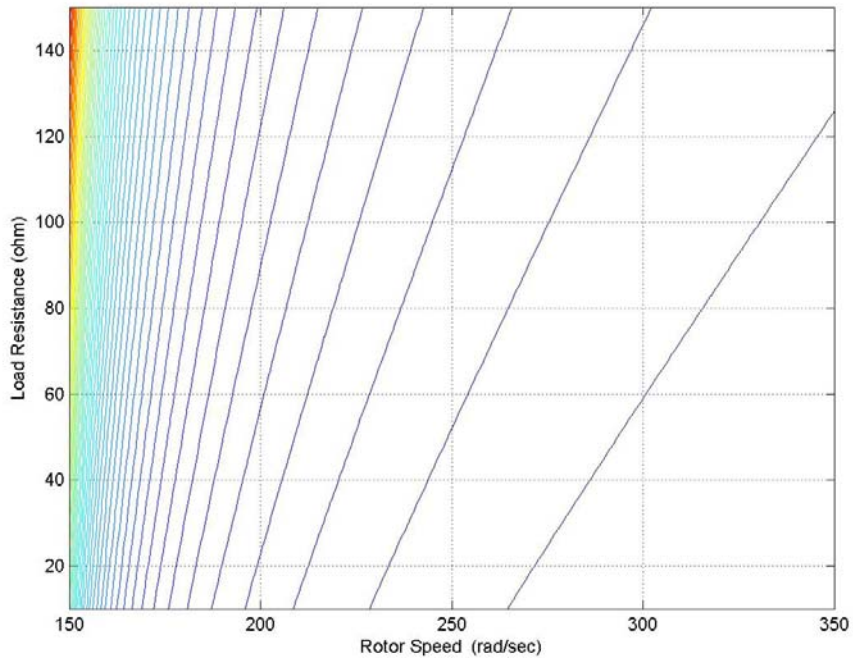


Figure 8.26: Variation of the magnitude of the modulation index with magnetizing flux linkage λ_m and load resistance R_L

As seen from Figure 8.24, for a fixed load resistance, an increase in rotor speed requires a larger modulation index. Also a decrease in the load resistance decreases the value of modulation index required, for the same rotor speed.

The parameter used as a measure of the load resistance that the system can handle is plotted as a function of the magnetizing flux and the operating slip. The ability for the system to be loaded is studied by varying the operating slip between a chosen range of values. However considering the system to be operating under minimum copper loss, the operating slip is calculated for each value of magnetizing flux, hence the nature of response of R_o is influenced by the slip calculation.

The variation of R_o with the magnetizing flux, using the slip calculated by Equation 8.76 is shown in Figure 8.27.

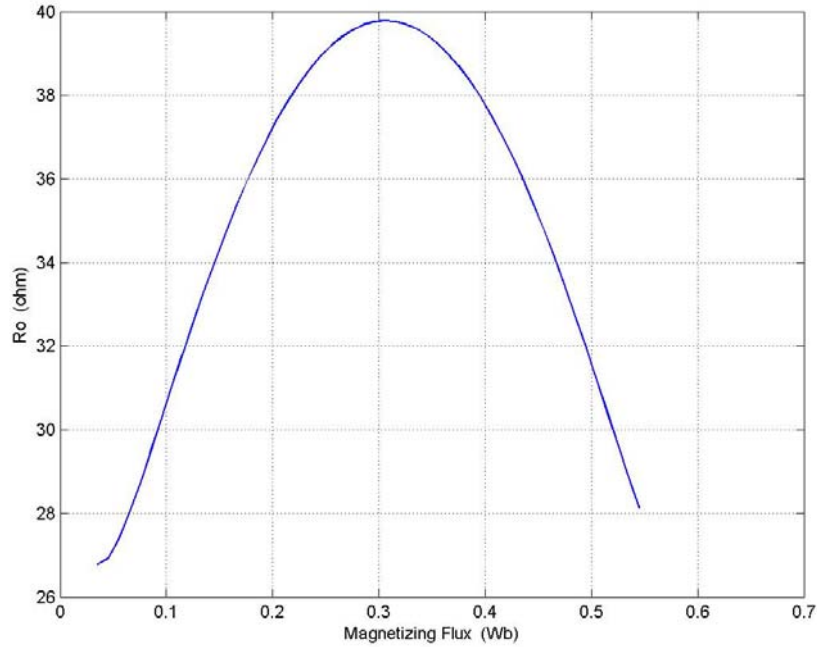


Figure 8.27: Variation of the magnitude of the modulation index with magnetizing flux linkage λ_m and load resistance R_L

8.5.3 Influence of λ_m on Output DC voltage

For a fixed value of magnetizing inductance, under minimum copper loss operation, the magnitude of the modulation index is fixed and corresponds to one point on the M vs λ_m curve. For each value of the modulation index, there is a range of values of the dc voltage at which the system can operate. From Figure 8.15, also there are two values of magnetizing flux that can be satisfying the same value of the modulation index (discussed in section 8.4). The dc voltage plots are obtained for each value of the magnetizing flux as shown in Figure 8.28. Considering four different operating

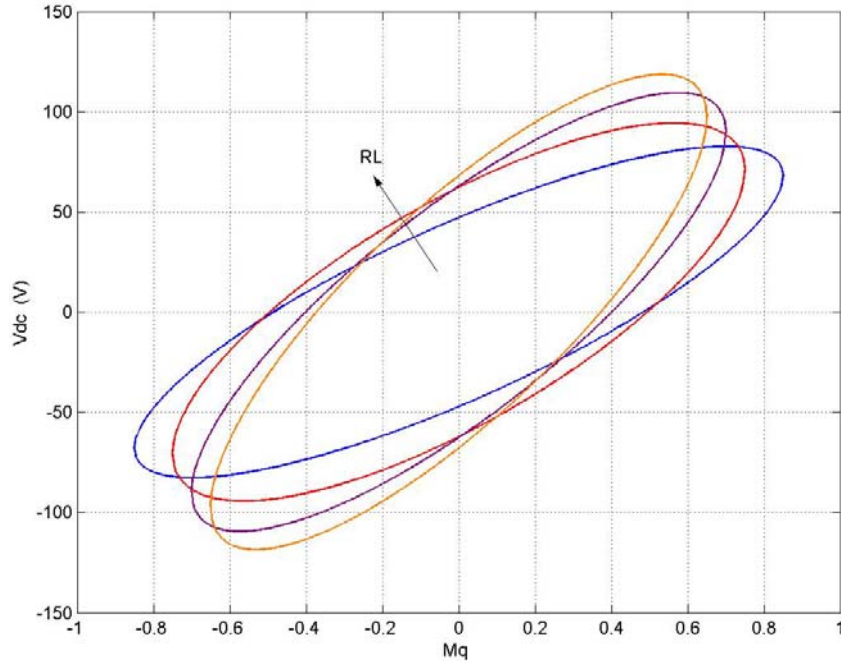


Figure 8.28: Variation of output dc voltage with the q-axis component of the modulation index for varying load conditions for the λ_{m1}

conditions and the corresponding operating points from Figure 8.21 shows the effect of the change in load resistance.

λ_{m1} is the first (smaller), and λ_{m2} is the second (larger) value of the flux linkage that satisfies the chosen value of the modulation index.

The load resistance in Figures 8.28 to 8.31 has been varied between $R_L = 40\Omega$, 50Ω , 60Ω , and 70Ω . The range of dc voltages obtained when λ_{m2} is considered, are very high and not possible practically as the machine parameters used are for a 2 hp induction machine. Therefore the set of voltages considered are the dc voltages calculated using the smaller value of the magnetizing flux λ_{m1} .

The variation of the dc voltage with the d-axis modulation signal is shown in Figures 8.30 and 8.31. The nature of variation is the same as with the q-axis modulation index.

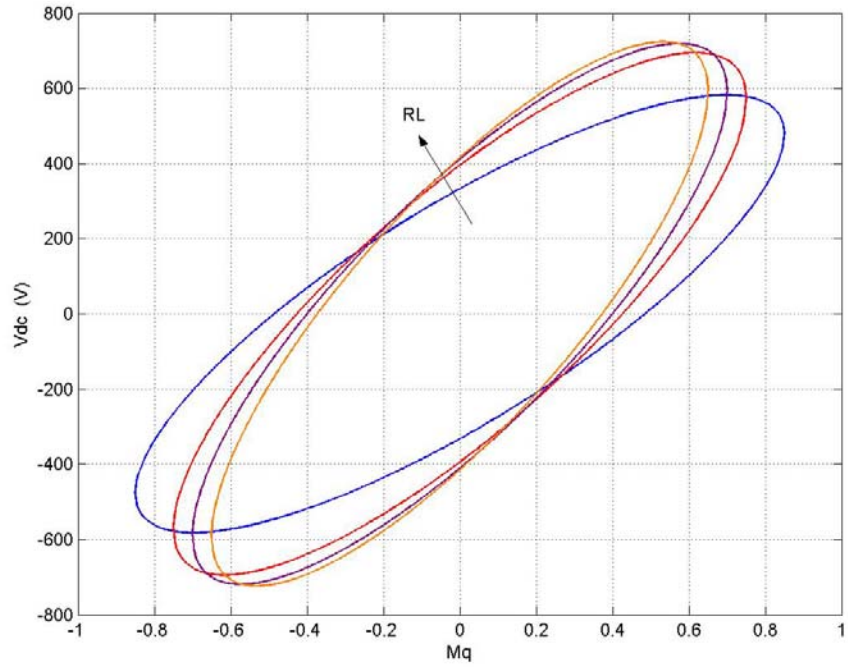


Figure 8.29: Variation of output dc voltage with the q-axis component of the modulation index for varying load conditions for the λ_{m2}

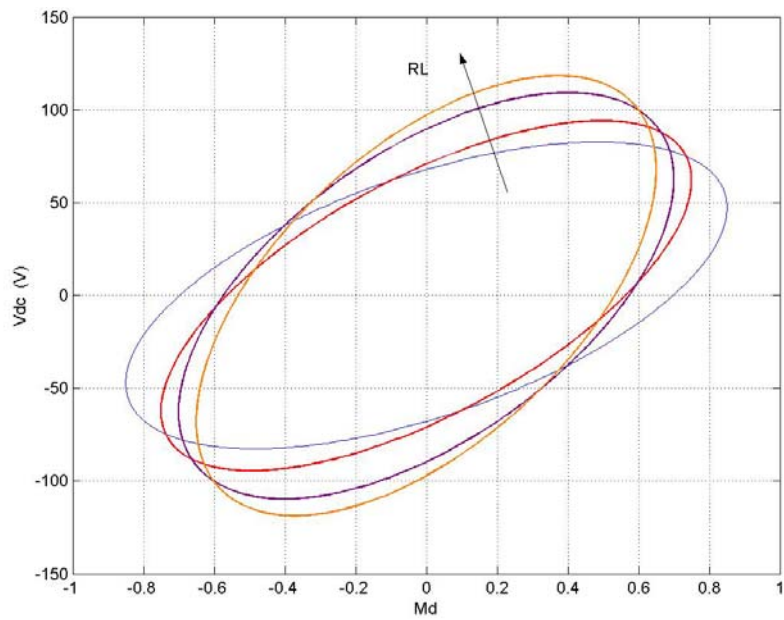


Figure 8.30: Variation of output dc voltage with the d-axis component of the modulation index for varying load conditions for the λ_{m1}

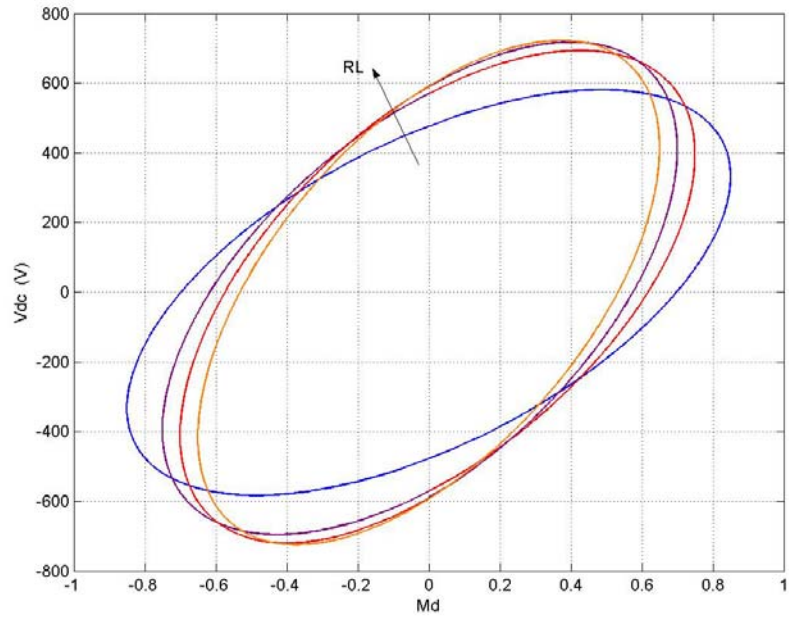


Figure 8.31: Variation of output dc voltage with the d-axis component of the modulation index for varying load conditions for the λ_{m2}

The output power of the rectifier is calculated for the set of dc voltages obtained for λ_{m1} . The nature of variation of the output power with the q-axis modulation signal is illustrated in Figure 8.32. In this case, the y-axis divides the plot symmetrically.

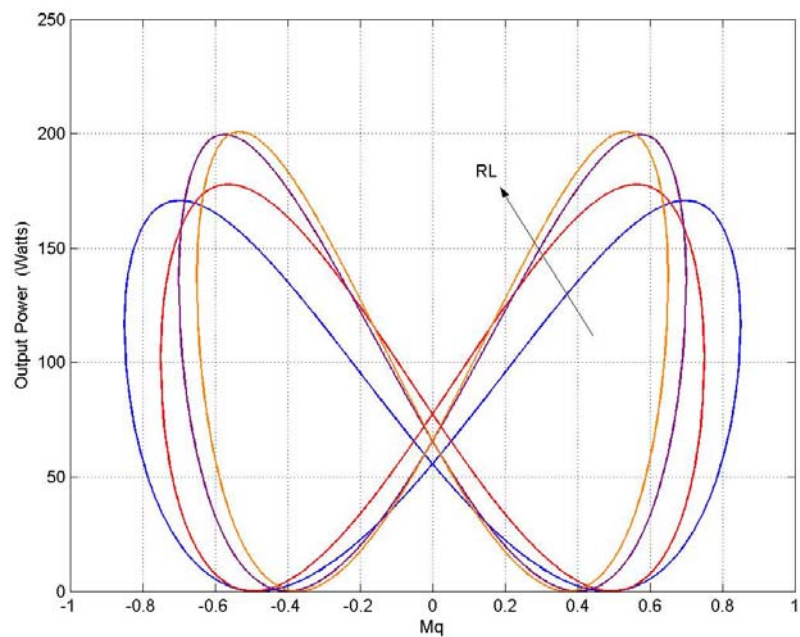


Figure 8.32: Variation of output power with the q-axis component of the modulation index for varying load conditions for the λ_{m1}

The nature of the dc voltage contour is the same as described in section 8.4.2. Therefore applying the same analysis, the major and minor axes of the dc voltage ellipse can be determined from Equations 8.71 and 8.72. In this case as well, the magnetizing flux is varied between 0 and 0.6 Wb. The modulation indexes used in the calculations are 0.25, 0.5, and 0.75. The load resistance is kept constant at 40Ω and the slip is calculated using the minimum loss condition.

Figure 8.33 illustrates the variation of the major axis length with magnetizing flux, and Figure 8.34 shows the variation of the minor axis length with the magnetizing flux.

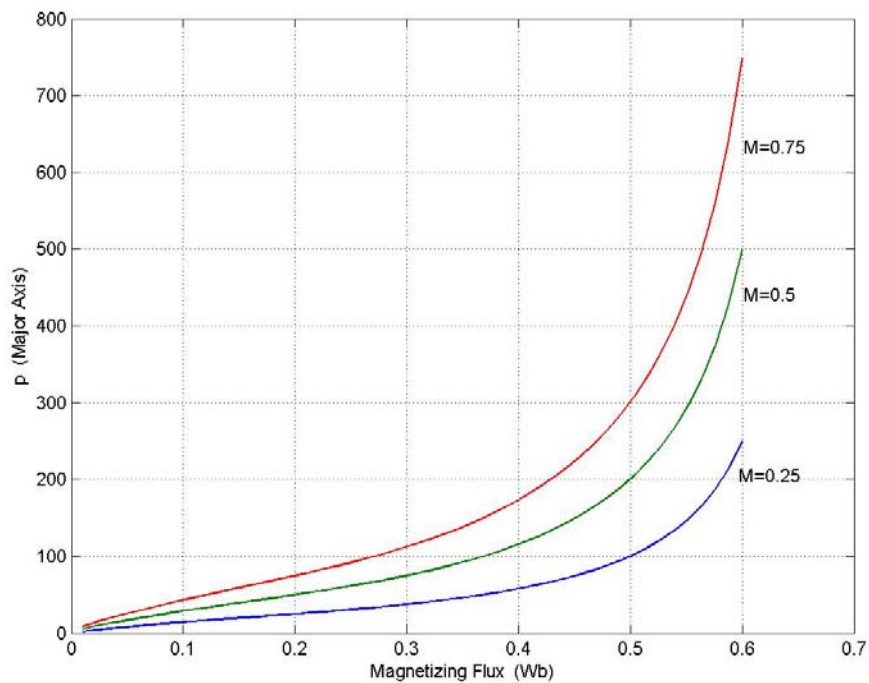


Figure 8.33: Variation of major axis length with the magnetizing flux for different values of 'M', for a fixed load resistance, rotor speed

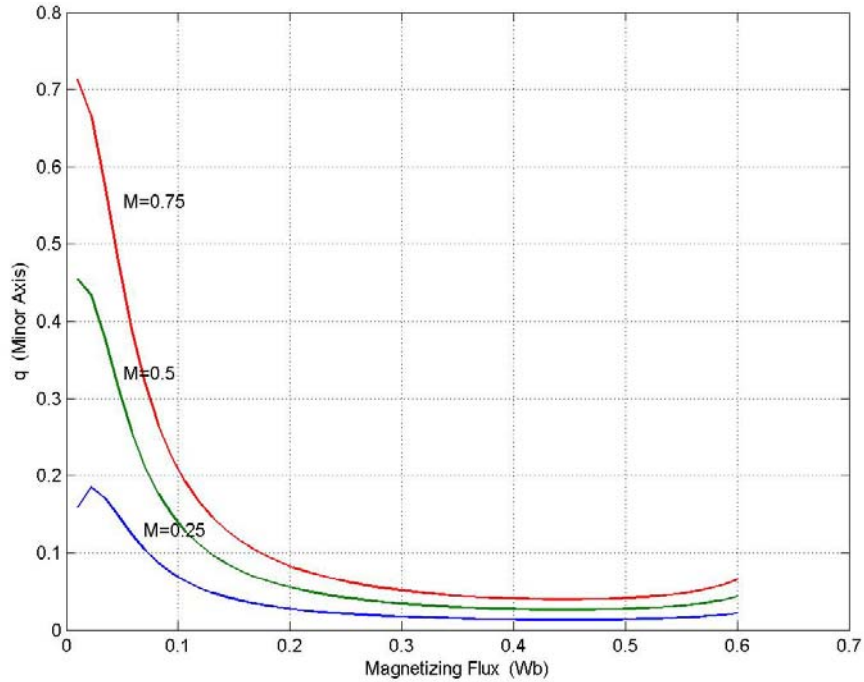


Figure 8.34: Variation of minor axis length with the magnetizing flux for different values of 'M', for a fixed load resistance, rotor speed

This chapter discusses in detail the effect of saturation on the self-excitation requirements of the induction generator. The system is studied under two conditions:

- Rated slip.
- Slip calculated under a condition of minimum copper loss in the machine

The detailed discussion develops the range of dc voltages that the system can operate at for a chosen magnetizing flux linkage value.

CHAPTER 9

ROTOR FLUX VECTOR CONTROL OF THREE-PHASE INDUCTION GENERATOR-RECTIFIER SYSTEM

9.1 Introduction

The use of induction generators has been gaining importance since the increase in the use of unconventional energy sources, such as wind and small hydro because of the inherent advantages of the machine such as low maintenance and brushless construction.

The control of an induction machine can be achieved broadly using two methods:

Scalar control

Vector control.

The scalar control of an induction machine is achieved by control of the magnitude of the control variables. However, this control method assumes no coupling effect in the machine.

Vector control of an induction machine can be carried out using either direct or indirect vector control methods, both of which are explained later in this chapter.

This chapter lays out the vector control of an induction motor and applies the scheme to an induction generator, as the model of the motor and the generator are the same, except for the current directions.

The proposed control scheme for the generator-rectifier system is put forth with a detailed derivation of the parameters of the controllers. The system is simulated under two conditions and the simulation results presented.

9.2 Vector Control of an Induction Machine

In general, an electric motor can be thought of as a controlled source of torque.

Independent control of the torque is achievable by control of the armature and field currents. In a separately excited DC machine, the armature and field currents can be controlled independently (as the currents are naturally decoupled). In the control of a dc machine, only the magnitude of the currents needs to be controlled in order to control the output torque and field flux independently, which is simple when compared to the control required for ac machines.

The separately excited dc motor can be represented by block diagram, Figure 9.1

The electromagnetic interaction between the field flux and the armature MMF results in two basic outputs:

An induced voltage proportional to the rotor speed.

An electromagnetic torque proportional to the armature current.

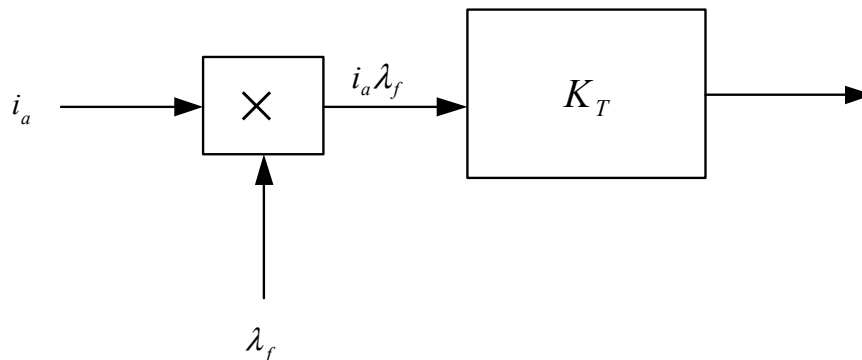


Figure 9.1: Block diagram representation of a separately excited dc motor.

In ac induction motor drives, a coordinated control of the stator current, magnitudes, frequencies, and phasors is required, hence the control is complex.

Also in an induction machine, there is inherent coupling between the flux and torque. This is because the flux and torque are functions of the voltage or currents and frequency. Therefore, the method of control of an induction machine is more complex.

9.3 Principle of Vector Control

The principle of vector control can be explained by assuming that at all instants of time, the position of the rotor flux linkage phasor is known. The rotor flux is defined as λ_r , and the angle is defined as θ_f (field angle). The position is defined from a stationary reference.

The principle of vector control of an induction machine aims at developing a model of the machine that is similar to a dc machine so as to simplify the control. As explained in the previous section, the control of a dc machine is simple as the two currents (armature and field) are independent, hence allowing for independent control of the field flux and the torque (or power in the case if a generator).

To simplify the model of an induction machine, the components of the stator current that produce the torque and field flux (rotor flux) need to be decoupled. This is achieved as explained below.

The q and d-axis currents of an induction machine, as shown in the equivalent circuit, Figure 9.2 are obtained using Equation (9.1)

$$\begin{bmatrix} I_{qs} \\ I_{ds} \end{bmatrix} = \frac{2}{3} \begin{bmatrix} \cos(\theta_f) & \cos\left(\theta_f - \frac{2\pi}{3}\right) & \cos\left(\theta_f + \frac{2\pi}{3}\right) \\ \sin(\theta_f) & \sin\left(\theta_f - \frac{2\pi}{3}\right) & \sin\left(\theta_f + \frac{2\pi}{3}\right) \end{bmatrix} \begin{bmatrix} I_a \\ I_b \\ I_c \end{bmatrix} \quad (9.1)$$

The stator current phasor can be expressed in terms of the q and d-axis currents.

The magnitude and phase angle of the stator current phasor are expressed in Equations (9.2) and (9.3).

$$I_s = \sqrt{(I_{qs})^2 + (I_{ds})^2} \quad (9.2)$$

$$\theta = \tan^{-1}\left(\frac{I_{qs}}{I_{ds}}\right) \quad (9.3)$$

The q and d-axis components of the stator currents are obtained by projecting the stator current on the q and d-axis, respectively.

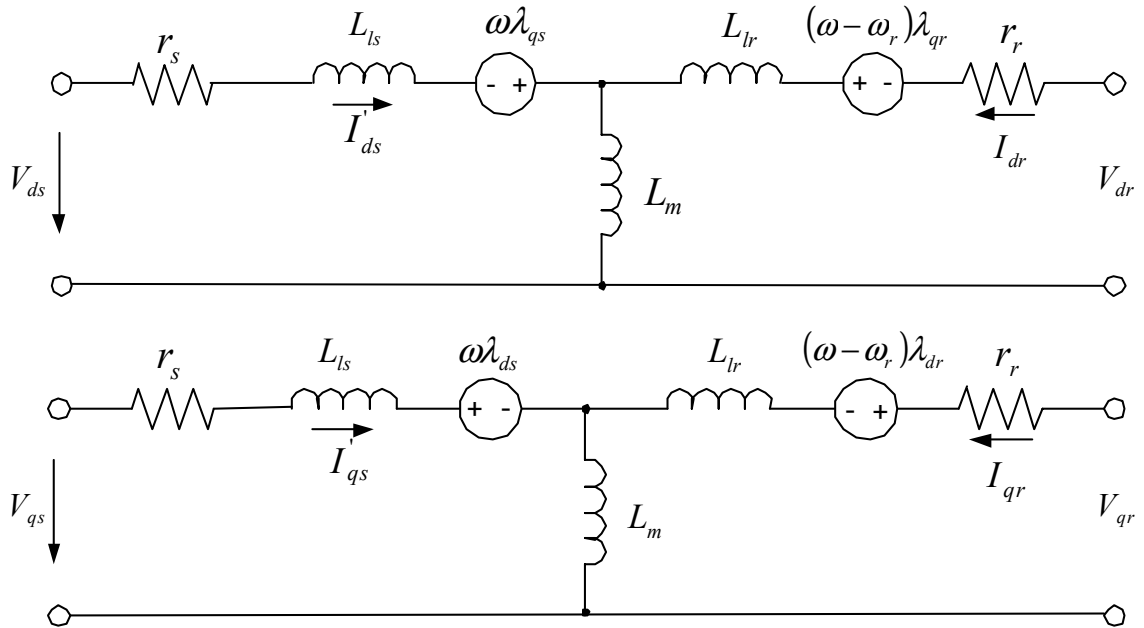


Figure 9.2: Equivalent circuit model of induction machine in the synchronous reference frame. (a) d-axis (b) q-axis

The stator current I_s produces both the rotor flux as well as the torque. The method used in implementing field control of an induction machine is resolving the stator current along the rotor flux vector, hence this component of the current, I_f would be the field producing current. The perpendicular component of the current is the torque producing component I_T .

The phasor representation of the stator currents (q and d-axis components) along with the flux alignment is illustrated in Figure 9.3.

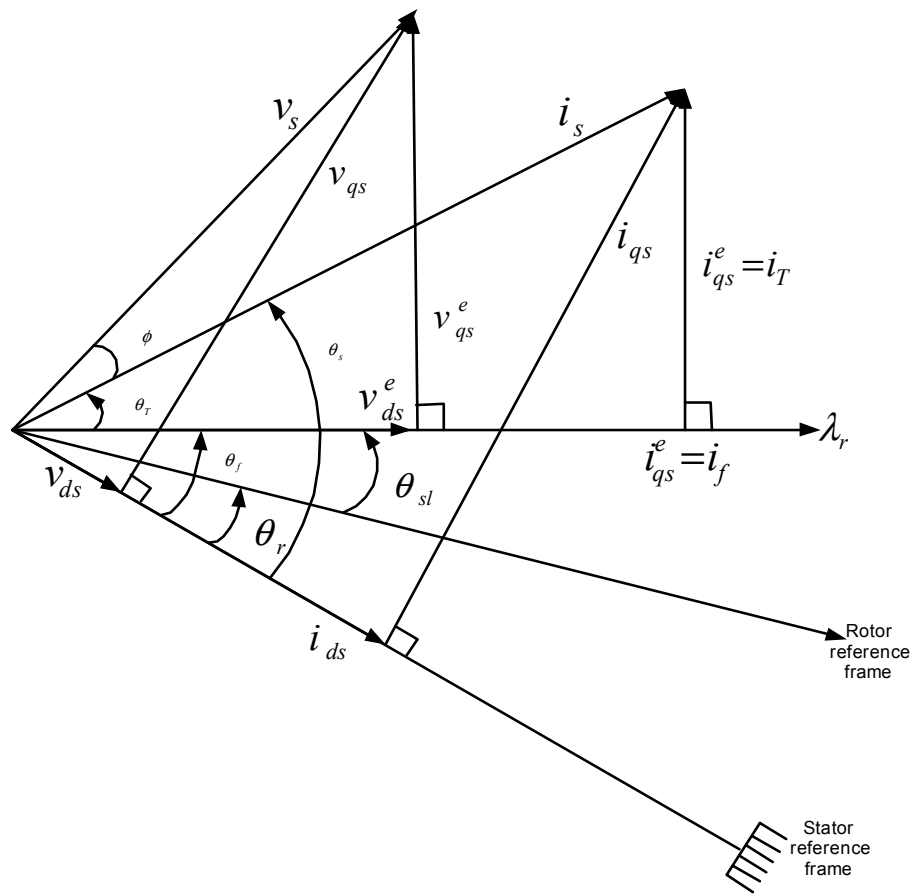


Figure 9.3: Phasor representation of the stator currents and flux alignment

The two components of the current I_f and I_T are dc quantities at steady state as the relative speed with respect to the rotor field is zero. The rotor flux linkage has a speed equal to the sum of the rotor and slip speeds as defined in Equation 9.3, and is equal to the synchronous speed. Therefore orientation of λ_r amounts to considering the synchronous reference frames and hence the current and torque producing components of the currents are dc quantities. Obtaining the instantaneous position of the rotor flux phasor. The field angle can be calculated using Equation 9.4.

$$\theta_f = \int (\omega_r + \omega_{sl}) dt$$

ω_r = rotor speed

ω_{sl} = slip frequency

Vector control of induction machines can be subdivided into two categories as

Direct field orientation

Indirect field orientation.

In direct field orientation, the rotor flux position is electrically determined by measuring the flux using Hall effect sensors, and in. Indirect schemes measure the rotor position and utilize the slip relation to compute the angle of the rotor flux relative to the rotor.

9.4 Vector Control of an Induction Generator

The control of an induction generator is implemented by applying the same technique used in the control of induction motors, as explained in the previous section.

Analogous to the DC motor, in the DC generator the main flux (due to the field current) and the load current can be controlled independently. The generated voltage in a DC generator is given by

$$E_a = k\phi\omega_a \quad (9.2)$$

E_a = armature generated voltage

k = dependant on the armature winding

ϕ = flux per pole

ω_a = angular speed of the armature.

In the DC generator, an increase in the load increases the armature current without affecting the field current. The schematic for a dc generator is given in Figure 9.4. In an induction generator, the two components of the current control the power and flux, respectively. Field orientation control schemes in induction generators decouple the equations so as to obtain a form of the induction generator that can be treated as a DC generator.

There are three different types of field-oriented control schemes that can be applied to induction generators:

Rotor flux oriented

Stator flux oriented

Magnetizing flux oriented.

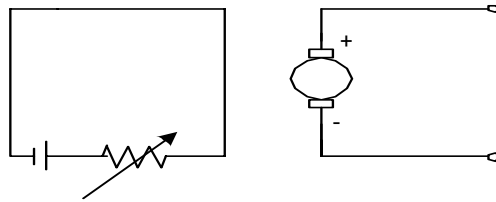


Figure 9.4: Schematic of a separately excited dc generator.

The control scheme implemented in this chapter employs rotor flux orientation.

The method of field orientation applied in this chapter is indirect field orientation (rotor field orientation).

For an induction machine, indirect vector control is implemented using the model equations of the induction machine.

$$V_{qs} = r_s I_{qs} + p\lambda_{qs} + \omega_e \lambda_{ds} \quad (9.3)$$

$$V_{ds} = r_s I_{ds} + p\lambda_{ds} - \omega_e \lambda_{qs} \quad (9.4)$$

$$0 = r_r I_{qr} + p\lambda_{qr} + (\omega_e - \omega_r) \lambda_{dr} \quad (9.5)$$

$$0 = r_r I_{dr} + p\lambda_{dr} - (\omega_e - \omega_r) \lambda_{qr} \quad (9.6)$$

To achieve field orientation, the resultant rotor flux linkage is aligned with the d-axis to assume field orientation. Therefore the resultant flux linkage is equal to the d-axis rotor flux and the q-axis rotor flux is equal to zero, and the d-axis rotor flux is equal to the resultant rotor flux λ_r i.e.

$$\begin{aligned} \lambda_{qr} &= 0 \\ \lambda_{dr} &= \lambda_r . \end{aligned} \quad (9.7)$$

Substituting the above conditions in the rotor voltage Equations (9.5) and (9.6), the equations can be expressed as

$$0 = r_r I_{qr} + (\omega_e - \omega_r) \lambda_r \quad (9.8)$$

$$0 = r_r I_{dr} + p\lambda_{dr} . \quad (9.9)$$

The field orientation in the dq variables can be represented as a phasor diagram, Figure 9.5.

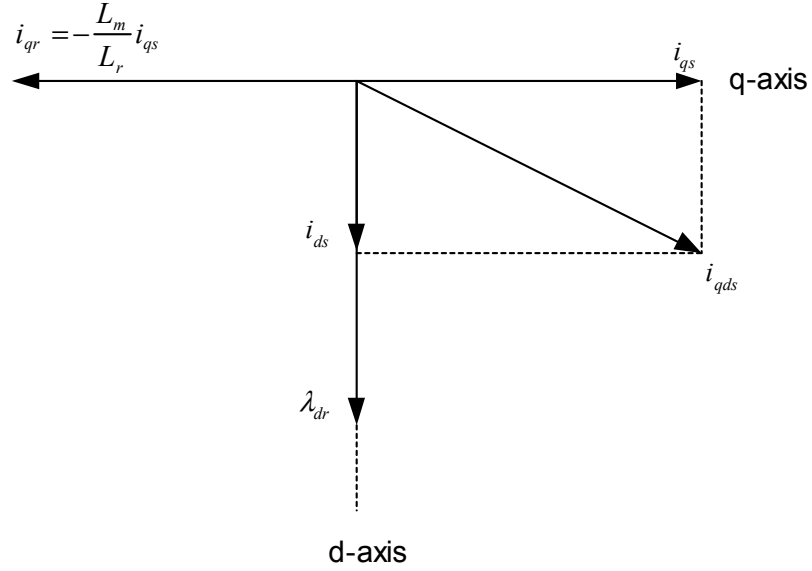


Figure 9.5: Field orientation of the Orientation of rotor flux on d-axis

The model developed for the induction generator implementing the field orientation explained above is presented.

The q-axis rotor flux λ_{qr} can be expressed in terms of the stator and rotor q-axis currents as

$$\lambda_{qr} = L_m I_{qs} + L_r I_{qr} . \quad (9.10)$$

Substituting the above conditions, Equation (9.7) in (9.8), the q-axis rotor current can be expressed in terms of the q-axis stator current as

$$I_{qr} = \frac{-L_m}{L_r} I_{qs} . \quad (9.11)$$

Similarly, the d-axis rotor current can be expressed in terms of the d-axis stator current and the rotor flux λ_r .

$$\lambda_{dr} = L_m I_{ds} + L_r I_{dr} \quad (9.12)$$

$$\lambda_r = L_m I_{ds} + L_r I_{dr}$$

Therefore,

$$I_{dr} = \lambda_r - \frac{L_m}{L_r} I_{ds} \quad (9.13)$$

Substituting for the q and d-axis rotor currents in Equations (9.7) and (9.8), respectively, resulting in the following equations:

$$I_{ds} = \frac{1}{L_m} (1 + \tau_r) \lambda_{dr} \quad (9.14)$$

$$\tau_r = \frac{L_r}{r_r}. \quad (9.15)$$

The slip can be calculated by substituting Equation (9.11) in (9.8)

$$(\omega_e - \omega_r) = \omega_s = \frac{L_m}{T_r} \cdot \frac{I_{qs}}{\lambda_r}. \quad (9.16)$$

Equation (9.12) has the same form as the field equation for a separately excited dc machine.

The final step in the transformation of an induction machine to the model of a separately excited dc machine is obtained by the torque equation.

The torque equation for an induction machine is

$$T_e = \frac{3P}{4} (i_{qs} \lambda_{dr} - i_{ds} \lambda_{qr}). \quad (9.17)$$

Substituting equation (9.7) in (9.17)

$$T_e = \frac{3P}{4} (i_{qs} \lambda_r). \quad (9.18)$$

Therefore, from Equation (9.18) it is can be seen that the torque is a function of the product of the rotor flux and torque producing current, I_{qs} .

9.5 Controller Design for an Induction Generator-Rectifier System

The control of the dc voltage is achieved by modeling the system using the technique of input-output linearization [A.4]. The model of the induction generator as derived is non-linear.

The method of linearization used in the design of the control scheme is “Feedback linearization,” which is a method of exact linearization of the system model using the following method.

A nonlinear compensation, which cancels the nonlinearities included in the system, is implemented as an inner feedback loop.

A controller, which ensures stability and some predefined performance, is designed based in the conventional theory;

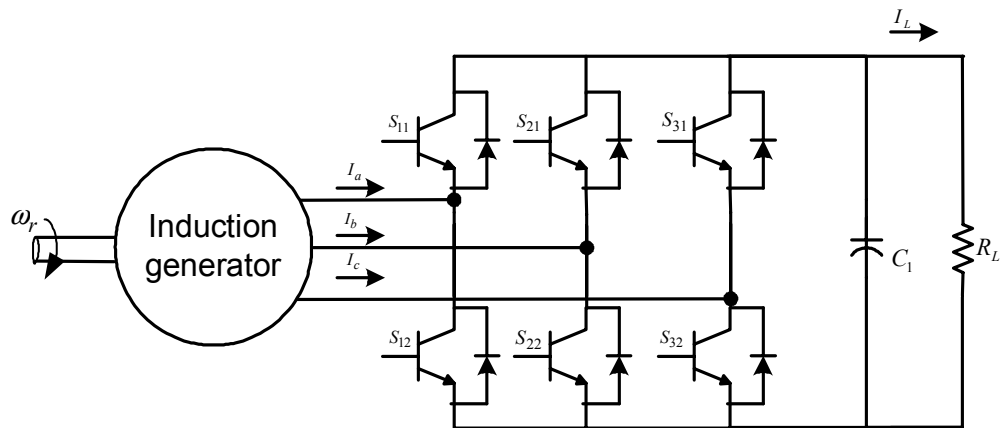


Figure 9.6: Generator system

this linear controller is implemented as an outer feedback loop. For example, consider the third order system

$$px_1 = \sin(x_2) + (x_2 + 1)x_3 \quad (9.19)$$

where p is the differential operator $p = \frac{d}{dt}$.

$$px_2 = x_1^5 + x_3 \quad (9.20)$$

$$px_3 = x_1^2 + u \quad (9.21)$$

$$y = x_1 \quad (9.22)$$

To generate a direct relationship between the output y and the input u , Equation (9.20) is differentiated, yielding

$$py = px_1. \quad (9.23)$$

Therefore, from Equations (9.19) and (9.22)

$$py = px_1 = \sin(x_2) + (x_2 + 1)x_3. \quad (9.24)$$

As the output y is not directly related to the input 'u', the process of differentiation is carried out again.

$$p^2 y = (x_2 + 1)u + f(x_1, x_2, x_3) \quad (9.25)$$

$$\text{where } f(x_1, x_2, x_3) = (x_1^5 + x_3)(\cos x_2 + x_3) + (x_2 + 1)x_1^2. \quad (9.26)$$

There now exists an explicit relation between the input and output. If the control input is chosen to be of the form

$$u = \frac{1}{x_2 + 1}(v - f_1) \quad (9.27)$$

where v is a new input to be determined, the nonlinearity in the above equation is canceled and a simple linear double integration relationship between the input and output and ‘ v ’ is obtained.

The design of an ac controller for this double-integrator relationship is simple, because of the availability of linear control techniques.

The next step in the analysis is to apply the feedback linearization control technique as explained above to the control of the induction generator. The induction machine equations expressed using the state variables adopted in this control scheme are as in Equations (9.28) to (9.31).

The model equations for an induction generator in the d-q reference frame are

$$V_{qs} = r_s I_{qs} + p\lambda_{qs} + \omega_e \lambda_{ds} \quad (9.28)$$

$$V_{ds} = r_s I_{ds} + p\lambda_{ds} - \omega_e \lambda_{qs} \quad (9.29)$$

$$0 = r_r I_{qr} + p\lambda_{qr} + (\omega_e - \omega_r) \lambda_{dr} \quad (9.30)$$

$$0 = r_r I_{dr} + p\lambda_{dr} - (\omega_e - \omega_r) \lambda_{qr} \quad (9.31)$$

The control scheme aims at using the rotor fluxes and stator currents as state variables to control the dc voltage at the output of the rectifier.

Equations (9.28) – (9.31) are the system equations in the dq reference frame. The state variables in the equations include the stator currents and fluxes $I_{qs}, I_{ds}, \lambda_{qs}, \lambda_{ds}$ and rotor currents and fluxes $I_{qr}, I_{dr}, \lambda_{qr}, \lambda_{dr}$, respectively. The control scheme to be implemented has the stator currents and rotor fluxes as the state variables. The first step in the analysis is to express the system equations in terms of the desired state variables.

$$\begin{bmatrix} \lambda_{qr} \\ \lambda_{qs} \end{bmatrix} = \begin{bmatrix} L_r & L_m \\ L_m & L_s \end{bmatrix} \begin{bmatrix} I_{qr} \\ I_{qs} \end{bmatrix} \quad (9.32)$$

i.e.

$$\lambda_{qs} = L_r I_{qr} + L_m I_{qs} \quad (9.33)$$

$$\lambda_{qr} = L_m I_{qr} + L_s I_{qs} \quad (9.34)$$

Using the above set of equations, the rotor current can be expressed in terms of the stator currents and the rotor fluxes as

$$I_{qr} = \frac{1}{L_r} \lambda_{qr} - \frac{L_m}{L_r} I_{qs}. \quad (9.35)$$

Similarly the d-axis fluxes and currents are expressed in Equations (9.36) and (9.37).

$$\lambda_{ds} = L_s I_{ds} + L_m I_{dr} \quad (9.36)$$

$$\lambda_{dr} = L_m I_{ds} + L_r I_{dr} \quad (9.37)$$

From Equation (9.37) the d-axis rotor current is

$$I_{dr} = \frac{\lambda_{dr}}{L_r} - \frac{L_m}{L_r} I_{ds}. \quad (9.38)$$

Eliminating the rotor currents in Equations (9.33) and (9.36) results in expressions for the stator q and d axis fluxes in terms of the desired state variables for the system.

$$\lambda_{qs} = L_s I_{qs} + L_m \left[\frac{1}{L_r} \lambda_{qr} - \frac{L_m}{L_r} I_{qs} \right]. \quad (9.39)$$

Simplifying Equation (9.39)

$$\lambda_{qs} = L_\sigma I_{qs} + \frac{L_m}{L_r} \lambda_{qr} \quad (9.40)$$

$$\text{where } L_{\sigma} = L_s - \frac{L_m^2}{L_r} \quad (9.41)$$

Following the same method as described for the q-axis stator flux, the d-axis stator flux can be expressed in terms of the desired state variables as

$$\lambda_{ds} = L_{\sigma} I_{ds} + \frac{L_m}{L_r} I_{dr}. \quad (9.42)$$

Substituting Equations (9.35), (9.38), (9.40) and (9.42), in Equations (9.28) to (9.31) results in the desired system equations expressed in terms of the state variables for the control scheme.

$$V_{qs} = r I_{qs} + L_{\sigma} p I_{qs} + \omega_e L_{\sigma} I_{ds} - \frac{r_r L_m}{L_r^2} \lambda_{qr} + \frac{\omega_r L_m}{L_r} \lambda_{dr} \quad (9.43)$$

$$\text{where } r = r_s + \frac{r_r L_m^2}{L_r^2} \quad (9.44)$$

Similarly the d-axis voltage equation

$$V_{ds} = r I_{ds} + L_{\sigma} p I_{ds} - \omega_e L_{\sigma} I_{qs} - \frac{r_r L_m}{L_r^2} \lambda_{dr} + \frac{\omega_r L_m}{L_r} \lambda_{qr}. \quad (9.45)$$

The q and d axis rotor voltage equations are expressed in Equations (9.44) and (9.45), respectively:

$$0 = \frac{r_r}{L_r} \lambda_{qr} - \frac{r_r L_m}{L_r} I_{qs} + p \lambda_{qr} + (\omega_e - \omega_r) \lambda_{dr} \quad (9.46)$$

$$0 = \frac{r_r}{L_r} \lambda_{dr} - \frac{r_r L_m}{L_r} I_{ds} + p \lambda_{dr} - (\omega_e - \omega_r) \lambda_{qr}. \quad (9.47)$$

Rearranging Equations (9.43) and (9.45) to (9.47), the state equations for the induction generator can be expressed in terms of the desired state variables.

$$L_{\sigma} p I_{qs} = V_{qs} - r I_{qs} - \omega_e L_{\sigma} I_{ds} + \frac{r_r L_m}{L_r^2} \lambda_{qr} - \frac{\omega_r L_m}{L_r} \lambda_{dr} \quad (9.48)$$

$$L_{\sigma} p I_{ds} = V_{ds} - r I_{ds} + \omega_e L_{\sigma} I_{ds} + \frac{r_r L_m}{L_r^2} \lambda_{qr} + \frac{\omega_r L_m}{L_r} \lambda_{dr} \quad (9.49)$$

$$p \lambda_{qr} = \frac{-r_r}{L_r} \lambda_{qr} + \frac{r_r L_m}{L_r} I_{qs} - (\omega_e - \omega_r) \lambda_{dr} \quad (9.50)$$

$$p \lambda_{dr} = \frac{-r_r}{L_r} \lambda_{dr} + \frac{r_r L_m}{L_r} I_{ds} + (\omega_e - \omega_r) \lambda_{qr} \quad (9.51)$$

The dc voltage equation of the rectifier connected to the stator terminals of the induction machine is

$$C_p V_{dc} = \frac{3}{2} (M_{qs} I_{qs} + M_{ds} I_{ds}) - \frac{V_{dc}}{R_L} \quad (9.52)$$

Equations (9.46) to (9.51) and (9.52) are the state equations of the system, and are used in the controller design.

The control scheme used in this system assumes the rotor flux to be aligned along the d-axis; thereby the value of the q-axis rotor flux is zero, i.e. $\lambda_{qr} = 0$.

The state equation for λ_{qr} is used to calculate the slip speed.

$$p \lambda_{qr} + \frac{r_r}{L_r} \lambda_{qr} = + \frac{r_r L_m}{L_r} I_{qs} - (\omega_e - \omega_r) \lambda_{dr} = \sigma_{qr} \quad (9.53)$$

where σ_{qr} is the output of the q axis rotor flux controller.

Similarly the state equations for the system can be rewritten as

$$L_{\sigma} p I_{qs} + r I_{qs} = V_{qs} - \omega_e L_{\sigma} I_{ds} + \frac{r_r L_m}{L_r^2} \lambda_{qr} - \frac{\omega_r L_m}{L_r} \lambda_{dr} = \sigma_{qs} \quad (9.54)$$

$$L_{\sigma} p I_{ds} + r I_{ds} = V_{ds} + \omega_e L_{\sigma} I_{ds} + \frac{r_r L_m}{L_r^2} \lambda_{qr} + \frac{\omega_r L_m}{L_r} \lambda_{dr} = \sigma_{ds} \quad (9.55)$$

$$p\lambda_{dr} + \frac{r_r}{L_r}\lambda_{dr} = +\frac{r_r L_m}{L_r}I_{ds} + (\omega_e - \omega_r)\lambda_{qr} = \sigma_{dr}. \quad (9.56)$$

$$CpV_{dc} + \frac{V_{dc}}{R_L} = \frac{3}{2}(M_{qs}I_{qs} + M_{ds}I_{ds}) = \sigma_{dc} \quad (9.57)$$

Equation (9.57) can be expressed as

$$CpV_{dc}^2 + \frac{V_{dc}^2}{R_L} = 3(V_{qs}I_{qs} + V_{ds}I_{ds}) = \sigma_{dc}. \quad (9.58)$$

The outputs of the current controller σ_{qs} and σ_{ds} are used to calculate the reference q and d axis voltages, V_{qs} and V_{ds} . The equations used to calculate the reference values of the q-axis voltage, d-axis voltage, q-axis current, d-axis current and reference slip are obtained from Equations 9.53 to 9.58.

$$(\omega_e - \omega_r) = -\frac{\sigma_{qr}}{\lambda_{dr}} + \frac{r_r L_m}{L_r} \cdot \frac{I_{qs}}{\lambda_{dr}} \quad (9.59)$$

$$I_{ds}^* = \left[\sigma_{dr} - (\omega_e - \omega_r)\lambda_{qr} \right] \frac{L_r}{r_r L_m} \quad (9.60)$$

$$I_{qs}^* = \left(\frac{\sigma_{dc}}{3} - V_{ds}i_{ds} \right) \cdot \frac{1}{V_{qs}} \quad (9.61)$$

$$V_{qs}^* = \sigma_{qs} + \omega_e L_\sigma I_{ds} - \frac{r_r L_m}{L_r^2} \lambda_{qr} + \omega_r \frac{L_m}{L_r} \lambda_{dr} \quad (9.62)$$

$$V_{ds}^* = \sigma_{ds} - \omega_e L_\sigma I_{qs} - \frac{r_r L_m}{L_r^2} \lambda_{dr} - \omega_r \frac{L_m}{L_r} \lambda_{qr} \quad (9.63)$$

There are three main loops in the control scheme, as shown in Figure 9.7.

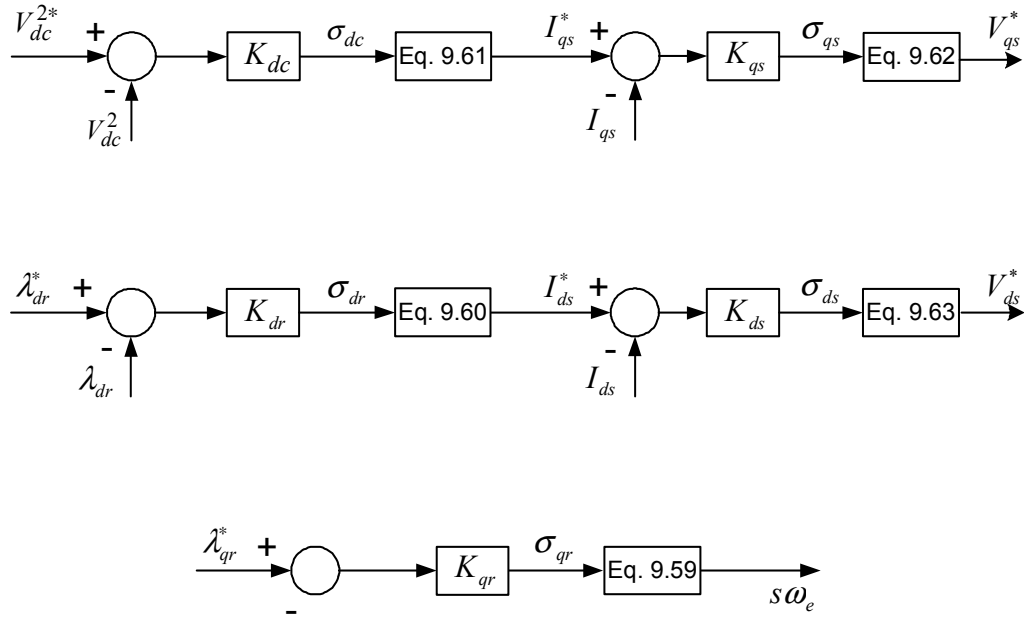


Figure 9.7: Control Structure for machine

The first loop is used to calculate the q axis current using the output of the dc voltage controller σ_{dc} and the output of the current controller σ_{qs} is used to calculate the reference q axis voltage V_{qs}^*

In the second loop, σ_{dr} the output of the d-axis rotor flux controller is used to calculate the d-axis stator current I_{ds} , and the output of the current controller σ_{ds} is used to calculate the d-axis reference voltage V_{ds} . The third loop is used to calculate the slip as explained earlier.

The reference voltages that are calculated using the current controllers, as explained above are fed to the inverter and the desired modulation signals are generated to control the dc voltage. This control scheme described above is as shown in Figure 9.8.

$$\sigma_{qs} = \left(K_p + \frac{K_i}{s} \right) (I_{qs}^* - I_{qs}). \quad (9.66)$$

The transfer function of the q-axis current controller can be expressed as $\frac{I_{qs}}{I_{qs}^*}$.

From Equations (9.65) and (9.66) the transfer function of the q-axis current controller is obtained as below.

$$L_\sigma p I_{qs} + r I_{qs} = \left(K_p + \frac{K_i}{s} \right) (I_{qs}^* - I_{qs}) \quad (9.67)$$

$\left(K_p + \frac{K_i}{s} \right)$ can be expressed as $\left(\frac{pK_p + K_i}{p} \right)$, the above equation can be

rewritten differential form as

$$L_\sigma p^2 I_{qs} + r p I_{qs} = (pK_p + K_i) (I_{qs}^* - I_{qs}).$$

The transfer function expressed as a ratio of the output divided by the input of the controller is then expressed as

$$\frac{I_{qs}}{I_{qs}^*} = \frac{pK_{p3} + K_{i3}}{L_\sigma p^2 + p(r + K_{p3}) + K_{i3}}. \quad (9.68)$$

Similarly the transfer functions of the other controllers in the control scheme are obtained. The method of deriving the expression for the transfer functions is exactly above. The final expressions for the transfer functions are

$$\frac{\lambda_{qr}}{\lambda_{qr}^*} = \frac{pK_{p1} + K_{i1}}{p^2 + p\left(\frac{r_r}{L_r} + K_{p1}\right) + K_{i1}} \quad (9.69)$$

$$\frac{\lambda_{dr}}{\lambda_{dr}^*} = \frac{pK_{p2} + K_{i2}}{p^2 + p\left(\frac{r_r}{L_r} + K_{p2}\right) + K_{i2}} \quad (9.70)$$

$$\frac{I_{ds}}{I_{ds}^*} = \frac{pK_{p4} + K_{i4}}{L_\sigma p^2 + p(r + K_{p4}) + K_{i4}} \quad (9.71)$$

The transfer function of the dc voltage controller is obtained using Equation (9.56). The equation for the transfer function is

$$\frac{V_{dc}^2}{V_{dc}^2} = \frac{pK_{p5} + K_{i5}}{Cp^2 + pK_{p5} + K_{i5}} \quad (9.72)$$

Using the transfer functions derived for each controller, the parameters of the controller can be determined by using the Butterworth Polynomial. As explained earlier, the controllers used are PI controllers. The parameters of each controller need to be determined, i.e. K_p and K_i . The method of determining the parameters involves comparing the coefficients of the transfer function of the controller with the coefficients of the Butterworth Polynomial. The Butterworth Polynomial has the form

$$p^2 + \sqrt{2}\omega_0 p + \omega_0^2 \quad (9.73)$$

The Butterworth method locates the eigen values of the transfer function uniformly on the left half of the s-plane on a circle of radius ω_0 with its center at the origin, as illustrated in Figure 9.9. The transfer functions of the controllers in this control scheme are of second order; thereby the coefficients of the denominator of the transfer function are compared with the second order Butterworth polynomial. Therefore the parameters of the controller are calculated using the following equations.

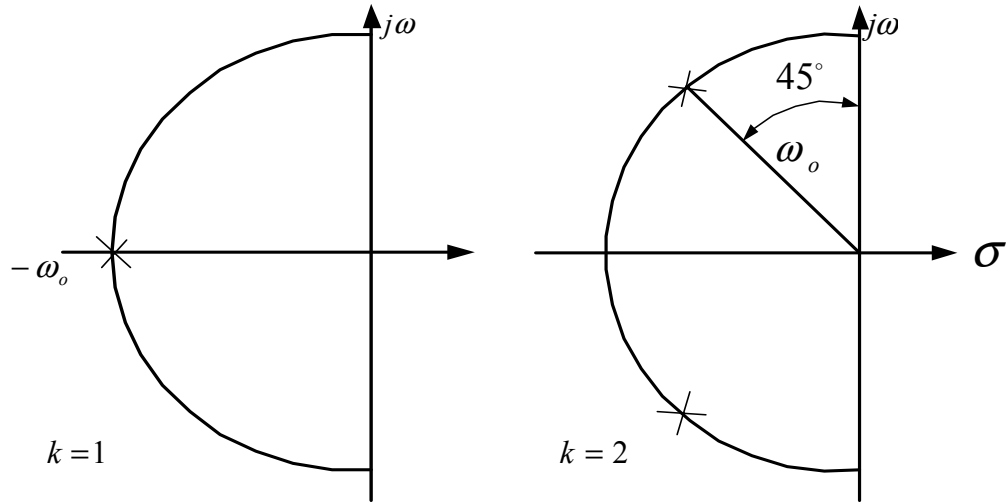


Figure 9.9: Pole placement using Butterworth polynomial

The parameter 'k' used in Figure 9.9 is equal to the number of poles in the left-half s-plane.

Table 9.1: Controller Parameters

$K_{p1} = \sqrt{2}\omega_0 - \frac{r_r}{L_r} = 5$	$K_{i1} = \omega_0^2 = 100$
$K_{p2} = \sqrt{2}\omega_0 - \frac{r_r}{L_r} = 150$	$K_{i2} = \omega_0^2 = 20000$
$K_{p3} = \sqrt{2}L_\sigma\omega_0 - r = 150$	$K_{i3} = L_\sigma^2\omega_0^2 = 8000$
$K_{p4} = \sqrt{2}L_\sigma\omega_0 - r = 150$	$K_{i4} = L_\sigma^2\omega_0^2 = 8000$
$K_{p5} = \sqrt{2}C\omega_0 = 0.1$	$K_{i5} = \frac{C}{2}\omega_0^2 = 10$

The parameters of the controllers are calculated by choosing ω_0 . Higher values of ω_0 would mean a faster controller.

9.6 Dynamic Simulation of the Induction Generator-Rectifier System Using Rotor Flux Vector Control

The dynamic simulation has been carried out using the control scheme derived in the previous section, for the induction generator-rectifier system using indirect rotor flux vector control.

The parameters of the system used in the dynamic simulation are shown in Table 9.1.

As explained in section 9.3, the q-axis rotor flux is set to zero by aligning the d-axis with the rotor flux. Therefore, the q-axis rotor flux in the simulation is equal to zero, and the d-axis rotor flux (which is equal to the resultant rotor flux) is set to be equal to 0.45 Weber. The reference dc voltage is chosen to be equal to 200V, and the load resistance is chosen to be equal to 100 Ω .

Table 9.1: Machine parameters used in dynamic simulation

$r_s = 1.54\Omega$
$r_r = 0.9088\Omega$
$L_{ls} = 0.004H$
$L_{lr} = 0.004H$

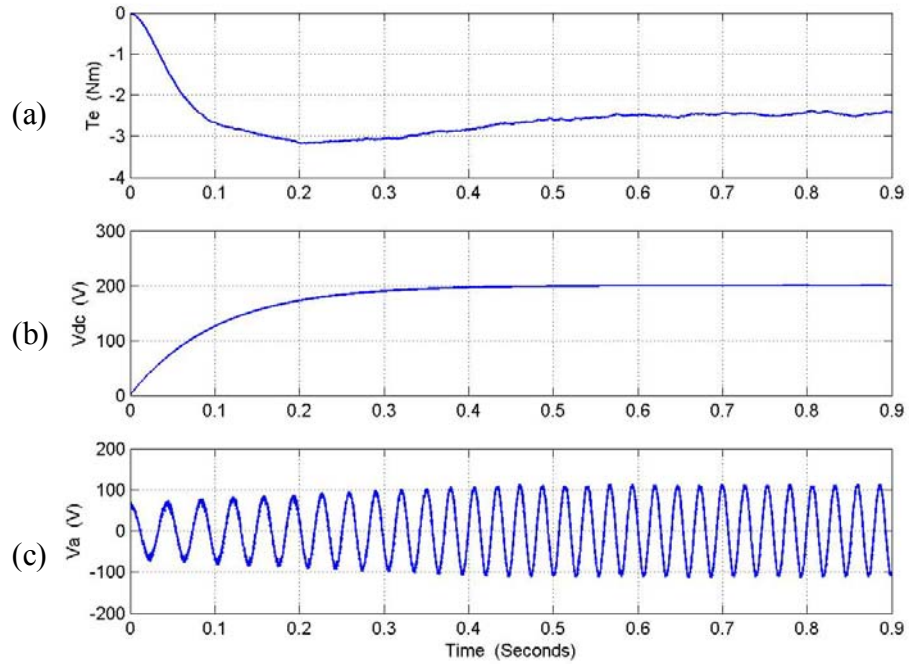


Figure 9.10: Simulation results for starting process, from top: (a) electromagnetic torque T_e , (b) dc voltage V_{dc} , (c) phase 'a' voltage V_a

The first set of simulation results Figures 9.11 to 9.21 show the starting and dynamic response of the induction generator-rectifier system. Figure 9.10(a) shows the buildup of the electromagnetic torque T_e , output dc voltage and phase 'a' voltage of the generator.

The dc voltage reaches a steady state value of 200V in 0.5 seconds and remains constant. The electromagnetic torque is negative as the induction machine is generating, and the q-axis current is negative. The phase voltage (phase 'a') is purely sinusoidal as can be seen in Figure 9.10(c).

The starting process of the q-axis voltage, d-axis voltage and load current is illustrated in Figure 9.11. The load and d-axis voltage reach steady state values before the q-axis voltage.

The response of the stator voltage frequency, slip frequency, and the rotor speed can be seen in Figure 9.12. The rotor speed in this simulation is ramped up from 100 to 240 rad/sec, the speed reaches a steady state value at 0.45 seconds. The rotor speed is kept constant at 240 rad/sec for this simulation. The slip frequency during the starting process is -4 rad/sec.

Figures 9.13, 9.14, and 9.15 show the dynamic response of the system to a load change from 100Ω to 25Ω .

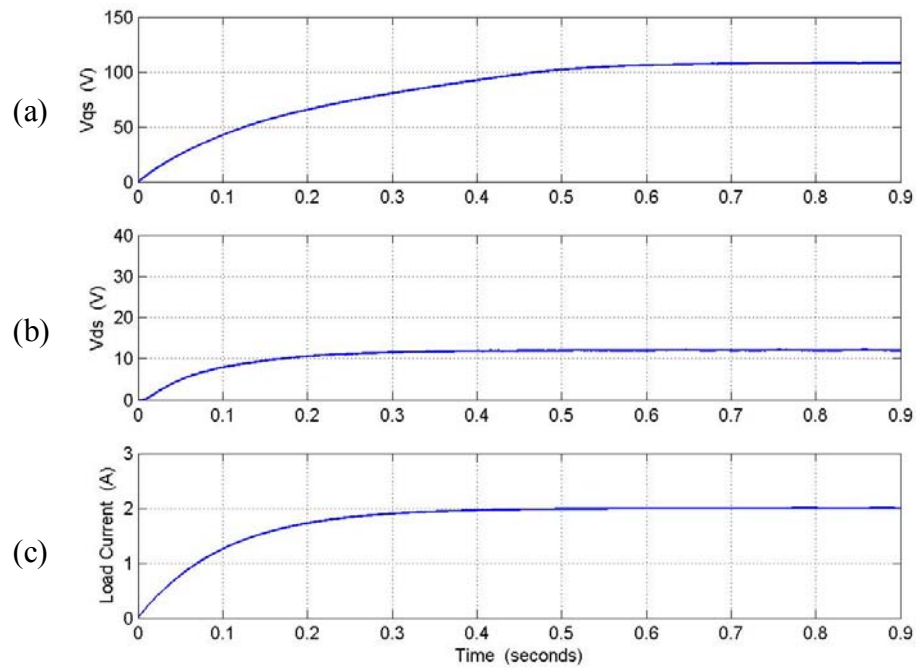


Figure 9.11: Simulation results for starting process, from top: (a) q-axis voltage V_{qs} (b) d-axis voltage V_{ds} , (c) load current I_L

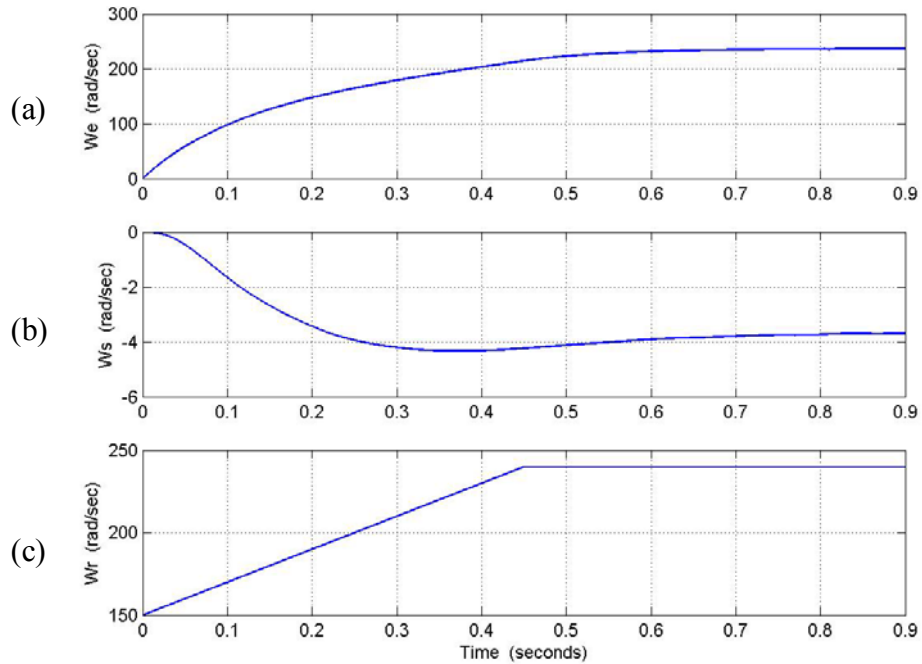


Figure 9.12: Simulation results for starting process, from top: (a) voltage frequency ω_e (b) slip frequency ω_s , (c) rotor speed ω_r

The load is changed at $t = 1$ sec and remains at 25Ω for the entire time of the simulation. As can be seen from Figure 9.13 (a), the load change (an increase in the load on the system) causes the electromagnetic torque to increase from -2 Nm to -8.5 Nm. Also the change in the load causes the dc voltage to drop to 197.5 volts for less than 0.5 seconds, thereby illustrating the effectiveness of the control scheme. The second set of plots, Figure 9.14, illustrate the nature of response of the q-axis voltage, d-axis voltage and the load current. As the load resistance is decreased, and the dc voltage is controlled at 200V, the load current increases by four times due to the proportionate decrease in the load resistance connected to the output of the rectifier.

As mentioned earlier, the rotor speed is maintained at a constant value of 240rad/sec. For an increase in the load on the system, the operating slip of the generator increases. The effect of the increase in the slip is seen on the stator voltage frequency ω_e .

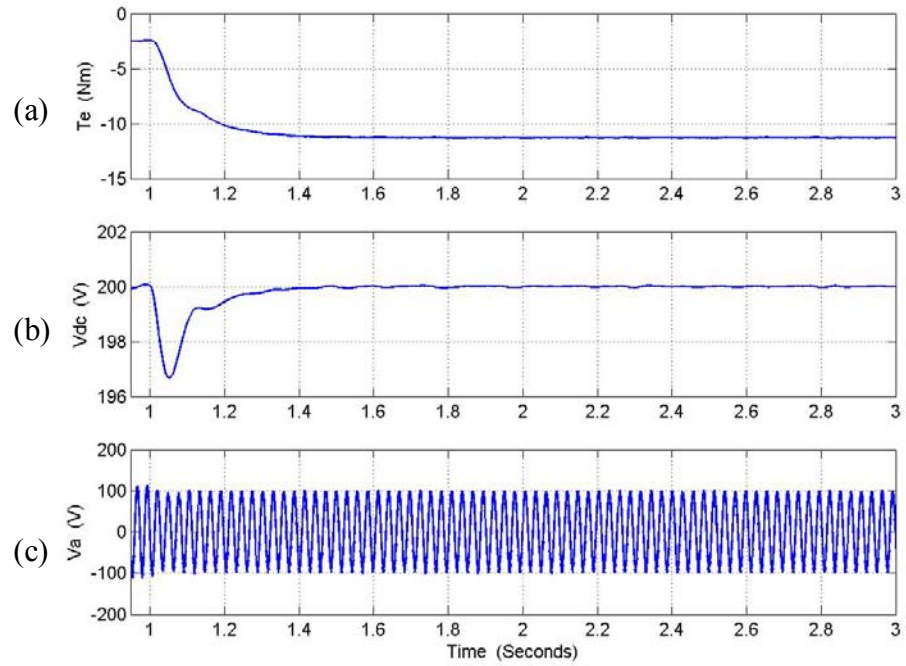


Figure 9.13: Simulation results for dynamic process, from top: (a) electromagnetic torque T_e (b) dc voltage V_{dc} , (c) phase 'a' voltage V_a

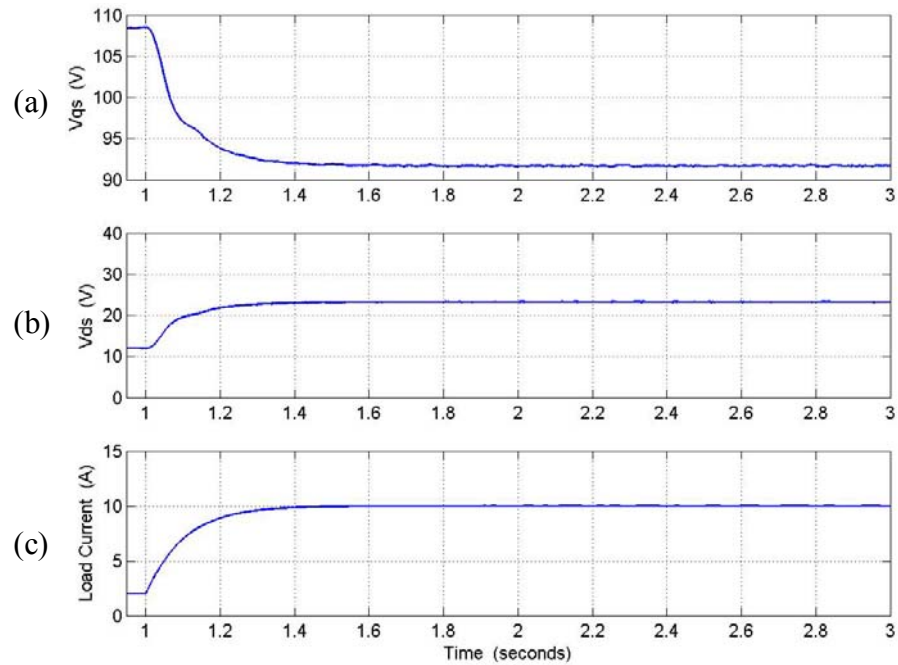


Figure 9.14: Simulation results for dynamic process, from top: (a) q-axis voltage V_{qs} (b) d-axis voltage V_{ds} , (c) load current I_L

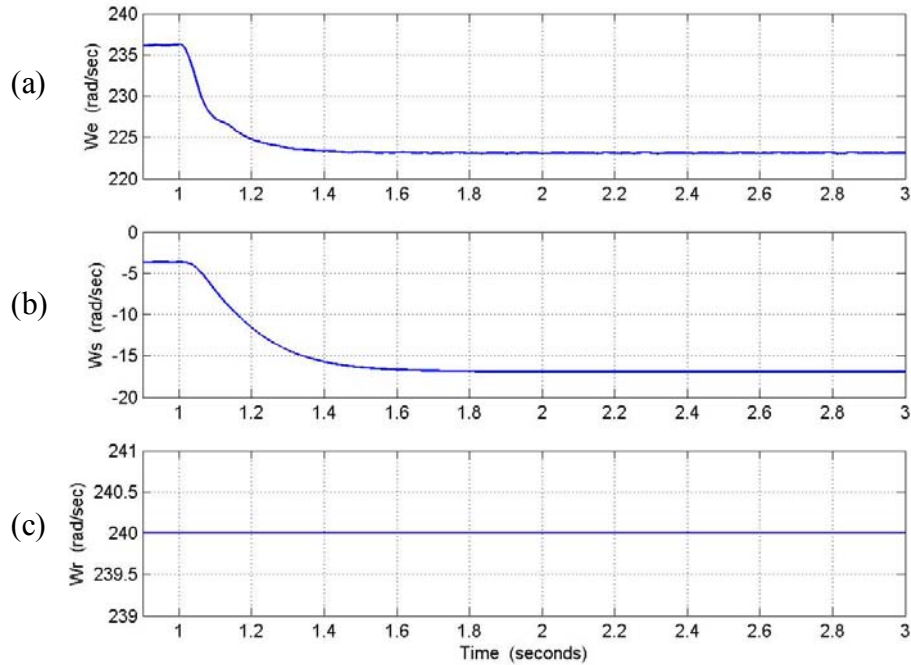


Figure 9.15: Simulation results for dynamic process, from top: (a) voltage frequency ω_e (b) slip frequency ω_s , (c) rotor speed ω_r

The second simulation performed for the generator-rectifier system is to see the response of the system to varying rotor speeds for a constant load resistance. Figures 9.16 to 9.21 show the starting process and dynamic response of the system for changing rotor speeds. The starting process is just the same as that shown in Figures 9.11 to 9.15.

The stator voltage frequency, slip frequency, and the rotor speed are shown in Figure 9.16. The rotor speed is ramped to 240 rad/sec, and kept constant until $t = 2$ seconds.

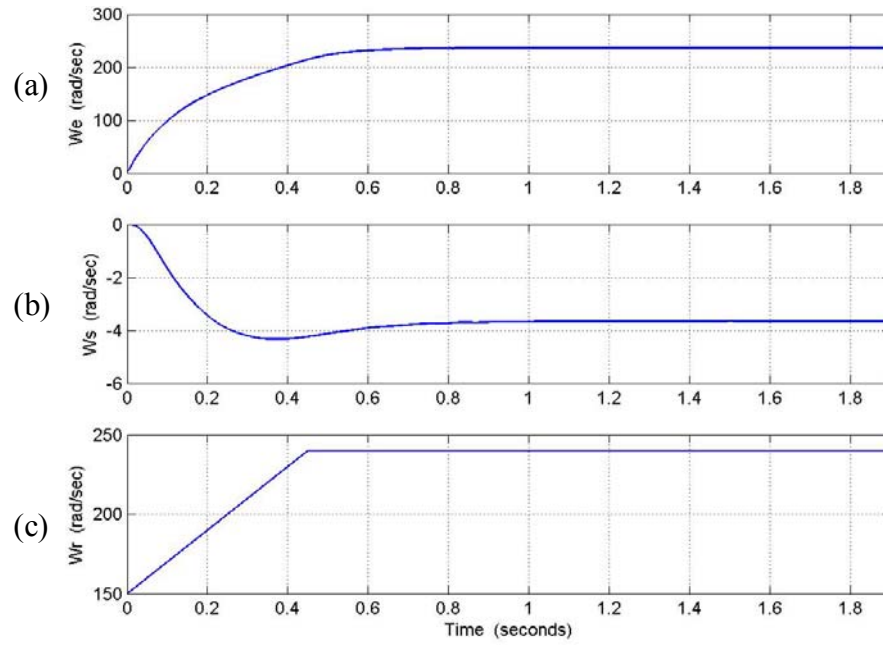


Figure 9.16: Simulation results for starting process, from top: (a) voltage frequency ω_e (b) slip frequency ω_s , (c) rotor speed ω_r

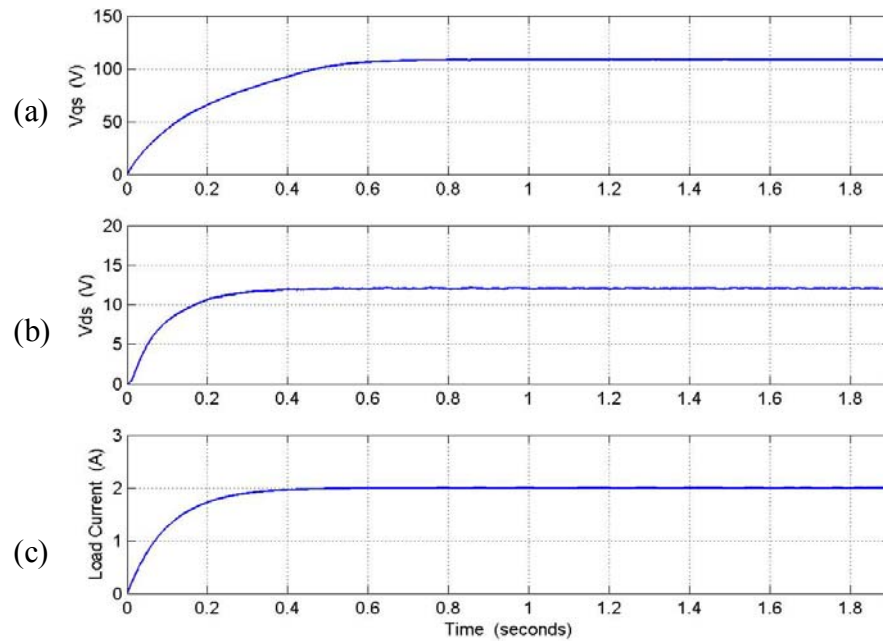


Figure 9.17: Simulation results for starting process, from top: (a) q-axis voltage V_{qs} (b) d-axis voltage V_{ds} , (c) load current I_L

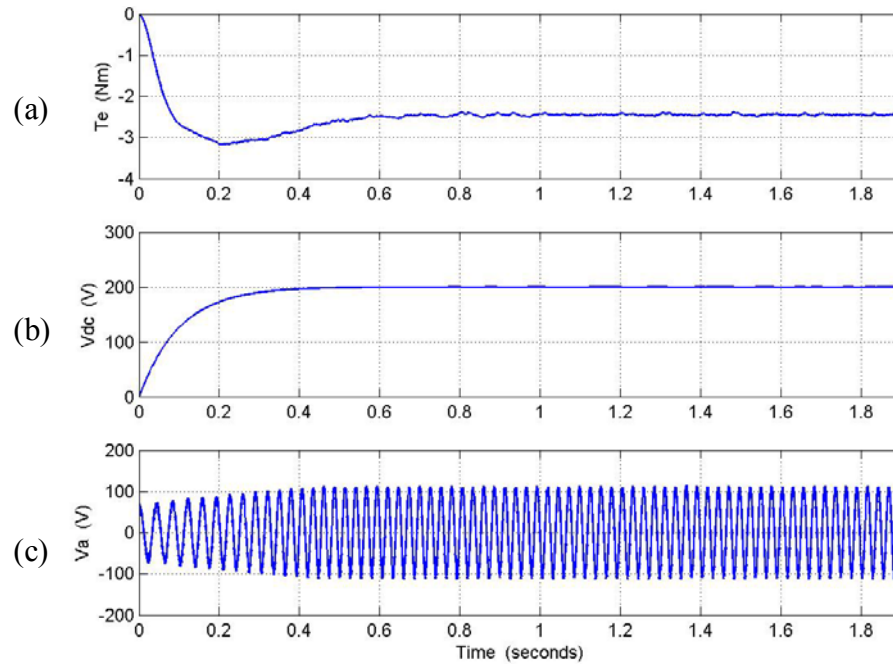


Figure 9.18: Simulation results for starting process, from top: (a) electromagnetic torque T_e (b) dc voltage V_{dc} , (c) phase 'a' voltage V_a

The starting process of the q and d-axis voltage is illustrated in Figure 9.17. As in the previous simulation, the q-axis stator voltage takes reaches a steady state value after the d-axis voltage and load current. The electromagnetic torque, dc voltage and phase 'a' voltage is shown in Figure 9.18.

After the system reaches steady state, the rotor speed is changed. The rotor speed is dropped to 200 rad/sec at $t = 2$ seconds and then increased to 240 rad/sec at $t = 4$ seconds. The change in the rotor speed causes the q-axis voltage to drop to 90V during the period of time for which the rotor speed is 200 rad/sec and then increase to 109V when the rotor speed is increased to 240 rad/sec at $t = 4$ seconds. The d-axis voltage remains at a constant value during the change in the rotor speed, and the load current remains constant showing the stability of the dc voltage when the rotor speed is changed.

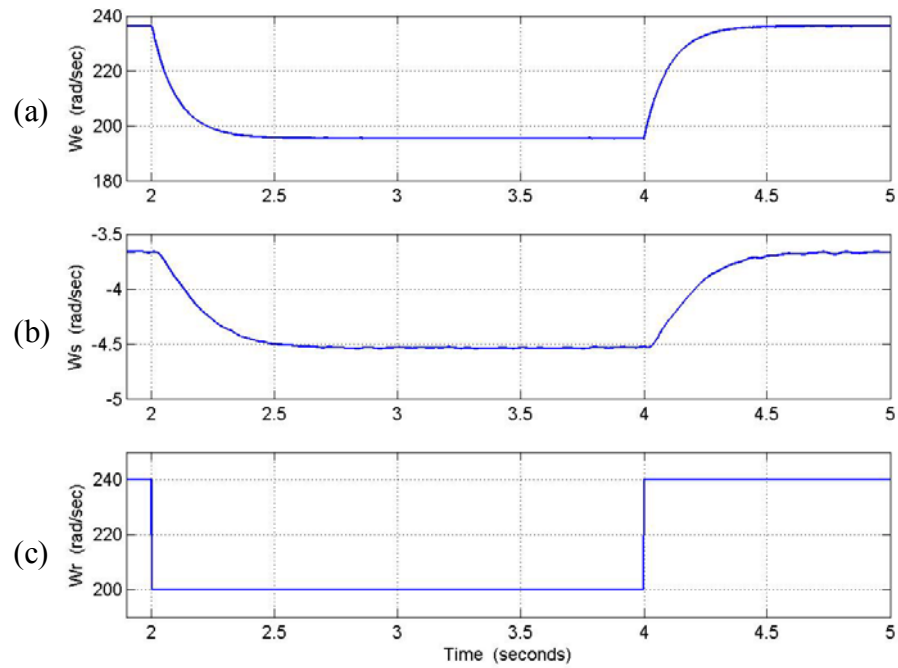


Figure 9.19: Simulation results for dynamic process, from top: (a) voltage frequency ω_e (b) slip frequency ω_s , (c) rotor speed ω_r

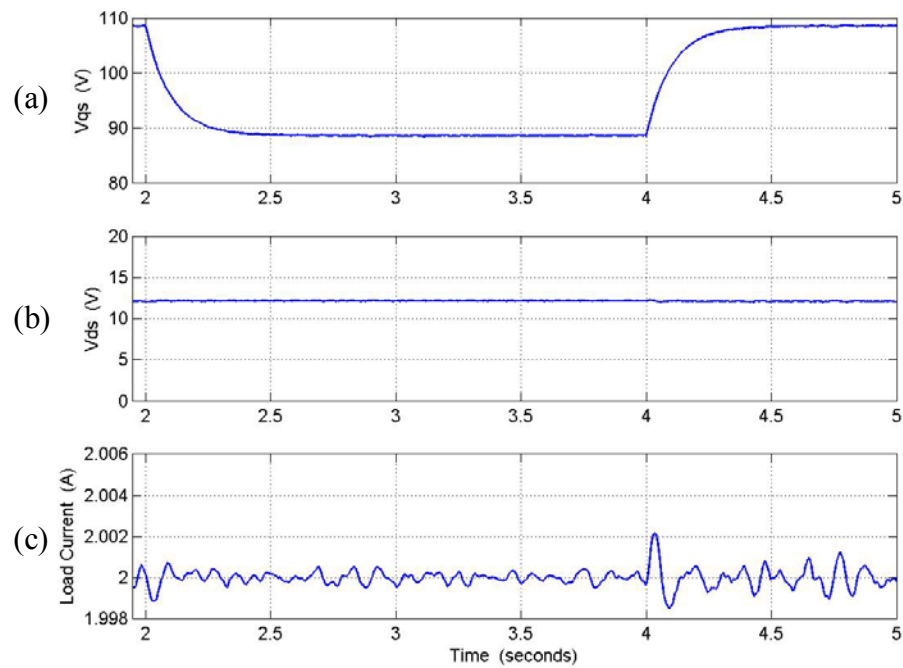


Figure 9.20: Simulation results for dynamic process, from top: (a) q-axis voltage V_{qs} (b) d-axis voltage V_{ds} , (c) load current I_L

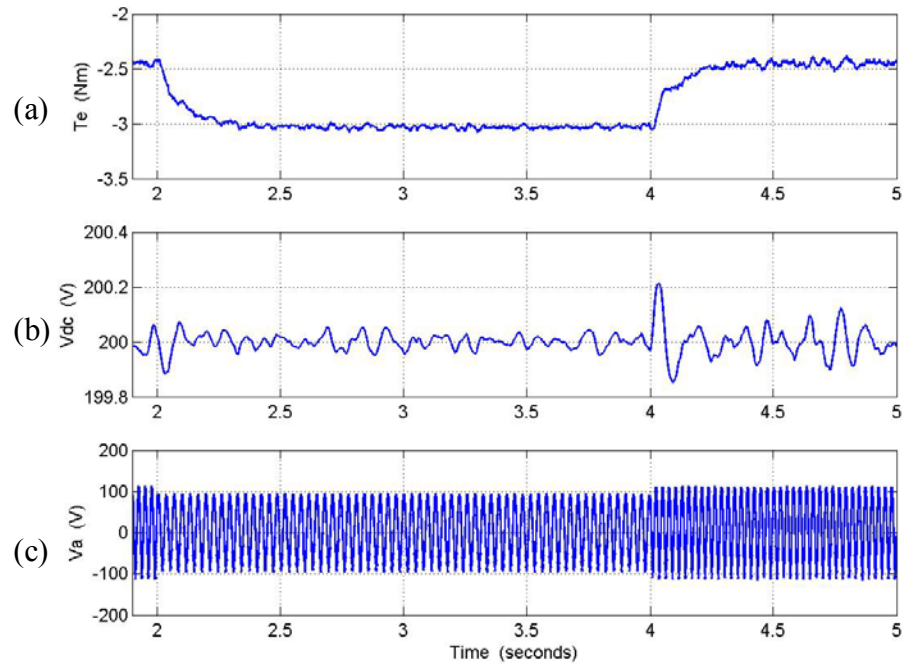


Figure 9.21: Simulation results for dynamic process, from top: (a) electromagnetic torque T_e , (b) dc voltage V_{dc} , (c) phase 'a' voltage V_a

The nature of response of the electromagnetic torque, dc voltage, and phase 'a' voltage to a change in rotor speed is shown in Figure 9.21. For a decrease in the rotor speed, the electromagnetic torque increases. The dc voltage remains unchanged and is constant at 200V.

For a decrease in the rotor speed, the phase voltage of the generator decreases, and returns to the initial value (before the change in the rotor speed), when the rotor speed is increased from 200 rad/sec to 240 rad/sec.

The effectiveness of the proposed control scheme in controlling the dc voltage of the rectifier is illustrated by the dynamic simulation results. To test the robustness of the controller design, the system is operated under varying load conditions and varying rotor speeds.

9.7 Experimental Results for Rotor Flux Vector Control Scheme

The experimental results for the proposed vector control scheme are presented in this section. The nature of the experimental setup has been detailed in Chapter 11.

Figure 9.22 shows the dynamic response of the line-line voltages, V_{AC} , and V_{BC} and the phase currents I_A , and I_B . The experimental waveforms have been obtained by running the machine at a constant rotor speed of 1320 rpm. The capacitor on the dc side of the rectifier is given an initial value of 20V. The reference dc voltage used is 220V.

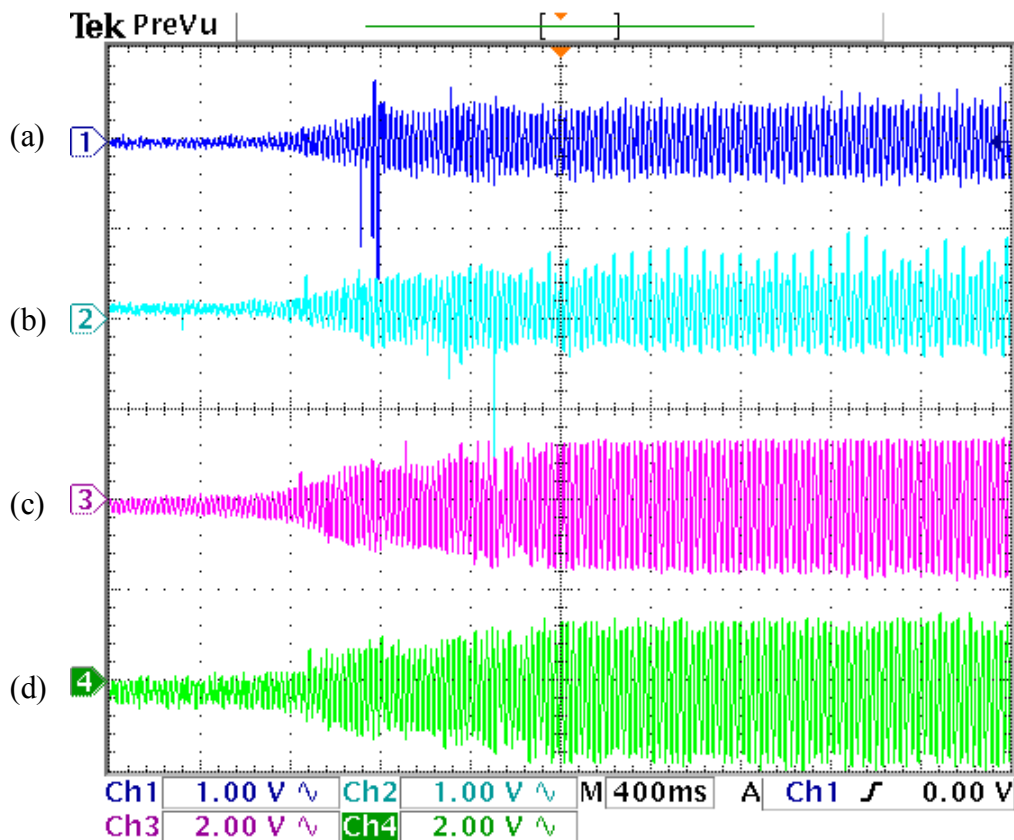


Figure 9.22: Dynamic response of the 2 hp induction generator. Reference dc voltage = 220V , rotor speed= 1320 rpm , load resistance = 80 Ω . (a) line-line voltage, V_{AC} (350 V/div); (b) line-to-line voltage V_{BC} (350 V/div); (c) phase A current (7.5 A/div); (d) phase B current (7.5A /div)

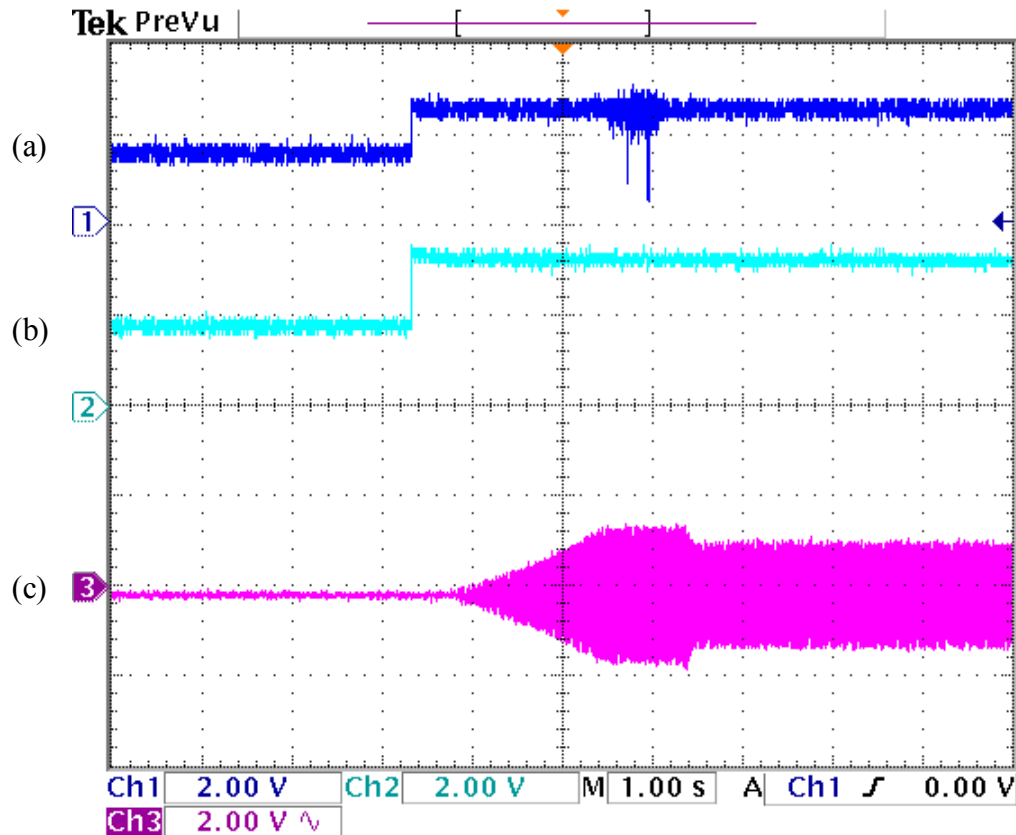


Figure 9.23: Dynamic response of the 2 hp induction generator. Reference dc voltage = 220V , rotor speed= 1320 rpm , load resistance = 80 Ω . (a) dc voltage V_{dc} (137.5 V/div); (c) d-axis rotor flux (1.36/div); (d) phase A modulation signal (1.36 /div)

The voltage buildup of the generator during startup is shown, illustrating the increase in the line to line voltage from 0 to 130V. Figure 9.23 shows the increase in the dc voltage at the output of the rectifier, the d-axis rotor flux and the modulation signal for the phase ‘a’.

The dc voltage, from Figure 9.23 increases from 20V to 220V. The increase in the dc voltage as well as the d-axis rotor flux is not a smooth buildup, however, the dc voltage tracks the reference dc voltage used. The values of the reference d-axis rotor flux used in the experiment is 0.25Wb. The modulation signal for phase ‘a’ is shown in 9.23(c).

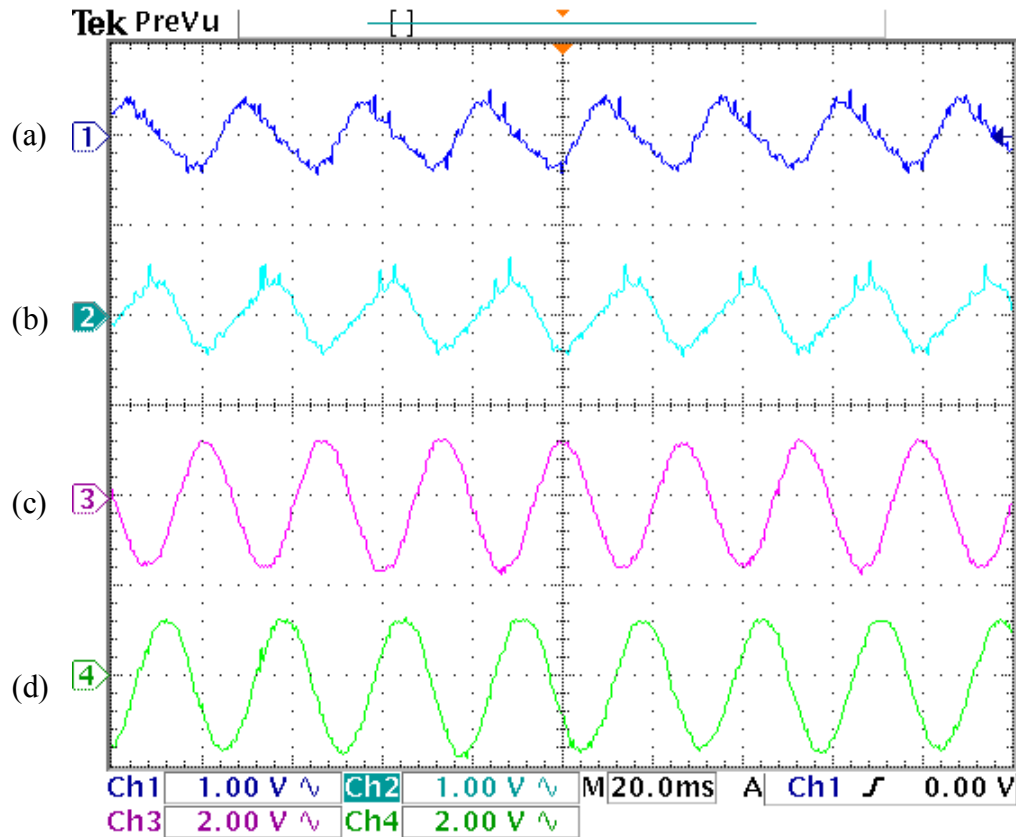


Figure 9.24: Steady-state response of the 2 hp induction generator. Reference dc voltage =220V, rotor speed= 1320 rpm , load resistance = 80 Ω . (a) line-line voltage, V_{AC} (350 V/div); (b) line-to-line voltage V_{BC} (350 V/div); (c) phase A current (7.5 A/div); (d) phase B current (7.5A /div)

Figures 9.24 and 9.25 show the operation of the generator at steady-state. The line to line voltages and phase currents are shown in Figure 9.24, and the dc voltage, d-axis rotor flux and the modulation signal for phase ‘a’ are shown in Figure 9.25. As can be seen from Figure 9.22, the line to line voltages have some high frequency components. This is due to the switching transients of the boost rectifier. The phase currents are pure ac with no noise. The steady state value of the phase current of 3 amperes, and the line to line voltage has a steady state value of 110V.

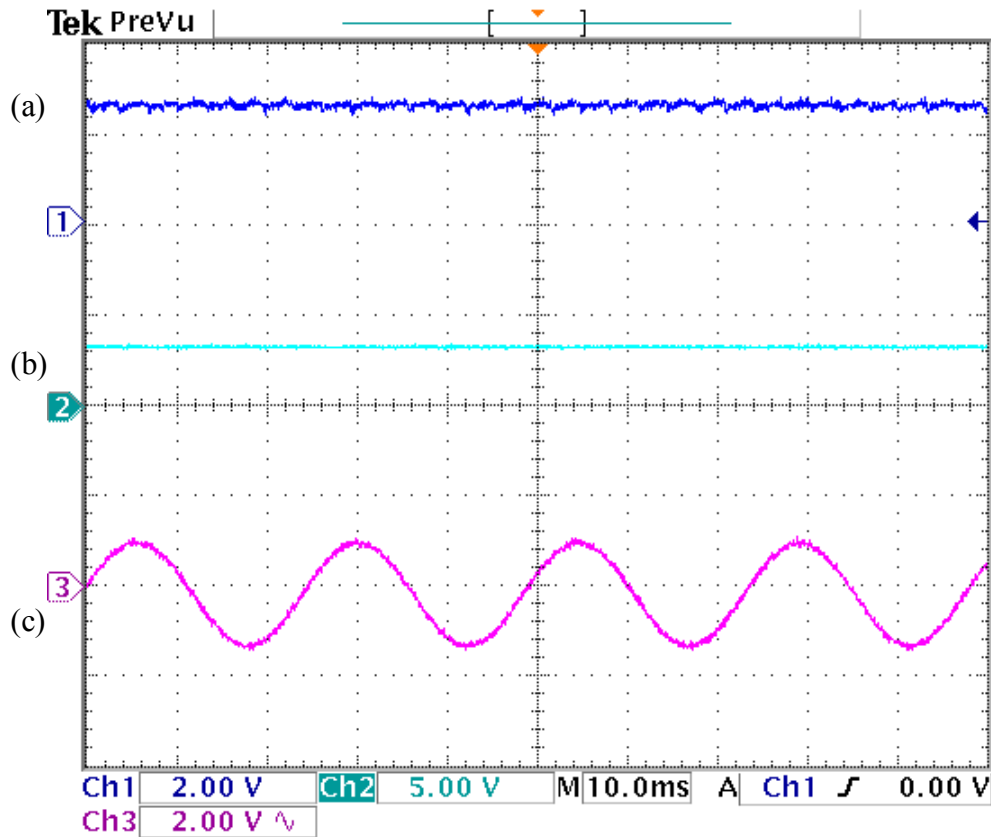


Figure 9.25: Dynamic response of the 2 hp induction generator. Reference dc voltage = 220V , rotor speed= 1320 rpm , load resistance = 80 Ω . (a) dc voltage V_{dc} (137.5 V/div); (c) d-axis rotor flux (1.36/div); (d) phase A modulation signal (1.36 /div)

Similarly, the steady state waveforms for the dc voltage, d-axis rotor flux and phase ‘a’ modulation signal is shown in Figure 9.25. The dc voltage reaches a steady state value of 220V, which is the same as the reference dc voltage. The d-axis rotor flux is a constant dc value, illustrating the effectiveness of the flux estimation algorithm used in the code.

CHAPTER 10

CONTROL OF THREE-PHASE INDUCTION GENERATOR USING NATURAL VARIABLES

10.1 Introduction

Induction generator control has been implemented using the rotor flux model of the induction machine in Chapter 9. The control uses the synchronous reference frame to calculate the modulation signals required in switching the rectifier connected to the generator as shown in Figure 10.1.

The implementation of a similar scheme that would use the stationary reference frame as the frame of transformation to obtain the desired modulation signals is proposed in this chapter. The model of the induction generator used in the control scheme in this chapter is the natural variables model.

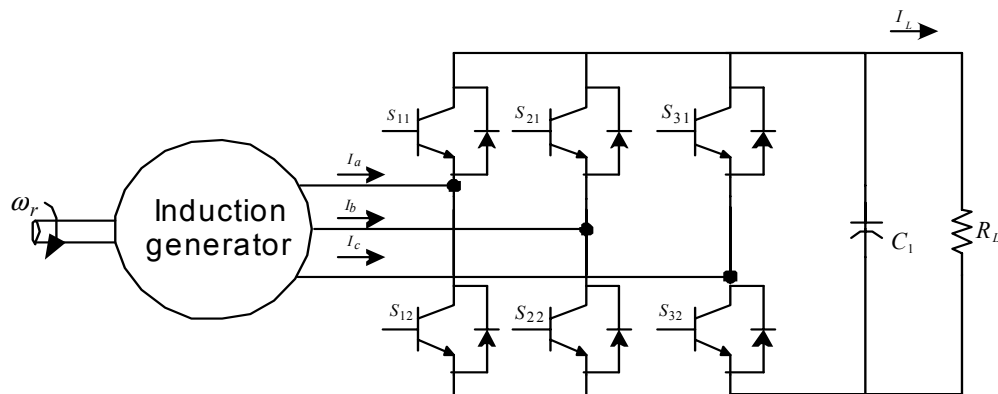


Figure 10.1: System Model

The development of the model (explained in detail in Chapter 5), is briefly discussed here, and the derivation of the control scheme and parameters of the controller are discussed in detail. The system is operated under a condition of minimum loss [C.1, C.9].

The proposed scheme is simulated and the robustness of the scheme is tested by seeing the response of the system under different conditions of rotor speed as well as load.

The method of control, i.e. indirect vector control is implemented using the stationary reference frame; therefore, the rotor flux position does not need to be determined in order to implement the control scheme. The details of indirect vector control have been dealt with in detail in Chapter 9 and hence are not repeated here.

10.2 Natural Variables Model of Induction Generator

The model of the induction machine used in the control scheme proposed in this chapter is the natural variables model.

The natural variables of the machine are the electromagnetic torque T_e , the reactive torque T_r , and the rotor/stator flux. The natural variables are so called because these variables can be easily related to and also these terms are reference frame independent.

The natural variables model (derived in Chapter 5) is summarized below

$$T_e = k(\lambda_{dr}I_{qs} - \lambda_{qr}I_{ds}) \quad (10.1)$$

$$T_r = k(\lambda_{dr}I_{ds} + \lambda_{qr}I_{qs}) \quad (10.2)$$

$$\lambda_{rr} = \lambda_{qr}^2 + \lambda_{dr}^2 \quad (10.3)$$

where $\frac{3P L_m}{4 L_r}$.

The model equations of the induction generator expressed in terms of the rotor fluxes and stator currents as state variables (from Chapter 5) are expressed in Equations (10.4) to (10.7).

$$pI_{qs} = \frac{1}{L_\sigma} V_{qs} - rI_{qs} + \frac{r_r L_m}{L_\sigma L_r^2} \lambda_{qr} - \frac{L_m}{L_r L_\sigma} \omega_r \lambda_{dr} - \omega_e I_{ds} \quad (10.4)$$

$$pI_{ds} = \frac{1}{L_\sigma} V_{ds} - rI_{ds} + \frac{r_r L_m}{L_\sigma L_r^2} \lambda_{dr} + \frac{L_m}{L_r L_\sigma} \omega_r \lambda_{qr} + \omega_e I_{qs} \quad (10.5)$$

$$p\lambda_{qr} = -\frac{r_r}{L_r} \lambda_{qr} + \frac{r_r L_m}{L_r} I_{qs} - (\omega_e - \omega_r) \lambda_{dr} \quad (10.6)$$

$$p\lambda_{dr} = -\frac{r_r}{L_r} \lambda_{dr} + \frac{r_r L_m}{L_r} I_{ds} + (\omega_e - \omega_r) \lambda_{qr} \quad (10.7)$$

$$r = \frac{r_s}{L_\sigma} + \frac{r_r L_r^2}{L_\sigma L_r^2}$$

The model equations for the induction machine are obtained by differentiating equations (10.1) to (10.3) and using the voltage equations of the induction machine, Equations (10.4) to (10.7).

$$pT_e = k(\lambda_{dr} pI_{qs} + I_{qs} p\lambda_{dr} - \lambda_{qr} pI_{ds} - I_{ds} p\lambda_{qr}) \quad (10.8)$$

$$pT_r = k(\lambda_{dr} pI_{ds} + I_{ds} p\lambda_{dr} + \lambda_{qr} pI_{qs} + I_{qs} p\lambda_{qr}) \quad (10.9)$$

$$p\lambda_{rr} = 2\lambda_{qr} p\lambda_{qr} + 2\lambda_{dr} p\lambda_{dr} \quad (10.10)$$

Substituting (10.4) to (10.7) in (10.8) to (10.10)

$$pT_e = \frac{k}{L_\sigma} (\lambda_{dr} V_{qs} - \lambda_{qr} V_{ds}) - \left(r + \frac{r_r}{L_r} \right) T_e - \omega_r T_r - \frac{kL_m}{L_\sigma L_r} \omega_r \lambda_{rr} \quad (10.11)$$

$$pT_r = \frac{k}{L_\sigma} (\lambda_{qr} V_{qs} + \lambda_{dr} V_{ds}) - \left(r + \frac{r_r}{L_r} \right) T_r + \omega_r T_e + \frac{kL_m}{L_\sigma L_r} \omega_r \lambda_{rr} + \frac{r_r L_m}{kL_r \lambda_{rr}} (T_e^2 + T_r^2) \quad (10.12)$$

$$p\lambda_{rr} = 2 \left[\frac{-r_r}{L_r} \lambda_{rr} + \frac{r_r L_m}{kL_r} T_r \right] \quad (10.13)$$

To complete the model of the induction generator-boost rectifier system, the capacitor voltage equation for the boost rectifier connected to the generator, as derived in Chapter 7 needs to be expressed in terms of the natural variables. The equation is derived as follows:

$$CpV_{dc} = \frac{3}{2} (M_{qs} I_{qs} + M_{ds} I_{ds}) - \frac{V_{dc}}{R_L} \quad (10.14)$$

The desired equation is obtained by expressing the q and d-axis currents in terms of the natural variables, this is done as follows.

$$\begin{bmatrix} T_e \\ T_r \end{bmatrix} = k \begin{bmatrix} \lambda_{dr} & -\lambda_{qr} \\ \lambda_{qr} & \lambda_{dr} \end{bmatrix} \begin{bmatrix} I_{qs} \\ I_{ds} \end{bmatrix} \quad (10.15)$$

Therefore,

$$\begin{bmatrix} I_{qs} \\ I_{ds} \end{bmatrix} = \frac{k}{\lambda_{rr}} \begin{bmatrix} \lambda_{dr} & \lambda_{qr} \\ -\lambda_{qr} & \lambda_{dr} \end{bmatrix} \begin{bmatrix} T_e \\ T_r \end{bmatrix}. \quad (10.15)$$

The currents can therefore be expressed as

$$I_{qs} = \frac{k}{\lambda_{rr}} (\lambda_{dr} T_e + \lambda_{qr} T_r) \quad (10.16)$$

$$I_{ds} = \frac{k}{\lambda_{rr}} (\lambda_{dr} T_r - \lambda_{qr} T_e). \quad (10.17)$$

Substituting for the q and d-axis currents in Equation (10.14), the capacitor voltage equation expressed in terms of the natural variables is

$$C_p V_{dc}^2 + \frac{V_{dc}}{R_l} = -\frac{3}{2} \frac{k}{\lambda_{rr}} \left[M_{qs} (\lambda_{dr} T_e + \lambda_{qr} T_r) + M_{ds} (\lambda_{dr} T_r - \lambda_{qr} T_e) \right]. \quad (10.18)$$

Therefore, Equations 10.11 to 10.13 and 10.18 are the model equations of the induction generator-rectifier system in terms of the natural variables.

10.2.1 Loss Minimization using Natural Variables Model

The system, as mentioned earlier, is operated under a condition of minimum loss. The condition for minimum loss is obtained by expressing the total losses in the machine in terms of the natural variables and minimizing the loss equation [C.1].

The total losses in the system expressed in terms of the natural variables is obtained from [C.1] as

$$P_L = \frac{3}{2k^2} \cdot \frac{r_r}{\lambda_{rr}} (T_e^2 + T_r^2) + \frac{3}{2} \cdot \frac{r_r}{L_r^2} \cdot \lambda_{rr} - \frac{3}{k} \cdot \frac{r_r L_m}{L_r^2}. \quad (10.19)$$

The loss is minimized when the rotor flux λ_{rr} is given by Equation (10.19)

$$\lambda_{rr} = \sqrt{\frac{\frac{3}{2k^2} r (T_e^2 + T_r^2)}{\left(\frac{3}{2} \cdot \frac{r_r}{L_r^2} \right) - \frac{3c}{L_m} + \frac{3r}{L_r^2}}}. \quad (10.20)$$

The parameters used in Equation (10.20) are defined by Equations (10.21) to (10.22).

$$r = r_s + \frac{r_r L_m^2}{L_r^2}$$

$$c = \frac{r_r L_m}{L_r^2}$$

$$k = \frac{3PL_m}{4L_r} \quad (10.21)$$

Therefore, using Equation (10.20), the reference rotor flux is calculated. As can be seen from the equation, the reference rotor flux is dependant on the values of the electromagnetic torque and reactive torque. Therefore, for a change in the rotor speed the electromagnetic torque varies and hence the calculated reference flux varies. This can be seen from the dynamic simulation results shown in section 10.4.

10.3 Controller Design for Natural Variables Model

The proposed control scheme for the induction generator-rectifier system is derived in this section.

In this control scheme, as in the control scheme proposed in Chapter 9, the dc voltage is controlled and the modeling of the system is achieved using input-output linearization. The implementation of input-output linearization is described in detail in Chapter 9, and therefore not repeated here. The state equations derived in section 10.2 are used in the design of the controllers.

There are five loops in the control scheme, each loop is used to calculate the reference value used in the controllers. The five loops are illustrated in Figure 10.2.

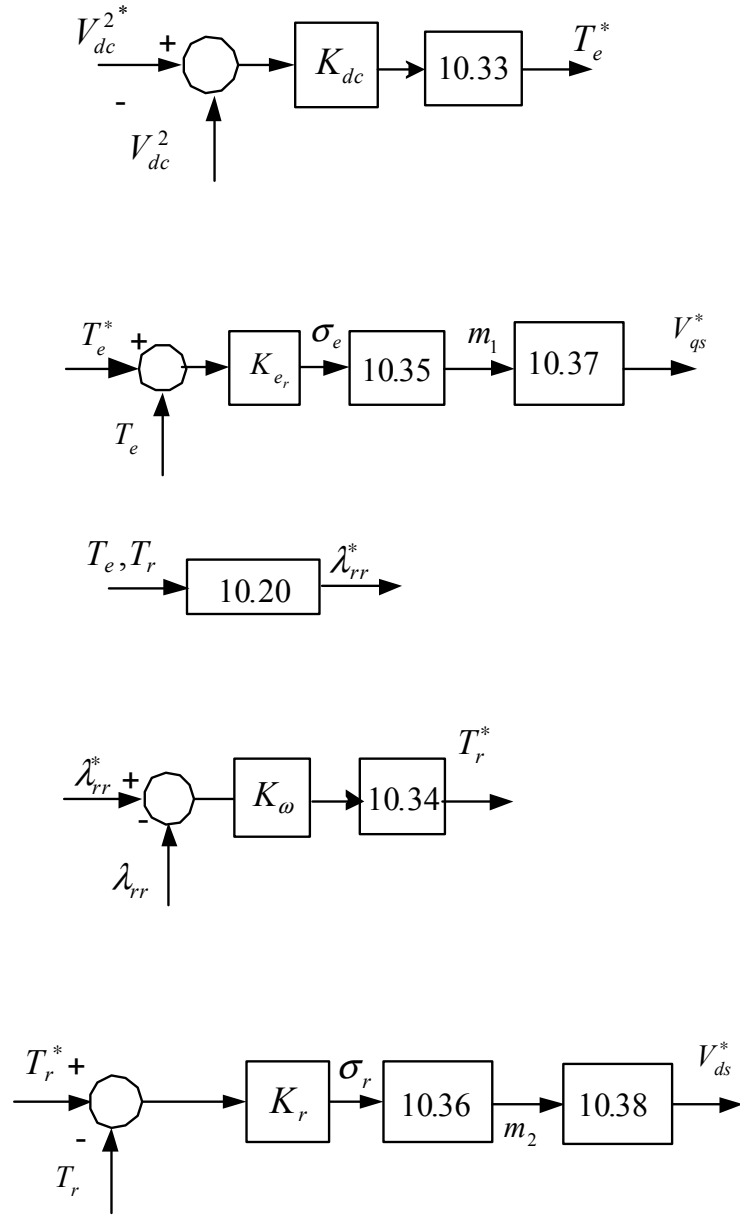


Figure 10.2: Control loops in proposed control scheme.

The first loop is the dc voltage loop, which is used to calculate the reference electromagnetic torque. The second loop shown in Figure 10.2 is used to calculate the d-axis voltage and correspondingly the modulation signal for the d-axis. Similarly, the q-axis modulation signal is calculated using the reactive power control loop. The reference reactive power is calculated using the rotor flux control loop, and the reference rotor flux

is calculated using loss minimization, explained in the previous section. The parameters m_1 and m_2 are derived in the latter part of this section.

The equations for the control scheme are summarized below.

$$pT_e = \frac{k}{L_\sigma} (\lambda_{dr} V_{qs} - \lambda_{qr} V_{ds}) - \left(r + \frac{r_r}{L_r} \right) T_e - \omega_r T_r - \frac{kL_m}{L_\sigma L_r} \omega_r \lambda_{rr} \quad (10.22)$$

$$pT_r = \frac{k}{L_\sigma} (\lambda_{qr} V_{qs} + \lambda_{dr} V_{ds}) - \left(r + \frac{r_r}{L_r} \right) T_r + \omega_r T_e + \frac{kL_m}{L_\sigma L_r} \omega_r \lambda_{rr} + \frac{r_r L_m}{kL_r \lambda_{rr}} (T_e^2 + T_r^2) \quad (10.23)$$

$$p\lambda_{rr} = 2 \left[\frac{-r_r}{L_r} \lambda_{rr} + \frac{r_r L_m}{kL_r} T_r \right] \quad (10.24)$$

$$C_p V_{dc}^2 + \frac{V_{dc}}{R_l} = -\frac{3}{2} \frac{k}{\lambda_{rr}} \left[M_{qs} (\lambda_{dr} T_e + \lambda_{qr} T_r) + M_{ds} (\lambda_{dr} T_r - \lambda_{qr} T_e) \right] \quad (10.25)$$

From Equations (10.22) to (10.25) the output of the controllers in the proposed control scheme are defined.

$$\sigma_e = pT_e + \left(r + \frac{r_r}{L_r} \right) T_e = \frac{k}{L_\sigma} M_1 - \omega_r T_r - k \frac{\omega_r L_m}{L_\sigma L_r} \lambda_{rr} \quad (10.26)$$

$$\sigma_r = pT_r + \left(r + \frac{r_r}{L_r} \right) T_r = \frac{k}{L_\sigma} M_2 + \omega_r T_e + k \frac{r_r L_m}{L_\sigma L_r} \lambda_{rr} + \frac{r_r L_m}{kL_r \lambda_{rr}} (T_e^2 + T_r^2) \quad (10.27)$$

$$\sigma_{rr} = p\lambda_{rr} + \frac{2r_r}{L_r} \lambda_{rr} = \frac{2r_r L_m}{kL_r} T_r \quad (10.28)$$

$$\sigma_{dc} = C_p V_{dc}^2 + \frac{V_{dc}}{R_l} = -\frac{3}{2} \frac{k}{\lambda_{rr}} \left[(V_{qs} \lambda_{dr} - V_{ds} \lambda_{qr}) T_e + T_r (V_{qs} \lambda_{qr} + V_{ds} \lambda_{dr}) \right] \quad (10.29)$$

where m_1 and m_2 are defined as

$$m_1 = (\lambda_{dr} V_{qs} - \lambda_{qr} V_{ds}) \quad (10.30)$$

$$m_2 = (\lambda_{qr} V_{qs} + \lambda_{dr} V_{ds}). \quad (10.31)$$

The output of the controllers are defined as follows:

σ_e = output of electromagnetic torque controller

σ_r = output of reactive torque controller

σ_{rr} = output of rotor flux controller

σ_{dc} = output of dc voltage controller.

Using the above definitions for the outputs of the four controllers in the control scheme, the equations used in calculating the reference quantities using the outputs of the controllers are derived as follows. The proposed control scheme is shown in Figure 10.3.

As explained earlier, the reference electromagnetic torque is calculated using the output of the dc voltage controller.

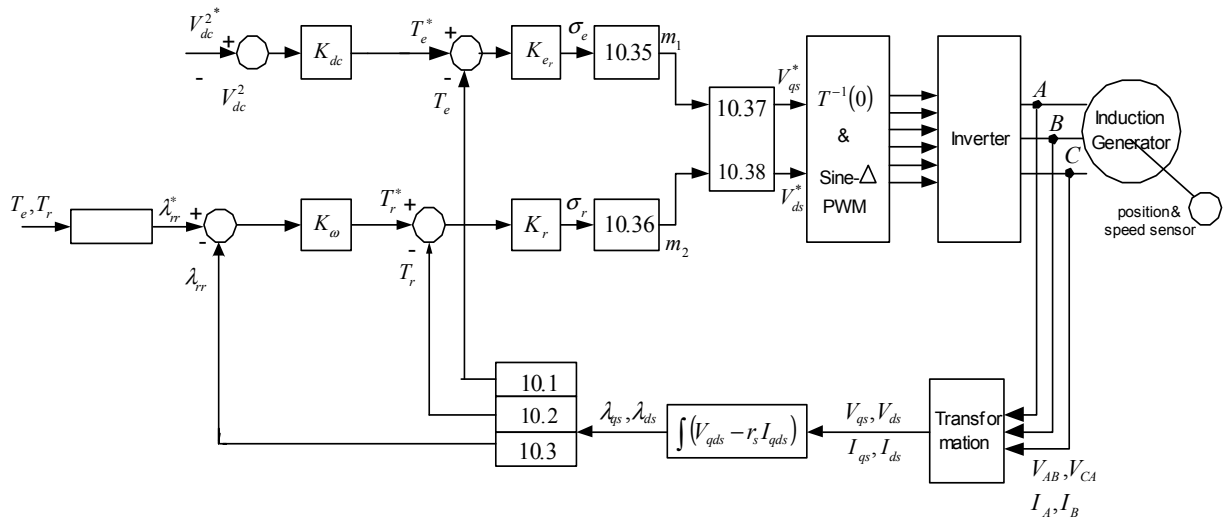


Figure 10.2: Control scheme using natural variables

Using Equation (10.29)

$$-\frac{2\lambda_{rr}}{3k}\sigma_{dc} - T_r(V_{qs}\lambda_{qr} + V_{ds}\lambda_{dr}) = T_e(V_{qs}\lambda_{dr} - V_{ds}\lambda_{dr}) \quad (10.32)$$

$$\Rightarrow T_e^* = \frac{1}{(V_{qs}\lambda_{dr} - V_{ds}\lambda_{dr})} \left[\frac{-2\lambda_{rr}}{3k}\sigma_{dc} - T_r(V_{qs}\lambda_{qr} + V_{ds}\lambda_{dr}) \right]. \quad (10.33)$$

Similarly, the reference reactive torque is calculated using the output of the rotor flux controller as

$$T_r^* = \sigma_{rr} \times \frac{kL_r}{2r_r L_m}. \quad (10.34)$$

The reference rotor flux is calculated using Equation (10.20).

The q and d-axis voltages used in calculating the modulation signals (in the stationary reference frame) are obtained using Equations (10.30) and (10.31).

The calculated values of m_1 and m_2 are obtained using the outputs of the electromagnetic torque and reactive torque controller, respectively. The equations used in calculating the variables are

$$m_1 = \frac{L_\sigma}{k} \left(\sigma_e + \omega_r T_r + k \frac{\omega_r L_m}{L_\sigma L_r} \lambda_{rr} \right) \quad (10.35)$$

$$m_2 = \frac{L_\sigma}{k} \left[\sigma_r - \omega_r T_e - k \frac{r_r L_m}{L_\sigma L_r^2} \lambda_{rr} - \frac{r_r L_m}{k L_r \lambda_{rr}} (T_e^2 + T_r^2) \right]. \quad (10.36)$$

Therefore, the q and d-axis voltages are calculated using Equations 10.37 and 10.38

$$V_{qs} = \left(\frac{m_1 \lambda_{dr} + m_2 \lambda_{qr}}{\lambda_{rr}} \right) \quad (10.37)$$

$$V_{ds} = \left(\frac{m_2 \lambda_{dr} - m_1 \lambda_{qr}}{\lambda_{rr}} \right). \quad (10.38)$$

The controllers used in this control scheme are PI (proportional integral) controllers. The PI controller has the following structure:

$$G(s) = k_p + \frac{k_i}{s}.$$

The output of each of the four controllers can be defined as

$$\sigma_r = \left(K_p + \frac{K_i}{s} \right) (T_e^* - T_e). \quad (10.39)$$

To design the PI controllers for the control scheme, the transfer function of each controller is obtained, using which the constant gain parameters of the PI controllers are calculated.

$$\left(K_p + \frac{K_i}{s} \right) \text{ can be expressed as } \left(\frac{pK_p + K_i}{p} \right), \text{ the above equation can be}$$

rewritten differential form, where $p = \frac{d}{dt}$.

The transfer function expressed as a ratio of the output divided by the input of the controller is then expressed as

$$\frac{T_e}{T_e^*} = \frac{pk_{p1} + k_{i1}}{p^2 + \left(r + \frac{r_r}{L_r} + k_{p1} \right) p + k_{i1}}. \quad (10.40)$$

Similarly, the transfer functions of the three other controllers are obtained as

$$\frac{T_r}{T_r^*} = \frac{pk_{p2} + k_{i2}}{p^2 + \left(r + \frac{r_r}{L_r} + k_{p2} \right) p + k_{i2}} \quad (10.41)$$

$$\frac{\lambda_{rr}}{\lambda_{rr}^*} = \frac{pk_{p3} + k_{i3}}{p^2 + \left(\frac{2}{L_r} + k_{p3}\right) + k_{i3}} \quad (10.42)$$

$$\frac{V_{dc}^2}{V_{dc}^2} = \frac{pk_{p4} + k_{i4}}{Cp^2 + pk_{p4} + k_{i4}}. \quad (10.43)$$

Having obtained the transfer functions for each controller, the parameters of the controller can be determined by using the Butterworth Polynomial. As explained earlier, the controllers used are PI controllers. The parameters of each controller need to be determined, i.e. k_p and k_i .

The method of determining the parameters involves comparing the coefficients of the transfer function of the controller with the coefficients of the Butterworth Polynomial (as explained in Chapter 9). The Butterworth Polynomial has the form

$$p^2 + \sqrt{2}\omega_0 p + \omega_0^2. \quad (10.44)$$

The Butterworth method locates the eigen values of the transfer function uniformly on the left half of the s-plane on a circle of radius ω_0 with its center at the origin.

Therefore comparing the coefficients of the transfer function with the coefficients of the second order Butterworth polynomial, the constant gain parameters of the controllers for the scheme are expressed as

$$k_{p1} = \sqrt{2}\omega_0 - \left(r + \frac{r_r}{L_r}\right) = 0.01 \quad (10.45)$$

$$k_{i1} = \omega_0^2 = 25000 \quad (10.46)$$

$$k_{p2} = \sqrt{2}\omega_0 - \left(r + \frac{r_r}{L_r}\right) = 0.138 \quad (10.47)$$

$$k_{i2} = \omega_o^2 = 10 \quad (10.48)$$

$$k_{p3} = \sqrt{2}\omega_o - \frac{2}{L_r} = 0.139 \quad (10.49)$$

$$k_{i3} = \omega_o^2 = 10000 \quad (10.50)$$

$$k_{p5} = \sqrt{2}C\omega_o = 0.01 \quad (10.51)$$

$$k_{i3} = C\omega_o^2 = 40000 . \quad (10.52)$$

The parameters are therefore calculated using Equations (10.45) to (10.52) by selecting values of ω_o .

The dynamic simulation for the control scheme is performed and the results are presented in the next section.

10.4 Dynamic Simulation of Control Scheme Using Natural Variables

The simulation of the proposed control scheme has been performed under two different operating conditions. The first set of results illustrates the operation of the system under a constant rotor speed and varying load conditions.

The second set of plots show the operation of the of the system under varying rotor speed and constant load conditions.

Figures 10.3 and 10.4 show the starting process for the simulation of the induction generator (natural variables model) operating with a constant rotor speed and varying load. The parameters of the machine are in Table 10.1.

Table 9.1. Machine parameters used in dynamic simulation

Per-phase stator resistance = $r_s = 1.54\Omega$	Stator leakage inductance = $L_{ls} = 0.004H$
Per-phase rotor resistance =	Rotor leakage inductance = $L_{lr} = 0.004H$

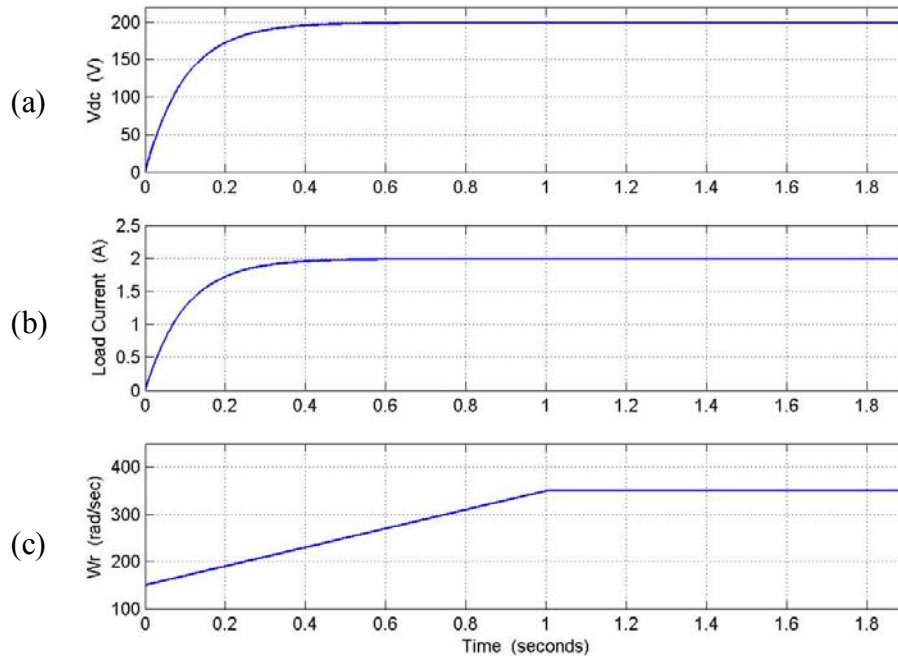


Figure 10.3: Simulation results for starting process, from top: (a) dc voltage V_{dc} (b) Load current voltage I_L , (c) rotor speed ω_r

The load resistance is 100Ω and the reference dc voltage is 200V. The dc voltage, load current reach steady state values at $t = 0.5$ seconds. The rotor speed is ramped from 100 rad/sec to 390 rad/sec, and kept constant for the entire period of the simulation.

Figure 10.4 shows the electromagnetic torque, T_e , reactive torque T_r and rotor flux at the start of the simulation. The electromagnetic torque oscillates for 0.2 seconds and reaches steady state at 0.5 seconds. The electromagnetic torque is negative as the

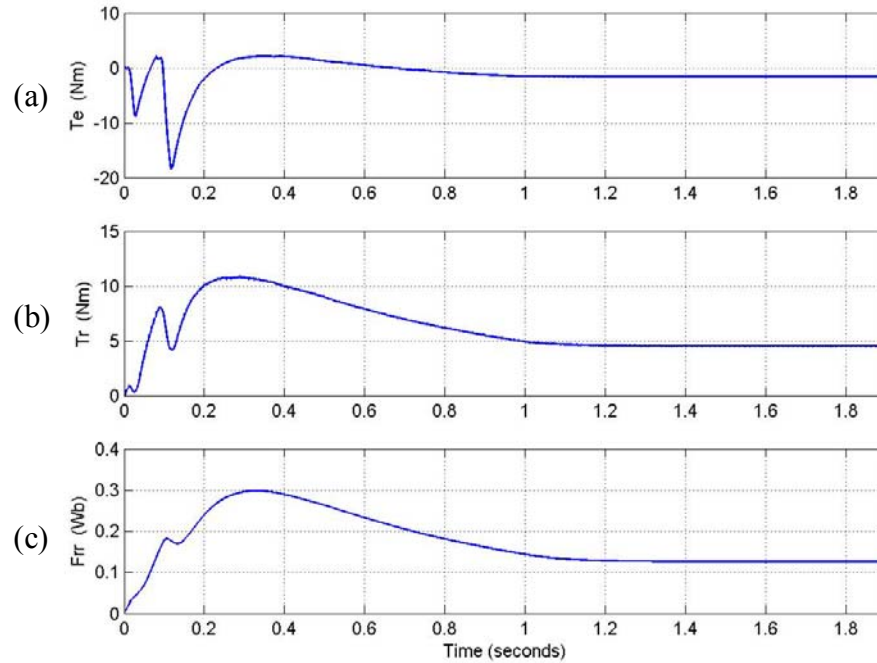


Figure 10.4: Simulation results for starting process, from top: (a) electromagnetic torque T_e , (b) reactive torque T_r , (c) rotor flux λ_{rr}

machine is generating. The reactive torque T_r is positive and takes almost one second to reach a steady state value. Similarly, the rotor flux takes almost 1 second to reach a steady value of 0.12 Wb.

The load resistance at the start of the simulation is 100Ω , at $t = 2$ seconds, the load resistance is decreased to 45Ω , and the response of the system to the change in load with a constant rotor speed is shown in Figures 10.5 and 10.6.

Figure 10.5 shows the response of the system to a change in the load resistance. The dc voltage is constant, hence showing the effectiveness of the dc voltage controller.

The decrease in the load resistance is evident from the change in the load current. The load current increases from 2A to 4.5A. As mentioned earlier, the rotor speed is kept constant at 390 rad/sec.

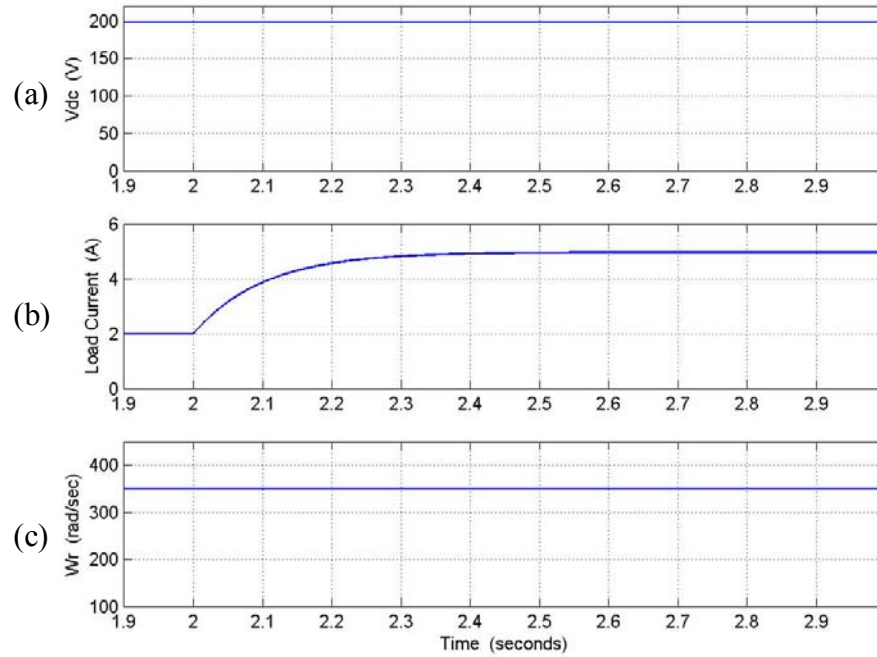


Figure 10.5: Simulation results for dynamic process, from top: (a) dc voltage V_{dc} (b) Load current I_L , (c) rotor speed ω_r

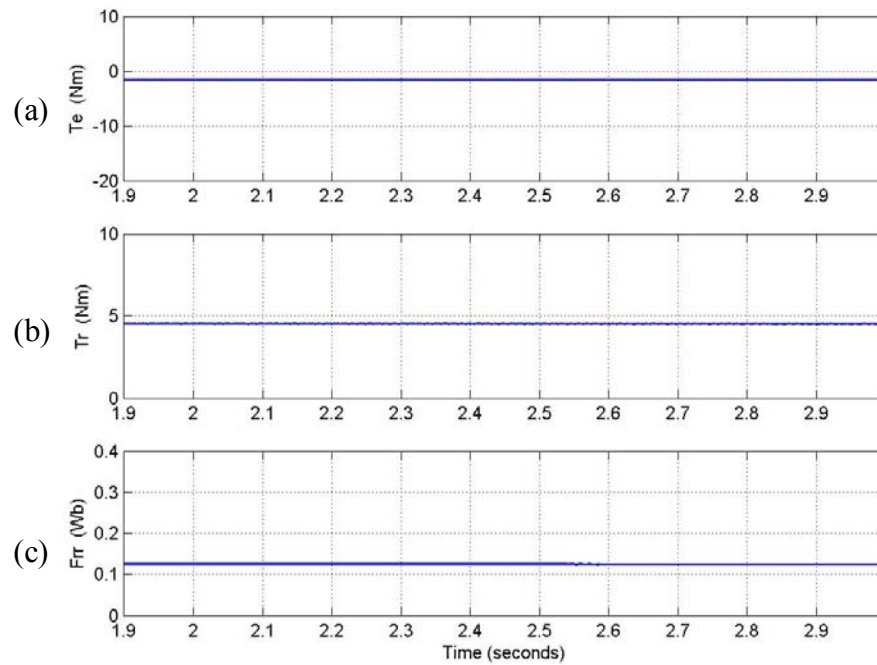


Fig 10.6: Simulation results for dynamic process, from top: (a) electromagnetic torque T_e , (b) reactive torque T_r , (c) rotor flux λ_{rT}

The second set of results are obtained by performing the simulation under constant load and varying rotor speeds. In this case, the load resistance is kept constant at 100Ω . The rotor speed is initially ramped to 390 rad/sec and at $t = 2$ seconds decreased to 300 rad/sec, and increased to 390 rad/sec at $t = 4$ seconds. The nature of response of the variables during the starting process, as illustrated in Figures 10.7 and 10.8 are similar to those obtained for the constant rotor speed varying load simulation, Figures 10.3 and 10.4.

Just as in the previous simulation, the variables plotted are the three natural variables, the rotor speed, dc voltage, and load current. In this simulation as well the reference dc voltage is 200V.

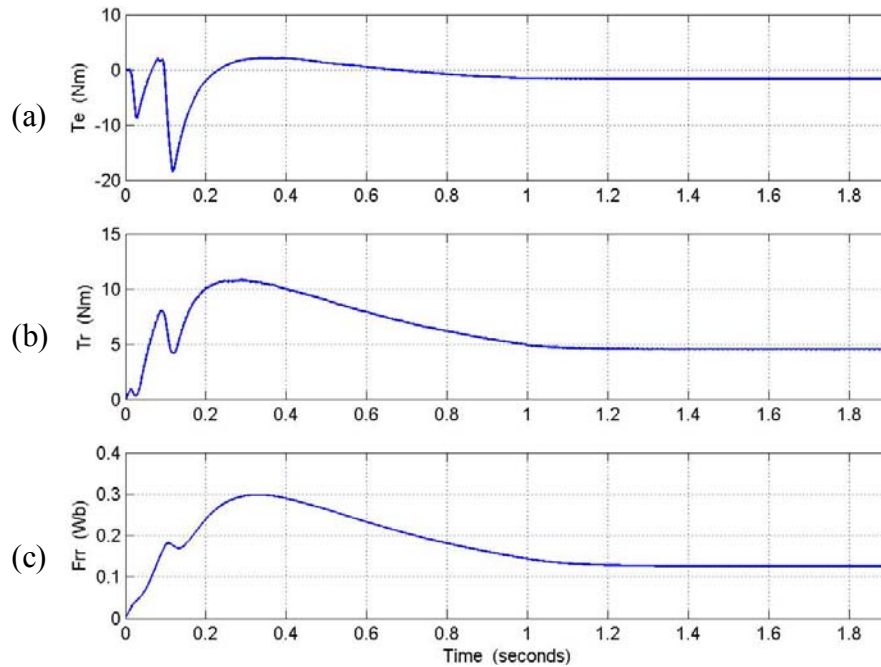


Figure 10.7: Simulation results for starting process, from top: (a) electromagnetic torque T_e , (b) reactive torque T_r , (c) rotor flux λ_{tr}

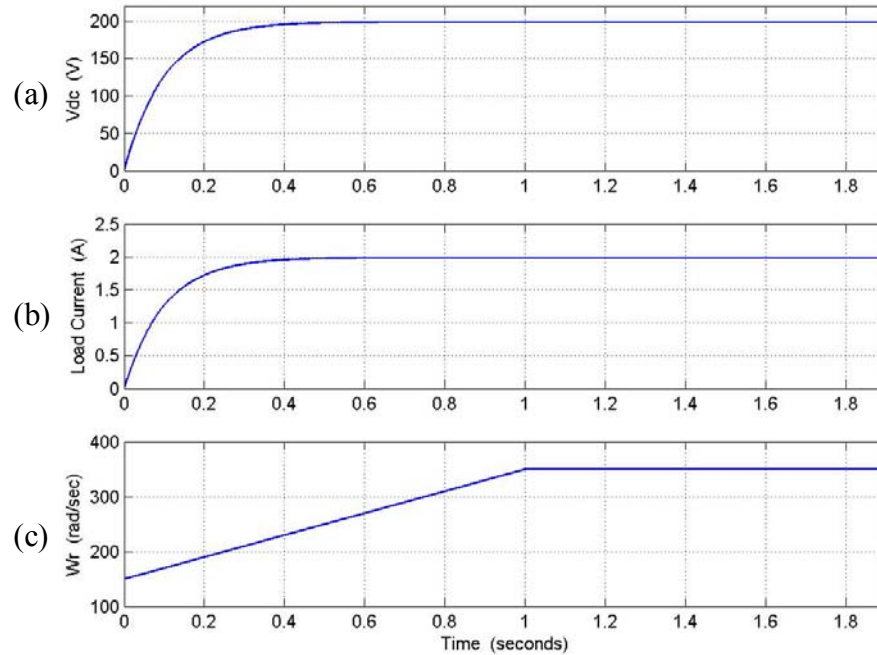


Figure 10.8: Simulation results for starting process, from top: (a) dc voltage V_{dc} (b) Load current voltage I_L , (c) rotor speed ω_r

Figures 10.9 and 10.10 illustrate the nature of response of the system to varying rotor speeds. As the reference rotor flux is calculated using the equation for loss minimization, the reference flux is a function of the electromagnetic torque and reactive torque, therefore the nature of change of the three variables, electromagnetic torque, reactive torque, and rotor flux are similar.

The dc voltage remains constant at 200V during the rotor speed change, and the load current also remains unchanged, as the load is constant.

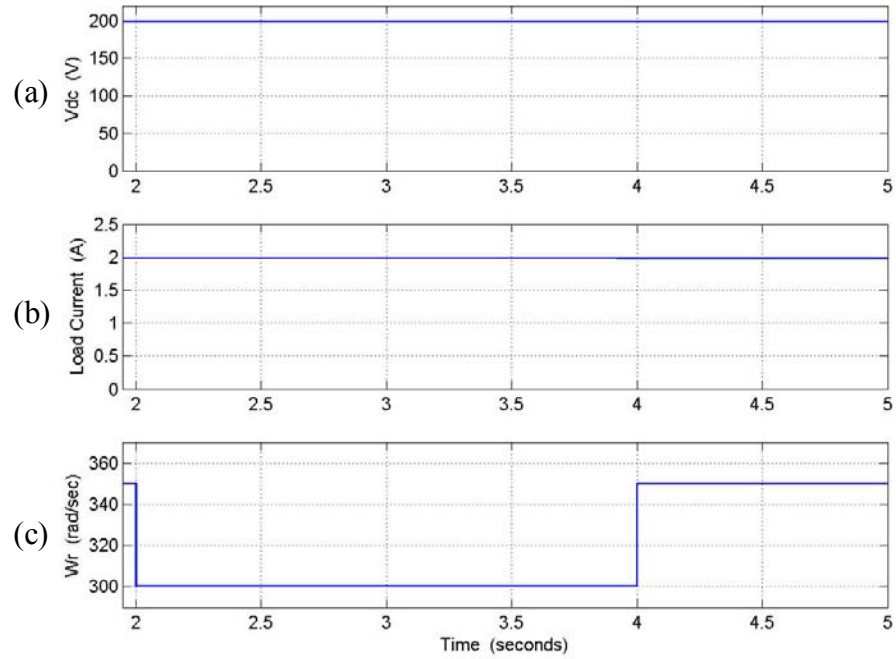


Figure 10.9: Simulation results for starting process, from top: (a) dc voltage V_{dc} (b) Load current voltage I_L , (c) rotor speed ω_r

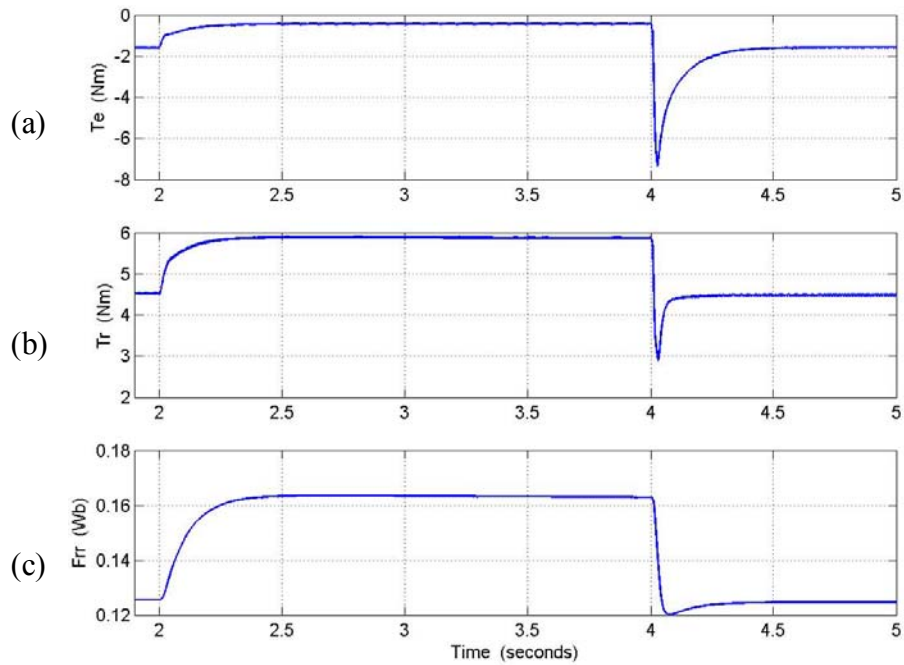


Figure 10.10: Simulation results for starting process, from top: (a) electromagnetic torque T_e (b) reactive torque T_r , (c) rotor flux λ_{Tr}

In Figure 10.10, when the rotor speed is decreased to 300 rad/sec, the electromagnetic torque decreases, and when the speed is brought back to 390 rad/sec, the torque returns to the initial value.

Similarly, for a decrease in rotor speed, the reactive torque and rotor flux increase, and return to the initial value when the rotor speed is brought back to 390 rad/sec.

CHAPTER 11

HARDWARE IMPLEMENTATION

11.1 Introduction

This chapter deals with the nature of the hardware implementation for the experimental verification of the proposed control scheme.

The closed-loop control scheme implemented is discussed in detail in Chapter 9. The control scheme uses rotor flux and stator currents as the state variables used to control the dc voltage.

The implementation has been carried out on a 2 hp induction machine, using the TMS320LF2407A floating point DSP with 40 MHz cycle frequency. The machine parameters have been determined using three tests, no-load, blocked rotor and dc test (discussed in detail in Chapter 5).

11.2 Experimental Setup

The block diagram representation of the experimental setup is shown in Figure 11.1. Each component of the setup will be discussed briefly and the nature of the DSP implementation discussed. The schematic illustrates the various components used in the system buildup.

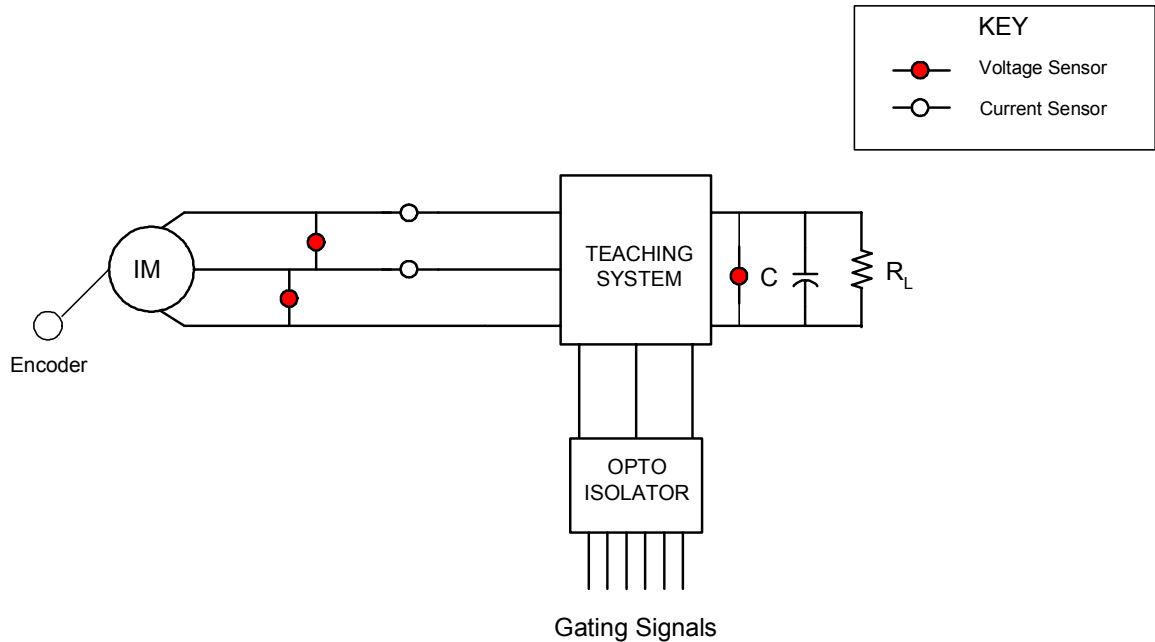


Figure 11.1: Schematic of experimental setup

11.2.1 Encoder

The rotor position, used in the calculation of the rotor flux position, is determined by using an encoder. An encoder is a device that converts motion into a sequence of digital pulses. By counting a single bit or by decoding a set of bits, the pulses can be converted to relative or absolute position measurements. The encoder used in to determine the rotor position in this experiment is an absolute encoder.

The nature of representation of the rotor position can be either grayscale or binary. The difference between the two is the number format representation of the rotor position. A Grayscale encoder converts the position of the rotor to a grayscale number format, and the binary encoder represents the position of the rotor in binary form.



Figure 11.2: Schematic of experimental setup

The encoder used in the experimental setup is the 845G Absolute Encoder. The encoder has a 19-pin connector and an open collector output. The encoder used is illustrated in Figure 11.2.

The encoder used in the experiment is a 12-bit grayscale encoder. However, the position of the rotor needs to be represented in binary format to be able to obtain the actual position and speed of the rotor. This is because, in grayscale number format, for every change in position only 1-bit changes, therefore the conversion from grayscale to binary has been performed using the DSP. The conversion can be performed using XOR gates, as well.

To read the rotor position, the 12 bits of the encoder are connected to the I/O ports of the DSP.

11.2.1 Sensors

The sensors used in this experiment are for voltage as well as current measurement. There are two sets of sensors used in voltage measurement. The sensors

used are the LV 25-P and LV 100-1000. The sensors have been designed for operation in the desired region by varying the measuring resistance values. A phase shifter circuit is used to invert the sensed currents and voltage. The parameters measured are read into the DSP using I/O ports. The DSP code takes into account the phase shifter used in the hardware.

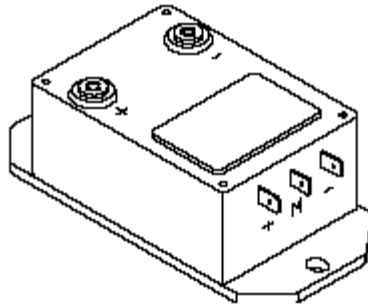


Figure 11.3: Voltage sensor used in ac voltage measurement

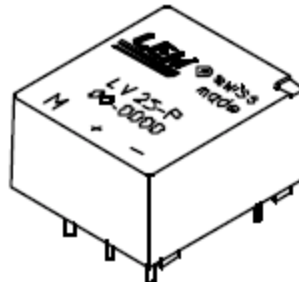


Figure 11.4: Voltage sensor used in dc voltage measurement

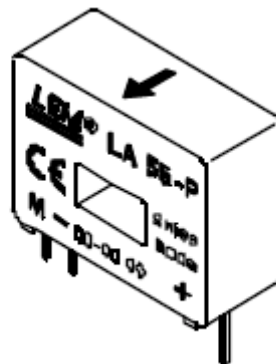


Figure 11.5: Current sensor used in line current measurement

The current sensors used are the LA 55-P, illustrated in Figure 11.5.

11.2.2 Rectifier Design

The rectifier used in the experiment is a SEMIKRON teaching system. The system is designed for different types of applications. The system has the following components.

Base drives (SKHI 22)

Semikron IGBT's (SKM 50 GB 123 D0)

Capacitor on dc side of the rectifier (2200 750V)

The gate pulses from the DSP are connected to the base drive of the teaching system for the switching of the devices. The gate pulses are connected to the base drives through an opto-isolator, TLP 250. The base drive is used to drive one leg of the rectifier. Also the base drive has in-built short-circuit protection used in protecting the devices in case of a short circuit. This operates by the measurement of the collector to emitter voltage for each device. Each base drive generates an error signal, which is connected to the DSP to shut down the system in case of a fault. As there are three error signals, the error signals are connected through AND gates to the DSP.

The IGBT used in the teaching system is a block that forms one leg i.e. two devices of the rectifier.

The development of the DSP code used in the control of the DC voltage of the rectifier has been formulated in assembly language. The implementation has included flux estimation to determine the fluxes used in the control scheme to calculate the operating slip of the generator.

CHAPTER 12

CONCLUSION AND SCOPE FOR FUTURE WORK

This chapter aims at summarizing the contributions made by this thesis. The different areas worked on will be dealt with in separate sections. The previous work done in this area has been detailed in Chapter 2 to establish some background on the work carried out in this thesis.

The scope for future work is discussed and some suggestions are made based on the work developed in this thesis. The first section discusses the work done in the area of boost rectifiers, summarizing the models and results obtained for the proposed connection schemes.

The second section summarizes the work done on the steady-state excitation and vector control of the proposed induction generator-ac/dc boost rectifier system. Also the control scheme using natural variables is discussed.

12.1 Series-Parallel Boost Rectifiers

The work done on the series-parallel connection of boost rectifiers includes the development of the model of a single rectifier in the abc and qd (synchronous reference frame). The models of the series and parallel rectifier are then developed based on the model of the single rectifier. The connection of the series and parallel rectifiers is at the output, therefore the rectifiers are operated using independent sources. The effect of the zero-sequence circulating current is considered for the third scheme dealt with in Chapter

4. The first topology considered does not allow a path for the flow of the circulating current; however the second is studied under different conditions of neutral voltage.

The operation at unity power factor is of vital importance; therefore the proposed connection schemes are studied analytically for this operating condition at steady state. The conditions for unity power factor being obtained, the dynamic simulation of both the series as well as parallel connections of the rectifiers are carried out. Results for both topologies show the unity power factor operation of the schemes corresponding to a single point in the steady-state plots obtained. The parallel topology is operated using independent sources of varying frequencies. The parallel rectifier topology is shown to have an additional degree of freedom, which is used to control the power delivered by each rectifier by considering a power-partitioning factor α . The effect of the factor α on the q and d-axis modulation signals is illustrated by steady-state plots in Chapter 4.

12.2 Induction Generator-Boost Rectifier System

The property of an induction generator to self-excite is discussed in detail, following which the model of the induction generator boost rectifier system is proposed. The model of the system is obtained in the abc and qd reference frames. The model used is studied extensively at steady state. The steady-state analysis performed studies the system under varied operating conditions to determine the excitation requirements of the generator. The magnitude of the modulation index is used as a measure of the self-excitation requirements of the induction generator.

Inclusion of the effect of magnetic saturation on the performance of the system is highlighted. Also the analysis conducted studies the system at rated slip as well as under

a condition of minimum copper loss. The condition for minimum copper loss is derived and correspondingly, to satisfy the desired condition, the system requires operating at a particular value of operating slip. The in-depth analysis studies the nature of variation of the magnitude of the modulation index with changes in magnetizing flux as well as changing operating slip, i.e. for a given value of magnetizing flux, the slip for the operation of the machine at minimum copper loss is calculated. Using the calculated value of the slip, the magnitude of the modulation index required by the generator to self-excite is calculated. The variation of the modulation index with varying rotor speed and load conditions is illustrated.

The VSI assisted induction generator scheme for the generation of AC voltages proposed in Chapter 6 is studied extensively at steady state, the bi-directional power flow is illustrated under varying load conditions, and the effect of the operating slip on the system is studied.

A rotor flux vector control scheme is proposed for the system under consideration. The method of input-output linearization is used to decouple the model equations of the system. The control scheme proposed aims at the regulation of the dc voltage of the rectifier. This is achieved by a closed-loop control scheme involving determination of the reference q and d-axis voltages to determine the modulation signals for the rectifier. The parameters of the controller are obtained by comparison of the coefficients of the transfer functions of the controllers with the coefficients of the second order Butterworth Polynomial. The simulation performed studies the system under varying conditions of load and rotor speed. The effectiveness of the control scheme is illustrated by the dc voltage regulation at the reference value. The proposed control

scheme is experimentally verified using a 2 hp induction machine connected to a boost rectifier. The hardware design of the system and the different components used in the build-up of the experimental setup in discussed in Chapter 11.

The second control scheme proposed uses the natural variables model of the induction machine. The natural variables model of the induction machine is developed, and used in the control scheme proposed for the induction generator-rectifier system. The application of the natural variable model involves the stationary reference frame, thereby simplifying the analysis as compared to the rotor flux vector control scheme proposed. The advantage of using the natural variables model is the elimination of the synchronous reference frame transformation. To augment the advantages, the system is chosen to operate under conditions of minimum loss. This is achieved by calculation of the reference rotor flux using an equation for the rotor flux derived for operation of the system under minimum loss. The inclusion of this function is shown in the schematic of the control scheme. The proposed scheme is tested under condition of varying load and changing rotor speed. The dc voltage regulation is achieved, verifying the effectiveness of the proposed control scheme.

12.3 Scope for Future Work

The scope for future work is highlighted in this section. The suggestions made are discussed with respect to the work done in this thesis.

The study on the boost rectifier systems, the series as well as parallel configurations are made using an open-loop system, whereby the control of the dc

voltage at the output is obtained by selection of the modulation signals fed to each rectifier. However under practical conditions, varying loads on the rectifiers would require a closed-loop system whereby the unity power factor operation as well as the dc voltage regulation of the proposed schemes can be achieved. Also the power-partitioning factor α in the case of the parallel rectifiers can be used to minimize the loss in the overall system.

Also the operation of the parallel system using input sources of varying frequencies has been achieved, a similar system for the series rectifiers can be developed, as using different frequency inputs widens possible application areas for the series and parallel rectifiers.

The steady-state excitation conditions have been studied under a operation of the system at minimum copper loss. However, the core loss in the system has not been considered. The effect of the core-loss is more involved and would have an impact on the operation of the system.

The induction generator-rectifier system can be studied using the parallel connection of three-phase boost rectifiers studied in Chapter 4, where the rectifiers are assumed to have the same source. Such a scheme would increase the reliability of the system.

The VSI-assisted induction generator scheme in Chapter 6 is studied at steady state, the open-loop simulation of the system can be performed to verify the model and steady state analysis developed. Also the model proposed studies a voltage source converter, a similar scheme using a current source inverter can be studied. The

practicality and effectiveness of the current source converter replacing the voltage source converter is yet to be determined.

The rotor flux control scheme proposed uses a reference value of d-axis rotor flux. To operate the system under conditions of minimum loss, an additional calculation step is required, whereby the reference flux is calculated using a loss minimization equation, as in the case of the control scheme using the natural variable model of the system.

The natural variables model of the induction generator-rectifier system proposed for dc power generation, has been simulated, experimental studies can be made for verification of the control scheme for varying operating conditions. The system is modeled using the rotor flux as a state variable; a similar scheme can be developed for the stator flux, as stator flux reduces the calculations in the analysis.

REFERENCES

Books

- [A.1] P. Wood, *Switching Power Converters*, Van Nostrand Reinhold Company, 1981.

- [A.2] Vas Peter, *Parameter Estimation, Condition Monitoring and Diagnosis of Electric Machines*, Oxford: Clarendon Press; New York: Oxford University Press, 1993.

- [A.3] P. C. Krause, O. Wasynczuk, and S. D. Sudhoff, *Analysis of Electric Machinery*, IEEE Press, 1995.

- [A.4] Marian. P. Kazmierkowski, R. Krishnan and Frede Blaabjerg, *Control in Power Eletronics Selected Problems*, Academic Press, New York, 2002.

- [A.5] R. Marino and P. Tomei, *Non-linear Control Design, Geometric, Adaptive and Robust*, Prentice Hall, New York, 1995.

- [A.6] B. Friedland, *Control System Design, An Introduction to State-Space Methods*, McGraw-Hill, New York, 1986.

- [A.7] R. Krishnan, *Electric Motor Drives, Modeling, Analysis and Control*, Prentice Hall, New Jersey, 2001

- [A.8] B. K. Bose, *Power Electronics and Variable Frequency Drives*, IEEE Press, Piscataway, NJ, 1996

- [A.9] N. Mohan, T. M. Undeland and W. P. Robbins, *Power Electronics Converters, Applications and Design*, 2nd ed. New York: John Wiley& Sons 1995.

- [A.10] D. W. Novotny, T. A. Lipo, *Vector Control Dynamics of AC Drives*, Oxford: Clarendon Press; New York: Oxford University Press, 1996.

- [A.11] M. Vygodsky, *Mathematical Handbook -Higher Mathematics*, Mir Publishers 1975.

- [A.12] Chua, Leon. O, *Linear and Nonlinear Circuits*, McGraw-Hill, New York, 1987.

Series and Parallel Boost Rectifiers

- [B.1] Juan W. Dixan and Boon T. Ooi, “ Series and Parallel Operation of Hysteresis Current-Controlled PWM Rectifiers,” *IEEE Transactions on Industrial Applications*, vol. 25, no. 4, pp. 644–651, July/August 1989.

- [B.2] Shu-Zu Dai, Nelson Lujara, and Boon-Teck Ooi, “ A Unity Power Factor Current-Regulated SPWM Rectifier with a Notch Feedback for Stabilization and Active Filtering,” *IEEE Transactions on Power Electronics*, vol. 7, no. 2, pp. 356–363, April 1992.

- [B.3] In-Gyu-Park, Sang-Yong-Park, and Jong-Keun-Park, “ An Analysis of a Boost Rectifier,” *Proc IEEE IECON 1991 Annual Meeting*, Kobe, Japan, pp.519-524, 1991.

- [B.4] S.Fukuda and K. Koizumi, “ Optimal Control of a Three Phase Boost Rectifier for Unity Power Factor and Reduced Harmonics,” *Proc International Conference Power Electronics and Drive Systems*, vol. 1, pp. 34-39, February 1995.

- [B.5] S. Kwak and H. A. Toliyat, “ Optimised power distribution to minimise power rating of parallel rectifier,” *Electronic Letters*, vol 40, no 5, pp. 336-338, 2004.

- [B.6] Zhihong Ye, Dushan Boroyevich, Jae-Young Choi, and Fred C. Lee, “ Control of Circulating Current in Two Parallel Three-Phase Boost Rectifiers,” *IEEE Transactions on Power Electronics*, vol. 17, no. 5, pp. 609–615, September 2002.

- [B.7] Zhihong Ye, Dushan Boroyevich, “ A Novel Modeling and Control Approach for Parallel Three-Phase Buck Rectifiers,” *Thirty sixth IAS Annual Meeting*, vol. 1, pp. 350-356, 30 , 2001.

- [B.8] Bin Shi, Giri Venkataramanan, “ Parallel Operation of Voltage Source Inverters with Minimum Intermodule Reactors,” *39th IAS Annual Meeting*, Seattle WA, vol.1, pp. 162-168, 2004.

- [B.9] Peter M. Barbosa and Fred C. Lee, “ Design Aspects of Paralleled Three-Phase DCM Boost Rectifiers,”*30th Annual IEEE PESC*, Kobe, Japan, vol. 1, pp. 331-336, 1999.
- [B.10] Olorunfemi Ojo, Olufemi Osaloni, Parag Kshirsagar, “ The Generalized Discontinuous PWM Modulation Scheme for Theree-Phase Voltage Source Inverters,” *Proc IEEE IECON 2003 Annual Conference*, Vol 2. pp.1629-1636, 2005.

Induction Generator

- [C.1] Olorunfemi Ojo, Gan Dong, “ Sensorless Control of Induction Motor Using Natural Variables with Loss Minimisation,” *Proc IEEE APEC 2005 Annual Meeting*, Austin, TX, pp. 451-457, 2005.
- [C.2] Dawit Seyoum and Muhammad Fazlur Rahman, “ The Dynamic Characteristics of an Isolated Self-Excited Induction Generator Driven by a Wind Turbine,” *IEEE Transactions on Industry Applications*, vol. 25, no. 4, pp. 936–941, July/August 2003.
- [C.3] Olorunfemi Ojo, “ Dynamic and System Bifurcation in Autonomous Induction Generators,” *IEEE Transactions Industry Applications*, Vol 31, pp. 918-924, July/August 1995.
- [C.4] D. Seyoum, M. F. Rahman, and C. Grantham, “ Inverter supplied voltage controlsystem for an isolated induction generator driven by a wind turbine,” *Proc. IEEE IAS 2003 Annual Meeting* , Salt Lake City, pp 568-576, 2003.
- [C.5] D. W. Novotny, D. J. Gritter, and G. H. Stodtmann, “ Self Excitation in Inverter Driven Induction Machines”” *IEEE Trans. Power Apparatus and Systems Applications*, Vol PAS-96, pp. 1117-1125, July/August 1977.
- [C.6] R. C. Bansal, “ Three-Phase Self-Excited Induction Generators: An Overview,” *IEEE Trans. Energy Conversion*, Vol. 2, pp. 292-299, June 2005.
- [C.7] Yanhong Xue, Shaotang Chen, “ Instability Issues for Control System in Induction Generator,”*Proc. IEEE IAS 2001 Annual Meeting* , Chicago, pp 110-117, 2001.

- [C.8] Shashank Wekhande, Vivek Agarwal, "A Simple Wind Driven Self Excited Induction Generator with Regulated Output Voltage," *IEEE Telecommunications Energy Conference*, 1999 pp. 364-369, 1999.
- [C.9] S. N. Bhadra, K. V. Ratnam, and A. Manjunath, "Study of voltage build up in a self-excited, variable speed induction generator/ static inverter system with dc side capacitor," *Proc. 1996 International Conference on Power Electronics Drives and Systems*, Vol 2, pp. 964-970, 1996.
- [C.10] Mohamed Orabi, M. Z. Youssef, and P. K. Jain, "Investigation of Self-Excited Induction Generators for Wind Turbine Applications," *34th IAS Annual Meeting*, vol. 1, pp. 509-515, 1999.
- [C.11] Shashank Wekhande, Vivek Agarwal, "A Variable Speed Constant Voltage Controller for Self-Excited Induction Generator with Minimum Control Requirements," *IEEE Proc. PEDS '99*, Hong Kong, pp. 98-103, 1999.
- [C.12] A. H. Al-Bahrani, N. H. Malik, "Steady State Analysis and Performance Characteristics of a Three-Phase Induction Generator Self Excited With a Single Capacitor," *IEEE Transactions Energy Conversion*, vol 5, no 4, pp. 725-732, 1990.
- [C.13] G. V. Jayaramaiah and B. G. Fernandes, "Analysis of Voltage Regulator for a 3- Φ Self-Excited Induction Generator Using Current Controlled Voltage Source Inverter," *Proc. IEEE IPEMC 2004 Annual Meeting*, vol 3, pp 1404-1408, 2004.
- [C.14] Lahcene Ouazene and George McPherson, "Analysis of the Isolated Induction Generator," *IEEE Transactions on Power Apparatus and Systems*, vol. PAS-102, no. 8, pp. 2793-2798, July/August 1983.
- [C.15] S. S. Murthy, O. P. Malik and A. K. Tandon, "Analysis of Self-Excited Induction Generators," *Proc IEE, Part C*, no 6, pp. 260-265, 1982.
- [C.16] J. A. A. Melkebeek, "Magnetizing-Field Saturation and Dynamic Behaviour of Induction Machines," *Proc IEE, Part B*, vol 130, no 1, pp. 1-10, 1983.

- [C.17] J. A. A. Melkebeek and D. W. Novotny, “ Steady- State Modeling of Regeneration and Self-Excitation in Induction Machines,” *IEEE Transactions on Power Apparatus and Systems*, vol. PAS-102, no. 8, pp. 2725–2733, July/August 1983.
- [C.18] Olorunfemi Ojo and Gan Dong, “ Efficiency Optimizing Control of Induction Motor Using Natural Variables,” *Proc IEEE APEC 2004 Annual Meeting*, Anaheim, CA, pp.1622-1627, 2004.
- [C.19] Ashok Mishra and Olorunfemi Ojo, “ Analysis of an Induction Motor Fed From A Six-Step Voltage Source Inverter,” *Proc IEEE Southeastcon 1991 Annual Meeting*, Williamsburg,VA, pp.1001-1004, 1991.
- [C.20] Fuminobu Naito and Kenichi Abe, “ Control of Self-Excited Induction Generators,” *Proc IEEE PES 2002 Annual Meeting*, vol 3, pp.2368-2372, 2002.
- [C.21] Olorunfemi Ojo, “ Minimum Airgap Flux Requirement for Self-Excitation Stand-Alone Induction Generators,” *IEEE Transactions on Energy Conversion*, vol. 10, no. 3, pp. 484–492, September 1995.
- [C.22] S. S. Murthy, C. Nagamani and K. V. Satyanarayana, “ Studies on the Use of Induction Motors as Self-Excited Inductio Generators,” *IEEE Transactions on Energy Conversion*, vol. 3, no. 4, pp. 842–848, December 1988.
- [C.23] D. Seyoum, C. Grantham and F. Rahman, “ An Insight Into the Dynamics of Loaded and Free Running Isolated Self-Excited Induction Generators,” *International Conference on Power Electronics, Machines and Drives*, 2002, pp. 580 – 585, 2002.
- [C.24] T. F. Chan, “ Capacitance Requirements of a Three-Phase Induction Generator Self-Excited With a Single Capacitance and Supplying a Single-Phase Load,” *IEEE Transactions on Energy Conversion*, vol. 17, no. 1, pp. 90–94, March 2002.
- [C.25] S. R. Silva and R. O. Lyra, “PWM Converter Excitation of Induction Generators,” *Power Electronics and Applications, 1993*, vol. 8 , pp. 174 – 178, 1993.

- [C.26] Olorunfemi Ojo and Innocent Ewean Davidson, “ PWM-VSI Inverter-Assisted Stand-Alone Dual Stator Winding Induction Generator,” *IEEE Transactions on Industry Applications*, Vol. 36, NO. 6, November/December 2000
- [C.27] Yang Ye, Mehrad Kazerani, Victor H. Quintana, “ Current –Source Converter Based STATCOM: Modeling and Control,” *IEEE Transactions on Power Delivery*, Vol. 20, no 2, April 2002
- [C.28] Ziyad M. Salameh, Margaret A. Casacca, and William A. Lynch, “ A Mathematical Model for Lead-Acid Batteries,” *IEEE Transactions on Energy Conversions*, Vol. 7, no 1, March 1992.
- [C.29] Olorunfemi Ojo, Innocent E. Davidson, “ A Dual Stator Winding Induction Generator with a Four Switch Inverter-Battery scheme For Control” *39th Annual PESC*, 2000, vol 1, pp. 230 – 234, 2000.
- [C.30] E. Muljadi and T. A. Lipo, “Series Compensated PWM Inverter with Battery supply applied to an isolated induction generator,” *IEEE Transactions on Industry Applications*, Vol 30, Issue 4, pp. 1073-1082, July/August 1994.

VITA

Jyoti Sastry was born in NewDelhi, India, on November 18, 1981. In 1999, she joined the four-year Bachelor of Engineering degree program in Electrical and Electronics Engineering at Birla Institute of Technology, Mesra and graduated in May 2003. In Fall 2003, she joined Tennessee Technological University. She is currently working in the field of Power Electronics and Drives.